HIGH TEMPERATURE OXIDATION OF Pt-BASED ALLOYS

Jamiu Kolawole Odusote

A thesis submitted to the Faculty of Science, University of the Witwatersrand, in fulfilment of the requirements for the degree of Doctor of Philosophy in Science.

June 2011

DECLARATION

I, Jamiu Kolawole ODUSOTE, declare that this thesis is my own work, unless where otherwise acknowledges. It is being submitted for the degree of Doctor of Philosophy in Science at the University of the Witwatersrand, Johannesburg. It has not been submitted before for any degree or examination in any other University.

------------------------ ------------ day of ------------------------, 2011

Signature

ABSTRACT

High temperature oxidation of Pt_{84}:Al_{11}:Cr_3:Ru_2 (at.%) in air between 1150°C-1350°C, for up to 500 hours in both water-quenched and air-cooled specimens was investigated. Mass gains and thicknesses of the Al_2O_3 scales were measured. Surface and cross-section morphologies of the oxide scales were examined using a field-emission scanning electron microscopy with EDS. Cross-sectional examination was also done by cutting the samples in a cross beam FIB workstation. Phase identification was done with X-ray diffraction and Raman spectrometry. Room temperature stresses in the oxide scales were measured by using an argon-ion laser, and were found to be compressive and low.

Well-adhering and protective external α-Al_2O_3 scales formed on all specimens, without spallation. Cross sections showed protrusions of the alloy into the scale; which allowed mechanical keying of the scale to the substrate, and were mainly responsible for the good adherence. No internal oxidation was observed. Parabolic scale growth kinetics were established, and rate constants and activation energies were deduced. Oxidation rates in both the quenching media were close at lower exposure temperatures, while at higher temperatures, the scale growth rate of the air-cooled specimens was faster.

Microscopic observations showed that the oxide grain sizes increased with increased oxidation time at all temperatures, and the morphology changed from small flakes to large oxide grains with time. The growth mechanism of the α-Al_2O_3 scale was proposed to be mainly by inward diffusion of oxygen along the oxide grain boundaries, with some outward diffusion of aluminium ions along the short circuit paths.

Oxidation of both water-quenched and air-cooled Pt_{84}:Al_{11}:Cr_3:Ru_2 (at.%) specimens followed the same trends, with water-quenched specimens displaying slightly better properties. Compared to most other Pt-, Ni-and Fe-based superalloys, the scales on Pt_{84}:Al_{11}:Cr_3:Ru_2 (at.%) specimens possessed slower growth rates, lower activation energies and room-temperature compressive stresses. Thus, Pt_{84}:Al_{11}:Cr_3:Ru_2 (at.%) possesses potential for high temperature applications.

DEDICATIONS

To Almighty God for making this research a success, despite all odds.

To my parents for their care and prayers.

To my beloved wife and children for their understanding and support.

ACKNOWLEDGEMENTS

First and foremost, my profound gratitude to God Almighty, He was, He is and He shall.

I wish to express my gratitude and deep appreciation to my supervisor, Professor Lesley Cornish, for nurturing me till the end of this research work, when all hope seems to have lost. I will remain grateful to you, for your effective supervision, mentorship, dedication, understanding and moral support. Thank you and cheers!

I would like to thank Professors J. Rodrigues (Head of School, School of Physics) and John Carter (Fomer postgraduate coordinator, School of Physics) for managing the situation effectively, when things were getting out of order. Thank you so much for rescuing the sinking boat. Professor D. Joubert (Postgraduate coordinator, School of Physics) is also thanked for accepting to be my administrative supervisor.

My appreciation also goes to Drs G. Malgas and S.K. Pillai and Mr T. Malwela for putting in extra hours during the microscopic observation of my samples at the characterization unit, Nanocentre, CSIR, Pretoria. Also, Messrs C. Oliphant and R. Erasmus are thanked for their assistance during the SEM analysis at NMISA and Raman and Luminescence spectroscopy at University of the Witwatersrand, respectively. I also wish to Professor Dave Billing for training and access to the XRD instrument at the School of Chemistry, Wits University. Dr. Levitt and Professor M.J. Witcomb are thanked for their support during the sample preparation.

I am indeed grateful to Department of Science and Technology (DST)/National Research Foundation (NRF) Centre of Excellence in Strong Materials for funding this research and providing other financial support. The administrative manager and staff of the Centre are thanked for their love and support. I also wish to express my appreciation to the Financial Aid Office, University of the Witwatersrand, for her financial support. Mintek is thanked for support, especially Drs R. R. Süss and L. Chown.

My profound appreciation goes to all the postgraduate students of my supervisor, for their love, understanding and companionship. Mr. Josias Van der Merwe of the School of Chemical and Metallurgical Engineering, University of the Witwatersrand, is highly appreciated for giving me permission to use the high temperature furnace for the oxidation tests. The assistance of Mr

Olugbenga Johnson in getting my specimens well prepared before and after oxidation is acknowledged. I also wish to thank the technical and support staff of the School of Physics and the School of Chemical and Metallurgical Engineering, University of the Witwatersrand, for their contributions to the success of this work.

AIso, I wish to thank my parents and guardians for their care and love since my childhood. Thank you papa and mama!

To all my friends and family, especially Mr Bilianu Oborien, Dr Adam Muritala, Mr Suraju Obayopo, Mr. Suraju Aderoju, Dr A. Ajibola, Engr Gafar Oniyide, Engr M. Olajumoke and host of others. Thank you all for your good companionship and support.

Finally, but not the least, my profound gratitude and appreciation go to my beloved wife, Dr Fatimat Abolanle ODUSOTE, for understanding, support, endurance and above all, taking good care of my parents and children throughout this period. I promise to continue to love you more. To my children, Oyinkansola, Oyindamola and Oyinlola, thank you for your endurance and cooperation with mummy, while I was away. I LOVE YOU ALL!!!.

TABLE OF CONTENTS

LIST OF FIGURES

LIST OF TABLES

CHAPTER ONE

1.0 Introduction

The demand for materials capable of withstanding aggressive environments and higher operating temperatures above the capabilities of existing materials has led to considerable research and alloys development. The on-going researches to further increase the high temperature capabilities of the currently used nickel-based superalloys (NBSAs) materials are yielding little improvement [2006Ree]. This is because these alloys have already been exposed to temperatures up to 90% of the melting temperature of the base metal Nickel, Ni, in some applications, especially in aircraft gas turbine engines [1987Sim]. Application of coatings on the Ni-based superalloys gas turbine hot section components improved their high temperature capabilities, as shown in Figure 1.1. Coatings also improved the environmental stability by protecting the substrate alloys against environmental degradation [1995Fri]. Unfortunately, coatings are not reliable in aerospace applications, where catastrophic components failure is a serious problem. Thus, NBSAs are nearing their applications limit in aerospace industry and hence, alternative materials have to be developed.

Pt-based alloys with a structure similar to the nickel-based superalloys are being developed for potential ultra-high temperature application in aggressive environments [2000Wol, 2000Hil, 2003Cor]. The goal is to produce a range of alloys with superior high temperature mechanical strength; that is, high and reliable tensile, rupture, creep and thermo-mechanical fatigue properties as well as better environmental stability (high temperature oxidation and hot corrosion resistance) than NBSAs. The Pt-based alloys are being developed as a possible replacement for some of the currently used nickel based superalloy components, in applications where higher operating temperatures of about 1300°C to 1350°C, as well as better environmental resistance are critical but higher density effect is less harmful.

Platinum was selected as the base metal because of its higher melting point {1796°C for Pt compared to 1455°C for Ni, face centred cubic (f.c.c.) crystal structure similar to that of Ni}, and excellent environmental stability [1962Kni]. However, high density and cost are the major drawbacks to the use of Pt, but it is likely that the Pt-based alloys can still find applications in aerospace industry [1988Wha]. The density could be slightly reduced by addition of light-weight elements in alloying. Pt is recyclable and imparts good properties to the alloy; these could compensate for the high cost [2002Cor].

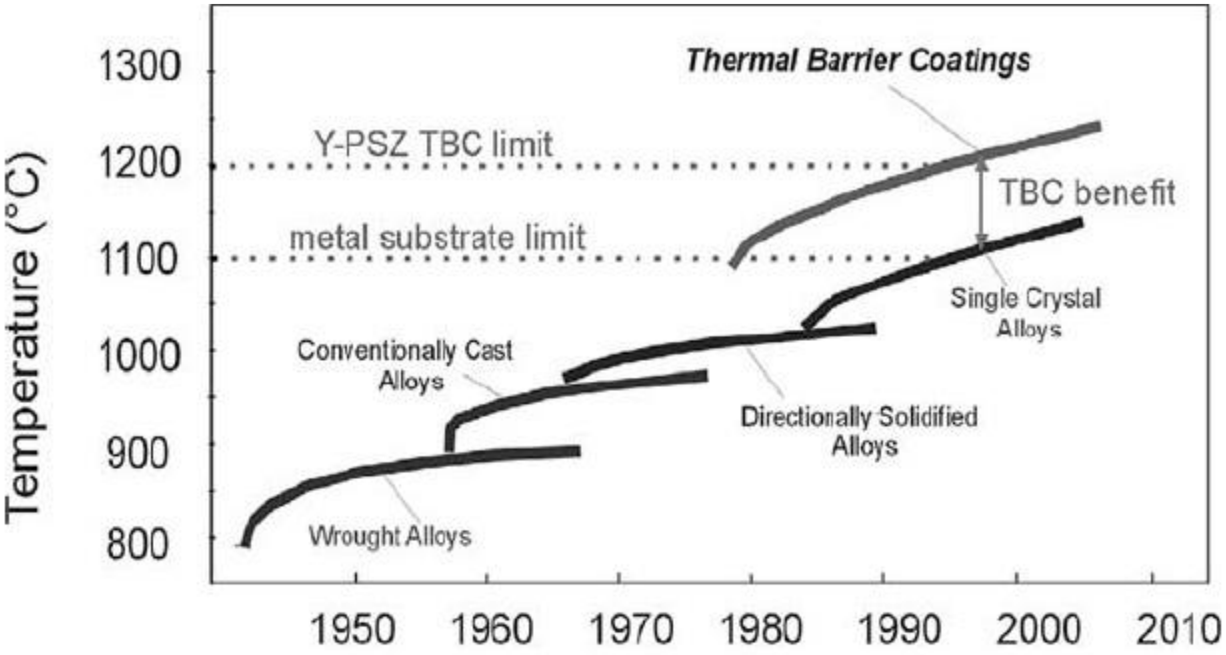

Figure 1.1. Contribution of coatings and advanced processing techniques to improve operating temperature of NBSAs [2003Sch].

Significant progress has been made by various research groups on the development of Pt-based alloys with comparable higher temperature mechanical strength to most Ni-based superalloys. Fischer et al. [1999Fis], Hill et al. [2001Hil2], Cornish et al. [2002Cor] and Wenderoth et al. [2005Wen1] reported that the presence of two-phase coherent microstructures, similar to those of Ni-based superalloys, consisting of a face centred cubic (f.c.c.) matrix (γ) strengthened by ordered f.c.c. ($L1_2$) intermetallic precipitates (γ') contribute to the higher temperature mechanical strength of the Pt-based alloys. In addition, presence of high γ/γ' lattice mismatch and cuboidal γ' morphology was also found to be advantageous [2001Fis, 2001Hil6].

However, most of these previous studies focused mainly on alloy additions to improve the high-temperature mechanical strength with only few investigations used as a screening exercise addressed the oxidation behaviour of these alloys at high temperatures. Hence, there is a need to carry out a detailed study on high temperature oxidation behavior of the developed Pt-based alloy with highest potential. The purpose of this research work is to examine the ultra-high temperature oxidation behaviour of the quaternary Pt-based alloy developed at Mintek and University of the Witwatersrand, Johannesburg. This will help to determine their suitability for application in aggressive high temperature environments, such as in turbine engines.

Samples of water-quenched and air-cooled alloy specimens with composition Pt_{84}:Al_{11}:Cr_3:Ru_2 (at.%) developed at the University of the Witwatersrand and Mintek were selected for this study. This was based on their promising mechanical properties due to the presence of the desirable two-phase γ/γ' microstructure, higher γ' precipitate volume fraction and hardness values.

It should be noted that alloy compositions are in atomic percent (at.%) except otherwise stated and the subscript denotes the atomic % of each of the elements in the alloy.

1.1 Background and Motivation

Before the gas turbine, applications which demand that metals must sustain high stress without fracture or plastic deformation when red hot did not exist. The early turbine engines were operating at 700°C and their blades were made from special stainless steels [1987Sim]. Since the efficiency of a turbine engine depends largely on the operating temperature, great effort has been made in increasing the operating temperature of the early turbine engines. This has led to the development of ever-improved superalloys which are exposed to extreme temperatures and required to withstand aggressive environmental conditions as well as high mechanical stresses [1987Sim, 1997Dur, 2006Ree]. Other applications for superalloys are in waste incinerators, nuclear reactors, submarines, space vehicles, steam power plants, and petrochemical equipment [1987Sim].

The first superalloys were based on a Ni-20Cr composition and this composition has been greatly improved upon through advanced production processes and alloying. Modern single crystal nickel-based superalloys can be used at temperatures up to 1100°C, which represents about 90 % of the melting temperature of their base metal, Ni [1987Sim, 1997Dur, 2006Ree]. As a result of superior high-temperature mechanical properties and excellent resistance to environmental attack, Ni-based superalloys find their widest application in the gas turbine industry constituting over 50% of the gas turbine weight [1987Sim, 2006Ree].

Further increase in the operating temperature of turbine engines will improve their efficiency, reduce their fuel consumption and CO_2 emission, and enable greater thrust [1987Sim, 2003Yok]. Thus, these serve as motivations for increasing interest in developing Pt-based alloys for higher temperature applications above that of single crystal nickel-based superalloys [2000Wol]. Apart from the land-based turbine industry, which is the ultimate target for the Pt-based alloys [2007Cor], other option for future successful exploitation is the use of Pt as coatings on suitable base materials [2010Pot].

1.2 Specific Objectives of this Study

This study builds on alloy development at the University of the Witwatersrand and Mintek. It will focus on detailed study of the high temperature oxidation of water-quenched and air-cooled Pt_{84}:Al_{11}:Cr_3:Ru_2 (at.%) specimens. This will be achieved through the examination of the surface and cross-sectional morphologies of the scale layers, determination of the scale growth kinetics and mechanisms, as well as the stresses in the oxide scales. This will assist in future commercialization of the alloy.

1.3 General Overview of the Thesis

Chapter 2 reviews the literature on high temperature materials with emphasis on the Ni-based alloys. Alternative high temperature materials that could serve as possible replacements for NBSAs components in high temperature applications are also discussed in this chapter. This chapter also captured the review on the development of Pt-based superalloys as an analogous alloy to NBSAs. Chapter 3 details the description of the production of the bulk alloys, metallographic preparation of the as-received alloy samples before and after oxidation, characterization of the as-polished specimens, as well as the oxidation tests procedures of the alloy specimens. The characterization techniques of the oxidized specimens are also discussed in chapter 3. This include thermo gravimetric analysis for oxidation kinetics, X-ray diffraction (XRD) and Raman spectroscopy for phase identification, scanning electron microscopy (SEM) with EDS for examination of the surface and cross-sectional morphologies of the oxide layers, and focused-ion beam FESEM for cross-sectional examination of the scale layers. Procedures for evaluation of the stresses in the oxide scales, using photostimulated Cr^{3+} luminescence piezospectroscopy are also highlighted. The results obtained after the isothermal oxidation of both the water-quenched and air-cooled specimens in air at 1150°C, 1250°C and 1350°C for various time intervals are presented in chapter 4. Discussion of the results is presented in chapter 5, while chapter 6 highlights the conclusions and recommendations.

CHAPTER TWO

2.0 Literature Review

This literature review is divided into four sections. Section 2.1 and 2.2 review high temperature materials with more emphasis on Ni-based superalloys and possible alternative materials to replace the NBSAs. Development of precipitation-hardened Pt-based superalloys is reviewed in section 2.3. The microstructure and the mechanical properties of the Pt-based superalloys are discussed in subsection 2.3.1, while the hot corrosion and the oxidation properties are reviewed in subsections 2.3.2 and 2.3.3 respectively. Section 2.4 reviews the general oxidation of metals and alloys with subsections describing the mechanisms and kinetics of formation of protective alumina scale.

2.1 High Temperature Materials

High temperature materials are classes of materials which have the capabilities of maintaining their mechanical properties as well as their environmental stability when used at temperature equal to or greater than, about two thirds of their melting temperatures. These materials consist primarily of superalloys (Ni, Co, Fe), refractory materials, intermetallic compounds, composites and some ceramic materials [2006Ree]. Based on their ability to exhibit exceptional mechanical strength and good oxidation and hot corrosion resistance at elevated temperatures, their most demanding applications are found in aircraft jet engines, industrial gas turbines, rockets, nuclear reactors and heat exchangers.

2.1.1 Superalloys

The most widely used among the families of superalloys are nickel-based superalloys (NBSAs). They are the materials of choice for high temperature applications when significant resistance to spontaneous deformation under sustained load as well as resistance to oxidation (as in the case of gas turbine engines) is required [2006Ree]. The unique microstructure of NBSAs which comprises the face-centred-cubic (f.c.c.) (γ) matrix phase and an intermetallic cuboidal f.c.c.

precipitate (γ’) phase have made them the most complex and most widely used high temperature structural materials. These alloys contain up to at least 12-13 important elemental constituents in addition to trace and "tramp" elements [1987Sim].

The chemical composition of these alloys establishes the phases present in the alloy. Hence, the desired structure and properties for specific applications can be achieved through proper selection of the alloys’ chemical composition [1990Lee]. The properties which are controlled include the mechanical strength, density, thermal expansion, thermal conductivity and surface stability [1987Sim]. The critical properties required in gas turbine engines include low density, low thermal expansion, high thermal conductivity, high and reliable tensile, creep, rupture and thermo-mechanical fatigue resistance [1987Sim, 1988Wha]. Other properties include the ability to withstand aggressive operating atmospheres in terms of oxidation and corrosion resistance.

The development of the gas turbine engines has driven the development of the nickel-based superalloys since over 70% of an aircraft weight comprises these alloys [1979Bra]. There has been significant increase in the turbine inlet gas temperature (TIGT) of gas turbines from initial 700°C to about 1100°C with the development of modern single crystal NBSAs. The thermal efficiency of the turbine engines increases with increasing turbine inlet gas temperature (TIGT) [2006Gur]. The efficiency can be raised by about 1 % if the temperature capability of the gas turbine engines materials is increased by 40^{o}C (Courtesy NIMS).

The phases present in nickel-based superalloys are [1987Sim, 2006Ree]:

- Gamma matrix (γ): An f.c.c. nickel based continuous phase with a high concentration of solid -solution strengthening alloying elements.
- Gamma Prime (*γ’*): These are ordered f.c.c. precipitates, which have a structure based on Ni_3 (Al,Ti). The *γ’* usually precipitates coherently with the gamma (*γ*) matrix.
- Carbides and borides: Carbides are formed when carbon combines with reactive and refractory elements such as Hf, Ti and Ta to form MC carbides. These later decompose to form lower carbides such as $M_{23}C_6$ and M_6C, during heat treatment and service. Boron when combined with elements such as Cr or Mo form borides, which reside on the *γ* boundaries.

- Grain boundary *γ'*: This is a film of *γ'* generated along the grain boundaries during heat-treatment of stronger alloys.
- Topological Close-Packed (TCP)-type phases:- Plate like phases such as σ, μ and Laves, which can result in lower rupture strength and ductility, formed under certain conditions. These phases are usually avoided where possible.

However, the two major phases that determine the properties of Ni-based superalloys are the gamma matrix and the *γ'* precipitates and they are discussed further.

2.1.1.1 Gamma Matrix

Solid solution strengthening of the *γ*-matrix can primarily be achieved by additions of elements such as Al, Ta, Co, Fe, Ti, Mo and W as alloying additions. These elements are added to Ni matrix (*γ*) without phase instability due to the presence of incompletely filled third electron shell of Ni atom [1987Sim]. Alloying additions can also be used to control the lattice parameter of the *γ* matrix and thus the lattice mismatch between *γ* and *γ'*, as well as improving the hot corrosion and oxidation resistance [1987Sim, 1985Mis].

The solid solution strengthening elements differ from the atomic diameter of Ni by 1-13% and in terms of electron hole number by 1-17%. Thus, the solid solution strengthening effect can be related to local lattice distortion as a result of atomic diameter oversize [1987Sim]. Fleischer [1963Fle] proposed that strengthening of *γ* matrix can result from the local increase in elastic modulus of the lattice due to alloying. This is as a result of extra work to force a dislocation through regions of higher strength than the surrounding matrix. Internal strains generated by inserting solute atoms in an elastic matrix as well as the difference in moduli can be responsible for solid-solution strengthening of the matrix.

Alloying element addition can also increase the strength of the *γ* matrix by lowering the stacking-fault energy which makes cross-slip more difficult. High temperature, slow-diffusing elements such as W and Mo are rated as the most potent solid solution strengtheners, while Fe, Ti, Co and

V are weak solid-solution strengtheners [1987Sim]. Aluminium is rated as potent solid-solution strengthener but a good precipitation strengthener for Ni_3Al [1986McA, 1987Oya].

Surface stability of Ni-based superalloys can also be achieved through alloying additions to the γ-matrix. Additions of Cr and Al have been found to improve the surface stability of the γ-matrix. Chromium additions particularly improve the hot corrosion of components [2003Gur]. Addition of aluminium provides exceptional higher temperature oxidation resistance, more than Cr due to formation of protective, slow-growing and continuous α-Al_2O_3 scale [1987Tat]. Platinum additions to nickel-based superalloys as alloying elements or in coatings have been found to have a beneficial effect on both the oxidation and hot corrosion resistance [1984Tat, 2001Pur].

2.1.1.2 Gamma Prime Phase

Gamma prime, γ′, shown in Figure 2.1, is a very important A_3B intermetallic phase, which imparts strength to the gamma matrix (γ) without lowering the fracture toughness of the alloy due to its inherent ductility [1987Sim]. In the ordered, cuboidal face centred cubic (f.c.c.) A_3B intermetallic compounds, relatively electronegative elements such as Ni, Co, or Fe occupy the 'A' sites, and more electropositive elements such as Al, Ta, or Ti occupy the 'B' sites [1987Sim].

A high-nickel matrix favours precipitation of γ′ (based on $Ni_3(Al,Ti)$, which requires little size change as a result of the nickel atom being incompressible, due to its 3d electron state [1987Sim]. Homogeneous nucleation of precipitates with low interfacial energy and excellent long time stability is possible due to the compatibility of the γ' f.c.c. crystal structure and lattice constant with γ matrix [1983Ric].

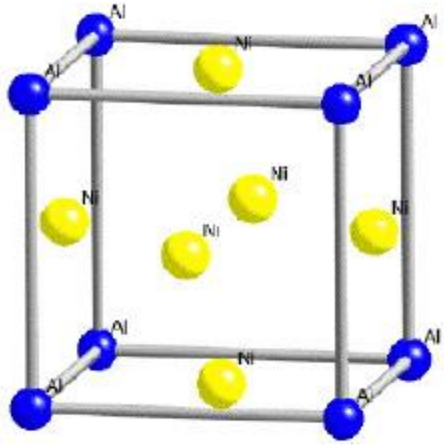

Figure 2.1. The crystal structure of an ordered f.c.c. γ' precipitates after Bhadesia [2003Bha].

The yield strength of γ' only decreases with increasing temperature beyond about 600°C as shown in Figure 2.2, when the thermal activation is sufficiently high enough to allow the dislocations to overcome the obstacles (γ'). However, most other materials show decreasing strength with increasing temperature simply because assistance from thermal activation makes it easier for dislocations to surmount obstacles [1987Sim, 2003Bha]. The ordering temperature of Ni_3Al (γ') depends strongly upon the degree of stoichiometry and the concentrations of any impurities, and is roughly equivalent to its melting temperature of about 1375°C [2006Ree]. The high temperature mechanical properties of NBSAs are limited to about 1100°C-1150°C due to the melting temperature of Ni matrix and Ni_3Al (γ') phases [2003Bha].

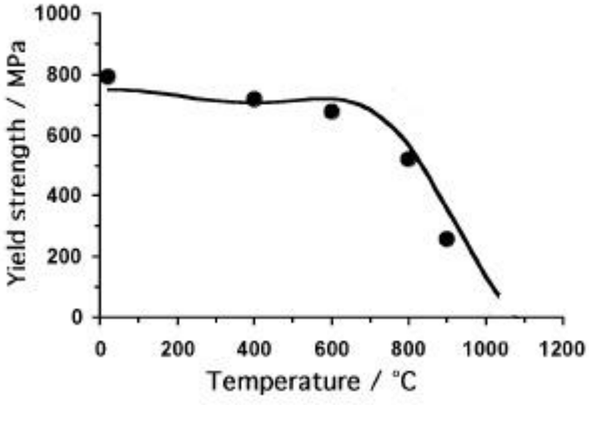

Figure 2.2. Yield strength versus temperature showing capabilities of the γ'-phase with increasing temperature [2003Bha].

Alloying additions can be used to strengthen the γ' phase, prevent excessive coarsening and alter its lattice parameters [2006Gur, 1984Och, 1991Chi]. Slow diffusing alloying elements, such as, Co, Nb or Mo retard the coarsening rate of the γ' phase. Thus, a fine γ' phase structure is maintained, even after prolonged exposure at higher temperatures. The strength of the alloy and its creep properties can also be altered by changing the lattice parameters of the precipitates which affects the lattice strains induced by precipitation [1987Sim].

2.1.1.3 Phase Relations between Gamma and Gamma Prime

Lower lattice misfit improves the creep properties and elevated temperature strength while high lattice misfit improves the low temperature strength of the alloy. In addition, the γ/γ' interface remains coherent and the interfacial energy remains low, provided that the lattice misfit between the lattice parameters of the γ and γ' phases is not too large [2006Ree].

The properties displayed by superalloys are found to depend critically on the coherency between the γ and γ' interface [1983Ric]. This is because the strength of the alloy at elevated temperature is determined by the nature of the interface between γ and γ' and coherency stresses [1989Nat, 1988Cha]. These properties are favoured by small values of the lattice misfit, δ, and a positive lattice misfit indicates that the lattice parameter of the γ' ($a_{\gamma'}$) is larger than that of matrix (a_{γ}), and vice versa [1983Ric]. The lattice misfit, δ is defined by:

$$\delta = 2 * \frac{\left(a\gamma' - a\gamma\right)}{(a\gamma' + a\gamma)} \tag{2.1}$$

The crystal structures, lattice parameters and orientation of the two phases determine coherency [1972Cha]. In order to form coherent interfaces, the two phases must have similar crystal structures and lattice parameters. However, coarsening of the γ' particles leads to loss of coherency and higher value of lattice misfit, δ [2006Ree]. Coherent precipitates are more likely to form in a fine, evenly dispersed network because coherent interfaces with small lattice misfits leads to lower interfacial energies and are less mobile [1987Sim, 1989Kau]. In addition, smaller particles can remain strained coherent, whereas layer particles, even with the same structure, become semi-coherent.

The shape of γ' has been found to vary between cuboidal, spherical or plate-like shapes [1987Sim]. This has been reported to be influenced by the value of lattice mismatch and low interfacial energy. For alloys of low misfit, the size of the γ′ precipitate needs to be larger before the effects of lattice misfit strain are sufficient to transform the particle shape [1983Ric]. Spherical shape is observed at 0-0.2% lattice mismatch, cuboidal shape at around 0.5-1.0% lattice mismatch and plates at mismatches above about 1:25% [1987Sim].

Development of γ' precipitates during heat-treatment in a number of different NBSAs revealed that there are correlations between the morphology, size and sign of the γ/γ' misfit [1983Ric]. The γ' growth sequence was observed to occur in the sequence spheres, cube, arrays of cubes and eventually solid-state dendrites as coarsening is increased with increasing degree of ageing [1983Ric]. The annealing of NBSAs under stress can alter the morphology of γ' to form plates of γ' in the <100> and <110> orientations [1987Sim, 1972Tie1]. This has a beneficial effect on the creep rupture properties and improves the yield strength at temperature up to 760°C.

2.1.2 Development in Processing of Nickel-Based Superalloys

Development of advanced processing technologies such as vacuum casting, directional solidification and development of single crystal alloys as well as improved chemical composition through alloying have resulted in gradual temperature increases and improved properties of nickel-based superalloys [2006Ree], as shown in Figure 2.3. There were considerable improvements in grain boundary creep strength of directionally-solidified alloys due to elimination of transverse grain boundaries [1985Hon]. Single crystal alloys, which are a modification of directionally-solidified alloys, possess improved creep resistance and higher melting temperature [2003Bha]. This is as a result of total elimination of grain boundaries and thus, premature failure that would have occurred when grain boundaries are present in the alloy is prevented. Most modern high temperature components, such as high pressure turbine blades, are produced as single crystal alloys. In developing new materials for higher temperature applications, proper consideration must be given to the processing techniques.

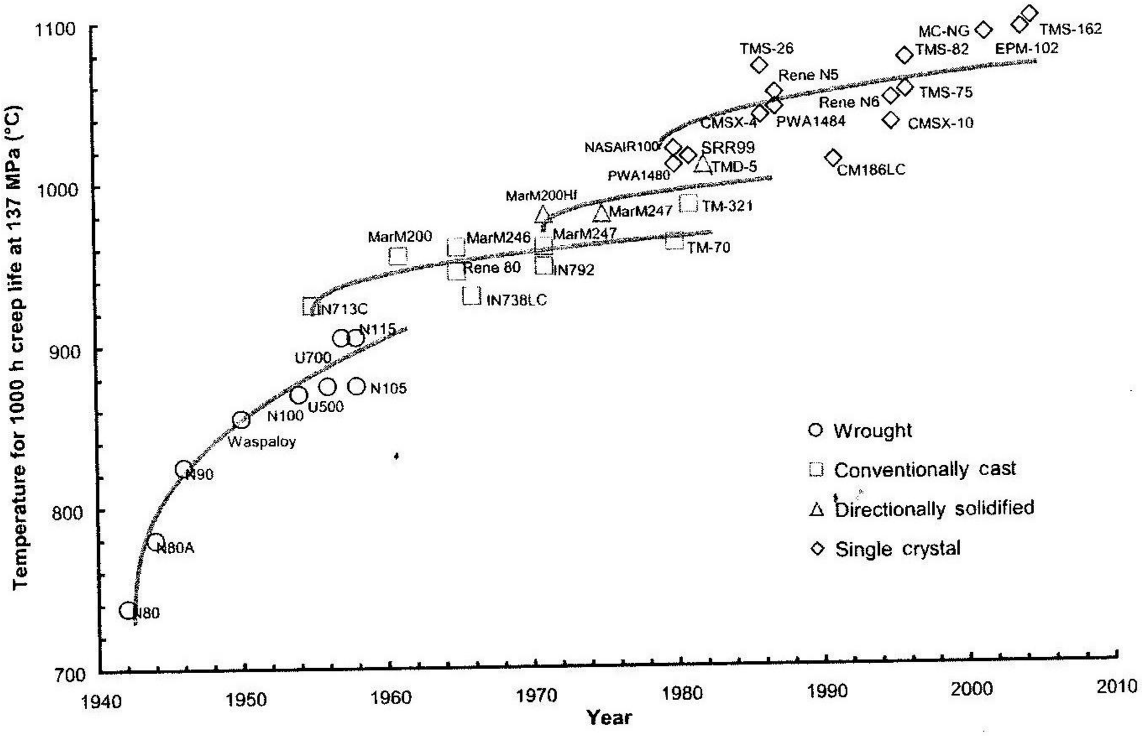

Figure 2.3. Improvement in high temperature capability of NBSAs through the development in processing technologies [2006Ree].

2.1.3 Chemical Composition and the Role of Different Alloying Elements

In order to produce the desired structure and properties that will promote higher temperature mechanical strength and excellent environmental resistance, the chemical composition of NBSAs must be carefully controlled. Increasing the amount of γ'-forming elements, such as Al and Ti, as well as refractory elements can be used to modify the chemical composition of NBSAs [1997Che, 2005Pom]. However, in single crystal alloys, there is a significant replacement of Ti with Ta which strengthened the γ' and also raised the solidus temperature [1997Dur].

Chromium content in NBSAs was previously about 20 wt%, but this has been drastically reduced over the years to about 5 wt% in single crystal alloys. This is to achieve high solubility of Al and Ti [2005Pom]. At temperatures below 950°C, Cr has been found to be a most effective alloying addition in increasing corrosion resistance [2005Pom, 1987Str1, 1979Bra]. Cr_2O_3 scale also provides good oxidation and hot corrosion resistance before the formation of volatile CrO_3 at temperatures above 950°C [1990Ell, 1979Bra]. However, excessive amounts of Cr and heavy metals, such as Mo and W, promote the formation of topologically close-packed (TCP) phases. These phases usually occur with highly embrittling platelet morphology [1997Dur]. Hence, overall amounts of Cr, Mo, and W must be well controlled in the alloys.

The presence of Al in the first generation NBSAs strengthened the matrix to a certain extent, promoted the formation of γ' and also aided the formation of stable Al_2O_3 scale, which provides excellent oxidation resistance at elevated temperature above 950°C [1997Dur, 1990Ell, 1987Sim]. Addition of Zr, Hf and Cr helped to improve the adhesion of Al_2O_3 scale to the alloy surface and thus reduce spallation. Other alloying elements in the first generation NBSAs included Ti, Co, V, Nb, Mo, W, and Ta.

Rhenium additions of about 3 at.% to the second generation NBSAs were found to increase their creep strength at higher temperatures [1997Dur]. However, higher Re contents of about 6 at.% in the third generation NBSAs resulted in precipitation of topologically close-packed (TCP) phases after long-terms high temperature exposure [1968Dar]. This has a disastrous effect on the alloy high temperature creep strength. Addition of ruthenium to a third generation nickel-based superalloy with high Re contents was found to reduce substantially the TCP precipitation rate. This was said to be as a result of reduction in the interface area fraction of alloy that is conducive for precipitate nucleation [2006Sat]. Furthermore, there was an increase in the solid solubility limits of solid solution elements in the matrix, particularly for Re and W. Alloying NBSAs with platinum-group metals have been reported to be effective in controlling the rate of TCP phase precipitation [2003Yok]. Table 2.1 lists the effects of some major alloying elements in NBSAs.

Table 2.1. Effects of major alloying elements in Ni-based superalloys [1997Dur, 1979Bra].

Elements	**Effects**
Chromium	Improves oxidation and corrosion resistance, promotes TCP phases, carbide former ($M_{23}C_6$ and M_7C_3)
Molybdenum	Strong solid solution strengthener, carbide former (M_6C and MC), increase alloy density, promotes TCP phases
Tungsten	Strong solid solution strengthener, promotes TCP phases
Tantalum	Strong solid solution strengthener, carbide former (MC)
Niobium	Strong γ and γ' strengthener, NbC former, promotes δ phases
Titanium	promotes the formation of γ', forms TiC
Aluminium	Increase the γ' volume fraction, improves oxidation resistance
Iron	Promotes TCP phases, decreases oxidation resistance
Cobalt	May raise or lower solvus, raises the γ' solvus temperature
Rhenium	Retards coarsening; increases misfit between the γ and γ'
Boron; Zirconium	Improve creep strength and ductility, inhibit carbide coarsening, boron when present in large amount forms borides
Carbon	Promotes the formation of various carbides
Silicon	Promotes the formation of protective silica scale
Rare earth elements, Zr & Hf	Improves adhesion of protective scales

2.1.4 Oxidation of Ni-Based Superalloys

Ni-Cr-Al systems usually form the basis of most Ni-based superalloys, and protective α-Al_2O_3 scales are generally form on these alloys after the transient oxidation period [1971Sto]. During the transient oxidation of Ni-Cr-Al alloys at 1000°C, formation of NiO and $Ni(Cr,Al)_2O_4$ together with Cr_2O_3 and metastable alumina was observed [1971Kea]. The metastable alumina transformed to α-Al_2O_3 upon its incorporation into the scale. According to Ni, Cr and Al-oxide maps, a continuous α-Al_2O_3 should form during oxidation, in the range of 1000-1100°C, if the Al content exceeds about 4 wt%, provided the Cr content lies about 10 wt% [1971Gig, 1971Wal].

Hence, formation of external α-Al_2O_3 scale during steady state period depends on the concentrations of Cr and Al in the Ni-Cr-Al alloys.

In a study of the oxidation behaviour of a single crystal (SC) Ni-based superalloy, which contains mainly Ni with 6.3 wt% Al, 6 wt% Cr, and some Co, Ti, Mo, W and Ta, at 1000°C, 1100°C and 1150°C, Li et al. [2003Li2] reported that the alloy displayed parabolic rate kinetics. The parabolic oxidation kinetics were controlled by the growth of the inner α-Al_2O_3 layer, which provided good protection. Internal oxides or nitrides were not observed beneath the inner α-Al_2O_3 layer after 1000 h oxidation at 1000°C, and after 200 h at 1100°C and 1150°C. However, subparabolic oxidation kinetics were exhibited by the same alloy when oxidised at 800°C and 900°C [2003Li1]. After prolonged oxidation at 1000°C -1150°C, a mixed scale that consisted of an outer layer of spinel [$(Ni,Co)_2Al_2O_4$; $NiCr_2O_4$)], a sublayer of mainly α-Al_2O_3 with small amount of spinel with thin layer of $CrTaO_4$-rich oxide, and an inner layer of α-Al_2O_3 were formed [2003Li2].

Huang et al. [2005Hua1] examined the isothermal oxidation behaviour at 1000°C, 1050°C and 1100°C and the cyclic oxidation behaviour at 1000°C of the directionally solidified Ni-based superalloy DS951. This alloy contain 7 wt% Al, 10 wt% Cr, 2 wt% Nb, 0.05 wt% C, 50ppm Y and some Co, W, Mo, balance Ni. During the isothermal oxidation, there was no internal oxidation and the DS951 alloy obeyed a two-stage parabolic oxidation kinetics. Although there was no weight loss observed during cyclic oxidation, there was development of faceted and needle-shaped AlN precipitates in the alloy subsurface region. Formation of MC carbides (M was predominately Nb with some Cr and W) along grain boundaries and interdendritic areas was observed.

Oxidation tests were conducted in air at 1100°C on CMSX-4 and RR3000, which are Ni-based superalloys used extensively in gas turbine applications [2007You]. After the tests were conducted for equal and extended periods of time, up to 100 h, it was observed that the oxide scale developed on RR3000 was much thicker than that on CMSX-4 alloy. The scale formed on RR3000 was porous and had a three-layered structure. (Ni, Co)O outer layer; a sublayer of $CrTaO_4$-rich oxide with different spinels [$(Ni,Co)Al_2O_4$ and $(Ni,Cr)_2O_4$]; and an inner layer of α-

Al_2O_3. Conversely, compact and well-adhering scale that consisted of only two layers was formed on the CMSX-4 alloy. The upper layer was mainly spinels and the inner layer was α-Al_2O_3.

2.1.5 Coating of Ni-Based Superalloys Turbine Blades

Protective coatings are designed for use on nickel-based superalloys which are currently being used on the turbine blades, in order to raise their temperature capabilities by inhibiting direct interaction between the superalloy substrates and aggressive environment [1987Sim]. A wide range of coatings based on diffusion, overlays and thermal barrier coatings (TBCs) have been designed to serve as a shield for turbine blades and other engine components against high temperature oxidation and hot corrosion through the development of protective oxide scales on the components [2005For].

Thermal barrier coatings (TBCs) are widely used in gas turbine engines, and allow for an increase in the operating temperature from about 1000°C to about 1200°C [2005Pom, 1999Sie]. Currently, TBC systems consist of three distinct layers (Figure 2.4) formed on the metal substrate in order to meet their multifunctional requirements. The ceramic top-coat is the layer that provides thermal insulation for the blade. This layer is rich in elements such as Al and Cr, and typically made of Yttria-Stabilised Zirconia (YSZ) which has shown outstanding performance due to its very low thermal conductivity and high thermal expansion coefficient [2006Gur]. In addition, the very high melting point (2700°C) of YSZ also makes it very suitable for this application.

Thermally grown oxide (TGO) is formed as a result of reaction between the ceramic top-coat and the bond coat at very high temperatures. TGO is engineered to form slow growing, uniform and defect-free α-alumina of about 1-10 μm thick. The metallic bond coat holds the ceramic top-coat to the substrate and is also an oxidation-resistant layer which is about 75-150 μm thick [2002Pad]. The layer usually contains a sufficient amount of oxide-forming elements like Al and Cr which help to guarantee an excellent protection against high temperature oxidation and hot corrosion [2008Gur]. The substrate is usually a Ni or Co-based superalloy which is air-cooled by hollow channels inside the turbine blade.

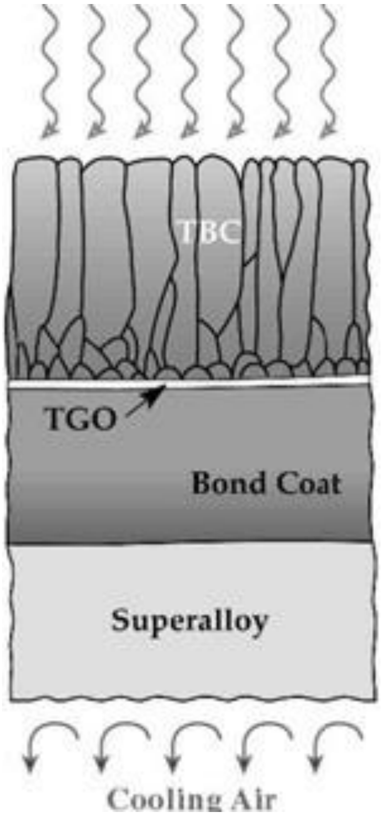

Figure 2.4. Thermal barrier coating (TBC) system with the thermally grown oxide (TGO), bond coat and substrate alloy [2003Cla].

There are a wide variety of high temperature oxidation and hot corrosion resistant coating types. Overlay coatings are of typical composition MCrAlY (where M is Ni or NiCo) and are used as a bond coat for TBCs [2005Pom]. They are usually formed as slow growing, highly adherent alumina scales due to the presence of the reactive element yttrium, which imparts excellent oxidation and corrosion resistances to the coatings. The presence of high amounts of Cr in the overlay coatings also makes them desirable protective coatings against low-temperature hot corrosion, which usually occurs at 650°C to 800°C (Type II hot corrosion). Overlay coatings are usually deposited on the substrates by physical deposition processes such as: thermal spraying, physical vapour deposition (PVD), electron beam physical vapour deposition (EBPVD), ion platting/sputtering and electroplating [1987Str2].

Development of the so-called “smart” coatings to address the problems associated with the different nature of environmental degradation, which varies from oxidation through Type I hot corrosion (high temperature corrosion commonly observed at around 850°C and 950°C) to Type II hot corrosion, is a most recent technological advance in overlay coating technology [2002Nic]. Smart coatings have been developed with an optimum composition of chromium and aluminium that will promote formation of highly adherent protective scales at temperature ranges between 650°C and 1100°C. This makes them resist high temperature oxidation as well as Type I and Type II hot corrosion.

Diffusion coatings, such as Cr-rich coatings and aluminide coatings have been found to be useful in protecting Ni-based alloys from environmental degradation [1971Gow, 1976Lie]. Platinum-modified nickel aluminide coatings were developed to improve the performance of the simple aluminide coatings [1999Zha, 2001Zha]. It was reported that formation of voids at the coating-alumina scale interface was suppressed due to the presence of Pt in aluminide coatings. This improves the oxidation and corrosion resistance of the coatings through better scale adhesion. The resistance to alumina scale spallation also improved as the amount of Pt in the coating was increased [1998Kri, 2001Pur].

2.2 Alternative Materials to Replace NBSAs

2.2.1 Intermetallic Compounds

Intermetallic compounds have attracted significant attention in recent years for a wide range of high-temperature aerospace applications, due to their properties lying between those of metals and ceramics [1991Sto, 1993Sto, 1995Woo]. The ability of these materials to retain high strength in some systems, lower diffusion rates, high melting temperatures and superior environmental resistance at elevated temperatures are some of their advantages over conventional metallic systems [1995Jen, 1995Sad]. However, the major drawback to the practical use of these alloys is the lack of ductility or fracture toughness at room temperatures [1995Sad]. Hence, most of the research work is focused on improving their ambient temperature ductility.

Aluminides and silicides develop a self-protective coating of alumina or silica and thus are the most likely to possess good oxidation resistance [1995Sad]. Consequently, they have received considerable attention as promising high-temperature among the various categories of intermetallic compounds. The B2 NiAl-based intermetallic compounds are attractive for components in gas turbine engines due to their relatively low density, high melting temperature, high thermal conductivity and excellent oxidation resistance. Unfortunately, poor room temperature strength of these alloys has limited their potential use as structural materials [1995Hac]. While NiAl exhibits brittle behaviour in both single-crystal and polycrystalline materials [1992Cha], Ni_3Al shows significant ductility in single-crystal form accompanied by severe brittleness in polycrystalline form [1985Liu and 1985Tag].

TiAl-based intermetallic compounds are advantageous for use in light-weight space applications because of their high specific strength [1995Sad]. Gamma-TiAl can be used as a possible replacement for some superalloys due to its stiffness, strength and adequate corrosion resistance. This alloy can possibly withstand higher application temperatures than the Ti alloys, though it still exhibits brittleness [1995Bar].

The RuAl compound has been identified as a promising high-temperature material for gas turbine engines with properties quite different from all other B2 aluminide systems [1990Fle, 1991Fle]. It possesses a very high melting temperature above 2050°C, which implies higher-temperature strength and a good creep resistance. In addition, RuAl has also been reported to possess excellent oxidation resistance up to 1000°C [1993Fle, 1999Lu, 2005Müc, 2007Cao]. Additionally, RuAl is reported to exhibit relatively high toughness/ductility in compression at ambient temperature, but also has low temperature sensitivity of the flow stress and low rate sensitivity [1963Fle, 1991Fle, 1993Fle, 1996Wol1, 1996Wol2, 1997Wol]. However, the addition of Ta to Ru-Al system resulted in a decrease of the 2% flow stress with temperature and extremely low toughness [2004Fen].

Single-phase RuAl-based alloys when oxidized are reported to form layered oxide structures [2003Sol]. The cyclic oxidation process is accelerated by the presence of the δ-Ru-rich eutectic along grain boundaries. The Pt-containing RuAl-based alloys exhibits superior oxidation performance which is proposed to be derived from Pt rejection to the Ru-rich layer subsequently formed during oxidation [2007Cao].

2.2.2 Ceramics and Ceramics-Matrix Composite

The need for increasing fuel efficiency, lowering exhaust emissions and higher performance are some of the factors that make ceramic materials to become attractive for automotive, aircraft and rocket engines [1992Her, 2002Lin]. Desirable properties which made ceramics and ceramic-matrix composites attractive candidates for use in high temperature applications relate to the good strength and creep resistance at high temperatures, low densities relative to metals, high bulk moduli, and good oxidation and corrosion resistance in severe environments.

2.2.2.1 Monolithic Ceramics

Among the wide varieties of monolithic ceramics examined for high temperature structural applications, only those based on silicon carbide (SiC) and silicon nitride (Si_3N_4) were found to possess the proper combination of properties that are required for practicable long term structural use at high temperatures up to around 2000°C. Good strength and creep resistance at high temperatures, good thermal shock resistance, low densities, oxidation and corrosion resistance in aggressive environments, and potential for low-cost raw materials are some of the desirable properties [2002Lev, 1997Ric, 1992Her]. However, low fracture toughness and brittle failure are the major drawbacks to the use of these classes of materials in high temperature applications.

Reaction-bonded Si_3N_4 (RBSN) and SiC matrix composites were developed in order to improve the low fracture toughness of the monolithic components, while maintaining their high temperature desirable properties [1992Bha]. These composites displayed better properties at room and elevated temperature but high cost of production and difficult fabrication process are some of the limitations to their use [1992Bha, 1997Ric].

2.2.2.2 Glass-ceramic Matrix Fibre Composites

Glass-ceramic matrix fibre composites are polycrystalline materials produced by melting glass from traditional raw materials to the vitreous state, in order to form a complex homogeneous silicate glass, which is then partly crystallized [1992Leh, 1979Doy]. The proper addition of fibres to glass or ceramic matrix systems allows the production of composite materials that display improved toughness and ductility [1992Leh]. These improvements have made glass-ceramic matrix fibre composites become attractive for use in high-temperature critical applications, such as in many engine and aerospace applications, where catastrophic components failure is a serious problem. However, high cost of reinforcing fibre coupled with the use of expensive hot-press processing has limited the use of glass-ceramic composite to applications where high cost of production can easily be justified, such as in military and aerospace.

2.2.3 Carbon-carbon Composites

In this subclass of ceramic composite materials, both the matrix and the reinforcement constituents are virtually pure carbon. Low density, high strength, and ability to retain the mechanical properties at ultra high temperatures are some of the properties that make this class of materials attractive for use in applications such as in hyper-velocity vehicles, where weight and exposure to high temperatures are critical [1992Maa]. Carbon-carbon composites maintain their specific strength and stiffness up to temperatures as high as 2200°C, and have few competitors among other materials for temperatures in excess of about 1000°C.

Reinforced carbon-carbon (RCC) materials are currently being used for the production of the nose cap and wing leading edges of the space shuttle as reusable oxidation-resistant thermal protection materials [1974Bur]. However, poor high temperature oxidation resistance of carbon-carbon composite materials, which usually begin to oxidize very fast at temperatures above 370°C, has severely restricted their use in many other high temperature applications where both excellent mechanical strength and good oxidation resistance are essential.

2.2.4 Refractory Metals and their Alloys

Refractory metals and their alloys are being considered as possible replacements for Ni-based superalloys in hot-section components within the gas turbine as a result of their high melting points, which determine the temperature limit of any material in a structural application [1965Tie]. These metals, all of which have body centre cubic (b.c.c.) structures, include molybdenum, niobium, tantalum, tungsten, and rhenium.

Rhenium and its alloys are very attractive for high temperature applications because of their ability to maintain excellent high temperature strength above any other refractory metal up to about 2000°C. This is due to the high melting point of Re, about 3180°C [1965Tie]. Tungsten-based HfC dispersion-hardened alloys also possess excellent strengths that are useful at elevated temperatures of about 1800°C [1996Yam]. Alloys of Nb with Nb_3Si and Nb_5Si_3 as the strengthening precipitates display improved mechanical properties at higher temperatures [2003Zha]. However, severe lack of oxidation resistance of these refractory metals and their alloys has limited their practical use as components within the gas turbines at elevated temperatures [1965Tie].

The use of coatings is being investigated in an attempt to overcome the oxidation problems associated with refractory metals and alloys. Several coating compositions ranging from ceramics, high melting point intermetallic compounds, and alloys based on Nb- and Mo-silicides with additions of W, B, and/or Ge have been investigated [1997Sub, 2003Bew]. However, because of very high risks associated with defects in coatings, which may result in catastrophic consequences if occurring in jet engines, it is essential that the base materials must possess significant oxidation resistance [1987Sim]. Thus, based on lack of significant oxidation resistance of refractory metals and their alloys, they are unlikely to serve as possible replacement for Ni-based superalloys components in jet engines.

2.2.5 Platinum Group Metals (PGMs) and their Alloys

Platinum Group Metals **(**PGMs) and their alloys are being investigated as possible materials for use at ultra-high temperatures because of their outstanding properties. Higher melting points, chemical stability, oxidation resistance, resistance to many molten oxides at high temperatures, as well as good mechanical properties at very high temperatures are some of these beneficial properties [1999Fis, 2000Lup, 2001Fis]. The metals of the platinum group particularly, platinum, rhodium and iridium, are widely used in the glass industry for high quality glass and glass fibre production, and in space technology for production of nozzles of rocket engines and capsules of radioactive power sources.

Fischer et al. [1999Fis] reported that alloying Pt with up to 20 wt% Ir and Rh increased its stress rupture strength. Increasing the alloying contents to 30 wt% of Ir and Rh at 1700°C was found to double the strength of Pt-Ir alloys, while the strength of Pt-Rh was only slightly affected. In addition, Pt-30 wt% Ir alloy was reported to display excellent ductility and superior elongation to fracture at 1700°C, but showed relatively high mass losses at temperature above 1100°C. This was due to selective oxidation of Ir after long exposure. The Pt-30 wt% Rh alloy was stable when oxidized at temperature above 1100°C, but Pt-Rh alloy with more than 20 wt% Rh are difficult to fabricate [1997Fis]. Loss of mechanical properties due to grain coarsening is another disadvantage of Pt-Rh alloys.

In order to further increase the range of possible applications of platinum materials at high temperatures, the effects of strengthening of platinum metals and their alloys through the introduction of finely dispersed stable particles, such as oxides, carbides, and silicides, into the alloy matrix were examined [1999Fis]. Oxides of zirconium and yttrium were used because they were found to possess very high thermodynamic stability, higher melting temperatures than the matrix, and insolubility in the matrix at very high temperatures. The dispersion hardened platinum (Pt DPH) and the dispersion hardened alloys, Pt-10 wt% Rh DPH and Pt-5 wt% Au were reported to show better ductility and significantly greater strengths, even at longer times, than the solution strengthened Pt alloys and pure Pt metals. However, welding of these dispersion hardened alloys usually resulted in substantial reduction in strength.

A new class of oxide dispersion hardened platinum material was developed through a new production process in order to overcome the problem associated with welding and reduction in ductility of the platinum in the previously developed Pt DPH materials [1968Dar]. These new Pt DPH materials were produced through casting by addition of oxides of zirconium, yttrium and, in some cases, cerium to the platinum in elemental form during melting. The semi-finished products (in form of sheets, rods or tubes) were later annealed in an oxidizing environment to aid the formation of finely dispersed oxide precipitates from the alloying elements through internal oxidation [2001Fis]. The new Pt DPH materials showed improved higher temperature strength, low creep rate as well as very good ductility at the temperature range between 1200°C and 1700°C, because the strengthening effect from the dispersed oxide particles was found to increase as the temperature increases. Their properties after welding have also improved significantly.

Yamabe-Mitarai, Koizumi, Murakami, Ro, Maruko and Harada at the National Institute of Materials Science (NIMS) in Japan, proposed development of a new class of superalloys based on platinum group metals [1996Yam and 1997Yam]. These superalloys are called "refractory superalloys" and have an f.c.c./$L1_2$ coherent two-phase structure analogous to those in Ni-based superalloys, but with considerably higher melting temperatures. Iridium and Rh were selected from the PGMs as the base metals in their investigation because of their f.c.c. crystal structures and higher melting temperatures [1996Yam, 1997Yam, 1998Yam]. Other properties of Ir metal include high temperature strength, good elevated temperature oxidation and corrosion resistance [2008Ohr]. Rhodium has a slightly lower melting point (1960°C) and was considered because of its smaller density (12.4 g/cm^3) compared with 20-22 g/cm^3 for the Ir-alloys, which are much higher than those of Ni-based superalloys 8.0-9.0 g/cm^3. Rhodium also possesses better oxidation resistance than Ir [1997Yam].

Mechanical properties and oxidation resistance of binary Ir-10Nb, Ir-15Nb, and Ir-15Ti (at. %) refractory superalloys at up to 1800°C were investigated by Yamabe, Koizumi, Murakami and Ro [1996Yam]. The binary alloys were prepared by arc-melting in an argon atmosphere. The microstructures of heat treated samples were examined by scanning electron microscopy (SEM), X-ray diffraction (XRD) as well as transmission electron microscopy (TEM). Their results revealed the presence of coherent f.c.c./$L1_2$ two-phase structures in Ir-15Nb and Ir-15Ti alloys, as well as a very high compressive strength of about 200MPa at 1800°C. The oxidation resistance of the refractory superalloys was found to be superior to those of W- and Nb-based conventional refractory alloys.

Yamabe-Mitarai et al. [1997Yam and 1998Yam] investigated the microstructure and high temperature strengths of Ir-15 at.% X (X=Ti, Ta, Nb, Hf, Zr, or V) and Rh-Y (Y=15 at.% Nb, Ti, Ta and 25 at.% Ta) binary alloys. It was found that two-phase γ/γ' coherent structures analogous to Ni-based superalloys were present in both sets of alloys. The compressive strengths of most of these superalloys (except with V and Ti additions) was found to be equivalent to, or higher than, those of the M247 and CMSX-10 commercially used Ni-based superalloys as shown in Figure 2.5.

At temperatures up to 1200°C, their strengths were above 800MPa and about 200MPa at 1800°C [1998Yam]. The compressive strength of Rh-15Nb alloys at 1500°C was found to be about 190MPa, which is equivalent to those of the strongest metallic materials available at this temperature, such as W-HfC alloys (197MPa) [1997Yam], as shown in Figure 2.6. The strength of Ir-based alloys was found to depend on the precipitate morphology, which is determined by the lattice misfits between the matrix and the precipitates [1999Yam1].

Precipitation hardening was reported to be more effective in a 3-dimensional maze of plate-like precipitates formed in Ir-Zr alloys with large misfits of about 2.19% than in the cuboidal precipitates formed in the Ir-Zr alloys with a lattice misfit of about 0.33% [1999Yam1]. Precipitation hardening was found to occur by shearing of the precipitates in the deformed Ir-Zr alloy with plate-like precipitates. Thus, the compressive strengths of Ir-Zr alloys were found to be higher than those of Ir-Nb alloys at room temperature and at 1200°C, and the precipitation hardening was higher at room temperature than at 1200°C in both alloys. The Ir-Nb alloys were found to display better creep properties than Ir-Zr alloys [2000Yam]. In addition, it was revealed that Ir-Nb alloys deformed by the by-pass mechanism and that their compressive strength reduced to about 130MPa at 1800°C from 800MPa at 1200°C. However, the strength is about 1200MPa at room temperature [1999Yam2].

In attempts to further improve the high temperature strength of Ir-based alloys above 1200°C, Yamabe-Mitarai et al. [2002Yam] studied the effect of additions of high melting temperature elements, Mo (melting point = 2617°C), W (melting point = 3380°C) and Ta (melting point = 2977°C). Addition of up to 20 at.% Ta was found to effectively improve the high temperature strength of a binary two-phase Ir-15Nb alloy. Above this concentration, the two-phase f.c.c./$L1_2$ structure in the Ir-15Nb alloy was lost and resulted in strength loss. Tungsten and Molybdenum additions showed only slight improvement in the alloys' high temperature strength despite the higher melting temperature and larger atomic size of W over Ta.

Yamabe-Mitarai and colleagues examined the effect of addition of Zr as a third element on the creep behaviour of Ir-Nb alloy at 1800°C under 137MPa [2005Yam]. Zirconium was chosen because of the f.c.c. and $L1_2$ two-phase regions, which are present in the binary Ir-Nb and Ir-Zr alloys, were connected to the Ir-Zr side from the Ir-Nb side in the Ir-Nb-Zr ternary system [2003Yam1]. The addition of up to 6 at.% Zr was found to lower the creep rate, and there was a change in lattice misfit between the f.c.c. and $L1_2$ phase [2005Yam]. High Zr contents did not improve the creep behaviour due to coarsening. In addition, the creep properties of the ternary Ir-Nb-Zr alloy have also been reported to be enhanced by the presence of fine $L1_2$ precipitates [2003Yam2, 2003Yam3].

Phase relationships and creep resistances of Ir-4.25 and 8.5, 12.75Nb-X (X= 3.75, 7.5, 11.25 Hf, or 4.5, 9, 13.5 Ta, or 3.75, 7.5, 11.25 Ti at.%) ternary alloys were investigated and all the alloys showed the presence of the f.c.c. and $L1_2$ two-phase structure [2005Hua1]. The three ternary alloys displayed better creep properties at 1800°C and 1650°C under 137MPa than Ir-Nb alloys. Among the three ternary alloys, Ir-Nb-Hf exhibited the strongest creep resistance and highest lattice misfit between the matrix (f.c.c.) and precipitates ($L1_2$). The creep resistance was least for Ir-Nb-Ta while Ir-Nb-Ti showed the lowest value for lattice misfit.

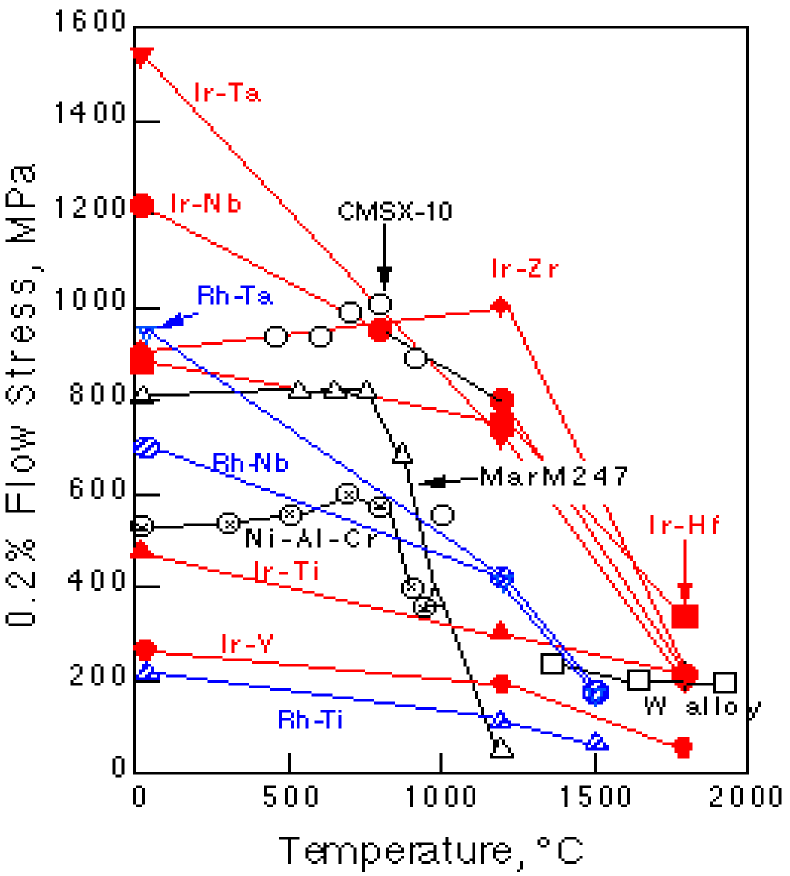

Figure 2.5. Temperature dependence of 0.2% flow stress during compression testing in as-cast Ir-based and Rh-based alloys compared with Ni-based and W-based alloys [1998Yam].

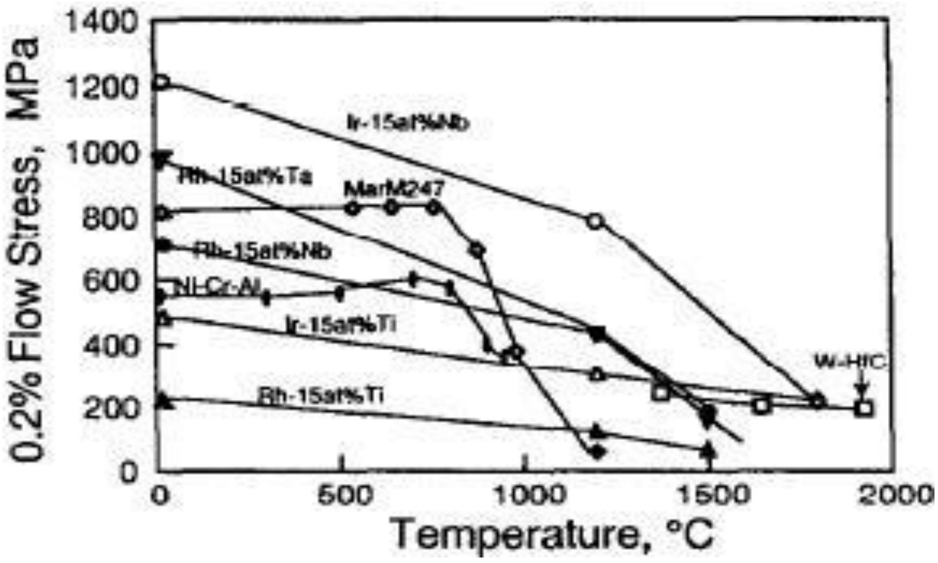

Figure 2.6. Temperature dependence of the 0.2% flow stress in Rh alloys [1997Yam].

Gu, Yamabe-Mitarai, Ro, Yokokawa and Harada studied the effects of boron doping on the high temperature strength and fracture behaviour of Ir-15 at.% Nb alloy [1999Gu1]. Addition of boron up to 200 ppm (wt%) increased the yield strengths of the binary alloy at room temperature and up to 1200°C, while it had little effect on the compression ductility. The fracture mode of the B-doped alloys changed to transgranular cleavage from intergranular fracture of the undoped alloys. In addition, the yield strength of the Ir-Nb (13-23 at.% Nb) two-phase refractory superalloys was found to increase with increasing Nb content up to 17 at.%, and then decreased [1999Gu2]. The fracture mode of the alloy also transformed from intergranular , when the Nb content was below 17 at.%, to transgranular in the alloy with above 17 at.% Nb. It was also found that the intergranular fracture in Ir-Nb two-phase alloys could be governed by controlling the microstructure around the grain boundaries.

Ir-based and Rh-based refractory superalloys are very dense and expensive when compared with Ni-based superalloys. In order to reduce the cost and density of these alloys, Gu and co-workers examined the possibility of replacing some of the Ir, or Rh, with Ni while attempting to maintain the desirable properties [1998Gu, 1999Gu3, 2002Gu]. The two-phase f.c.c./L1_2 structure was retained in Ir-Nb and Rh-Nb alloys with Ni additions of up to 20 at.% and 30 at.% respectively [1999Gu4]. Addition of up to 10 at.% Ni improved the strength, and changed the intergranular fracture mode in the binary alloys to a transgranular mode in the ternary alloys [1998Gu, 1999Gu2, 1999Gu3, 1999Gu4, 2002Gu]. The compression ductility of both the Ir-based and Rh-based alloys was found to improve with additions up to 50 at.% Ni [1998Gu, 1999Gu2, 1999Gu3]. Furthermore, addition of 1 at.% Ni greatly reduced the steady-state creep rate, as well as lattice misfit, and significantly improved the creep resistance of the ternary Ir-based alloys [2002Gu].

The possibility of developing new quaternary alloys by mixing two binary Ir-based and Ni-based alloys, which consist of coherent γ/γ’ two-phase structures in different proportions, was examined to reduce the cost and density of the Ir-based refractory superalloys [1999Yu1, 1999Yu2, 2000Yu, 2005Hua2]. This was aimed at utilizing the good ductility, low density and low cost of Ni-based superalloys in combination with high temperature strength of Ir-based refractory superalloys in the new quaternary alloys. In these quaternary Ir-Nb-Ni-Al alloys, two types of coherent f.c.c./$L1_2$-Ni_3Al and f.c.c./$L1_2$-Ir_3Nb structures as well as a three-phase region consisting of f.c.c., $L1_2$-Ni_3Al and $L1_2$-Ir_3Nb were observed at 1400°C [1999Yu1, 2000Yu]. Similar phases were also found in Ir-Ta-Ni-Al alloys, with Ir_3Ta instead of Ir_3Nb [2000Yu].

The compressive strengths of the Ir-Nb-Ni-Al alloys were found to be up to 350MPa, which is significantly higher than that of binary Ni-16.8 at.% Al alloy (11MPa), but lower than 500MPa for Ir-20 at.% Nb alloy at 1200°C [2000Yu]. However, the quaternary alloys' compressive strains were greatly improved relative to those of binary Ir-based alloys. The Ir-Nb-Ni-Al quaternary alloys also exhibited higher 0.2% flow stress and compressive strains compared with those of Ni-based superalloys at 1200°C [1999Yu2].

Huang et al. [2005Hua3] investigated phase relationships and mechanical properties of Ir-Nb-Ni-Al and Ir-Nb-Pt-Al quaternary alloys. The Ir-Nb-Ni-Al alloys displayed higher creep rates than binary and ternary Ir-based alloys. These alloys were also reported to show two-phase coherent f.c.c./$L1_2$ structures around the Ir-rich or Ni-rich corners and three or four-phase equilibrium with two types of $L1_2$ phases present. Only one f.c.c./$L1_2$ coherent two-phase structure with small lattice misfits between the matrix and the precipitate phases was found in the Ir-Nb-Pt-Al alloys. This combination displayed excellent creep resistance at 1400°C and 100MPa, and superior compressive strength than Ir-Nb-Ni-Al alloys with similar amounts of Ir at 1200°C.

Fairbank and co-workers at the University of Cambridge, United Kingdom, focused on the possibility of developing two-phase superalloy analogues based on Pt with additions of Hf and Zr as binary components, while Rh was a ternary addition. It was found that a two-phase f.c.c.-$L1_2$ (γ-γ') structure could not be developed in either the Pt-Zr or Pt-Hf system due to the formation of Pt_8Zr and Pt_8Hf [2003Fai]. However, the two-phase (γ-γ') structure was observed with the addition of Rh to the binary systems because it suppressed the formation of low temperature phases. A $Pt_{74.5}$:$Rh_{8.5}$:Hf_{17} (at.%) alloy was reported to have promising creep resistance and higher proof stress than the $Pt_{80.5}$:$Ti_{6.5}$:Cr_{13} (at.%) alloy also investigated [2000Fai1, 2000Fai2]. The oxidation properties of the alloys were not studied.

Oxidation behaviour of Rh-15 Ti, Rh-20 Ti and Rh-30 Ni-18 Nb (at.%) was investigated by Davis and Mahapatra [2002Dav] and Mahapatra et al. [2004Mah]. Their results revealed that these alloys have superior oxidation resistance beyond the operational limit for Ni-based superalloys. The binary Rh-xTi alloys (where x is 15 or 20 at.%) formed TiO_2 preferentially instead of Rh_2O_3 at higher temperatures [2002Dav]. The ternary alloy oxidized by forming alternate layers of Nb_2O_5 and RhO while NiO was formed on the surface in contact with air [2004Mah].

The potential of PGM-based superalloys as promising next generation higher temperatures materials has been highlighted. The presence of two-phase f.c.c./$L1_2$ structures enhanced the high temperature strength of the alloys, while good environmental stability was provided by the PGMs [1991Pan]. However, major disadvantages of most of the Ir and Rh-based refractory superalloys are their brittleness as well as high cost and density.

2.3 Development of the Precipitation-Hardened Pt-based Superalloys

Based on the good high temperatures properties displayed by Ir- and Rh-based alloys [1996Yam, 1997Yam, 1998Yam1, 1999Yam1, 1999Yam2, 2000Yu], and similarity in structure and chemistry of Pt and Ni, the research group based at Mintek and the University of the Witwatersrand proposed the development of Pt-based analogues to Ni-based superalloys [2000Wol]. Platinum with higher melting point (1769°C for Pt compared to 1455°C for Ni) and better environmental stability [1962Kni], could be developed with similar phases to Ni_3Al, and used for the highest temperature components, as well as in more aggressive environment [1999Wol1, 2000Wol, 2001Hil6].

The presence of the $L1_2$ structure of Ni_3Al (γ') phase is generally accepted as a prerequisite for excellent mechanical properties exhibited by NBSAs. This is because the ordered f.c.c. ($L1_2$) structure has a very close crystallographic relation with the Ni matrix, and hence can develop coherent interfaces with the matrix. This will make the coarsening of γ' more difficult because coherent interfaces with small lattice misfit lead to low interfacial energies [1987Sim]. However, unlike Ni-based superalloys which have only one form of high temperature Ni_3Al precipitate, phase diagrams of the Pt-Al system reported by Mishima and co-workers [1986Mis, 1987Oya] (Figure 2.7) and Massalski [1990Mas] (Figure 2.8) show that the $L1_2$ phase, which coexists with (Pt) at high temperatures, transforms to tetragonal Pt_3Al(r) at lower temperatures. The formation of coherent interfaces between a cubic and a tetragonal phase will be difficult, and this will affect the mechanical properties of the alloys. In order for the Pt-based alloys to be useful at higher temperature, the transformation of Pt_3Al at the Pt-rich side of stoichiometry to the tetragonal low-temperature allotropes should be avoided. Appropriate alloying and heat treatment should be carried out on the Pt-Al system to stabilize the more desirable high temperature $L1_2$ form of Pt_3Al.

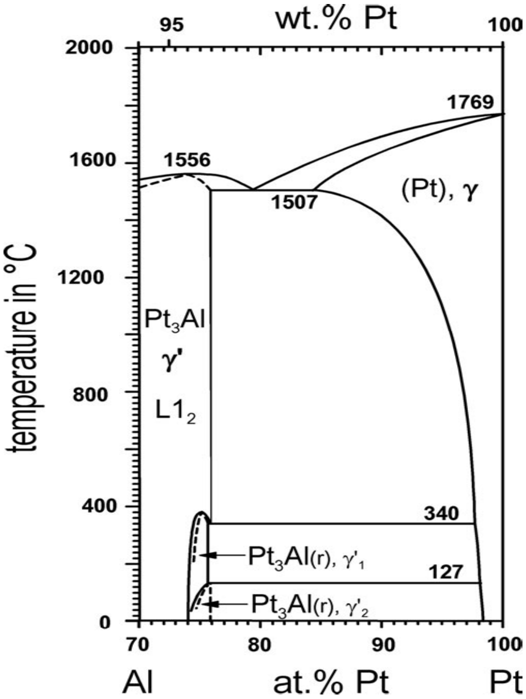

Figure 2.7. Pt-rich proportion of the Pt-Al phase diagram according to Mishima *et al*. [1986Mis, 1987Oya].

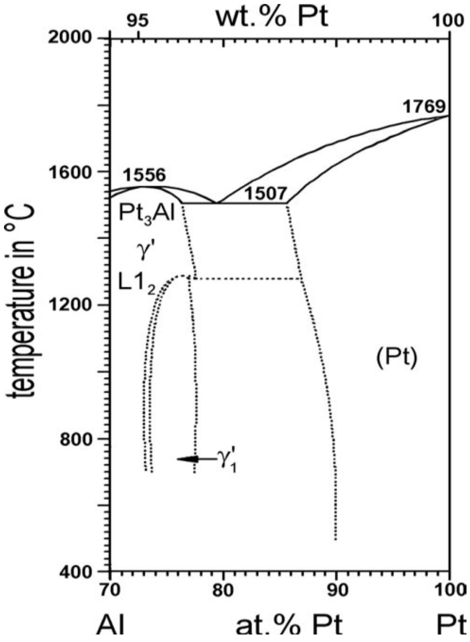

Figure 2.8. Pt-rich proportion of the Pt-Al phase diagram according to Massalski [1990Mas].

2.3.1 Microstructure and Mechanical Properties of the Pt-based Superalloys

The ability of superalloys to maintain their mechanical strength over the temperature ranges at which gas turbine components operate is a prime reason that attracts them for use in aerospace industry. This outstanding strength depends on their microstructure, which were derived from the phases established by the chemical compositions of the superalloys [1987Sim].

The preliminary investigations at Mintek and the University of the Witwatersrand [1999Wol1, 1999Hil, 2000Wol, 2001Hil2, 2001Hil3, 2001Hil6] focused on assessment of ternary Pt-X-Z compositions that would yield two-phase microstructures consisting of f.c.c. (Pt) matrix and ordered f.c.c. ($L1_2$) Pt_3X precipitates. The compositions were selected by studying the binary phase diagrams [1990Mas]. The 'X' represents an element forming a Pt_3X phase and 'Z' represents a solid-solution strengthening element for the Pt-matrix phase. Candidate Pt_3X-forming elements selected were Al, Ti, Ta and Nb. Candidate solid-solution strengthening elements selected were Ru, Ni, and Re. Pt-Al-Z and Pt-Ti-Z alloy systems were found to contain the desirable two-phase γ/γ’ microstructures and displayed promising mechanical properties at room temperature as well as high resistance to crack formation and propagation [2001Hil2]. The hardness values of the ternary alloys were found to be higher than 400HV_1. Increasing the Re concentration in the alloys above about 3 at.% resulted in precipitation of the Re-rich needle-like phase. Nb-containing alloys experienced large losses of Nb which indicated that the alloy was insufficiently stable. The presence of a lath-like second phase Nb showed that the two-phase γ/γ' microstructures could not be formed in Nb-containing alloys.

The phase relations and room temperature mechanical properties of eight Pt-Al-X ternary systems (X= Ru, Re, Cr, Mo, W, Ti, Ta and Ni) were examined after annealing at 1350°C for 96 hours [2002Hil]. Two-phase microstructures consisting of cuboidal $L1_2$ precipitates in an f.c.c. (Pt) matrix were formed in the Pt-based alloy Pt_{86}:Al_{10}:Z_4 (at.%). Addition of Cr as a ternary element was found to stabilize the cuboidal $L1_2$ (γ') phase, while Ru acted as a better solid solution strengthener [2000Hil, 2002Hil, 2001Big1, 2004Cor, 2006Cor, 2009Cor1]. However, the high temperature $L1_2$ form of Pt_3Al was not stabilized by the 2 at.% Ru addition. The lowest misfit between γ/γ' was found when the Ru amount was between 3-5 at.% and over 20 at.% Al [2001Big2]. Both the W- and Ni-containing alloys contained the lower temperature form of γ' phase. Molybdenum substituted for Pt in Pt_3Al in molybdenum-containing alloys, producing coarse microstructures. Addition of Ta, Ti and Cr was found to stabilize the high temperature $L1_2$ form of γ' and also produced the required microstructure.

The effects of various substitutional alloying additions on the precipitate morphology, lattice mismatch and high-temperature strengths of precipitation-strengthened ternary Pt-Al-X alloys (X= Cr, Ir, Ti, Ta and Ru) were investigated [2001Hil5]. Ternary alloys containing Ti, Cr and Ta showed the presence of a two-phase microstructure similar to those in NBSAs and their high temperature strengths were found to be dependent on the proportion of the γ' phase. Addition of both Cr and Ti were found to stabilize the cubic ($L1_2$) form of Pt_3Al [2001Hil1]. Alloys with Ru and Ir additions, with 'maltese cross' precipitates, displayed the lowest strength due to the low proportion of γ' phase in their microstructures. The lattice misfits, δ of these alloys at room temperature and 800°C are shown in Table 2.2 [2001Hil5]. The high temperature compressive flow stress of the ternary Pt-Al-X alloys had earlier been found to be higher than the commercial NBSA MAR-M247 above 1150°C [2001Hil4].

Table 2.2. Comparative lattice misfits of selected Pt_{84}:Al_{10}:Z_4 alloys comprising (Pt) matrix and ~Pt_3Al precipitates (ppt) [2001Hil5].

Alloy	**~Pt_3Al type**	**Room temperature**			**800°C**		
		a_{matrix}, nm	**a_{ppt}, nm**	**Lattice matrix, δ**	**a_{matrix}, nm**	**a_{ppt}, nm**	**Lattice matrix, δ**
Pt_{84}:Al_{10}:Cr_4	$L1_2$	3.9022	3.8741	-0.0072	3.9390	3.9103	-0.0073
Pt_{84}:Al_{10}:Ir_4	D0’$_c$	3.8983	3.8507	-0.0123	3.8747	3.8747	-0.0128
Pt_{84}:Al_{10}:Ru_4	D0’$_c$	3.9001	3.8530	-0.0121	3.8967	3.8967	-0.0098
Pt_{84}:Al_{10}:Ta_4	$L1_2$	3.8941	3.8682	-0.0067	3.8961	3.8961	-0.0073
Pt_{84}:Al_{10}:Ti_4	$L1_2$	3.8921	3.8642	-0.0072	3.9246	3.8961	-0.0073

Douglas et al. [2004Dou] carried out a detailed TEM study of Pt_{86}: Al_{10}: X_4 alloys (X = Cr, Ru, Ti, Ir and Ta) in order to determine the interactions of dislocations with the precipitates and to compare the different effects of the ternary elements addition on the ~Pt_3Al precipitates. The samples used for this experiment had been compressed to a true strain of about 3% at different temperatures (21, 800, 1000 and 1300°C). The γ lattice parameters in the ternary Pt-Al-X alloys determined by selected area electron diffraction were slightly different from those reported by Hill and co-workers [2002Hil]. This was as a result of calibration differences in the microscope’s camera. All the patterns were reported to be of <112> zone type. The morphology of the precipitates in most of the investigated alloys was not the same. When a binary Pt-Al alloy was studied in an attempt to resolve the two different versions of the Al-Pt phase diagram [1986McA, 1987Oya], a modified version of the tetragonal lower temperature forms of γ’-Pt_3Al, DO’c unit cell (Figure 2.9) structure was identified and the transformation producing it was confirmed to be displacive [2007Dou, 2009Dou].

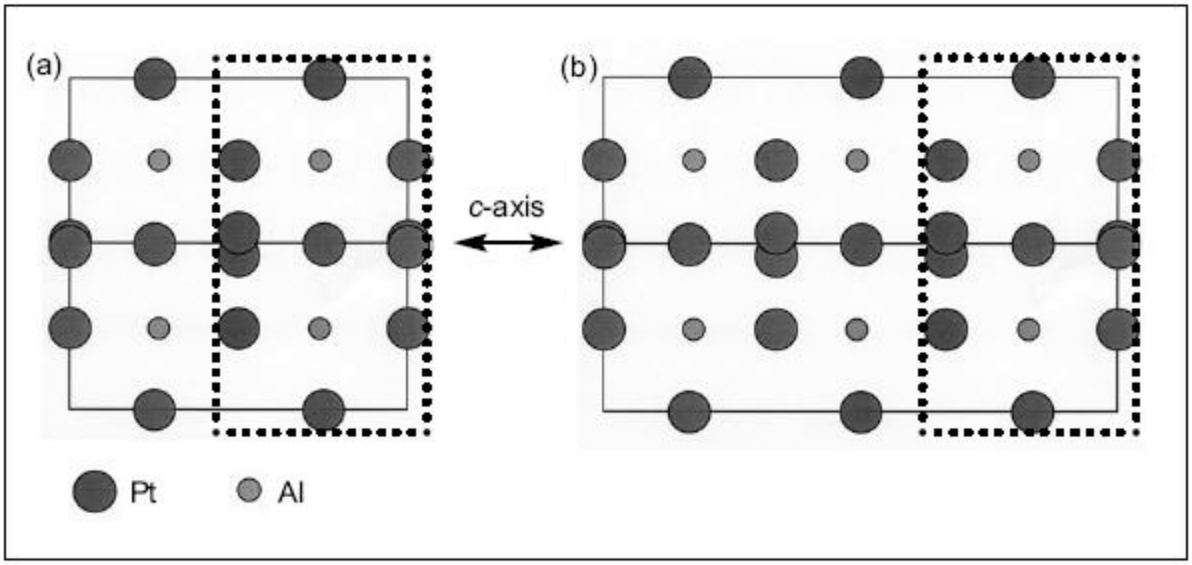

Figure 2.9. (a) Unit cell of the D0’$_c$ structure of a typical Pt_3Al precipitate in a Pt_{86}:Al_{14} (at.%) alloy, B = [110]; (b) Unit cell of the modified tetragonal D0’c structure of a Pt_3Al precipitate, B = [110] [2007Dou].

The effects of alloying additions on the creep properties of Pt-Al-X alloys at 1300°C were examined by Süss et al. [2002Süs2]. The ternary elements (X= Cr, Ir, Ru, Ta, and Ti) selected had potential to improve the high-temperature mechanical properties and phase stability of the ternary alloys [2001Big1, 2001Hil1, 2001Hil5]. The ferritic ODS alloy PM2000 was used as a benchmark alloy as shown in Figure 2.10. The ratio of Pt:Al:Z in all the tested alloy samples was standardised to Pt_{86}:Al_{10}:Z_4, for easy comparison. All the tested Pt_{86}:Al_{10}:Z_4 alloy samples had lower strength than PM2000, and Pt-Al-Cr possessed highest strength. The creep curves of the benchmark alloy, PM2000, and three Pt-based alloys Pt_{86}:Al_{10}:Z_4 tested at 1300°C and 30MPa, shown in Figure 2.11 revealed that for any of the three Pt-based alloys, no primary creep stage could be observed within the measurement error of the creep test facility. After secondary creep, the Pt-based alloys experienced significant tertiary creep, which led to fracture strain values between 10 and 50% at 1300°C. Resolving different stages of the creep curves was impossible for the benchmark alloy, PM2000, because of very low creep rates together with fracture strains below 1 percent [2002Süs2].

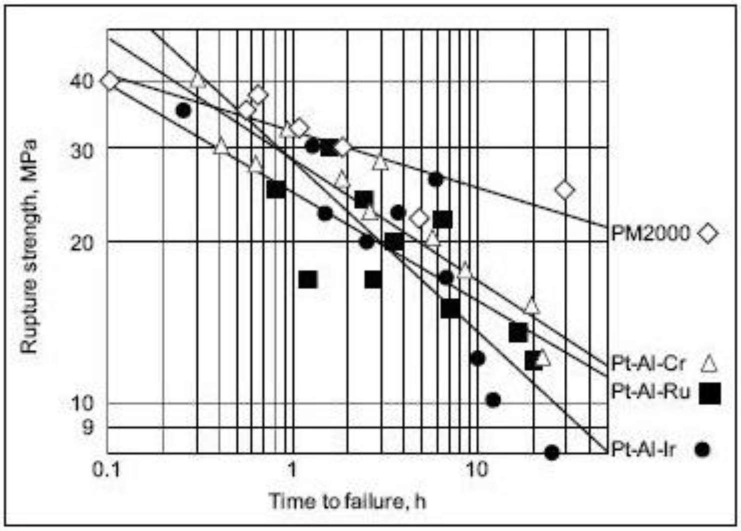

Figure 2.10. Stress-rupture curves of PM2000 and Pt_{86}:Al_{10}:Z_4 (at.%) alloys at 1300°C in air [2002Süs2].

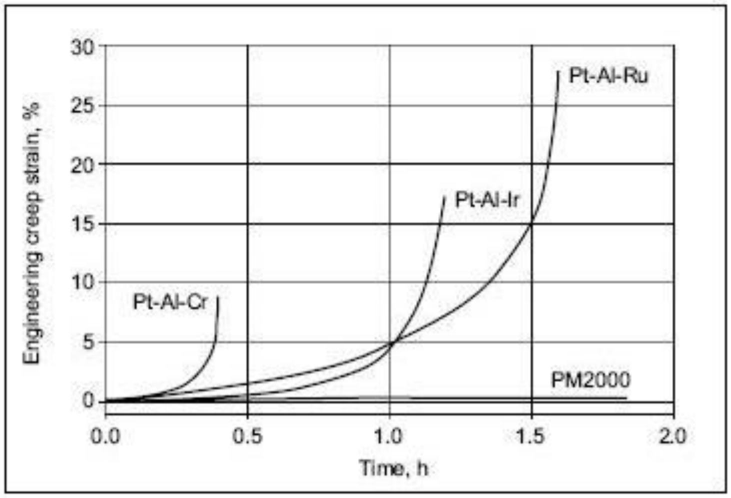

Figure 2.11. Creep curves of PM2000 and Pt_{86}:Al_{10}:Z_4 (at.%) alloys tested at 1300°C and 30MPa [2002Süs2].

Figure 2.12 shows the stress-rupture curves of ferritic ODS alloy, the benchmark alloy, and Pt_{86}:Al_{10}:Cr_4, the most promising Pt-based alloy, together with 10 hours stress-rupture strength values at 1300°C of several conventional solid-solution strengthened Pt-based alloys [1968Dar], as well as that of zirconia grain stabilised (ZGS) platinum, an oxide dispersion strengthened platinum alloy. There was a considerable increase in 10 hour stress-rupture strength values at 1300°C by a factor of 8 from 2.2 MPa for the pure Pt matrix to 17 MPa for Pt_{86}:Al_{10}:Cr_4 (Figure

2.12). This was said to be the effect of strengthening that was achieved by precipitation of γ' particles. Addition of 30 wt% Rh to solid solution strengthened Pt-Rh alloys is necessary before the higher strength of Pt_{86}:Al_{10}:Cr_4 can be reached [2002Süs2]. The strength of Pt_{86}:Al_{10}:Cr_4 is higher than the solution strengthened Pt-based alloys with 10 and 20 wt% Rh. However, this is impracticable due to high price of Rh and difficulty in machining Pt-Rh with more than 20 wt% of Rh. Higher temperature creep strength of Pt-based alloys is more than those of Ni- and Co-based superalloys, whose strength become reduced as a result of dissolution of their precipitates in this higher temperature regime. The Pt-based, Pt_{86}:Al_{10}:Z_4 alloy systems have a creep strength that is comparable to those of mechanically alloyed ferritic ODS alloys.

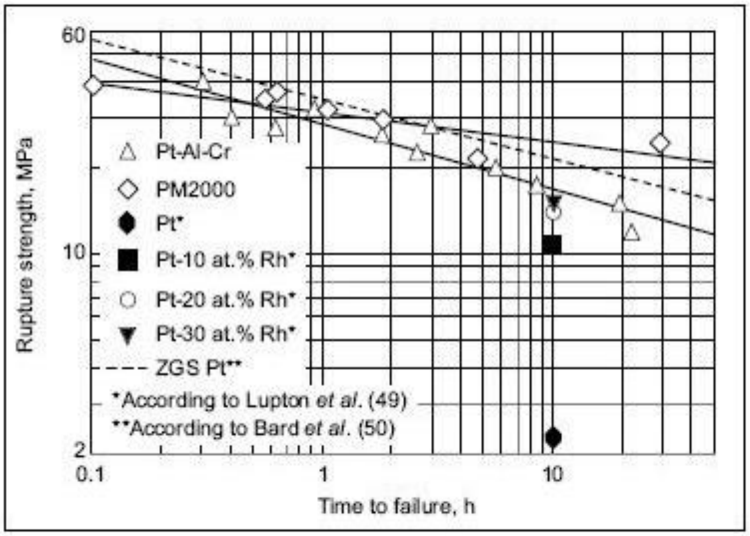

Figure 2.12. Stress-rupture curves at 1300°C of PM2000, Pt, ZGS platinum and Pt_{86}:Al_{10}:Cr_4 [2002Süs2].

Several quaternary alloys were developed based on the results of the ternary Pt-Al-Cr and Pt-Al-Ru systems by Cornish et al. [2002Cor]. An alloy with composition Pt_{84}:Al_{11}:Cr_3:Ru_2 (at.%) was found to be optimum because it contained only the two-phase γ/γ’ mixture and had the highest hardness value among the alloys studied. In an effort to improve the volume fraction of γ’ precipitates and the microstructure of the alloys, they were heat treated further for 96hrs at 1623K in air [2003Cor, 2009Cor2]. A decrease in the hardness of most of the alloys was observed after the second heat treatment, and this was reported to be due to the loss of aluminium as a result of oxidation [2002Cor]. The creep results of the Pt_{84}:Al_{11}:Cr_3:Ru_2 alloy were worse than for Pt_{86}:Al_{10}:Cr_4 (at.%) and for dispersion hardened (DPH) Pt alloy, while the high-temperature compressive strength of the Pt_{84}:Al_{11}:Cr_3:Ru_3 alloy was found to be significantly higher than that of Pt_{86}:Al_{10}:Cr_4. Similarly, the Pt_{80}:Al_{14}:Cr_3:Ru_3 (at.%) alloy produced and annealed at 1300°C for 96 hours before quenching in water also showed better high temperature strength than Pt_{86}:Al_{10}:Cr_4 because of high volume fraction of ~Pt_3Al precipitates [2003Süs, 2004Ker].

Shongwe et al. [2008Sho] varied the compositions of several Pt-Al-Cr-Ru alloys to further improve the volume fraction of their γ' precipitates and hardness. The alloys were heat-treated in two stages; first at 1500°C for 18 hours and quenched in water, followed by 1100°C for 120 hours and then air-cooled. The alloy with the composition Pt_{78}:Al_{11}:Cr_6:Ru_5 (at.%) was reported to be most promising based on its higher γ' precipitates volume fraction and lower Pt contents as well as higher hardness value. The lattice misfits and the hardness values of the Pt-Al-Cr-Ru alloys are given in Table 2.3.

Table 2.3. Room temperature lattice misfits and hardness values of Pt-Al-Cr-Ru alloys [2008Sho].

Nominal Composition (at.%)	**Lattice misfit**	**Hardness (HV)**
Pt_{78}:$Al_{15.5}$:Ru_2:$Cr_{4.5}$	-0.0072	164
Pt_{80}:Al_{14}:Ru_3:Cr_3	-0.0102	361
$Pt_{81.5}$:$Al_{11.5}$:$Ru_{2.5}$:$Cr_{4.5}$	-0.0067	391
Pt_{82}:Al_{12}:Ru_2:Cr_4	-0.0044	378
Pt_{84}:Al_{11}:Ru_2:Cr_3	-0.0063	395
Pt_{85}:Al_7:Ru_3:Cr_5	-0.0089	380
Pt_{80}:Al_{11}:Ru_5:Cr_4	-0.0041	247
Pt_{80}:Al_{11}:Ru_3:Cr_6	-0.0079	237
Pt_{80}:Al_{11}:Ru_6:Cr_3	-0.0065	226
Pt_{78}:Al_{11}:Ru_5:Cr_6	-0.0049	357
Pt_{78}:Al_{11}:Ru_3:Cr_8	-0.0066	354
Pt_{78}:Al_{11}:Ru_8:Cr_3	-0.0088	396

The effects of addition of Ni or Co to Pt-Al alloys in an attempt to improve their properties, and decrease their cost and density was investigated [2003Cho, 2003Gla, 2004Cho]. Although the melting point of the alloy with Ni additions was surprisingly increased, the solution strengthening achieved and the hardness values were below expectations. Pt-Al-Co and Pt-Al-Co-Cr-Ru alloys with hardness values below 400 HV_{10} showed good formability (above 75% total reduction in thickness), while for hardness values above 450 HV_{10} the cold formability was poor (less than 40%) as shown in Figures 2.13 and 2.14. Addition of cobalt to the Pt-Al alloys improved their cold formability compared to those alloyed with Ru, Ni, and Cr [2003Cho, 2004Cho, 2008Süs].

The research groups at the University of Bayreuth, Bayreuth and University of the Applied Sciences in Jena, Germany focused on the development of superalloys based on the Pt-Al systems [2005Hül, 2006Pru, 2005Wen1, 2005Wen2]. This was based on earlier results of Hill and co-workers [2000Hil, 2001Hil1], which revealed that alloys based on Pt-Al displayed the highest potential both in terms of high oxidation resistance due to formation of protective Al_2O_3 scale and possible precipitation strengthened of Pt_3Al.

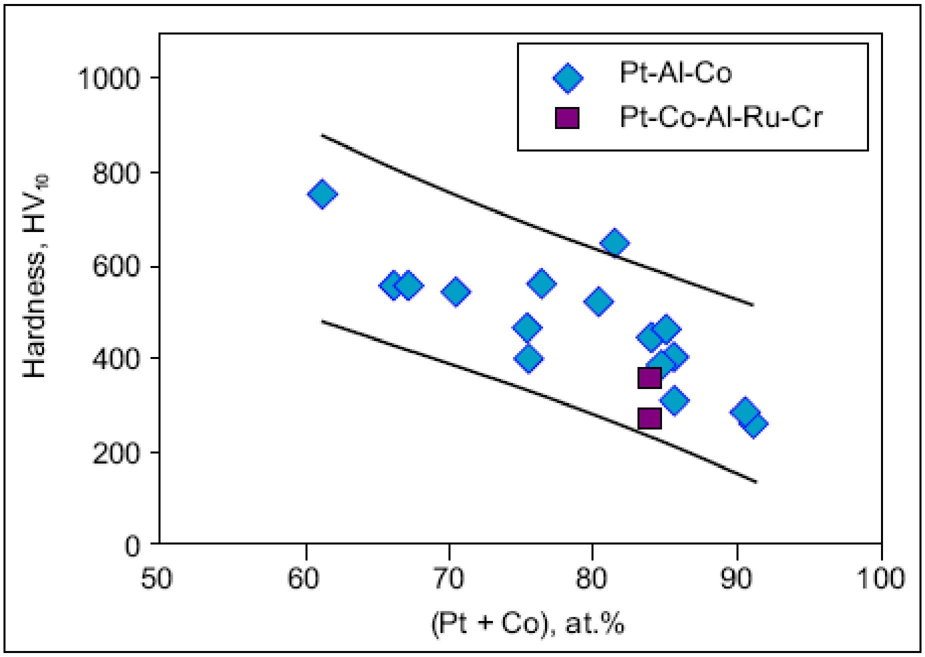

Figure 2.13. Hardness as a function of at.% (Pt + Co) for Pt-Al-Co alloys [2003Cho, 2004Cho, 2008Süs].

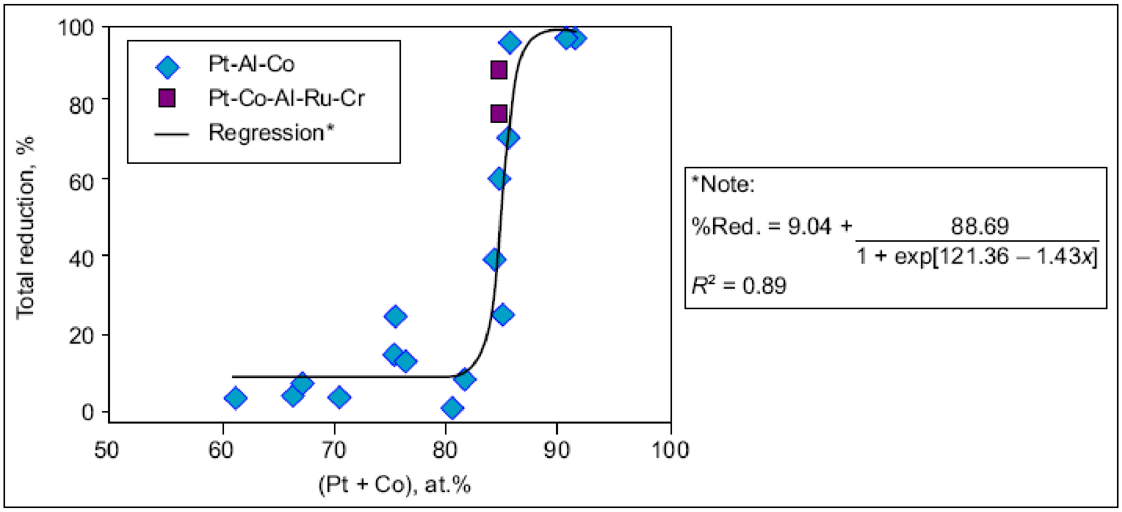

Figure 2.14. Total reduction (% Red.) as a function of at.% (Pt + Co) for Pt-Al-Co alloys [2003Cho, 2004Cho, 2008Süs].

The microstructure of precipitation-strengthened $Pt_{78.5}$:$Al_{12.5}$:Cr_3:Ni_6, Pt_{76}:Al_{12}:Cr_6:Ni_6 and Pt_{82}:Al_{12}:Ni_6 (at.%) alloys were investigated after homogenization heat-treatment and various cooling regimes [2004Vor]. Alloys with Cr additions showed the presence of the $L1_2$ ordered Pt_3Al phase at room temperature. Air cooling led to precipitation of 200nm sized γ' cubes with 30% volume fraction. However, formation of γ' was almost suppressed after water quenching of heat-treated $Pt_{78.5}$:$Al_{12.5}$:Cr_3:Ni_6 (at.%) alloy. Higher Cr contents in Pt_{76}:Al_{12}:Cr_6:Ni_6 increased the volume fraction to about 50% and the precipitate size to 500nm.

Vorberg et al. [2005Vor] investigated the dislocation structures at the γ/γ' phase boundary of the Pt_{79}:Al_{14}:Cr_3:Ni_4, Pt_{77}:Al_{14}:Cr_3:Ni_6, Pt_{75}:Al_{14}:Cr_3:Ni_8 alloys by means of transmission electron microscopy (TEM). The results revealed that the shape of the γ'-precipitates changed from irregular, to cubic and finally to spherical as the Ni contents increased. The matrix of all the alloys was found to be free from dislocations. Increasing the Ni concentration of the alloys from 4 at.% to 6 at.% led to a reduction in the lattice misfit between γ and γ' from 3.10^{-3} to 1.10^{-3}. This resulted in the formation a microstructure similar to that of Ni-based superalloys, consisting of perfectly coherent γ'-cubes.

The effect of adding Nb, Ta or Ti as a substitute for 5 at.% Al on microstructure and high temperature strength of ternary alloys with composition $Pt_{82:}Al_{12}$:Cr_6 (at.%) was examined by Wenderoth et al. [2008Wen]. It was observed that the γ'-solvus temperature and the mechanical strength were increased by the addition of these elements. However, Rudnik et al. [2008Rud] found that the addition of more than 9 at.% Ta to the ternary alloy promoted oxidation resistance, increased its high-temperature strength and phase stability, but decreased the γ’ volume fraction as well as the ductility of the alloy .

Based on their high melting points, Nb, Ta, and Ti were chosen to substitute for Ni in Pt_{82}:Al_7:Cr_6:Ni_5 (at.%) and the results showed the presence of the f.c.c. γ matrix and the $L1_2$-ordered γ' phases, as well as small cuboids of up to 300 μm, and coarse and irregularly shaped particles with a total volume fraction in between 10 and 20%. However, after homogenization and ageing for 264 h at 1200°C with water quenching, the volume fraction of the Nb-containing alloy was found to be about 34 %, while those of Ta- and Ti-containing alloys were 33 % and 35 % respectively. Ta- and Nb-containing alloys showed a superior mechanical strength over the Ni-based superalloy CMSX-4 at temperatures above 1200°C [2006Völ].

2.3.2 Hot Corrosion Behaviour of the Pt-based Superalloys

High temperature mechanical strength and environmental stability (hot corrosion and oxidation resistance) are critical properties when considering materials for application at high-temperature environments [2006Pin]. Hot corrosion could lead to degradation of materials at high temperatures, and its excessive attacks could result in subsequent catastrophic failure of components in service [1996Deb]. Therefore, it is essential to evaluate the hot corrosion behaviour of the Pt-based alloys being developed.

The high temperature corrosion behaviour of five Pt-based alloys and two samples of a single-crystal CMSX-4 NBSA were examined by performing a crucible test at 950°C to increase the corrosion kinetics [2006Mal, 2010Pot]. The nominal chemical compositions of the investigated Pt-based alloys are given in Table 2.2, and are $Ni_{66.5}$:$Cr_{6.5}$:Co_{11}:$Mo_{0.3}$:$W_{1.7}$:$Ta_{1.8}$:$Al_{11.3}$:$Ti_{0.9}$ for CMSX-4 having a 1.25 μm Pt_2Al-Pt_{67}:Al_{33} (at.%) coating. The samples were covered in analytical anhydrous Na_2SO_4 salt, which acted as the corrosive electrolyte inside a 200 ml alumina crucible that was placed inside a furnace with a static dry air environment [2006Mal]. The corrosion kinetics of the five Pt-based alloys and that of coated CMSX-4 alloy during exposure to Na_2SO4 at 950°C for the first 50 hours are shown in Figures 2.15 and 2.16.

Table 2.4. Nominal chemical composition of selected Pt-based alloys (at %) investigated [2006Mal].

Alloy	Pt	Al	Cr	Ru	Co
RS1	86	10	4	0	0
RS2	86	10	0	4	0
RS3	84	11	3	2	0
P420	79	15	0	0	6
P421	73	15	0	0	12

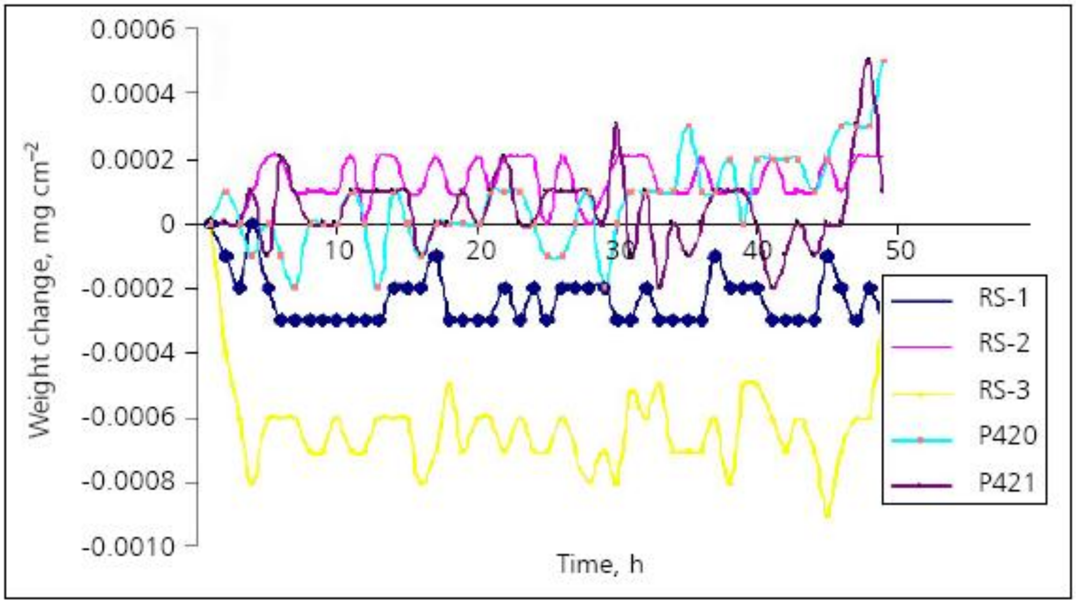

Figure 2.15. Corrosion kinetics of five Pt-based alloys of various compositions during exposure to Na_2SO_4 at 950°C for the first 50 hours [2006Mal, 2010Pot].

It was observed that there was very little change in the mass of the Pt-based alloy samples immersed in Na_2SO_4 at 950°C for 852 hours. This was due to the formation of a protective Al_2O_3

layer as detected by the XRD. By contrast, a mixture of compounds based mainly on Na and Ni was identified on the NBSA samples. Non-protective oxides which resulted in catastrophic corrosion were formed on the NBSA samples after the initial mass gain. The corrosion resistance of the Pt_{86}:Al_{10}:Cr_4 was found to be the best, while more pits were later observed on Pt_{86}:Al_{10}:Ru_4 and Pt_{84}:Al_{11}:Cr_3:Ru_2 than on Pt_{79}:Al_{15}:Co_6. In all cases, Pt-based alloys were much better in terms of corrosion resistance than those of coated and uncoated CMSX-4 samples. The scales of the Pt based alloys without Co were similar to each other and more adherent (Figure 2.17), giving superior protection against hot corrosion than Pt-Al-Co superalloys.

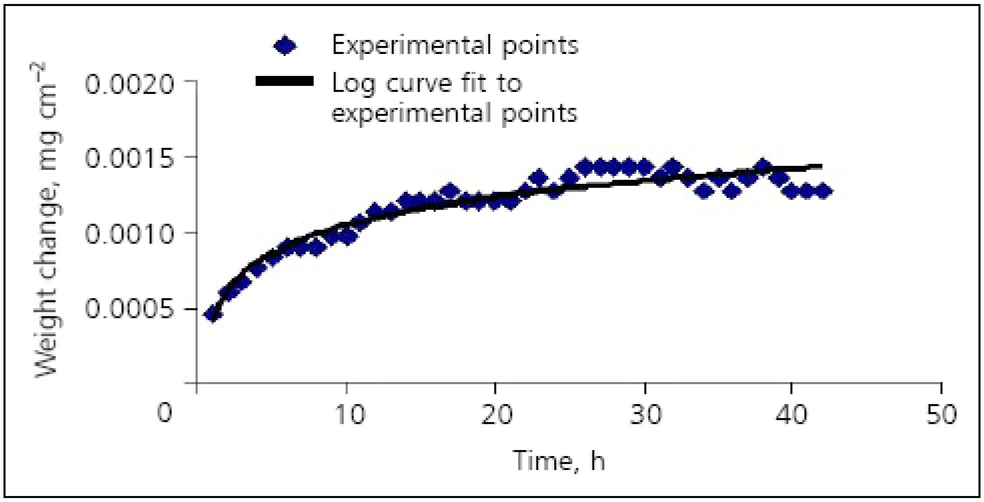

Figure 2.16. Corrosion kinetics of five Pt-based alloys of various compositions during exposure to Na_2SO_4 at 950°C for the first 50 hours [2006Mal, 2010Pot].

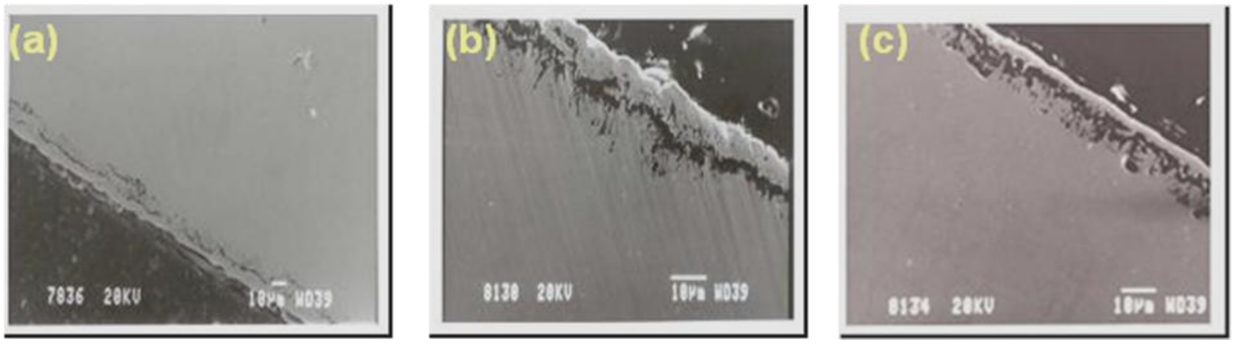

Figure 2.17. Secondary electron micrograph of the cross section of alloys: (a) RS-1; (b) RS-2; and (c) RS-3 after hot corrosion test at 950°C [2007Mal].

2.3.3 Oxidation Behaviour of the Pt-based Superalloys

Platinum, among the platinum group metals, is known for its superior oxidation resistance when heated in air at all temperatures [1958Pow]. Alloying Pt with Al improves its resistance to environmental degradation through the formation of external protective scale that hinders further reaction [1976Fel2]. Figure 2.18 shows the difference in oxidation properties between Pt and other high temperature materials, including some platinum group metals. However, this is an approximate comparison because the materials loss rates are not obtained under identical conditions.

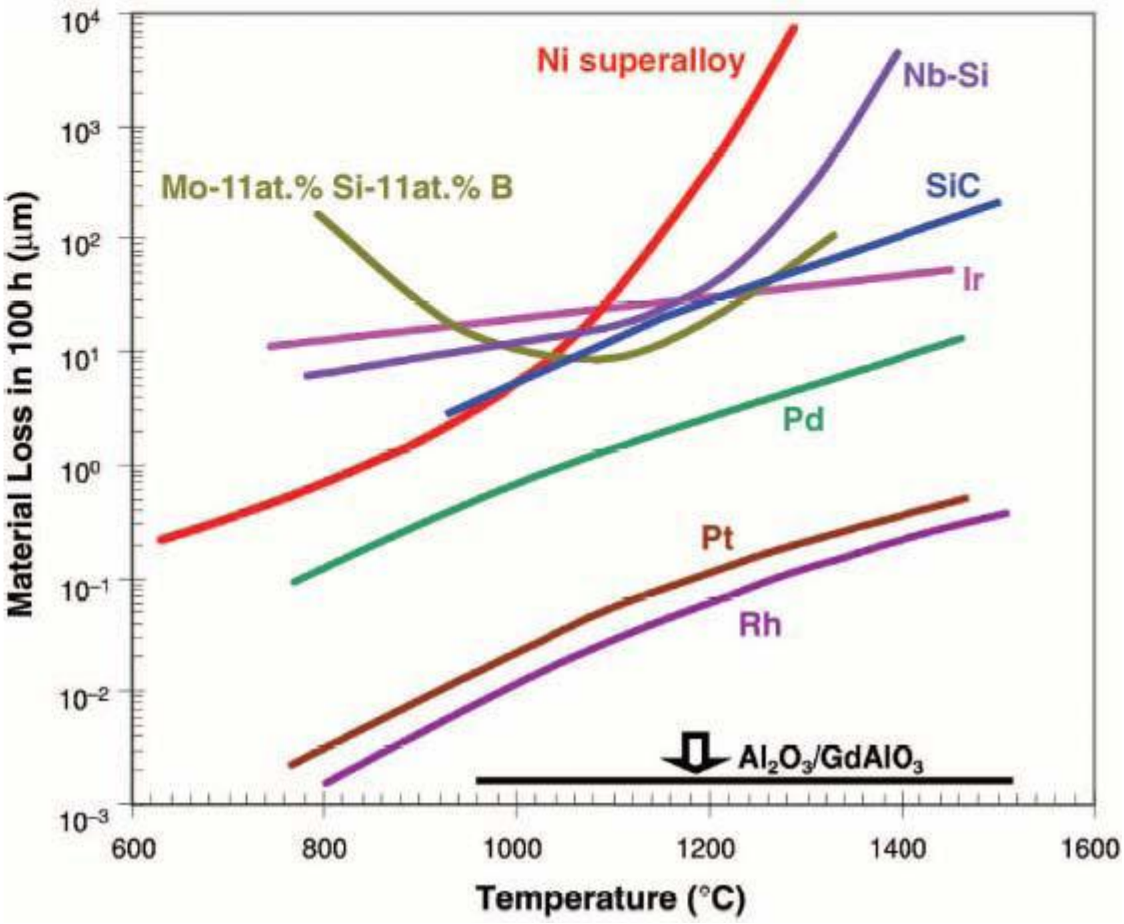

Figure 2.18. Oxidation/recession rates of selected high temperature materials [2003Zha].

Hill et al. [2000Hil] carried out preliminary investigations as part of the screening exercise to determine the oxidation resistance of the developed Pt-based alloys. The isothermal oxidation behaviour of several Pt-Al-X alloys was examined at 1200°C, 1280°C and 1350°C in air [2000Hil]. It was observed that protective external alumina scale was formed on the Pt-Al-Cr and Pt-Al-Ru alloys. Internal oxidation occurred in the Pt-Al-Ta, Pt-Al-Re and Pt-Al-Ti alloys (Figure 2.19). In another study, stepped oxidation tests were carried out on Pt-Al-Ni, Pt-Al-Ru, Pt-Al-Re, Pt-Nb-Ru and Pt-Ti-Ru alloys with varying compositions [2001Hil2]. As shown in Figure 2.20, the alloys containing Al exhibited better oxidation behaviour than the other alloys, through the formation of protective external alumina scale. There was extensive internal oxidation in the Pt-Nb-Re and Pt-Ta-Re alloys, while internal grain boundary oxidation was observed in the Pt-Ti-Ru alloys.

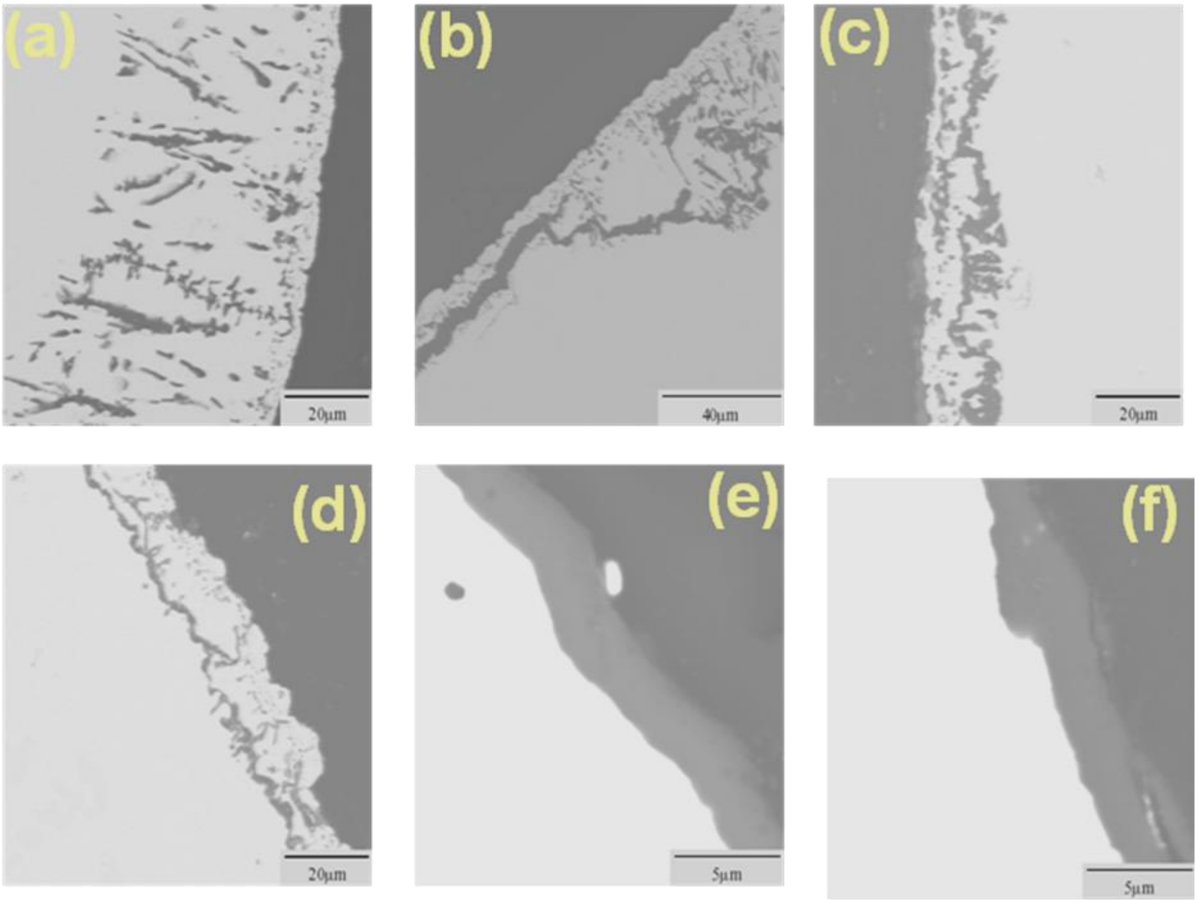

Figure 2.19. SEM-BSE images of transverse sections of the (a) Pt_{87}:Al_{10}:Re_3 (b) Pt_{83}:Al_{14}:Re_3 (c) Pt_{82}:Al_{14}:Ti (d) Pt_{82}:Al_{14}:Ta_4 (e) Pt_{76}:Al_{22}:Ru_2 (f) Pt_{82}:Al_{14}:Cr_4 [2000Hil].

Süss et al. [2001Süs1] studied the effect of various alloying additions on the isothermal oxidation behaviour of several ternary Pt-Al-Z (Z=Ti, Cr, Ru, Ta and Ir) alloys at 1350°C between 1 and 1000 hours. The nominal compositions of the ternary alloy samples were Pt_{86}:Al_{10}:Z_4, and they were tested against the ferritic ODS alloy PM2000 as a benchmark alloy. As shown in Figure 2.21, with the exception of the Pt-Al-Ta alloy, all other Pt-based alloys showed similar parabolic oxidation behaviour to the benchmark alloy by forming a protective alumina layer after an initial transient period during which discontinuous oxides were precipitated. However, the parabolic oxidation behaviour showed by the Pt-Al-Ir and Pt-Al-Cr alloys during the early stages of oxidation later became logarithmic. Thus, Pt_{86}:Al_{10}:Ir_4 and Pt_{86}:Al_{10}:Cr_4 alloys formed the thinnest continuous oxide layers after oxidation for 800 hours.

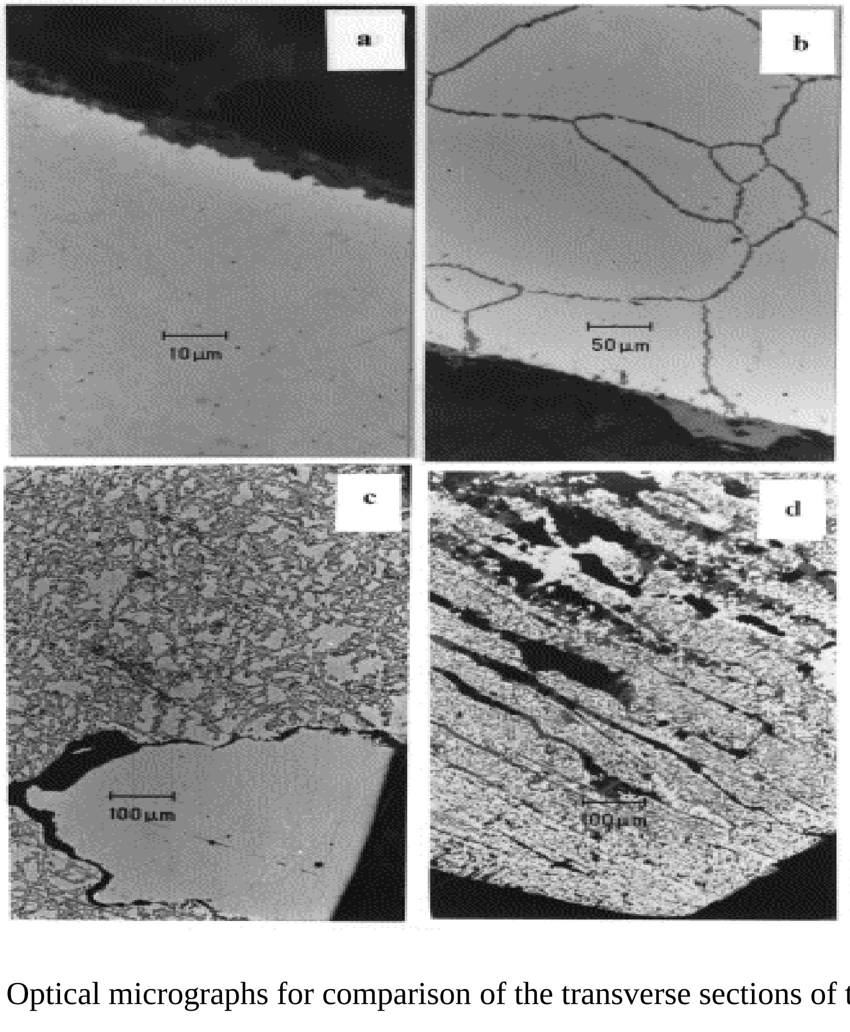

Figure 2.20. Optical micrographs for comparison of the transverse sections of the oxidized samples (a) Pt_{78}:Al_{14}:Ru_8; (b) Pt_{70}:Ti_{23}:Ru_7; (c) Pt_{72}:Ta_{24}:Re_4; (d) Pt_{73}:Nb_{24}:Ru_3 [2001Hil2].

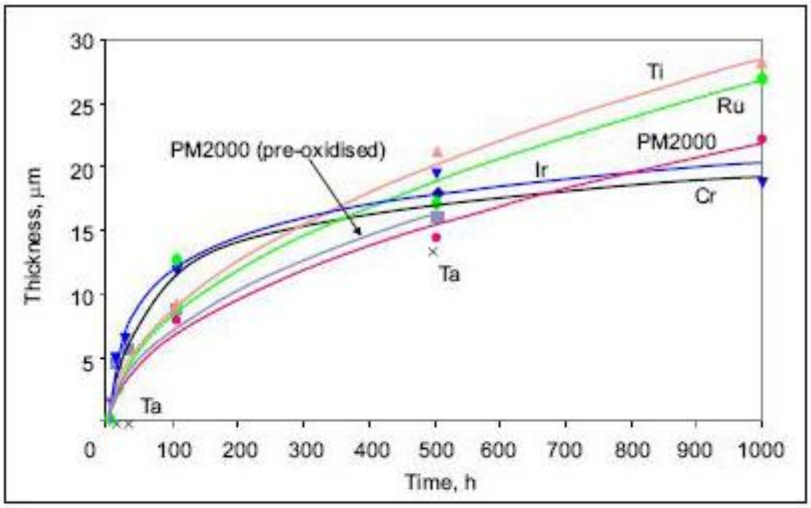

Figure 2.21. Results of the isothermal oxidation tests conducted on Pt-Al-Z alloys at 1350ºC, showing the specific mass changes with time over the first 1000 hours [2001Süs1].

Prior to the formation of an external protective alumina film, discontinuous alumina particles precipitated in a Pt matrix were formed during the transient period, as shown in Figure 2.22. In order to accelerate the formation of the continuous layer, and decrease the mass losses due to volatilisation, increasing the Al content of the alloys was suggested for further work [2001Süs1].

Based on their earlier results which revealed Pt_{86}:Al_{10}:Cr_4 alloy as promising with regard to high temperature strength and oxidation resistance, Süss et al. [2001Süs2] carried out further investigations to compare this alloy with Pt_{80}:Al_{14}:Cr_3:Ru_3. Ruthenium was added to increase the volume fraction of γ', while more Al was added in an effort to accelerate oxide scale formation. Isothermal oxidation of the samples in air at 1350°C for up to 1000 hours showed that neither a zone of discontinuous oxides, nor any other internal oxidation was formed on Pt_{80}:Al_{14}:Cr_3:Ru_3 alloy. However, it was thought that the oxidation rate of the alloy might be too severe after a very long exposure because after 10 hours' exposure (Figure 2.23), the scale was already about three times as thick as that observed for Pt_{86}:Al_{10}:Cr_4 after the same period. Hence, there is need for optimization of the quaternary alloy.

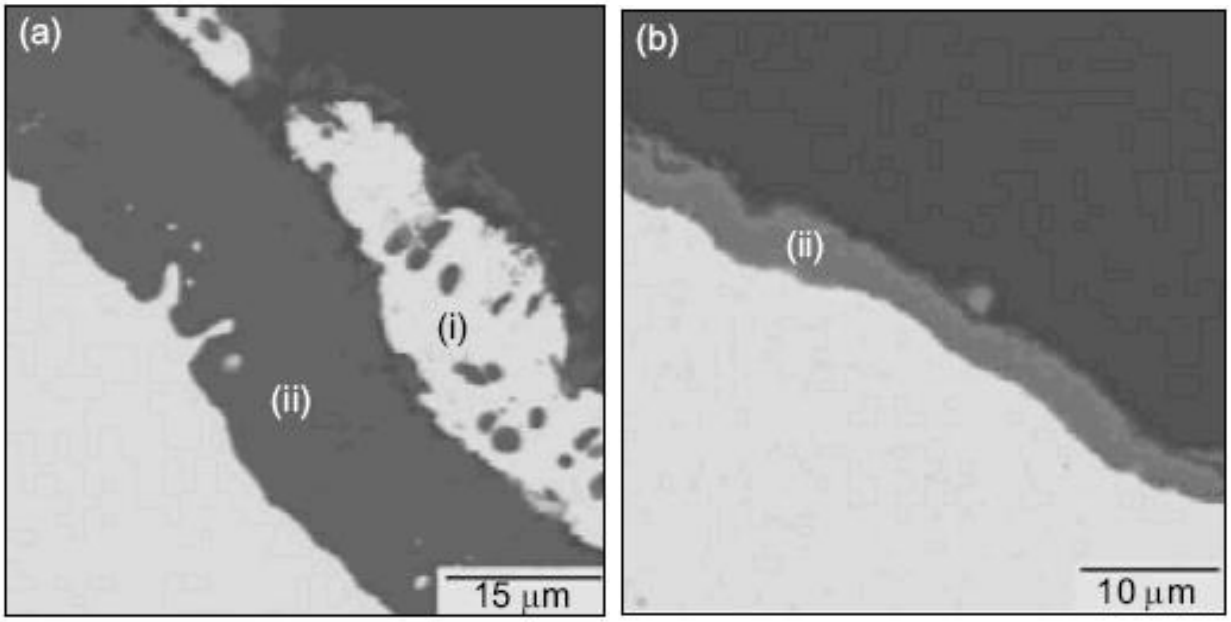

Figure 2.22. SEM-BSE images of transverse sections of the alloys isothermally oxidized at 1350°C for various times: Pt_{86}:Al_{10}:Cr_4 (at.%) for 1000 hours; (b) PM2000 for 10 hours; showing (i) transient oxidation, and (ii) continuous oxidation [2001Süs1].

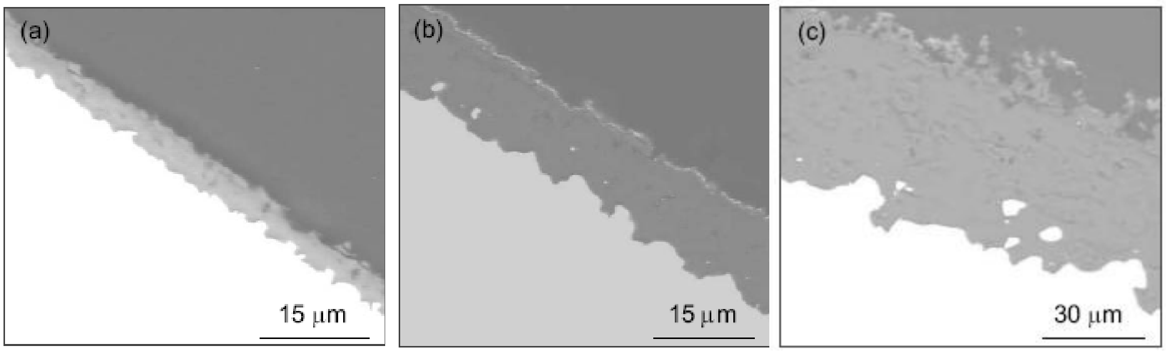

Figure 2.23. SEM images of the transverse sections of the Pt_{80}:Al_{14}:Cr_3:Ru_3 (at.%) alloy after exposure to air at 1350°C for an increasing amount of time (a) 1 h (b) 10 hours; (c) 500 hours [2001Süs2].

Wenderoth et al. [2007Wen2], one of the research group based in Germany, studied the isothermal oxidation behaviour of a precipitation hardened Pt_{77}:Al_{12}:Cr_6:Ni_5 alloy in the temperature range of 1100°C-1300°C after various time intervals from 0.4 h to 400 in still air. Formation of a dense and strongly adhering alumina scale at a rate faster than those of Pt-based alloys without Ni addition was observed. However, the growth rate declined after some time, possibly due to decrease in Ni concentration in the scale and grain coarsening in the scale. Addition of W as fifth alloying element (Pt_{75}:Al_{12}:Cr_6:Ni_5:W_2) led to internal oxidation and reduction in scale thickness [2007Wen1]. Pt_{75}:Al_{12}:Cr_6:Ni_5 alloys with 2 at.% Mo, Re, Ru additions also formed dense alumina scale after ageing in air for 120 h at 1200°C.

2.4 Oxidation of Metals and Alloys

Like most metals, alloys are thermodynamically unstable in oxidizing environments and tend to form oxides [1976Wal]. This process increases as the temperature increases, thereby creating the potential for failure of the component if too much of the substrate materials are consumed in the formation of these oxides. Therefore, for alloy to provide a useful working life, it must possess good oxidation resistance at the operating temperatures. Oxidation is therefore defined as a process in which an unstable metal or alloy reacts spontaneously with oxygen when exposed to air or oxygen at low and high temperatures to form the thermodynamically-favoured metal oxide, according to a reaction of the type given in Equation 2.2:

$$M(s) + \frac{1}{2}O_2(g) = MO(s) \tag{2.2}$$

However, the oxidation of metals and alloys are not usually only determined by the overall chemical process represented by the above equation. The mechanism of the diffusion processes and phase-boundary reactions usually determine the rate of the reaction. Generally, the slowest among the steps listed below will be rate determining [1965Hau].

1. Phase-boundary reactions (chemisorption of the non-metal molecules with simultaneous electron exchange and splitting of the molecules at the gas/oxide interface and transfer of the metal from the metallic phase, in the form of ions and electrons, to the scale at the metal/oxide interface with further reaction of the individual reactants and formation of the reaction products), nucleation and crystal growth.

2. Diffusion or transport of cations, anions and electrons through the scale complicated by a special migration mechanism because of the appearance of chemical and electrical potential gradients in the oxide scale.

3. Predominant transport processes in space-charge boundary layers in the case of thin oxide layers, especially at low temperatures.

Two further factors are also significant for the formation, composition and structure of the oxide layer:

4. The thermodynamic stability of the oxide that is formed.

5. The crystal structure of the oxide scale and of the metal or the alloy, which determines the adhesion between oxide scale and underlying alloy.

2.4.1 Mechanisms of Oxidation of Metals and Alloys

Consider the oxidation reaction given in Equation 2.3 [1974Law], where M is the reacting metal/alloy and M_xO_y the metal/alloy oxide:

$$xM(s) + \frac{y}{2}O_2(g) = MxOy \tag{2.3}$$

It is obvious that the first stage in oxidation involves the adsorption of oxygen at the metal/alloy surface. This will then result in the formation of either a surface oxide film or individual oxide particles within the alloy/metal matrix (internal oxide) when the oxygen dissolves [1974Law]. The driving force for the oxidation reaction above is the change in standard Gibbs free energy, ΔG (Equation 2.4) associated with the formation of oxide from reactants, a_i is the chemical activity of component i, PO_2 the oxygen partial pressure, T the absolute temperature and R the universal gas constant.

$$\Delta G = \Delta G^{\circ} + RT \ln \left(\frac{a_{MxOy}}{a^{x}{}_{M} PO_2^{\frac{y}{2}}} \right) \tag{2.4}$$

If $K = \frac{a_{MxOy}}{a^{x}{}_{M}\ PO_2^{y/2}}$, at equilibrium when ΔG = 0, then the above equation becomes:

$$-\Delta G^{\circ} = RT \ln[K] \tag{2.5}$$

where K is the equilibrium constant. Taking natural logarithms, Equation 2.5 becomes:

$$K = e^{\left(\frac{-\Delta G^{\circ}}{RT}\right)} \tag{2.6}$$

The minimum oxygen potential necessary to form a metal oxide can be obtained from Equation 2.6 when it is re-arranged to give Equation 2.7

$$Po_2^{\frac{y}{2}} = e^{\left(\frac{\Delta G^{\circ}}{RT}\right)} . \frac{a_{MxOy}}{a_M^x} \tag{2.7}$$

The equilibrium dissociation pressure of M_xO_y is $PO_2^{y/2}$. The ambient oxygen must exceed the equilibrium dissociation pressure, $PO_2^{y/2}$ before a metal oxide will form. Dissociation pressure of selected metal oxides and standard Gibbs free energy change data as a function of temperature are summarized in the Ellingham diagram shown in Figure 2.24.

However, once an oxide layer M_xO_y has developed on the metal/alloy surface, it acts as a barrier between the metal/alloy and oxygen. For the reaction to proceed further, one or both reactants must penetrate the oxide layer, i.e. either the metal must be transported through the oxide scale to react at the oxide-gas interface, or oxygen must be transported to the oxide scale-metal/alloy interface and react there [2006Bir]. The rate-determining step, i.e. the slowest process determining the reaction mechanism, may be one of several stages including transport of metal or oxygen through the oxide layer, mass or electron transport across one of the interfaces or electron-transfer processes associated with the chemisorption step [1974Law]. Hence, the kinetics of the system, rather than the thermodynamics of the reaction, controls the oxidation rate [1987Sto1].

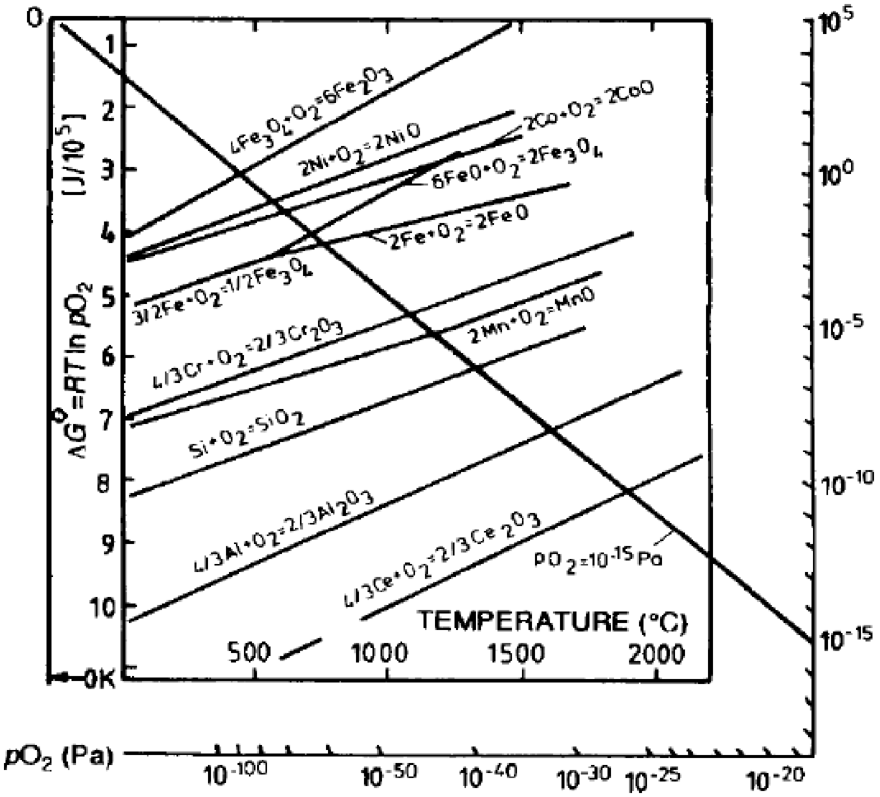

Figure 2.24. Ellingham diagram of oxides plotted against partial pressure [1981Gas].

2.4.2 Oxidation Kinetics of Metals and Alloys

A potential gradient (and usually concentration gradient) within a homogeneous solid phase causes diffusion of the atoms or ions via interstitial or vacant lattice sites [1962Kub]. According to Equation 2.8, the amount of solute *m* diffusing through a certain cross-section, *A*, per second is proportional to the concentration gradient *dc/dx* at this plane where the system is in equilibrium (with no other differences such as temperature, stress, etc):

$$m = A.D\left(dc/dx\right) \tag{2.8}$$

In Equation 2.8, c is concentration, *x* is the distance and *D* is the diffusion coefficient which is generally determined and tabulated. The rate of change of the concentration, *c*, at time *t*, at a point where the concentration gradient is *dc/dx* is given in Equation 2.9:

$$\frac{dy}{dt} = \frac{d}{dx}\left(D\frac{dc}{dx} \right) \tag{2.9}$$

or if D is taken to be independent of concentration, then Equation 2.10 will be obtained:

$$\frac{dy}{dt} = D\frac{d^2c}{dx^2} \tag{2.10}$$

However, solid-state diffusion of the reactants through the scale to a location where they can react together to form new oxide controls the growth of metal oxide scale [1962Kub, 2006Bir]. In this case, the species are generally ionised, so diffusion of both ionic and electronic defects is required and the overall diffusion rate is determined by the slower moving defect. The ionic defect is usually the slower-moving species for oxides growing on an alloy at high temperature [1987Sto1]. As the reaction proceeds at a constant rate, the oxide layer thickens, at the same time the flux of ions through the scale must be equivalent to the surface reaction rate. As the scales grow in thickness, there must be a reduction in the metal activity gradient across the scale, and consequently, a reduction in ionic flux along the diffusion paths and the reaction rate [1965Hau]. In such cases, a parabolic rate law is established.

Many metals oxidize more rapidly than expected from the measured bulk lattice diffusion rate. This is because transport of reactants through the scales, particularly at relatively low temperatures or for oxides such as Al_2O_3 or Cr_2O_3, is determined not only by bulk lattice diffusion but also by diffusion along low resistance, short circuit paths [1961Sme]. Possible short-circuit paths in growing scales include grain boundaries, dislocations, pores and microcracks [1987Str1]. It has been demonstrated that most oxide scales that appear to be relatively compact contain numerous microcracks when examined by non-conventional techniques [1973Han].

The presence of microcracks and pores in the scale provide direct access for oxygen and consequently the oxide scales do not act as a solid-state diffusion barrier as shown in Figure 2.25. In such cases, the oxidation process obeys a linear rate law [1965Hau]. There is evidence in the literature [1974Kue, 1987Abd, 1989Qua, 1994Doy] that confirms diffusion of both metal cations and oxygen anions along grain boundaries. However, enhanced dislocation diffusion in oxides is a well-known phenomenon, although its evidence is less emphatic [1987Str1]. When a scale grows by outward diffusion of metal cations, it facilitates dissociation of the oxide at the scale-metal interface, the oxygen reacting with the metal to form new oxide, while metal diffuses outwards to the surface where it reacts with further oxygen [1985Mro].

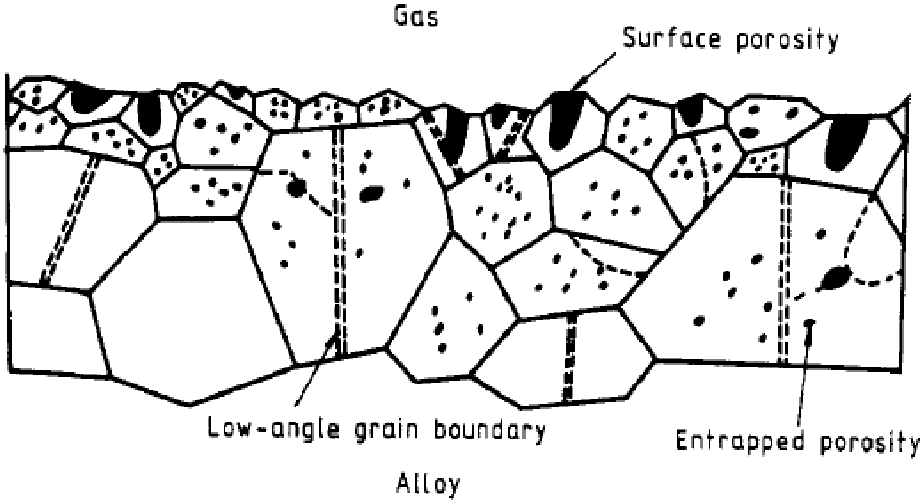

Figure 2.25. Schematic representation of Al_2O_3 scale developed on Ni-15%Cr-13%Al during oxidation in oxygen at 1150°C showing the presence of pores [1981Smi].

2.4.3 Rate Laws and Equations

2.4.3.1 Linear Rate Law

The linear rate law is usually observed during the initial scale growth when the diffusion in the oxide scale proceeds so fast that it does not contribute to the rate constant. When the oxidation of metal or alloy proceeds at a constant rate and a phase boundary process controls the overall rate of the reaction, it is said to obey the linear rate law expressed as [1965Hau,1983Bir]:

$$\frac{dy}{dt} = k_1 \tag{2.11}$$

where y is the scale thickness, t is the time and k_1 is the linear rate constant. Upon integration this yields:

$$y = k_1 t \tag{2.12}$$

2.4.3.2 Parabolic Rate Law

The parabolic rate law applies when the diffusion of ions through the scale is the rate controlling process as the initial rapid scale growth rate falls with time. This usually occurs during high temperature oxidation. This law assumes that the rate of oxide layer growth is inversely proportional to the layer thickness and can be expressed as Equation 2.13 [1962Kub]:

$$\frac{dy}{dt} = \frac{k_p}{t} \tag{2.13}$$

where y is the instantaneous oxide thickness at time t, and k_p is the parabolic scaling rate constant. Integration of Equation 2.13 yields:

$$y^2 = 2k_p t \tag{2.14}$$

2.4.3.3 Logarithmic Rate Law

The logarithmic law refers to the formation of very thin films of oxide only (between 0.0020-0.0040 μm) due to quick reduction of the initial rapid rate of scale formation to a very low rate of reaction. This usually occurred when metals or alloys are oxidized at low temperature of up to about 400°C. This law can be expressed by direct and inverse log laws as stated in Equations 2.15 and 2.16, respectively [1966Kof, 1965Hau]:

$$y = k_{log} \log(\mathrm{t} + t_0) + A \tag{2.15}$$

and

$$\frac{1}{y} = B - k_{il} \log t \tag{2.16}$$

where y is the oxide thickness and A, B, t_0, k_{log} and k_{il} are constants at time, t.

2.4.4 Formation of Protective Oxide Scales on Alloys at High Temperatures

Oxidation resistance of high temperature alloys depends on the formation of continuous and slowly growing oxide scales [1987Sto2, 2000Smi]. These alloys usually contain sufficient amounts of chromium and/or aluminium to ensure the development of protective external Cr_2O_3 or Al_2O_3 scales which grow at a reasonably slow rate. Nickel also found application in commercial alloys, but scales of NiO generally thicken at too fast a rate and thus give no protection to the alloys at higher temperatures [1987Sto1].

Cr_2O_3 and Al_2O_3 scales are reasonably stoichiometric oxides with low defect concentrations and thus develop relatively much more protective oxide scales than NiO scale, even in environments of high oxygen activity, particularly under isothermal conditions. However, Cr_2O_3 loses its protective nature when it reacts further with oxygen at temperatures above 900°C to form volatile CrO_3. This has restricted the effective use of Cr_2O_3-forming alloys to temperatures below about 900°C [1994Doy].

Alloys to be used in gaseous environments of high oxygen activity at temperatures above 900°C are developed to form external oxide scale. Ideally, this scale should be highly stable, free from stress, cracks or pores at high temperatures, coherent and must remain adherent to the substrate alloy, even under thermal cycling conditions [1987Sto1, 2000Smi]. In contrast, the major setback of Al_2O_3-rich scales is that they can be susceptible to cracking or spalling, especially under thermal cycling conditions [1987Sto1, 1987Sto2]. This can lead to enhanced oxidation due to formation of less-protective scales. In order to prevent this, the oxidation temperatures must be high enough to promote the formation and maintenance of α-Al_2O_3 scale in preference to the metastable aluminas, which are described in the following section [1992Pre]. In addition, the aluminum content must be sufficiently high to develop and maintain α-Al_2O_3 external scales [1970Woo, 1971Sto, 1992Pre]. According to Nanko, Ozawa and Maruyawa [1998Nan], the minimum amount of Al required in Pt-Al alloys to develop continuous external Al-oxide scale is 7.6 at.%. Felten and Pettit [1976Fel2] also reported that continuous external layers of α-Al_20_3 were developed on Pt-Al alloys containing 17 at.% Al, whereas a subscale of alumina developed on an alloy containing 4 at.% Al.

The presence of chromium in the M-Al-Cr (where M = Fe, Ni, Co) alloys was found to accelerate the formation and maintenance of external stable α-Al_2O_3 scale [1970Woo]. Chromium acts as a secondary oxygen getter and prevents internal oxidation of the aluminium. The proposed mechanism involves transient Cr_2O_3 (isostructural with α-Al_2O_3) providing nucleation sites for exclusive formation of α-Al_2O_3 [1992Bru]. Chromium addition to binary M-Al alloys also reduces the percentage of aluminium required to develop a continuous stable scale [1971Sto]. Addition of Pt to M-Cr-Al alloys has also been reported to improve adhesion of Al_2O_3 [1975Gig, 1976Fel1].

2.4.5 The Structure and Oxidation Kinetics of Al_2O_3 Scales

There are a large number of metastable crystalline alumina phases in addition to the thermodynamically stable α-Al_2O_3. The most common metastable (or transition) alumina polymorphs are γ (cubic spinel), δ (either tetragonal or orthorhombic) and θ (monoclinic) [1997Lev]. Another metastable form with structure similar to α-Al_2O_3, but has a shift in the stacking sequence on the anion sub-lattice, called κ alumina, has also been identified [1991Liu]. The metastable aluminas usually transformed to thermodynamically stable α-Al_2O_3 or corundum phase at temperature above 900°C by heating [1970Git]. The α-Al_2O_3 is constituted of hexagonally close-packed oxygen ions with two thirds of the octahedral interstitial sites occupied by trivalent cations.

It has been proposed that low concentrations and mobilities of ionic and electronic defects are responsible for the protection given by α-alumina at high temperatures [1983Kro]. Although the nature of the dominant native ionic defects is reported as not well established, it is believed that the concentrations of all defects depend on doping and oxygen pressure and that the ionic defects are the major species, while electrons and holes are the minorities. Transport processes in Al_2O_3 scales is reported to be dominated by impurity dopants, hence it is difficult to devise a definitive diffusion experiments [1985Ati].

Kroger [1983Kro] explained from the diffusion data for Al_2O_3 mostly obtained at very high temperatures (1600°C-1900°C) that both oxygen and aluminium are mobile in the oxide. The overall diffusion rates for the two species may be similar, depending on grain size. However, it is stated that Al diffuses through both the bulk lattice and the boundaries while oxygen diffuses only through the grain boundaries. Aluminium diffusion rates are measured to be similar in both the bulk lattice and in the oxide grain boundaries, indicating little enhanced diffusion along grain boundaries at these very high temperatures [1962Pal].

Reed and Wuensch [1980Ree] revealed that oxygen diffusion in the oxide lattice was apparently less than aluminium transport. The diffusion of oxygen in polycrystalline materials is enhanced by small grain size. This is proposed to be associated with diffusion of interstitial neutral oxygen atoms in the oxide grain boundaries [1980Wan]. Oxygen tracer measurements have been reported for growth of Al_2O_3 on Ni-Cr-Al alloys at 1100°C where it was found that inward oxygen transport is dominant and occurs by short-circuit paths such as fissures or grain boundaries [1982Ree]. Most of the other work supports inward diffusion of oxygen by these paths at high temperatures [1983Kro, 1980Ree, 1980Wan].

The ease of development of a steady-state α-Al_2O_3 layer depends on various factors [1987Sto1]. These include the alloy grain size, purity, surface finish and amount of cold work. Other factors are initial oxide film present, the oxygen partial pressure and method of bringing the specimen to temperature, especially if the alloy aluminium content is borderline to establishment of an Al_2O_3 layer.

2.4.6 Morphologies of Al_2O_3 Scales

Alumina-scales developed on alloys are often found to be non-uniform in thickness, with intrusions and/or protrusions at the scale-alloy and the scale-gas interfaces, respectively [2000Smi, 1980Hin1, 1976Fel2]. The formation of ridges or intrusions of oxide was proposed to be caused by the growth of new oxide at the alloy-scale interface [1980Sto, 1979Gol]. This gave rise to an irregular or roughened interface between the alloy and scale [1976Fel2, 2000Smi]. Localised thickening of the scale may result from outward diffusion of aluminium along short circuit paths, leading to formation of ridges or protrusion of oxide at the scale-gas interface

[1979Smi, 1988Smi]. Oxide ridges formed by the counter-current diffusion of aluminium and oxygen are often found to extend inward and outward in the same oxide [1980Hin1, 1980Hin2].

In general, the oxide grains in Al_2O_3 scales are found to be small and equiaxed towards the outer surface, but become coarser and more columnar towards the alloy-scale interface [2000Smi, 1976Fel2]. This change in oxide grain size has been explained mainly in terms of inward oxygen diffusion along grain boundaries [2000Smi, 1976Gol, 1979Gol] with also a minor contribution from outward diffusion of aluminium through the oxide lattice [1976Gol]. The equiaxed morphology is accounted for in terms of stress developed within the scale when new oxide is formed by the reaction between the inward diffusing oxygen and outward diffusing aluminium within the bulk scale near the oxide grain boundaries, as well as at the scale-alloy interface [1980Gol, 1987Sto1].

Wrinkled, wavy or convoluted alumina scales were proposed to be mainly associated with deformation caused by the build up of compressive stress within the oxide during lateral growth [1976Gol]. Lateral growth of oxide grains appeared to result from the growth of new oxide at oxide grain boundaries due to reactions between aluminium ions diffusing outwards and oxygen ions diffusing inwards. However, aluminium ions were proposed to move outward along short circuit paths within the alumina grains, whereas the oxygen ions move predominately along the alumina grain boundaries. This is because the diffusing aluminium and oxygen species are thought not to be able to pass each other while moving along the same path.

Alumina scales sometimes contain dispersed, isolated, intergranular voids and microporosity [1983Smi]. Small voids (10-200 nm) may grow into large isolated pores, possibly due to precipitation, supersaturation and condensation of oxygen vacancies. Transformation of γ-Al_2O_3 to α-Al_2O_3 which occurred with a volume contraction of 14.3% may also cause void formation. Filaments of oxides have also been observed on α-Al_2O_3 at the scale-gas interface on a number of alumina-forming alloys at different temperature ranges [1972Tie2, 1976Fou, 1978All]. In addition, α-Al_2O_3 and other metastable alumina can exist as whiskers [1964Bar].

2.4.7 Mechanisms of Al_2O_3 Scale Growth

The presence of interfacial voids or cavities at scale-alloy interface in Al_2O_3 scales has been revealed from a number of investigations [1974Gig, 1978All]. It has also been widely reported that much larger interfacial cavities are usually associated with convoluted scale configuration found in most ternary M-Al-Cr alloys [1976Gol, 1979Gol, 1980Gol, 1974Gig]. However, such configurations may be a function of alloy strength, surface finish or oxidation conditions, which does not always happen. It was proposed that the cavities may have resulted from oxygen vacancy diffusion and saturation, with precipitation following coalescence [1978Smi]. Outward diffusion of cations from substrate to the scale, such as during growth of transient oxides, is another possible cause of interfacial voids or cavities in the scale [1977Gib, 1981Gib]. If inward diffusion of oxygen is predominant, formation of voids or cavities may be associated with the incorporation of the metal ions into the scale. Vacancies or voids formation at the interface can result from a Kirkendall effect in the alloy [1974Kue, 1974Kum]. This will be from difference in diffusion rate of aluminium to the scale-alloy interface and of the other metals elements (Fe, Co, Ni, etc) in the opposite direction.

Scales with large interfacial cavities usually grow out of contact with the metal substrate, producing large oxide ridges, which result in convoluted scale [1980Gol]. Spalling and cracking of such convoluted scales were rarely observed during isothermal oxidation, but were very common during thermal cycling. However, there is formation of a new Al_2O_3 layer on the alloy surface after the failure of the scale. This is so because aluminium have been found not to be significantly depleted in the alloy beneath an Al_2O_3 scale and diffusion in Al_2O_3 scales is much slower than in the alloy [1973Jan]. In addition, the voids in the original scale allow more oxygen to penetrate to form new scale.

There is considerable dispute regarding the mechanisms to account for development of convoluted scale [1987Sto1]. It is proposed that it resulted from the growth of Al_2O_3 scale which is primarily from inward diffusion of oxygen down the oxide grain boundaries with little but significant contribution from lattice diffusion of Al^{3+}. The formation of new oxide within the existing scale is as a result of reactions between the two reacting species at or near the oxide grain boundaries [1976Gol, 1979Gol, 1980Gol]. The new oxide formed will lead to development of compressive stresses within the scale, thereby causing lateral growth of the entire oxide layer, deformation of the alloy substrate and eventually localised detachment of the scale from the alloy substrate [1987Sto1].

This scale detachment is unlikely to be as a result of void nucleation due to vacancy condensation, and usually occurs over abrasion markings, scratches or emergent grain boundaries on the metal surface. This is because significant vacancy super-saturation cannot normally be sustained at grain boundaries and interfaces, and nucleation of voids is also suppressed [1983Eva]. The presence of tensile stresses at the interface is another source of void formation [1975Raj, 1982Eva]. For example, during interfacial sliding, large local tensions which form in the presence of boundary waviness may permit formation of stable voids when the critical void nucleation stress is exceeded [1983Eva].

Segregation of sulphur impurities in the alloy to the scale-alloy interface is a significant cause of oxide scale detachment in Al_2O_3-forming alloys. It is proposed that the detachment may be as a result of degradation of interfacial adhesion, possibly by decreasing the chemical bond strength or producing interfacial voids [2000Smi]. Messmer and Briant [1982Mes] used quantum chemical molecular orbital techniques to show that presence of sulphur impurities at the metal grain boundaries usually lead to formation of heteropolar M-S (metal-sulphur) bonds by effectively pulling electrons from metal atoms and preventing these electrons from contributing to the stronger metallic-type bonds across metal grain boundaries. This argument is also applicable to the scale-alloy interface for the Al_2O_3-S-MCrAl system [1986Smi].

Impurity segregation effects may facilitate the initial loss of contact during lateral growth of the scale, however, it may not be the only factor responsible for poor scale adhesion [1987Sto1]. It was proposed to be more favourable to create new surfaces by detachment of scales above certain thickness than to cause creep of the oxide and maintain adhesion especially when the energy to deform an adherent scale by creep is more than the energy to generate new surfaces by delamination [1980Row]. There will be a continued lateral growth of the whole oxide scale after the detachment of the scale. This allows progressive coarsening of the convoluted morphology.

Oxide can be accommodated into the convoluted morphology probably by deformation of the scale or by either some intricacies of the mechanism.

The development of a convoluted scale has also been attributed to growth and impingement of large Al_2O_3 crystals at the underside of the scale following localised detachment. Aluminium evaporation from the substrate leads to the formation of such large crystals and their unrestricted growth causes buckling of the scale [1971Gig]. However, this mechanism has no metallographic evidence that support it. Convoluted scales have been suggested to be a transient features only [1983Rap]. It has been claimed that loss of oxide epitaxy with the alloy substrate following migration of alloy grain or sub-grain boundaries causes detachment of the adherent scale [1987Sto1]. In the absence of grain boundary migration during the process of oxidation especially at the early stages, initiation of scale detachment should not occur.

There is considerable dispute on the concept of formation of new oxide within an existing oxide scale leading to lateral oxide growth. It has been reported that chemical potential gradients consistent with the operation of sites for internal oxide formation within the bulk oxide scale may result from molecular diffusion of oxygen in oxide grain boundaries [1983Eva]. However, when oxidation occurs by anion and cation vacancy motion, either in the lattice or grain boundaries, formation of new oxide within the existing bulk scale may not be feasible [1978Spe]. Inhomogeneous mismatch strains result from non-uniform compression determined by the relative rates of oxygen and metal transport to internal boundaries.

Based on theoretical considerations, oxide has been reported only to be likely to form within the scale if both major and minor defects are interstitial, or if one is a charged vacancy and the other uncharged interstitial [1985Ati]. Fresh lattice sites would be created only at the scale interfaces, in the absence of interstitials. Hou et al. [1979Hou] reported that measurement of DC conductivity as a function of grain size for donor-and acceptor-dominated specimens revealed no preference for ionic conductivity along Al_2O_3 grain boundaries, which acted as barriers as the bulk scale. Thus, enhanced grain boundary diffusion is unlikely to involve molecular oxygen [1985Mro], but likely to involve a neutral species, probably oxygen interstitials [1983Kro].

The main factors responsible for spalling of Al_2O_3 scales on cooling are: the large areas of non-contact between the scale and the alloy at high temperatures [1979Gol], the concentration of thermal stresses in the scale around the interfacial cavities [1972Tie2], or in the convoluted regions [1979Gol], the low scale-alloy adhesion strength due to impurity segregation to the interface [1984Sme, 1985Fun] and the additional stresses caused by differential thermal contraction between the scale and alloy substrates.

2.4.8 Stress Development in a Growing Scale

High temperature materials rely on the formation and maintenance of protective oxide barrier, which separates the substrate from the environment, for resistance against high temperature oxidation [1971Sto, 1971Gig]. Stresses, which may induce spalling, buckling and cracking of the protective oxide barrier, are generated within the oxide scale as it grows. This may eventually lead to the loss of protective properties and accelerates the oxidation of the materials. High temperature oxidation of materials usually leads to degradation of mechanical properties and subsequent component failure. There are externally imposed stresses, such as those from applied load and internal generated stresses by oxidation process [2006Bir]. Stresses generated by the oxidation process can either be growth stresses (developed during the isothermal oxidation treatment by the growth of the scale) or thermal stresses (developed during cooling as a result of differences between the thermal expansion coefficients of the scale and of the substrate) [1995Hun, 2006Bir]. In order to ensure the maintenance of protective capacity of the oxide scale developed on the alloys at high temperature, it is necessary to understand the proposed mechanisms of development of both the growth and thermal stresses. The methods used for determining the stresses either in the underlying substrate or the scale will also need to be reviewed.

2.4.8.1 Growth Stresses

The proposed mechanisms of development of growth stresses in an oxide scale include the following:

(1) *Specific volume differences between the oxide scale and the metal*

The magnitude and the sign of the stress in the oxide scale depend on the Pilling-Bedworth ratio (PBR) defined as:

$$\text{PBR} = \frac{\text{Volume per metal ion in oxide}}{\text{Volume per metal ion in metal}}$$

When the PBR is greater than 1, the oxide is expected to be in compression, and the oxide will be in tension when the PBR is less than 1 [1987Sto2, 2006Bir]. The PBR of oxides of most metals and alloys is greater than 1 (Table 2.3), and thus form in compression.

Table 2.5. Some typical Pilling-Bedworth ratio values [1974Han].

Oxide	**Oxide-metal volume ratio**
NiO	1.65
Cr_2O_3	2.07
Al_2O_3	1.28
FeO	1.68
CoO	1.86

Nevertheless, compressive stresses could only develop on a scale if it grows by inward diffusion of oxygen at the scale-substrate metal/alloy interface. For an oxide forming at the oxide-gas interface on a planar specimen through outward diffusion of metal ions, stresses should not develop. However, the situation is complex in alumina forming-alloys because the alumina scales can be developed either by anionic or cationic preferential diffusion [1987Hun].

(2) *Epitaxial relationship between the oxide scale and the substrate*

Compression or tensile stresses based on the difference in lattice parameters between the metal/alloy substrate and the first-formed oxide may be induced by the epitaxial relationship between the oxide scale and the substrate [1987Sto2, 1995Hun, 2006Bir]. The epitaxial effect would only seem significant to generate stresses for thin scales i.e. those formed at low oxidation temperature after short time exposure.

(3) *Compositional changes in the alloy or scale*

Selective oxidation of one or more elements from the substrate during oxidation could lead to a change in the lattice parameter of the alloy and thus, generate stress [1987Sto2, 2006Bir]. Similarly, changes in scale composition through dissolution of oxygen or formation of internal oxides, carbides or nitrides could also result in stress development.

(4) *Vacancies generated during oxidation*

Vacancies are usually generated at the substrate-scale interface by metals or alloys which develop an oxide that grows through cationic preferential diffusion [1987Sto2]. The vacancies may accumulate at that interface and nucleate voids, which will reduce the substrate-scale adhesion and promote spalling, as a result of stress generation.

(5) *Local heterogeneities in the metal/alloy surface*

Local heterogeneities in the metal/alloy surface may generate stress at the scale-gas interface as a result of a difference in growth rates of the oxide scale on grains of different orientation [1987Sto2]. This will lead to non-uniformity in scale thickness at the substrate-scale interface across the grain boundary as usually observed during oxidation of a two-phase alloy.

(6) *Influence of specimen geometry*

The finite size of specimens and the resultant curvature (curved surfaces or sharp corners) serve as an important source of growth stresses [1987Sto2, 2006Bir]. However, the nature of the stress developing on a specimen depends on the curvature and the mechanism of the scale growth. Oxide scale forming on a planar specimen by outward diffusion of metal ions to the scale-gas interface does not generate stress because the scale should be able to follow the retreating scale-substrate interface.

(7) Oxide formation within the scale

Formation of new oxide at sites within the scale by inward migration of the oxidant along oxide grain boundaries or microcracks can lead to compressive stress generation within the scale [2006Bir].

2.4.8.2 Thermal Stresses

Thermal stresses are generated during cooling due to the differences between the coefficients of thermal expansion of the substrate and oxide scale. Thermal stress can be calculated with the Equations 2.17 and 2.18. The modified equations take into account the temperature dependence of the physical constants [1995Hun].

$$\sigma_{ox} = -\int_{T_i}^{T_f} \frac{\frac{E_{ox\,(T)}}{1-v_{ox}}\left(\alpha_{ox}(T)-\alpha_m(T)\right)}{1+\frac{t_{ox}}{t_m}\frac{E_{ox}(T)}{E_m(T)}\frac{1-v_m}{1-v_{ox}}}\,dT \tag{2.17}$$

$$\sigma_{m} = -\int_{T_i}^{T_f} \frac{\frac{E_{m\,(T)}}{1-v_{m}}\left(\alpha_{m}(T)-\alpha_{ox}(T)\right)}{1+\frac{t_{m}}{t_{ox}}\frac{E_{m}(T)}{E_{ox}(T)}\frac{1-v_{ox}}{1-v_{m}}}\,dT \tag{2.18}$$

where E is the Young's modulus, v the Poisson's coefficient, t the thickness, α thermal expansion coefficient, and the subscripts m and ox represent metal/substrate and oxide respectively.

The following two remarks are important for Equations 2.17 and 2.18 [1995Hun].

(1) The stress values obtained are for thermal stresses generated during cooling or heating, if stress relaxation does not occur.

(2) Both the thicknesses of the scale and of the substrate must contribute to thermal stresses obtained after cooling.

2.4.8.3 Calculation of Thermal Stress from Strain in the Scale

According to Lipkin et al. [1997Lip], the overall strain, $\mathcal{E}$ (*t*), in the scale can be calculated with Equation 2.19:

$$\varepsilon(t) = \varepsilon^T + \varepsilon^G(t) + \varepsilon^p(t) + \varepsilon^R(t) \tag{2.19}$$

where ε^T is the strain due to thermal expansion mismatch between the scale and the substrate upon cooling to room temperature, ε^G the oxidation time dependent lateral strain due to the Rhines-Wolf [1970Rhi] mechanism of plating out fresh oxide in the grain boundaries of the scale as caused by counter-ion diffusion, ε^p the oxidation time dependent volumetric phase transformation strain and ε^R time relaxation strain.

The room-temperature stress in the scale is related to the room temperature elastic strain as given by Equation 2.20, and the in-plane strains are symmetrically isotropic. The strains perpendicular to the scale surface are assumed to be unconstrained and under plane stress ($\sigma_{zz} = 0$).

$$\overline{\sigma}(t) = \frac{E_o}{1-\nu_o}\bar{\varepsilon}(t) \tag{2.20}$$

where $\overline{\sigma}(t)$ and $\overline{\varepsilon}(t)$ refer to the biaxial stress and strain components, E_o is the Young's modulus and v_0 Poisson's ratio of the oxide.

For most cooling rates, the thermal mismatch strain will be independent of time and is given by Equation 2.21, where $\varepsilon^T{}_{xx}$ and $\varepsilon^T{}_{yy}$ are the equi-biaxial strains, α_M and α_0 are the thermal expansion coefficient of the substrate metal, *m* and the oxide scale, *o*.

$$\varepsilon^T{}_{xx} = \varepsilon^T{}_{yy} = \overline{\varepsilon}^{T} = \int_{T_i}^{T_f} \left[\alpha_M(T) - \alpha_0(T)\right] dT \tag{2.21}$$

2.4.8.4 Techniques for Stresses Measurement

(1) The deflection technique allows for strain determinations *in situ* during isothermal treatment or cooling [1980Del, 1999Li]. The relationship between the oxide stress, σ_{ox}, and sample deflection, *D*, is given by Equation 2.23 [1984Zha].

$$\sigma_{ox} = -\left(\frac{E_m {x_m}^2 D}{3L^2 x_{ox}}\right) \tag{2.22}$$

where L is the sample length, E the Young's modulus, x_m is the substrate metal thickness and x_{ox} is the oxide thickness. This technique is suitable for qualitative or semi-quantitative comparisons, because the stress relieved is only a part of oxidation stress.

(2) Curvature technique allows for determination of the stress distribution in the scale and in the underlying substrate only at the room temperature [1987Zha].

(3) XRD can be used for stress and strain determination *in situ* and *ex situ*. Information on the strain can be obtained from the interplanar spacing variations [1989Sto], while the sin2ψ method can be used to determine the stresses [1986Lut, 1993Liu1, 1993Liu2, 1994Geo]. The parameter variations can be obtained from the following expression for an isotropic material [1993Liu1]:

$$\Delta 2\theta_{\varnothing,\psi} = \left\{-\frac{1}{2} s_2\left(hkl\right)\sigma_{\varnothing}\frac{2}{cot\theta}\right\} sin^2\psi + s_1\left(hkl\right)\left(\sigma_1 + \sigma_2\right)\frac{2}{cot\theta} \tag{2.23}$$

where $\Delta 2\theta_{\varnothing,\psi}$ is the Bragg angle stress-induced variation, σ_1 and σ_2 the principal in-plain stresses, $\sigma_{\varnothing}$ the stress in the *ø* direction, ψ the angle between the perpendicular to the sample and the measurement direction, *ø* the angle between the main direction and measurement direction in the sample plane, (*hkl*) is the diffracting plane, and $s_2(hkl)$ and $s_1(hkl)$ the X-ray elastic constants which can either be calculated or measured. The above equation relates the residual stresses in the materials to the induced Bragg angle variation.

(4) Raman spectroscopy is another technique that can be used to semi-quantitatively measure the distribution of stresses at high temperature either *in situ* or *ex situ* [1992Bir, 2006Kem]. This technique is non-contact, non-destructive, requires no special environment and offers the possibility to analyse small volumes with a lateral resolution of 1 µm [1998Cal]. The relative residual stress in the oxide films can be calculated from the Raman shift of the v1 mode. The Raman peaks shift to higher frequency for a compressive stress and to lower frequency for a tensile stress [1992Bir]. It should be noted that the beam absorption in the scale determines the depth of probe.

(5) Fluorescence spectroscopy is an alternative optical technique that is particularly suited for measuring the residual stresses in alumina-containing scales [1996Lip]. Most alloys designed for high-temperature applications rely on the formation of slow-growing alumina scales for protection against aggressive environments. Thus, this technique is suitable for measuring the residual stresses in the scale of Pt-based alloys being designed for high temperature applications. In this technique, the residual stresses are calculated from the fluorescence frequency shift, Δv, which can be obtained from the difference between the strong R2 fluorescence signals of stress-free sapphire and that of stressed oxide scale.

The relationship between the fluorescence frequency shift, Δv, and the stress in the oxide scale is described by the phenomenological equation [1996Lip]:

$$\Delta v_{stress} = \Pi_{ij}\sigma^{c}_{ij} = \Pi_{ij} a_{ki} a_{lj} \sigma_{kl} \tag{2.24}$$

where Π_{ij} is the ijth component of the piezospectroscopic tensor and σ^{c}_{ij} is the stress state in the crystallographic basis of the host crystal. In a general coordinate system, the stress state, σ_{ij}, is related to σ^{c}_{ij} by transformation matrix, a_{ij}. The above equation may be substantially reduced to Equation 2.25, because the off-diagonal terms of the piezospectroscopic tensor are nearly zero for alumina [1995He].

$$\Delta v_{stress} = \Pi_{ii}\sigma_{jj} - [\Pi_{a}(a_{i2}a_{j2} + a_{i3}a_{j3}) + \Pi_{m}(a_{i1}a_{j1} + a_{i3}a_{j3}) + \Pi_{c}(a_{i1}a_{j1} + a_{i2}a_{j2})]\sigma_{ij} \tag{2.25}$$

where the subscripts a, m and c refer to the respective crystallographic directions in the corundum (α-Al_2O_3) structure. Assuming that the probed volume by the exciting laser beam is a sufficiently large ensemble of grains in a polycrystalline material, the piezospectroscopic shift can be expressed to depend only on the first variant of the stress tensor as given in Equation 2.26 [1997Lip], which is obtained by averaging Equation 2.25 over all spatial orientations.

$$\overline{\Delta\nu} = \frac{1}{3}\Pi_{ii}\sigma_{jj} \qquad (2.26)$$

The stresses in the oxide scales having no particular crystallographic texture can be assumed to be equi-biaxial, such that $\sigma_{xx} = \sigma_{yy} = \bar{\sigma}$ and $\sigma_{zz} = 0$. In this limit, Equation 2.26 becomes:

$$\overline{\Delta\nu}\ (cm^{-1}) = \frac{2}{3}\Pi_{ii}\bar{\sigma} \qquad (2.27)$$

where $\overline{\Delta\nu}$ represents the frequency shift of the R2 lines of both the stress-free ruby and stressed α-Al_2O_3 scale, $\bar{\sigma}$ is the biaxial stress (the net effect of the growth stresses established at the oxidation temperature and the thermal expansion mismatch stress arising upon cooling). The experimentally measured value of Π_{ii} is 7.60 cm^{-1}/GPa for both of the R-lines [1995He].

Other information that can be obtained from the fluorescence measurements include the stress/strain gradients through the scale from the broadening of R-lines [1995Lip], and crystallographic texture of the scale from the intensity of the two R-lines [1997Lip].

The present study will evaluate the high temperature oxidation behaviour of the water-quenched and air-cooled Pt_{84}:Al_{11}:Cr_3:Ru_2 (at.%) alloy specimens in air. This will help to identify their ability to form a slow-growing, stable and adherent external alumina scale that serves to protect the underlying substrate alloy during high temperature applications. The evaluation will involve measurements of the stresses in the oxide scales, as well as the specific mass gain and thickness gain for determination of the scale growth kinetics after isothermal oxidation of the alloy specimens in air at 1150°C, 1250°C and 1350°C for various time intervals. The scale growth mechanisms will be determined based on the morphologies of the scale layers. The oxide scale features that will be studied will include: scale thickness, microstructure, surface and cross-sectional morphologies, oxide phases and composition. The detailed experimental procedures and characterization techniques that will be employed are presented in the next chapter.

CHAPTER THREE

3.0 Experimental Techniques

3.1 Introduction

The description of the production of the bulk alloys, metallographic preparation of the as-received alloy samples before and after oxidation, characterization of the as-polished and oxidized specimens, oxidation tests as well as oxide stress measurement procedures are detailed in this chapter.

3.2 Bulk Alloy Production

The Pt_{84}:Al_{11}:Cr_3:Ru_2 (at.%) alloys were manufactured by arc-melting the pure (at least 99.9 % purity) constituent elements and turned over several times under an argon atmosphere to achieve homogeneity [2002Cor]. The samples were then heat-treated at 1350^{o}C for 96 hours in a muffle furnace in air. The heat treatment temperature was chosen to reflect the proposed operating temperature of the alloy [2000Wol, 2001Hil]. After the heat treatment, the ingots were either air-cooled or water-quenched. Both the air-cooled and the water-quenched alloy ingots were supplied by Mintek for this experiment. The alloys were reported to be composed of a fine two-phase microstructure of (Pt) matrix, γ, and $L1_2$-Pt_3Al (γ') when examined by using scanning electron microscopy (SEM) equipped with energy dispersive X-ray spectroscopy (EDS) detector [2002Cor].

3.3 Metallographic Preparation

3.3.1 Sectioning

Approximately 1 mm thick slices were cut from the as-received water-quenched and air-cooled Pt_{84}:Al_{11}:Cr_3:Ru_2 (at.%) alloy polycrystalline ingots using electron discharge machining (EDM).

Some of these specimens were further cut into two using a wafering saw to obtain a total of about thirty specimens used for this investigation.

3.3.2 Grinding

All the specimens were mounted before grinding and polishing. The grinding on both sides was done with an automatic grinder/polisher machine using water as a lubricant on silicon carbide abrasive papers down to 1200 grit size finish. Each of the specimens was ground for about 3-5 minutes at machine speed of about 300 r.p.m. with a moderately heavy load of about 20 N at each of the grinding steps. The specimens were ultrasonically cleaned in water at temperature of about 80°C for 5 minutes in between the steps.

3.3.3 Polishing

After the grinding steps, the specimens were polished on both sides with an automatic grinder/polisher machine. Alcohol based lubricant was used with diamond suspension of 9 µm, 6 µm, 3 µm and 1 µm finish in succession. The machine speed was reduced to 150 r.p.m., while the applied load was kept at 20 N. The polishing time was between 2-4 minutes, depending on attainment of reasonable scratch-free surface. The specimens were removed from the mount after final grinding and polishing of one side by cutting the bakelite mount followed by breaking with vice. The specimens removed were then re-mounted in order to grind and polish the other side of the specimens.

Between each polishing step, the specimens were cleaned ultrasonically in hot water for about 5 minutes. After the final polishing step, the specimens were ultrasonically cleaned in hot water, followed by ethanol and/or acetone and dried with drier.

The as-polished specimens were observed to be reasonably scratch-free and flat with an optical light microscope, while scanning electron microscopy (SEM) was used to determine the elemental compositions of the alloy specimens prior to oxidation. The Bakelite mounts were broken after the final polishing step to remove the specimens, which were weighed at least five times on an analytical balance, prior to oxidation.

3.4 Oxidation Tests

Isothermal oxidation tests were conducted in air at 1150°C, 1250°C and 1350°C in alumina crucibles for various time intervals using a pre-heated front-loading muffle furnace (Figure 3.1). After various time intervals (Table 3.1), all specimens were taken out of the furnace and allowed to cool in air at room temperature. An insufficient amount of water-quenched alloy ingot prevented its inclusion in 200 and 500 hours oxidation tests. Each specimen was weighed at least five times before and after the oxidation tests using an analytical balance, and the mean mass gains and standard deviations were calculated. In order to ensure the accuracy of the measurements, the balance was allowed to stabilize before taking the readings.

Figure 3.1. Front-loading muffle furnace (Elite Model BRF 16/10-2216).

Table 3.1. Oxidation times (hours) used for testing Pt_{84}:Al_{11}:Cr_3:Ru_2 (at.%) alloy specimens.

Specimen type	**Oxidation time (hours)**					
Water-quenched	1	10	50	100	SNE	SNE
Air-cooled	1	10	50	100	200	500

SNE = sample not enough

3.5 Characterization and Analysis Equipment

3.5.1 Optical Microscopy

The morphologies of the as polished as well as the oxidised specimens were studied at magnifications up to 500X using axiocam optical microscope installed with the Axio vision 3.1 programs.

3.5.2 Scanning Electron Microscopy/Energy Dispersive X-Ray Spectroscopy

The microstructure and morphology of the as-polished and oxidized specimens were examined with a LEO-1530 field-emission scanning electron microscope (FESEM). All images were taken in backscattered electron (BSE) mode for phase contrast. The working distance (WD) between 15-16 mm and accelerating voltage of 20 kV were used during imaging. Overall and spot composition analyses were conducted with an Oxford INCA energy dispersive X-ray spectroscopy (EDS) detector attached to the LEO-SEM and the results were averaged from at least five different readings. The accelerating voltage was reduced to 15 kV during the EDS analysis to prevent the backscattered electron detector from blocking the EDS signals. This was also to ensure that excessive over-voltages were not used in generating the X-ray from the elements.

A JEOL JSM-7500F field emission scanning electron microscopy (FESEM) operated at 15 kV accelerating voltage and working distance of about 8-7 mm was used for surface and cross-sectional examinations of the oxide layers morphologies. All images were taken in secondary electron (SE) mode. Compositions analyses were conducted with dry silicon drift energy dispersive X-ray spectroscopy (EDS) detector attached to the JEOL-SEM. Prior to examinations, the specimens were carbon-coated to reduce the effect of charging by improving the conductivity of the alumina scale. However, some of the specimens were still charging during the surface and cross-section examinations.

3.5.3 Focused Ion Beam (FIB)-Field Emission Scanning Electron Microscopy

The cross-sections through the substrate alloy/oxide interfaces were examined using a focused ion beam workstation with GEMINI FESEM column (Zeiss, Model Neon 40), operating at a working distance (WD) of 5 mm in both milling and imaging modes. During the milling operation, the FIB system used a Ga^+ ion beam to raster over the sample surface at an accelerating voltage of 5 kV. However, the accelerating voltage was reduced to 2 kV when operating at imaging mode. A micro-section of approximate dimensions 20 x 25 x 15 μm^3 perpendicular to the substrate/oxide interface was milled on each of the oxidized specimens after coating with platinum using gas injection system (GIS). The milling operation was done inside the FIB-SEM workstation operated with a Ga^+ ion beam of 10 nA current and 30 kV acceleration voltage. This process was continued until the substrate was observed. The milled micro-section was then repeatedly etched/polished at lower beam currents of 4 nA, 2 nA and 500 pA (depending on surface roughness), and accelerating voltage of 30 kV until a smooth surface is obtained to facilitate the imaging. The cross-section images were taken to access the scale thickness as well as the ~Pt_3Al depletion zone. The detailed milling and imaging procedures are itemized below.

- A feature of interest was identified on the scale, and centred by placing a “crosshair” on it. This feature serves as reference point during tilting.
- The specimens were tilted in steps of 2°-5°-10°-20°-40°-54° after increasing the working distance to about 8 mm. However, to ensure that the feature of interest was still centred, the specimens were returned back to 0° tilt after the first 3 tilting steps.
- A cross-shaped navigation mark (X) (Figure 3.2) of approximate dimensions of 10 x 10 μm^2 was milled on the scale surface, after focusing the image. The milling operation was performed inside the FIB workstation operated with a Ga^+ ion beam of 4 nA current and 30kV accelerating voltage, and at WD of 5 mm.
- The gas injection system (GIS) was pulled out for deposition/coating the oxide surface with Pt of approximate dimensions 30 x 4 μm^2 (Figure 3.2). This was done with a Ga^+ ion

beam operating at 500 pA current and 30kV accelerating voltage. The Pt coating protected the oxide scale from cracking during milling.

- The GIS was returned, and trapezium shaped microsections of approximate dimensions 20 x 25 x 15 μm^3 (Figure 3.6) were milled perpendicular to the substrate/oxide interface. The milling was continued until the substrate could be observed. The milling current of the Ga^+ ion beam was 10 nA, while the accelerating voltage of 30 kV was used for fast removal of the layers.
- Following the coarse milling operation, the milled micro-section was repeatedly etched/polished with water at lower beam currents (4 nA, 2 nA and 500 pA depending on surface roughness), until a smooth surface was obtained. This facilitated the imaging of the cross-section with the SEM.
- The milled cross-sections were then examined and imaged at high magnifications with FIB-SEM in secondary electron (SE2) mode. The scale thicknesses were then measured at tilt angle of 34°.

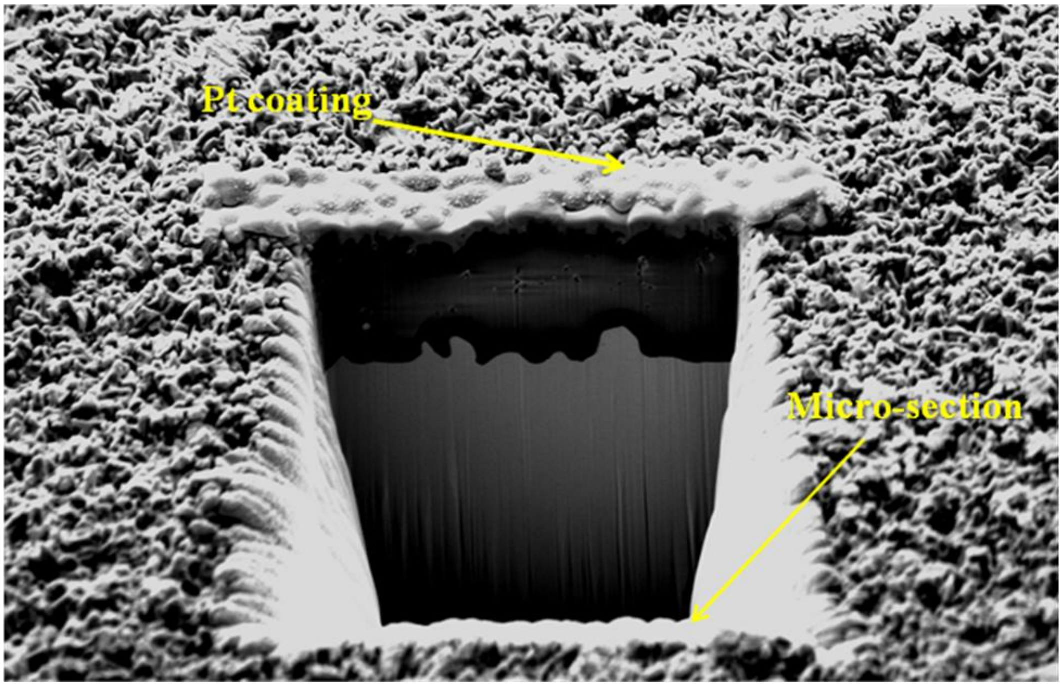

Figure 3.2. FIB-SEM image showing the Pt coating and milled micro-section perpendicular to the substrate/oxide interfaces.

3.5.4 X-Ray Diffraction (XRD)

Phase identification of the oxidized specimen surfaces was carried out using a Bruker D2 phaser, an X-ray diffractometer with a Cu K_α anode source. Continuous scans from 20 to 80^o (2 theta) with step size of 0.04^o per second were undertaken. The peaks in the diffraction patterns were identified by matching with known standard patterns, using DIFFRAC^{Plus} basic evaluation search and match programs, and data from the International Crystallography Diffraction Database (ICDD) [Appendix A].

The expected phases were also modelled with the software package Powdercell, which predicted the corresponding diffraction patterns of the (Pt) matrix, $L1_2$-Pt_3Al and Al_2O_3 phases [Appendix A]. This also provides information that assisted during the matching of the observed patterns.

3.5.5 Raman Spectroscopy

Raman spectroscopy with a Jobin-Yvon T64000 Raman spectrometer operated in single spectrograph mode and using a liquid N_2 cooled CCD was used for capturing the scan pattern of the oxidized specimen surfaces at room temperature. The spectra were collected by focusing the 514.5 nm line of an argon ion laser on the oxide scale regions by means of a microscope attachment of the Raman instrument. The depth of penetration of Raman spectroscopy is very low, and depends on the lateral and in-depth spatial resolution, of the order of 1000 nm-500 nm [2008Bră]. Hence, only the thin surface oxide film was captured and analysed within the acquisition time of 120 seconds for each of the specimens. A minimum of 2 scans from different spots was performed on each of the specimen. The observed spectra were matched with the standard corundum (α-Al_2O_3) spectrum obtained from RRUFF database (http: //rruff.info/) hosted by the University of Arizona, U.S.A.

3.5.6 Luminescence Piezospectroscopy

Stresses in the developed oxide scales were probed by exciting the scales using an argon-ion laser operating at 514.5 nm to obtain luminescence. The presence of trace amounts of Cr^{3+}, which is presumed to be a minor impurity in the alumina phase of the oxide scale, allowed for the observation of the luminescence. The excited luminescence spectra were collected with the same instrument used for Raman spectroscopy. Two distinct luminescence peaks, known as the R-lines doublet were observed due to the presence of Cr^{3+}. The line positions and widths were obtained by fitting the raw spectral data to a pseudo-Voigt function using commercial available Origin software. Prior to measurements on the oxide scale, the instrument was calibrated using the 690.75 nm emission line of a Hg lamp. The spectra data obtained in nanometer were converted to frequency before plotting and fitting. The luminescence spectrum of a synthetic ruby crystal was used as a stress-free reference. For each oxidation condition, at least five measurements were made on randomly selected areas of the oxidized specimen surfaces. The mean frequency shift for each set of five data points for the characteristic R2 luminescence line of α-Al_2O_3 was determined and used to calculate the biaxial stress values using the equation [1996Lip, 1993Ma]

$$\overline{\Delta\nu}\ (cm^{-1}) = \frac{2}{3}\Pi_{ii}\bar{\sigma} \tag{2.27}$$

where $\overline{\Delta\nu}$ represents the frequency shift of the R2 lines of stress-free and stressed α-Al_2O_3, $\bar{\sigma}$ is the biaxial stress. The experimentally measured value of Π_{ii} was 7.60 cm^{-1}/GPa for both of the R-lines [1995He]. It should be noted that the above equation is only suitable for oxide scales that have no particular crystallographic texture and are in state of biaxial compression, where $\sigma_{xx} = \sigma_{yy} = \bar{\sigma}$ and $\sigma_{zz} = 0$. The biaxial stress $\bar{\sigma}$ includes both the growth stresses generated at the oxidation temperature and the thermal mismatch stress developed on cooling [1996Lip]. Line broadening, which has been defined as the difference between the measured peak width of the stressed scale and the stress-free ruby crystal [1997Lip], was also calculated from the width values obtained after fitting the spectra data to a pseudo-Voigt function.

CHAPTER FOUR

4.0 Experimental Results

4.1 Microstructure of the as-polished specimens

The water-quenched and air-cooled Pt_{84}:Al_{11}:Cr_3:Ru_2 (at.%) ingots were metallographically prepared and examined with optical microscopy and scanning electron microscopy (SEM) in backscattered (BSE) mode prior to oxidation. The optical microscopy was used to observe each of the specimen surfaces after the final polishing step to ensure that they were reasonably flat and scratch-free prior to oxidation. The microstructures of as-polished water-quenched and air-cooled specimens are given in Figure 4.1. Water-quenched specimen (Figure 4.1a) shows the presence of the two-phase γ/γ' mixture, where the γ' phase, ~Pt_3Al, is represented by the dark contrast, while the γ (Pt) matrix, is the light region, while the air-cooled specimen (Figure 4.1b) could not be resolved, since all magnifications were alike. More pores were observed on the water-quenched specimen compared with the air-cooled. The overall composition (at.%) of the specimens as measured by energy dispersive X-ray spectroscopy (EDX) is given in Table 4.1. The EDX composition of the water-quenched is very close to the nominal value, while that of air-cooled specimens was different. The Al and Ru contents of the water-quenched alloy were higher than in the air-cooled specimens, while more Pt was in the air-cooled specimens. The Ru composition was variable, while there was less variation in Cr content in both.

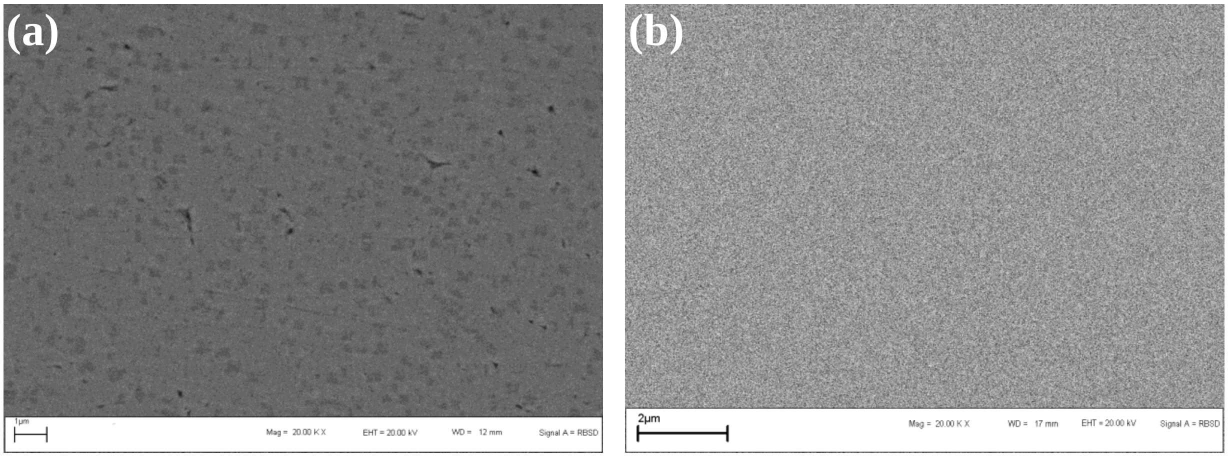

Figure 4.1. SEM-BSE micrograph of as-polished Pt_{84}:Al_{11}:Cr_3:Ru_2 (at.%) (a) water-quenched (b) air-cooled.

Table 4.1. EDX analysis of as-polished nominal Pt_{84}:Al_{11}:Cr_3:Ru_2 (at.%) samples.

Elements (at.%)	**Pt**	**Al**	**Cr**	**Ru**
Water-quenched	84.0 ±1.0	10.6 ± 1.0	3.2 ± 0.3	2.2 ± 0.2
Air-cooled	87.6 ± 0.4	8.9 ± 1.0	2.7 ± 0.2	0.8 ± 0.4

4. 2. Oxidation Kinetics

The mass gain for each of the oxidized alloy specimens was measured and normalized per unit area to obtain the oxidation kinetics of the water-quenched and air-cooled specimens at different exposure temperatures and times.

4.2.1. Water-quenched specimens

Figure 4.2 represents the curves of mass gain per unit area (specific mass gain) as a function of oxidation time, which are parabolic in nature. At all oxidation temperatures, no mass losses were observed, indicating good adherence of the scales to the substrate, as well as absence of scale spallation. The specific mass gains for the water-quenched specimens at 1350°C were much higher than those at 1150°C and 1250°C, whereas the specific mass gains at 1250°C were slightly above those at 1150°C.

The parabolic rate constants were calculated from the plot of Δm against $t^{1/2}$, using the parabolic equation of the form $(\Delta m)^2 = k_p . t + C$ [1962Kub, 1975Sme, 2006Bir], where Δm is the specific mass gain, k_p is mass-parabolic rate constant, t is exposure time and C is the intercept. Within the errors (usually obtained from standard deviation), the scale growth rate was faster at the initial stage, i.e., the transient stage, but later became slower above 10 hours exposure at all oxidation temperature. Thus, the curves were better fitted into parabolic law at longer exposure time above 10 hours. The mass-related parabolic rate constants calculated from the plots are presented in Table 4.2, which showed that the rate constants increased with increased oxidation temperature. The intercepts were very close, at least within the errors.

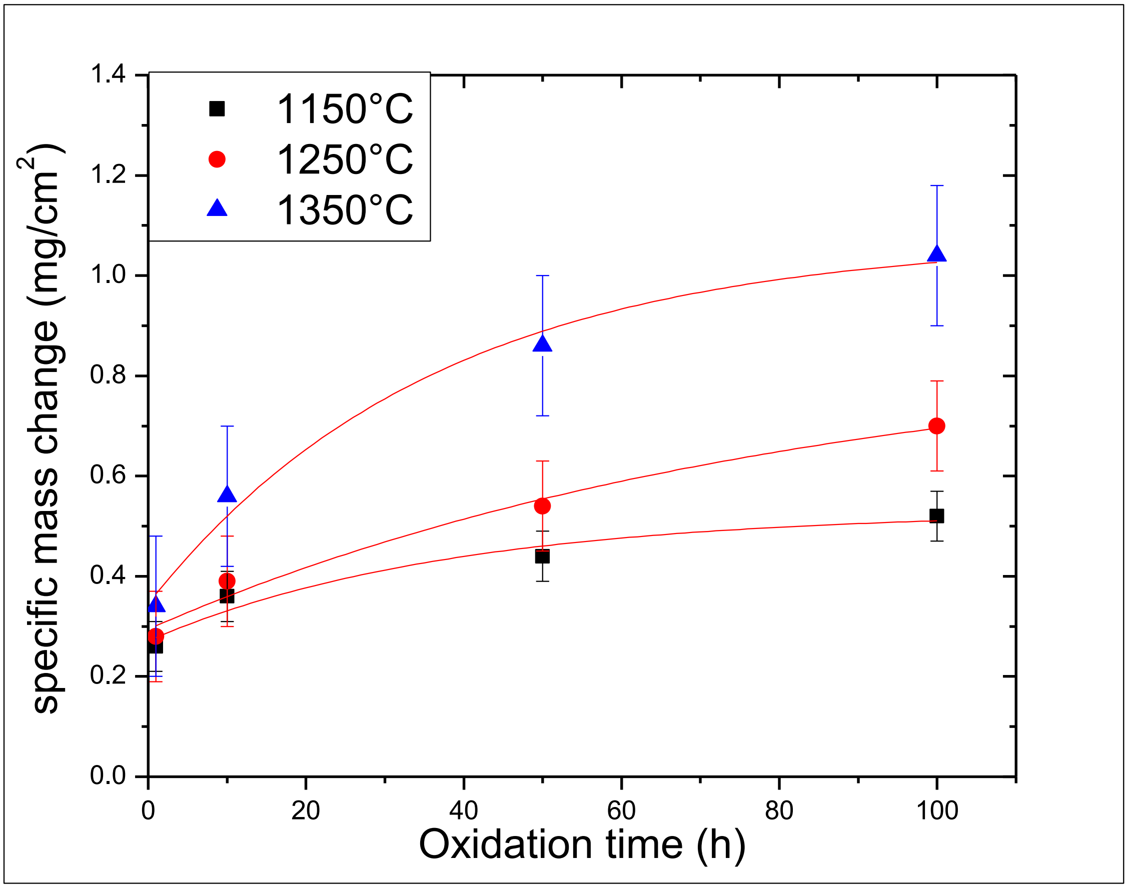

Figure 4.2. Specific mass change for water-quenched Pt_{84}:Al_{11}:Cr_3:Ru_2 (at.%) specimens with time after isothermal oxidation in air at 1150°C, 1250°C and 1350°C.

The oxidation kinetics for the oxide scale growth was also determined from the plots of the scale thicknesses versus oxidation time. Figure 4.3 shows that the oxide scale thicknesses increased according to a parabolic function of time. The large error bars are due to the waviness of the scale-alloy and the scale-gas interfaces, resulting from oxide protrusions/intrusions. However, the waviness increased with increased oxidation temperature and time; hence large errors bars were found. The parabolic scaling rate constants, k_{ps} were calculated using the parabolic equation $y^2 = k_{ps}.t + C$ [1962Kub, 2006Bir], where y is the instantaneous oxide thickness at time t, and C is the intercept. The results are presented in Table 4.2. Within the error, the scaling growth kinetics at all oxidation temperatures were faster during the transient stage up to 10 hours exposure, and later became more fitted into the parabolic curves. In addition, the parabolic scaling rate constants at 1350°C exceeded those for the specimens at 1150°C and 1250°C, with the lowest rate observed at 1150°C. The intercepts agreed fairly well with one another.

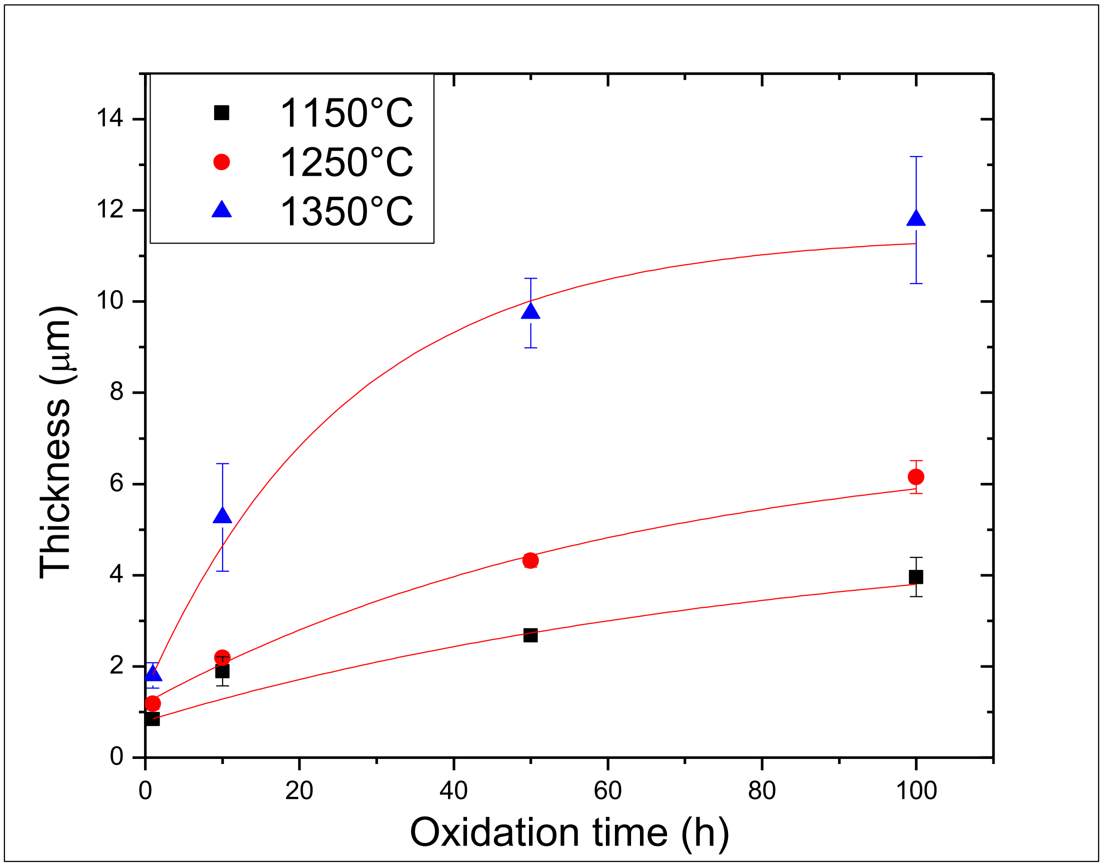

Figure 4.3. Oxide scale thickness with oxidation time for water-quenched Pt_{84}:Al_{11}:Cr_3:Ru_2 (at.%) after isothermal oxidation in air at 1150°C, 1250°C and 1350°C.

Table 4.2. Parabolic rate constants for water-quenched Pt_{84}:Al_{11}:Cr_3:Ru_2 (at.%) isothermally oxidized between 1150°C-1350°C in air for up to 100 hours.

Oxidation temperature (°C)	**Mass-related rate constants, k_p ($mg^2/cm^4.h$)**	**Intercept (mg^2/cm^4)**	**Thickness-related rate constants, k_{ps} ($\mu m^2/h$)**	**Intercept (μm^2)**
1150	0.0007 ± 0.0001	0.25 ± 0.05	0.0983 ± 0.0005	0.53 ± 0.07
1250	0.0021 ± 0.0001	0.24 ± 0.07	0.2808 ± 0.0007	0.58 ± 0.12
1350	0.0060 ± 0.0004	0.29 ± 0.13	1.5480 ± 0.0108	0.61 ± 0.33

4.2.2 Air-cooled alloy specimens

Plots of specific mass gain data from isothermal oxidation of air-cooled Pt_{84}:Al_{11}:Cr_3:Ru_2 (at.%) specimens in air at 1150°C, 1250°C and 1350°C as a function time are presented in Figure 4.4. The specific mass gain increased with increased oxidation time at all exposure temperatures. In addition, the specific mass gains at 1350°C are higher than those at 1150°C and 1250°C, indicating a faster rate of formation of alumina scale. Within the errors, the plots fitted well into parabolic rate up to 100 hours exposure. Above this exposure time, the scale growth rate became slower than expected for a parabolic law, and almost nearing constant after 200 hours oxidation.

Figure 4.5 shows the plot of scale thickness versus oxidation time of the specimens after isothermal oxidation in air at 1150°C, 1250°C and 1350°C. It was revealed that the scale thicknesses increased with increased oxidation time at a faster rate up to about 100 hours. However, the scale growth rate became slower at above 100 hours, and nearing a plateau after 200 hours. The error bars are due to the protrusions at the scale interfaces. The non-uniformity of the scales resulting from protrusions/intrusions of the oxide at the interfaces increased with increased oxidation time. Deep protrusions of the alloy into the scale were observed after 200 hours exposure at 1350°C, resulting in a very high error. Parabolic rate constants calculated for the specific mass gains, k_p as well as thickness, k_{ps}, are given in Table 4.3. Both the specific mass and thicknesses related parabolic rate constants of the specimens oxidized at 1350°C are higher than those at 1150°C and 1250°C. The lowest rates were obtained from the specimens isothermally oxidized in air at 1150°C. The specific mass during the transient oxidation stage, corresponding to the intercept are quite similar, while the thickness intercepts are more varied.

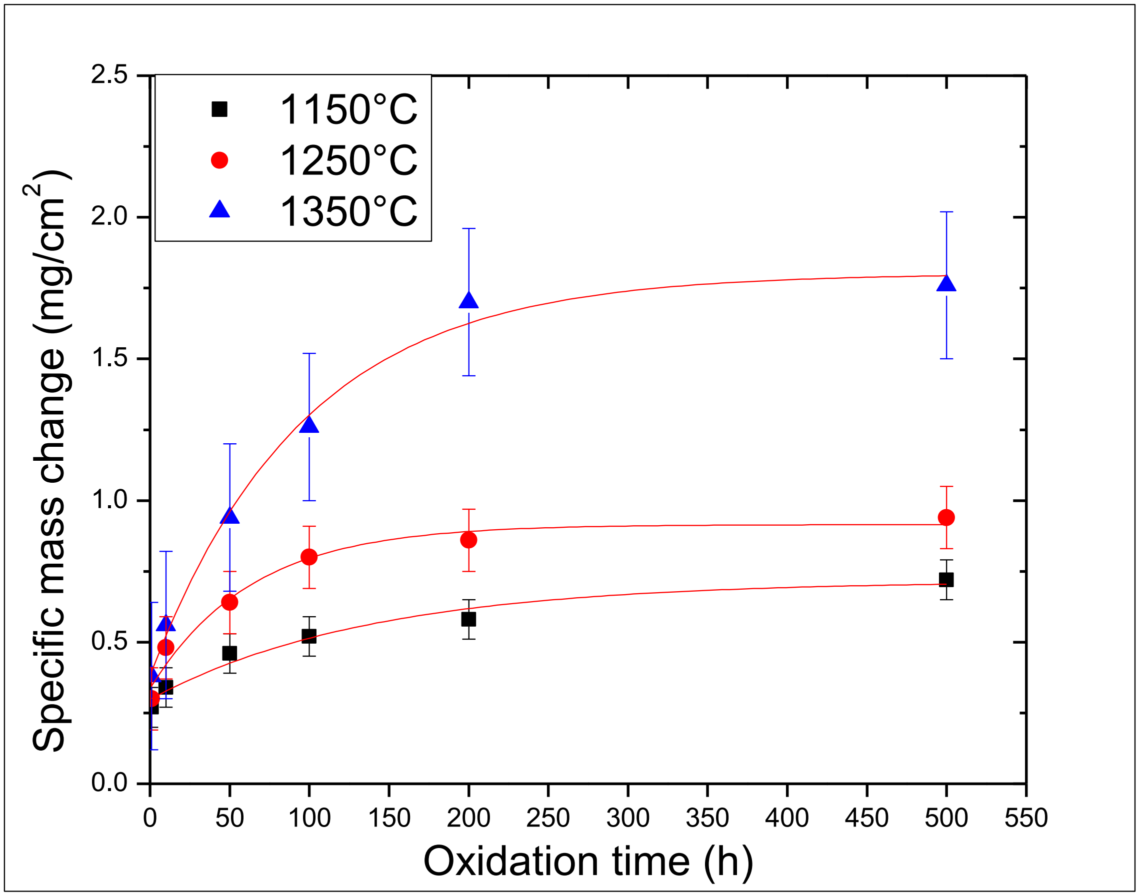

Figure 4.4. Specific mass change of air-cooled Pt_{84}:Al_{11}:Cr_3:Ru_2 (at.%) alloy with time after isothermal oxidation in air at 1150°C, 1250°C and 1350°C.

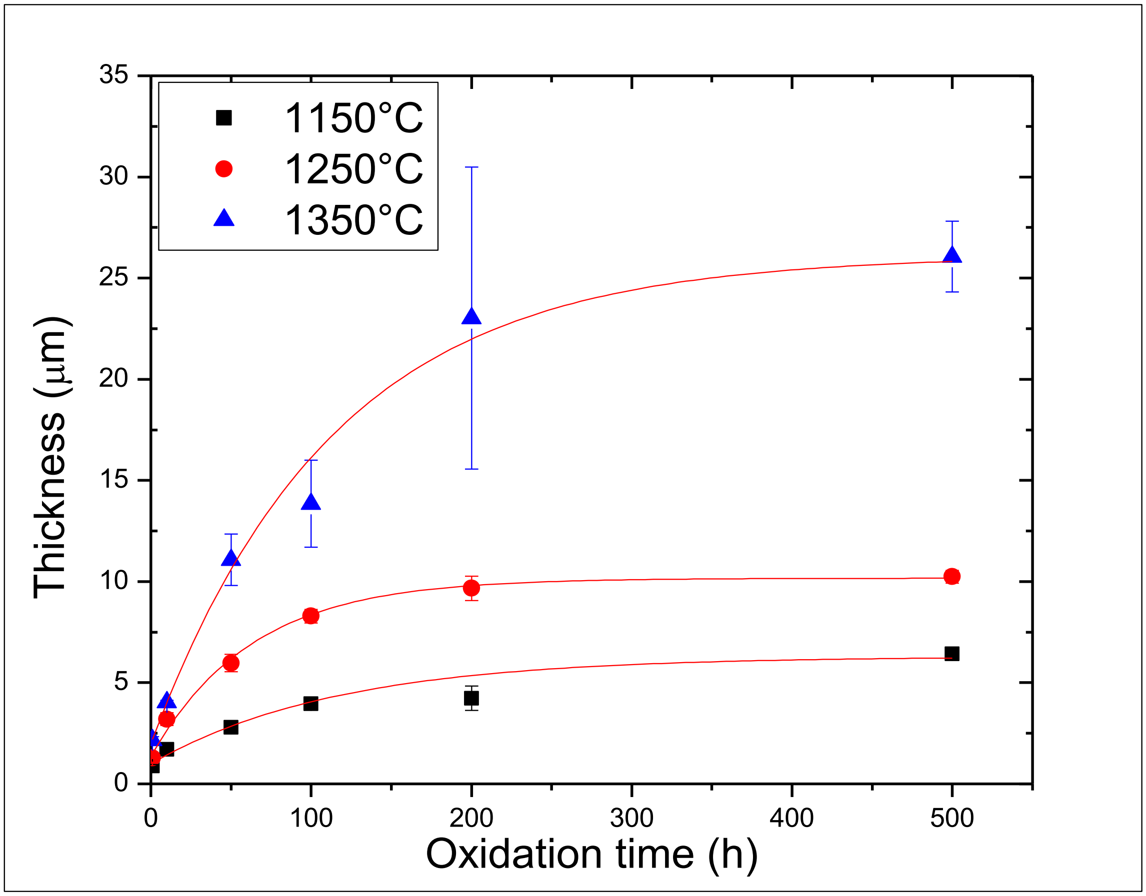

Figure 4.5. Oxide scale thickness with oxidation time for air-cooled Pt_{84}:Al_{11}:Cr_3: Ru_2 (at.%) after isothermal oxidation in air at 1150°C, 1250°C and 1350°C.

Table 4.3. Parabolic Rate Constants for air-cooled Pt_{84}:Al_{11}:Cr_3:Ru_2 (at.%) alloy isothermally oxidized between 1150°C-1350°C in air for up to 500 hours.

Oxidation temperature (°C)	**Mass-related rate constants, *k_p* ($mg^2/cm^4.h$)**	**Intercept (mg^2/cm^4)**	**Thickness-related rate constants, *k_{ps}* ($\mu m^2/h$)**	**Intercept (μm^2)**
1150	0.00044 ± 0.00002	0.28 ± 0.05	0.0756 ± 0.0002	0.71 ± 0.07
1250	0.00087 ± 0.00004	0.39 ±0.08	0.2340 ± 0.0003	1.57 ± 0.19
1350	0.00507 ± 0.00023	0.42 ± 0.18	1.6560 ± 0.0036	1.16 ± 0.18

4.3 Surface Morphology of the Oxide Layers

4.3.1 Optical Microscopy

4.3.1.1 Water-quenched specimens

Optical micrographs of the surfaces of the oxide layers on water-quenched Pt_{84}:Al_{11}:Cr_3:Ru_2 (at.%) specimens after isothermal oxidation in air at 1150°C, 1250°C and 1350°C for up to 100 hours are presented in Figures 4.6-4.8. The oxide layers were well-adhering to the substrate with no observation of spallation. Oxidation was observed on both the surfaces and along the grain boundaries in the specimens. The grain boundary oxidation became less discernable after 50 hours oxidation at 1350°C, while it appeared throughout all oxidation times at 1150°C and 1250°C. However, at all oxidation temperatures, the grain boundaries became less discernable with increased scale thicknesses at higher oxidation times. In additon, the scale became more uniform and covered the entire specimen surfaces.

4.3.1.2 Air-cooled Specimens

Figures 4.9-4.11 show the optical micrographs of the surfaces of the air-cooled Pt_{84}:Al_{11}:Cr_3:Ru_2 (at.%) specimens oxidised in air for 1150°C, 1250°C and 1350°C for up to 500 hours. Well-adhering oxide scales which showed no evidence of spallation during oxidation or after cooling in air were formed on all the specimens at all the investigated temperatures and exposure times. The appearance of the grain boundaries of the substrate on the oxide scales was possibly due to the non-uniformity as well as the thin nature of the scale. However, as the oxide scale thickness increased and became more uniform with increased exposure times across the investigated temperatures, the grain boundary oxidation apparently disappeared. The oxide scales formed on specimens oxidised at 1150°C revealed the presence of grain boundaries at all the exposure times, although above 50 hours exposure, the grain boundaries became less obvious. In addition, the scale formed after 1 and 10 hours exposures at 1150°C also appeared porous. After 200 hours exposure at 1250°C, the grain boundary became less discernable and dark. At 1350°C, the grain boundaries apparently disappeared after oxidation above 100 hours, while some on specimens oxidised for 50 and 100 hours appeared dark and thick.

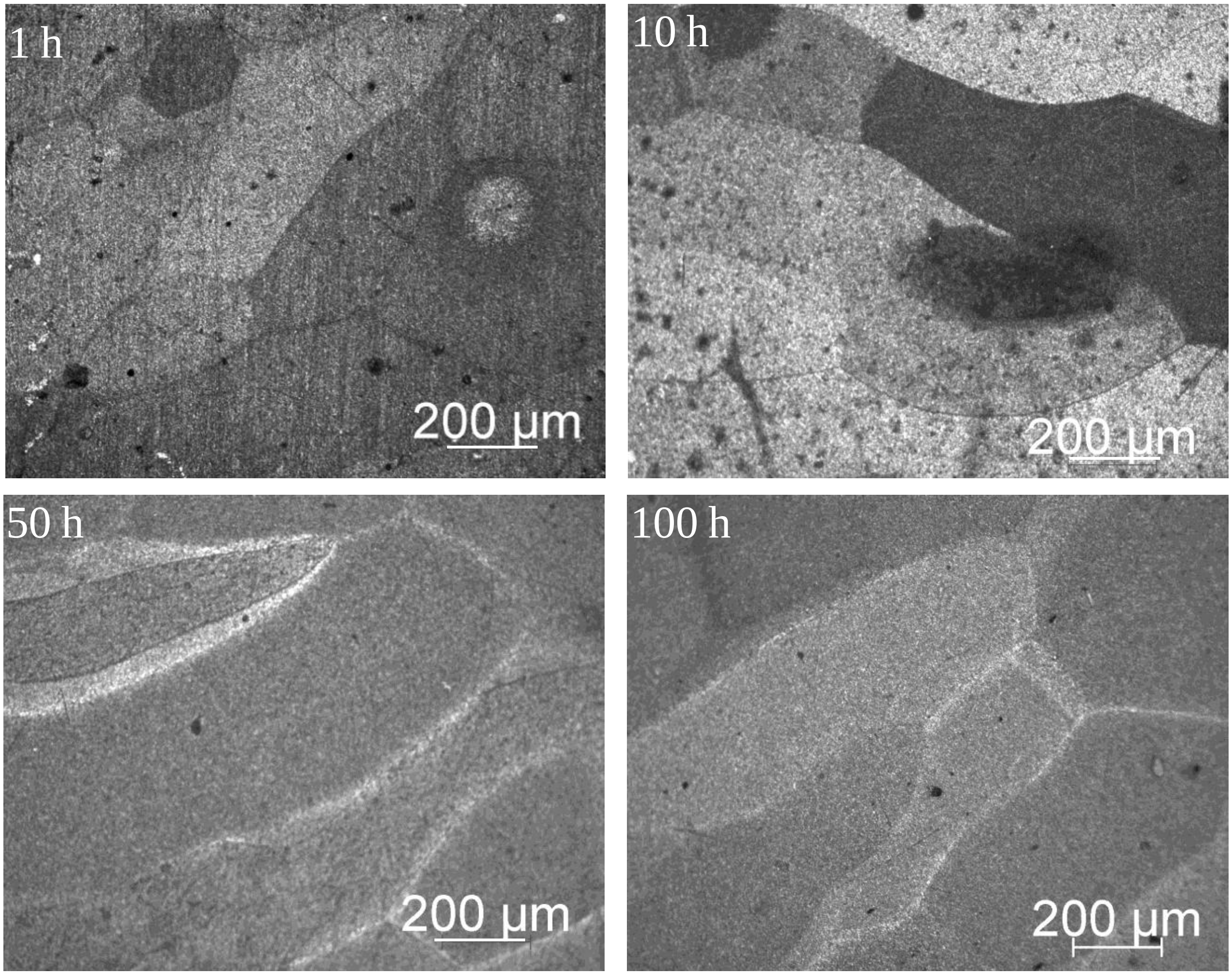

Figure 4.6. Optical micrographs showing surface morphology of oxidised water-quenched Pt_{84}:Al_{11}:Cr_3:Ru_2 (at.%) after isothermal oxidation in air at 1150°C for up to 100 h.

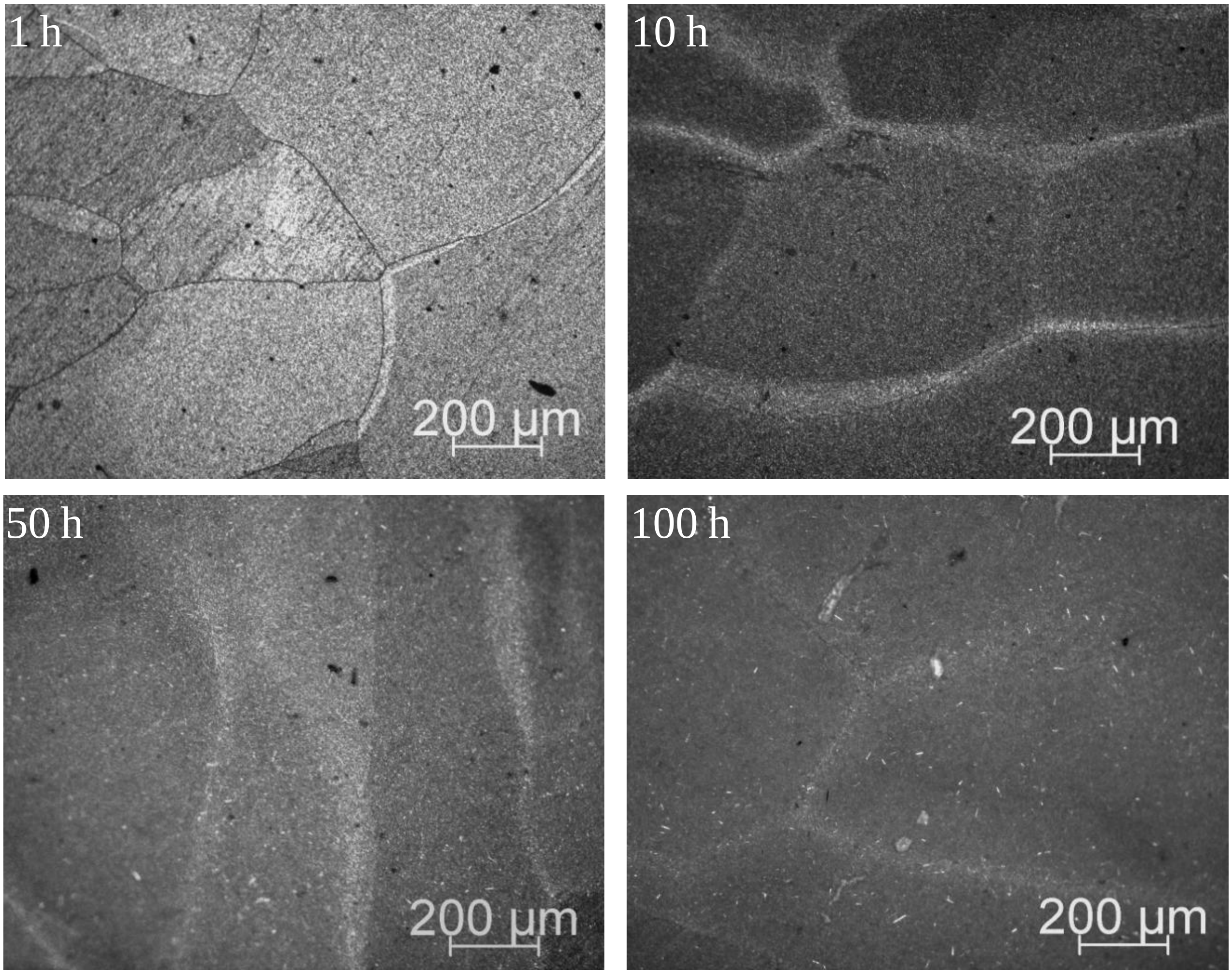

Figure 4.7. Optical micrographs showing surface morphology of oxidised water-quenched Pt_{84}:Al_{11}:Cr_3:Ru_2 (at.%) after isothermal oxidation in air at 1250°C for up to 100 h.

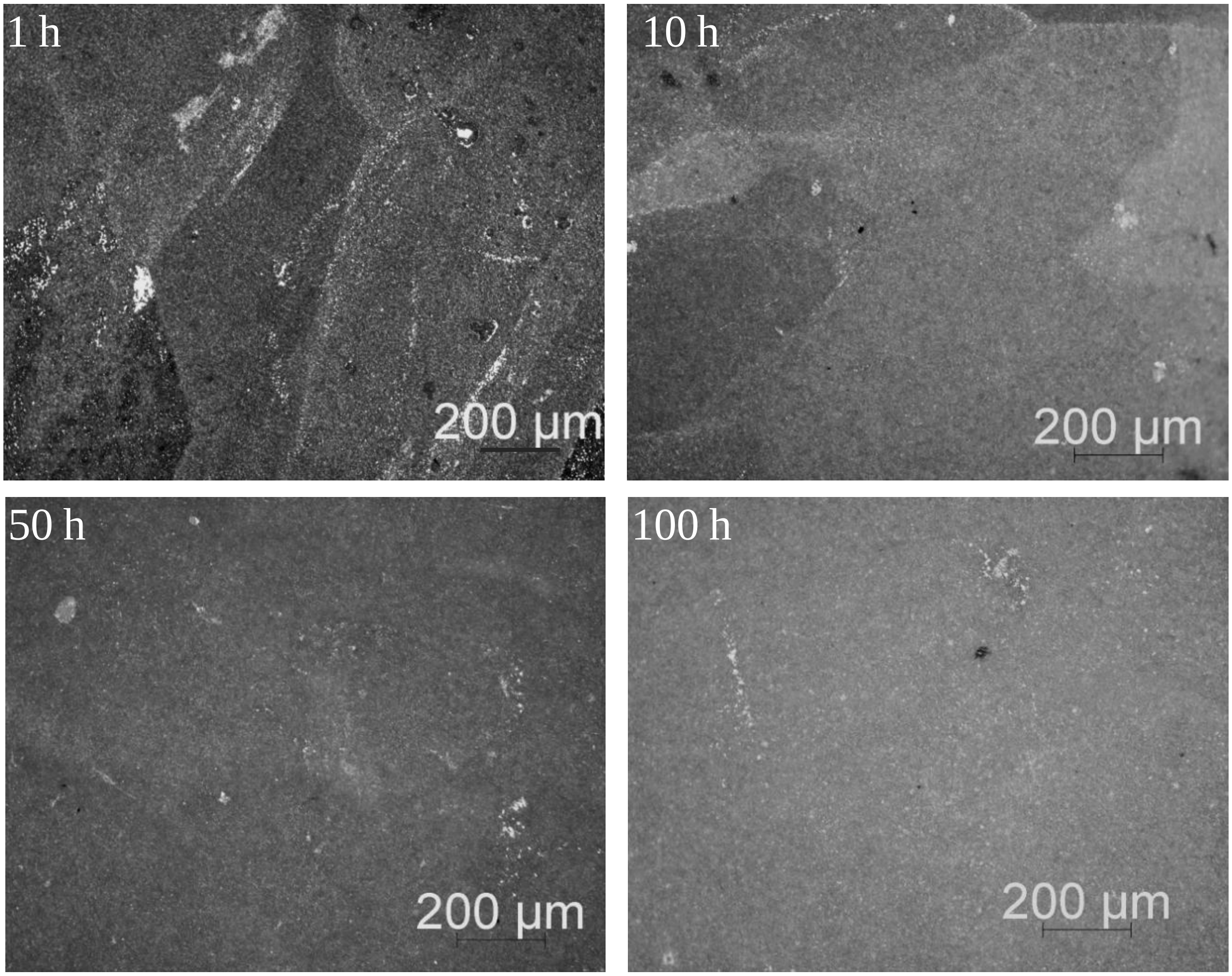

Figure 4.8. Optical micrographs showing surface morphology of oxidised water-quenched Pt_{84}:Al_{11}:Cr_3:Ru_2 (at.%) after isothermal oxidation in air at 1350°C for up to 100 h.

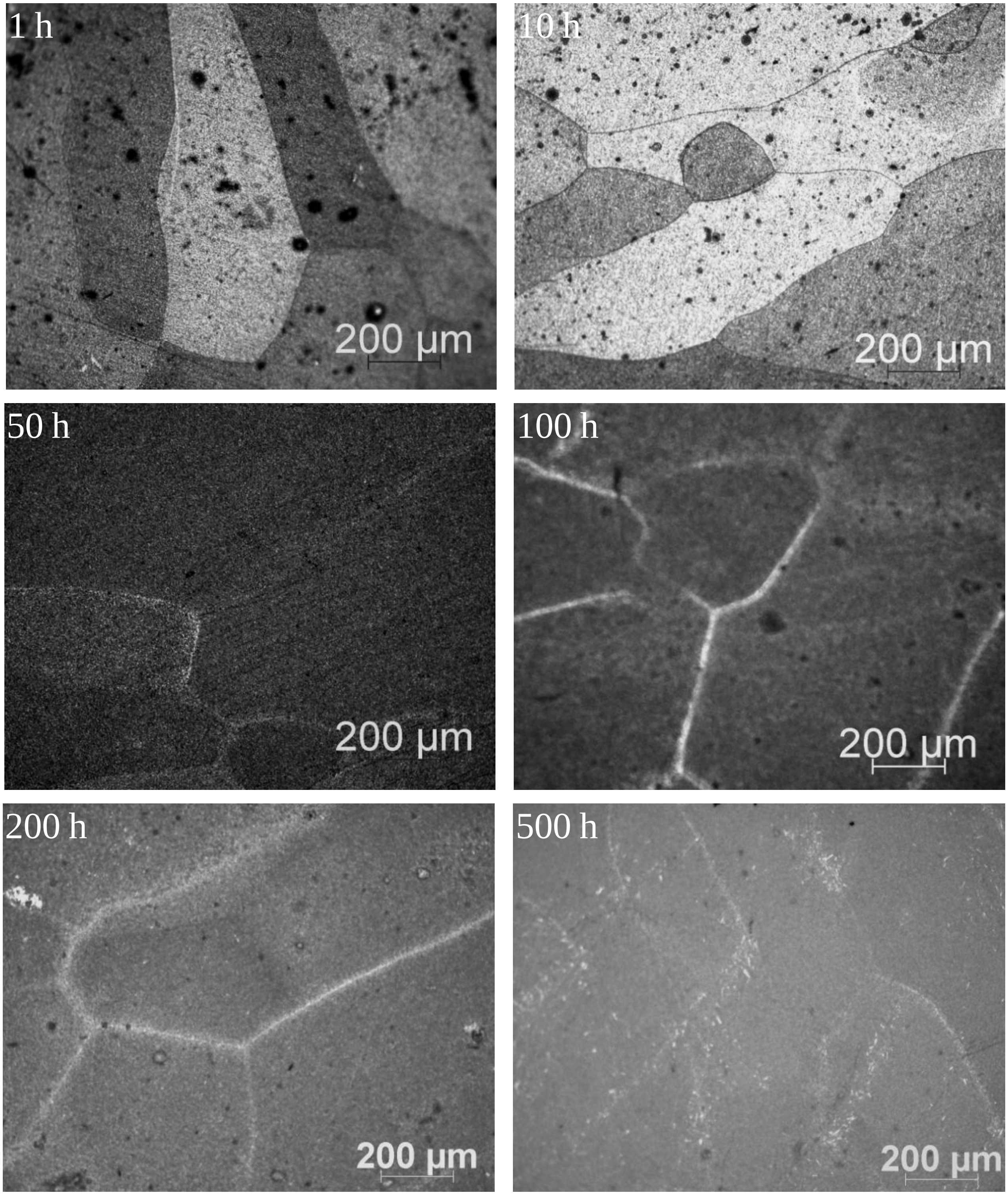

Figure 4.9. Optical micrographs showing surface morphology of oxidised air-cooled Pt_{84}:Al_{11}:Cr_3:Ru_2 (at.%) after isothermal oxidation in air at 1150°C for up to 500 h.

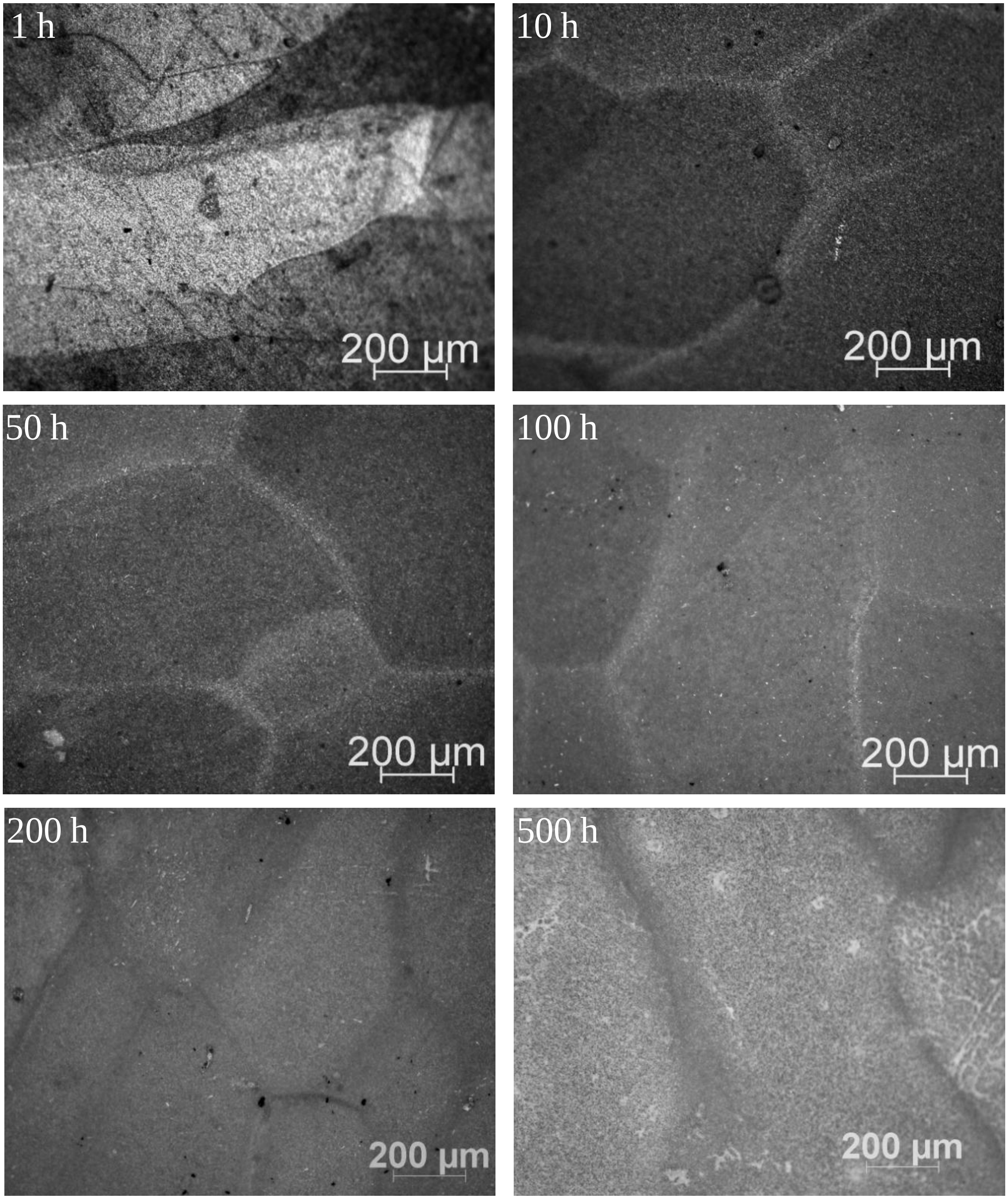

Figure 4.10. Optical micrographs showing surface morphology of oxidised air-cooled Pt_{84}:Al_{11}:Cr_3:Ru_2 (at.%) specimens after isothermal oxidation in air at 1250°C for up to 500 h.

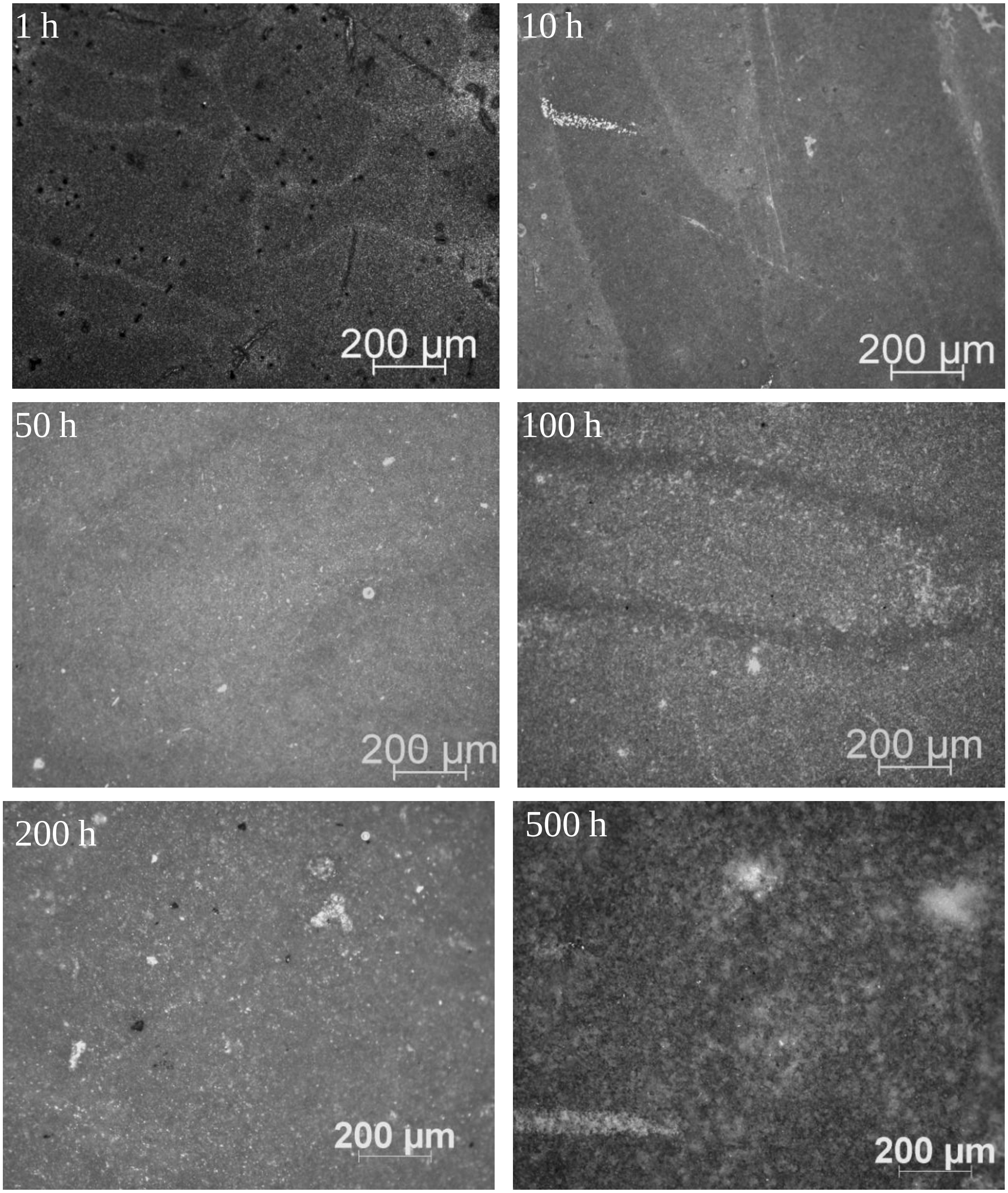

Figure 4.11. Optical micrographs showing surface morphology of oxidised air-cooled Pt_{84}:Al_{11}:Cr_3:Ru_2 (at.%) specimens after isothermal oxidation in air at 1350°C for up to 500 h.

4.3.2 SEM /EDS Analysis

4.3.2.1 Water-quenched Specimens

Scanning electron microscopy (SEM) examination of the oxidized water-quenched Pt_{84}:Al_{11}:Cr_3:Ru_2 (at.%) specimen surfaces after isothermal oxidation in air at 1150°C, 1250°C and 1350°C for up 100 h indicated that the scale was tightly adherent to the substrate with no evidence of spallation. After 1 hour oxidation at 1150°C, a scale morphology consisting of two-distinct features (labelled as spots 1 and 2) was revealed (Figure 4.12). Energy dispersive X-ray spectroscopy (EDS) point analysis showed that the crystals on the scale surface (spot 1) were composed mainly of Pt (~78.1 at.%), with lower amounts of Al (~15.2 at.%) and O (~6.7% at.%) (Figure 4.13). The point analysis of spot 2 showed the presence of Al (~38.5 at.%) and O (~59.6 at.%) as the major elements, corresponding to Al_2O_3, with small amounts of Pt (~0.6 at.%) and Cr (~1.4 at.%) (Figure 4.14). However, there are few unlabelled peaks, part of which are likely to belong to carbon, because the oxide scales were carbon coated prior to analysis in order to improve their conductivity, and thus charging effect.

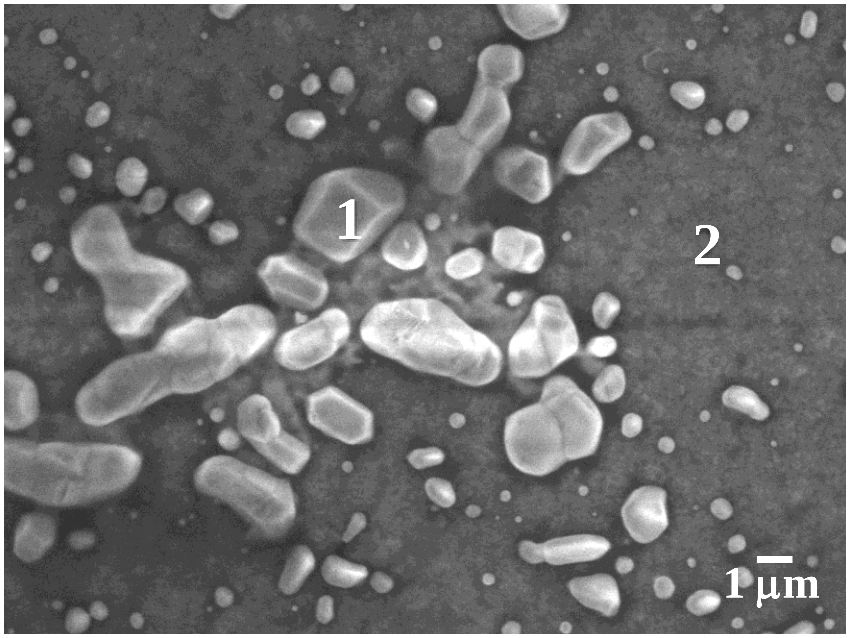

Figure 4.12. Surface SEM-SE image of water-quenched Pt_{84}:Al_{11}:Cr_3:Ru_2 (at.%) after 1 hour oxidation in air at 1150°C, showing (1) Pt-rich crystals (2) alumina scale.

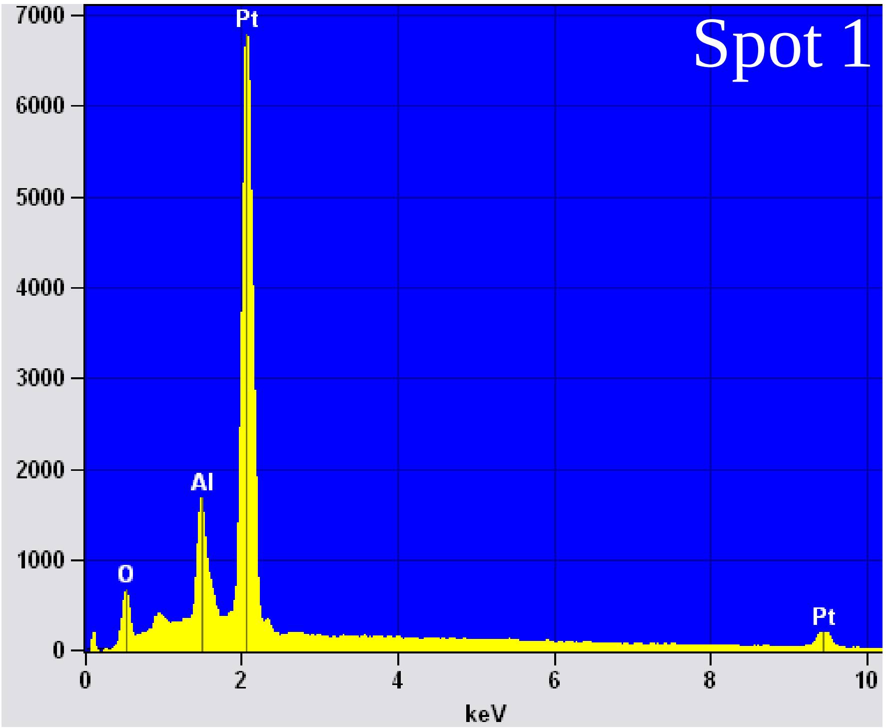

Figure 4.13. Surface EDS spectrum of water-quenched Pt_{84}:Al_{11}:Cr_3:Ru_2 (at.%) after 1 h oxidation in air at 1150°C showing the presence of Pt-rich island (spot 1 on Figure 4.12).

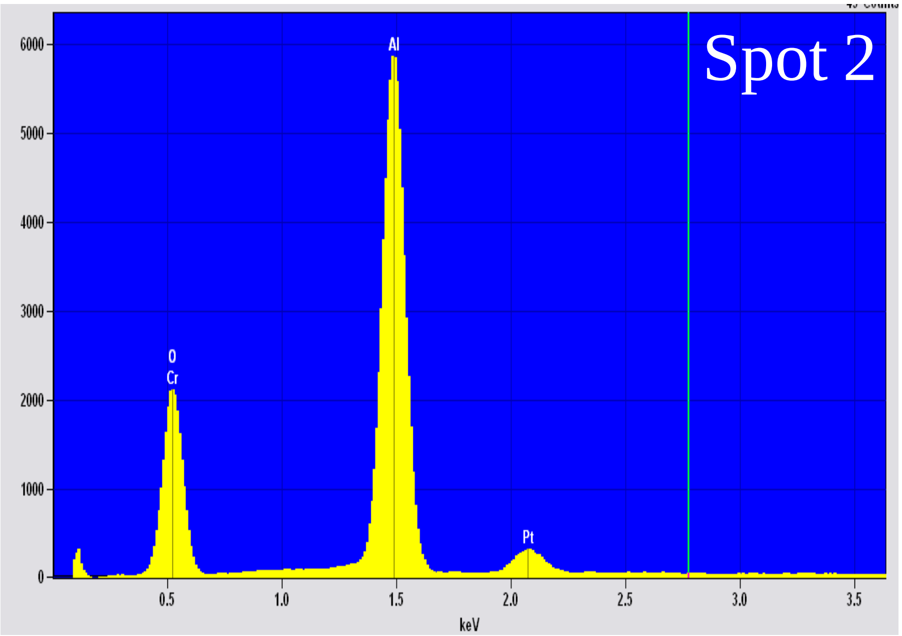

Figure 4.14. Surface EDS spectrum of water-quenched Pt_{84}:Al_{11}:Cr_3:Ru_2 (at.%) after 1 h oxidation in air at 1150°C showing the presence of Al_2O_3 (spot 2 on Figure 4.12).

A similar observation was made on the scale formed after 10 h oxidation as revealed by the X-ray elemental maps (Figure 4.15), which confirmed the presence of high concentrations of Al and O along with small amounts of Pt and Cr, with homogeneous distribution throughout. Thus, the scale layer was composed of Al_2O_3 and Pt-rich crystals after the early stages of oxidation up to 10 hours.

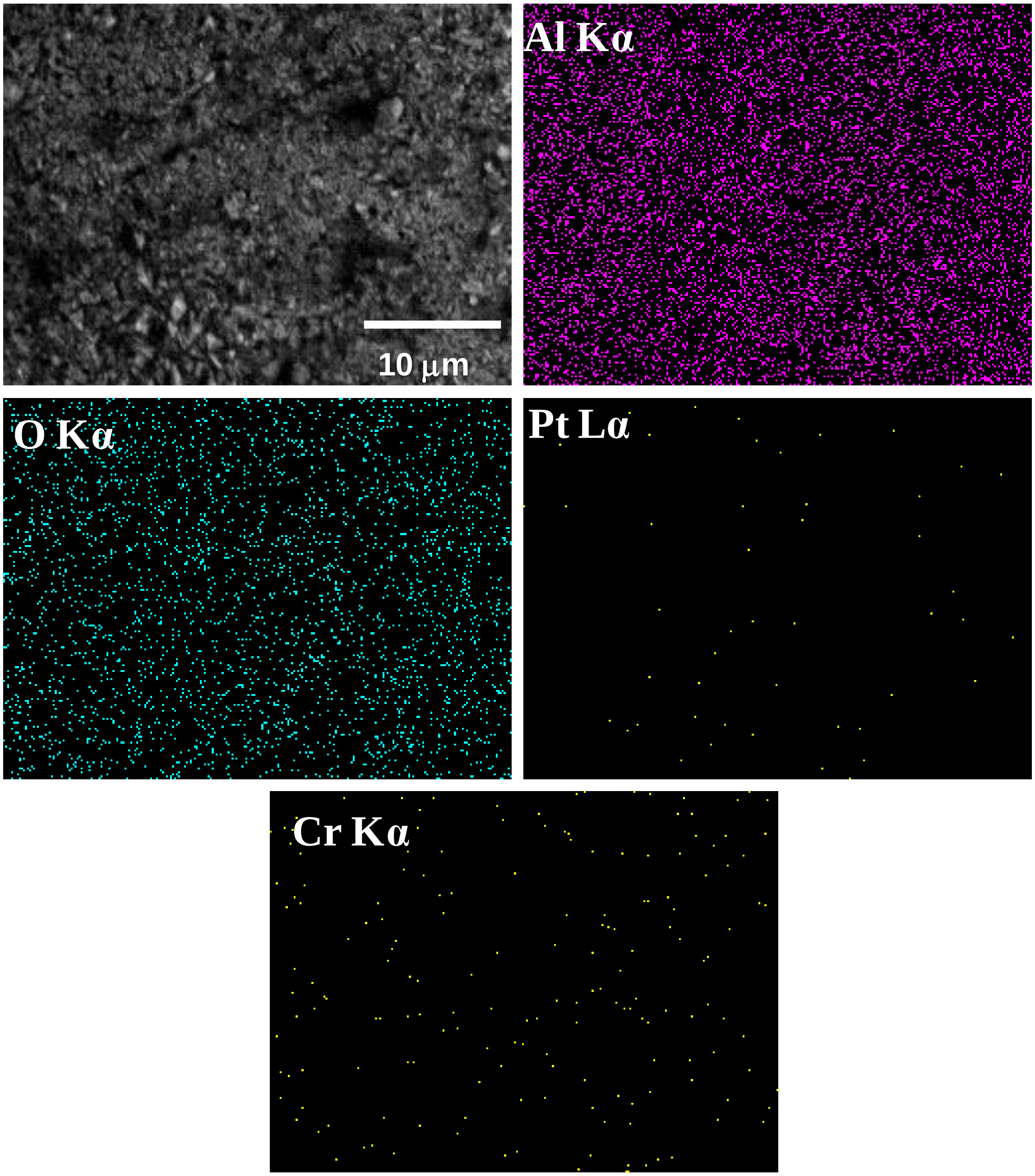

Figure 4.15. Element mapping images of Pt, O, Al, Cr of water-quenched Pt_{84}:Al_{11}:Cr_3:Ru_2 (at.%) after 10 h oxidation in air at 1150°C.

The surface morphology of the oxidized specimens changed after longer oxidation times with disappearance of Pt-rich crystals from the scale surfaces and formation of layered flake alumina structures (Figure 4.16), which were uneven and appeared porous. The distribution and sizes of the pores were not uniform, and they formed where the small flakes joined. Energy dispersive X-ray spectroscopy (EDS) was used to verify the oxide content of the scale after 50 hours oxidation in air at 1150°C, and revealed the presence of high concentration of O (~60.0 at.%) and Al (~40.0 at.%), corresponding to aluminium oxide, Al_2O_3 (Figure 4.17). The presence of Pt, Cr or Ru was not detected, indicating that the oxidized specimens were covered with only alumina scale after longer exposure times, and the interaction volume was not spreading to the substrate.

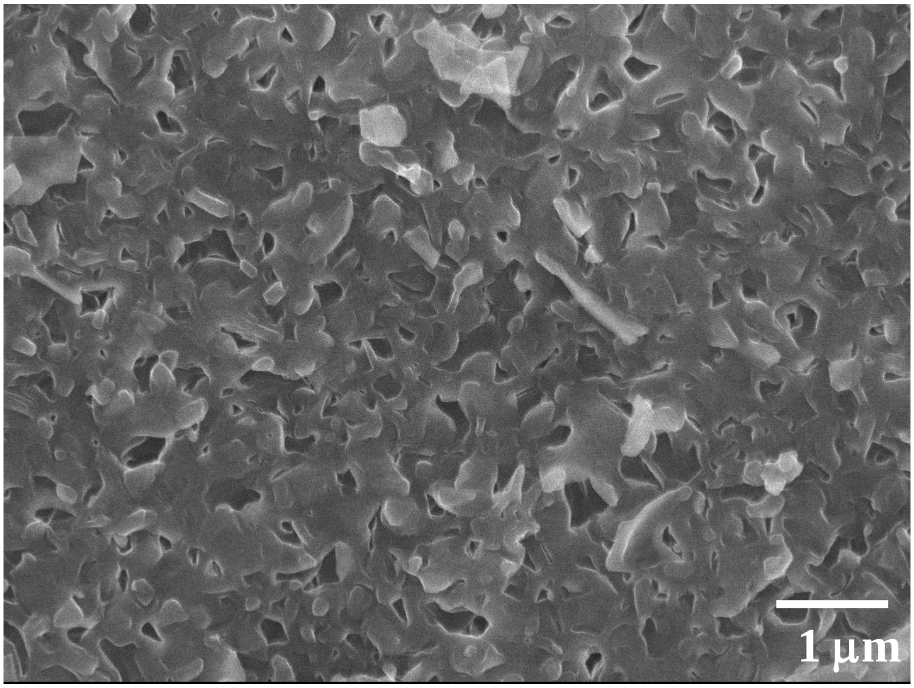

Figure 4.16. Surface SEM-SE image of water-quenched Pt_{84}:Al_{11}:Cr_3:Ru_2 (at.%) after 50 h oxidation in air at 1150°C.

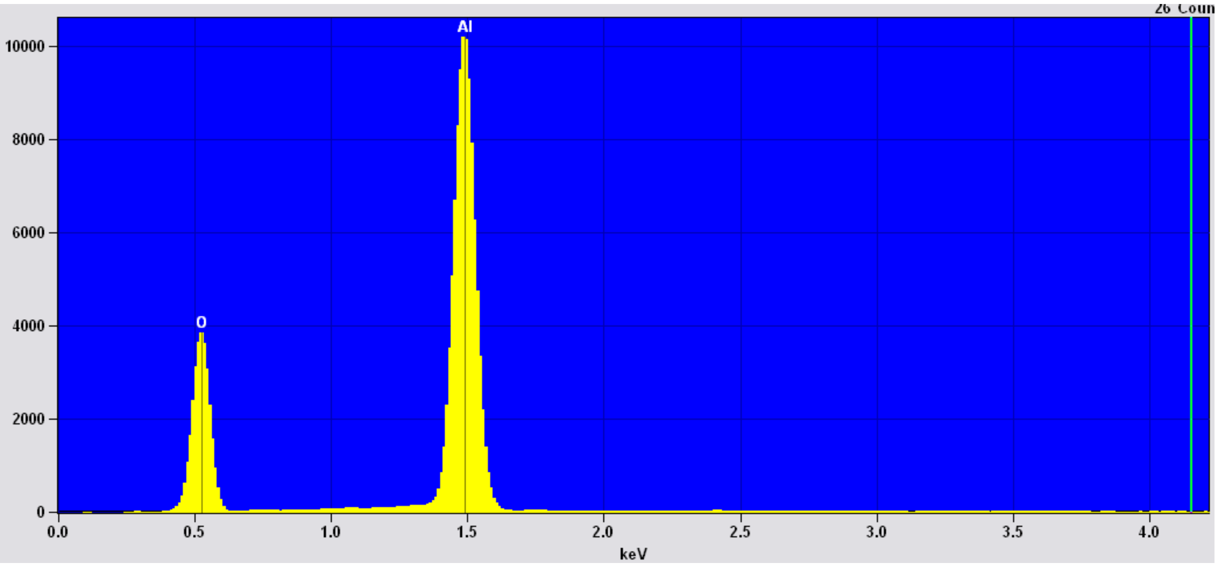

Figure 4.17. Overall surface EDS spectrum of water-quenched Pt_{84}:Al_{11}:Cr_3:Ru_2 (at.%) after 50 h oxidation in air at 1150°C, showing the presence of only Al and O peaks.

Scanning electron microscope images of the oxide scales formed on the specimens after 1 hour oxidation in air at 1250°C and 1350°C also revealed the presence of Pt-rich crystals, albeit being less facetted, (spot 1) between the alumina scale (spot 2) (Figures 4.18 and 4.19). However, the Pt-rich crystals on specimens oxidized at 1350°C were more coarse and irregular than those on specimens oxidized at lower temperatures. In addition, the Pt-rich crystals apparently grew directly on the alumina scale at 1350°C, instead of in between the scale as at 1150°C and 1250°C. Figure 4.20 shows the SEM image of oxide scale formed on the specimen after 10 hours oxidation at 1250°C. The scale exhibits a layered flake morphology with numerous pores forming where the flakes joined. Small grains of Pt-rich crystals were also observed on the scale surface, which were also non-uniform, but covered the whole specimen surface. After oxidation for 100 hours at 1250°C, the pores became less discernable with formation of well-defined grains of different shapes and sizes (Figure 4.21). EDS revealed that the scale layers formed after oxidation for 100 hours at 1250°C were composed of only Al (~40.0%) and O (~60.0%), corresponding to Al_2O_3 (Figure 4.22). The scale layer content of the specimen after oxidation for 50 hours was also confirmed with X-ray elemental maps (Figure 4.23), and also showed only Al and O with a uniform distribution, without any Pt, Cr or Ru.

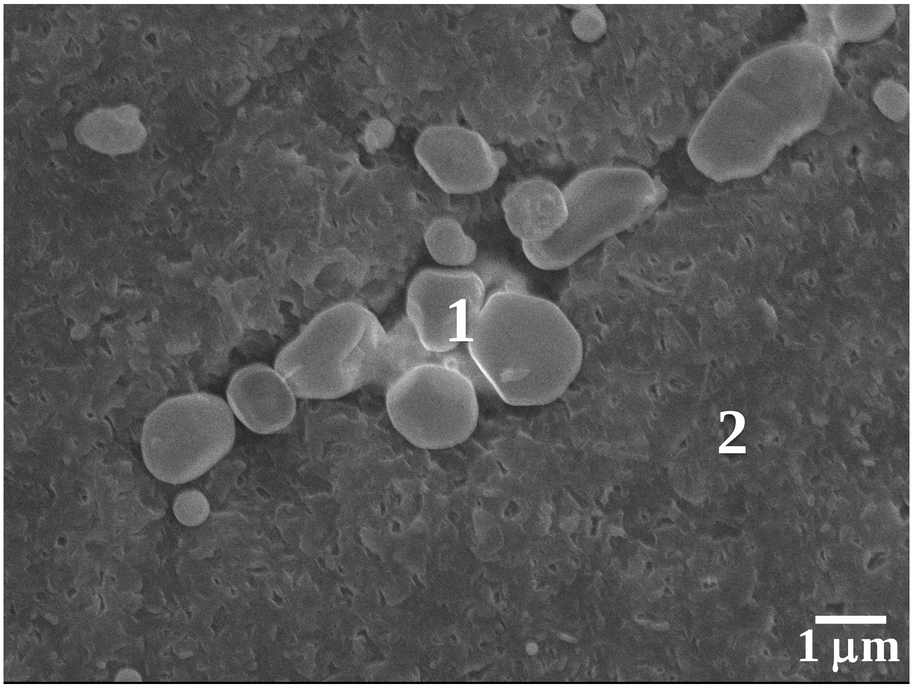

Figure 4.18. Surface SEM-SE image of water-quenched Pt_{84}:Al_{11}:Cr_3:Ru_2 (at.%) after 1 h oxidation in air at 1250°C, showing (1) Pt-rich crystals in between the scale (2) alumina scale.

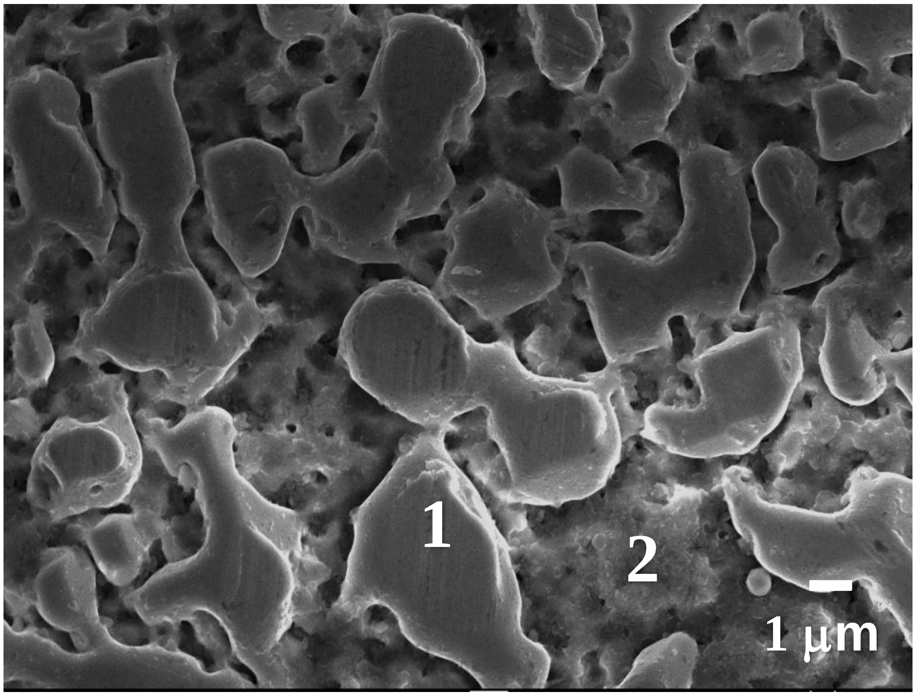

Figure 4.19. Surface SEM-SE image of water-quenched Pt_{84}:Al_{11}:Cr_3:Ru_2 (at.%) after 1 h oxidation in air at 1350°C, showing (1) Pt-rich crystals directly on the scale (2) alumina scale.

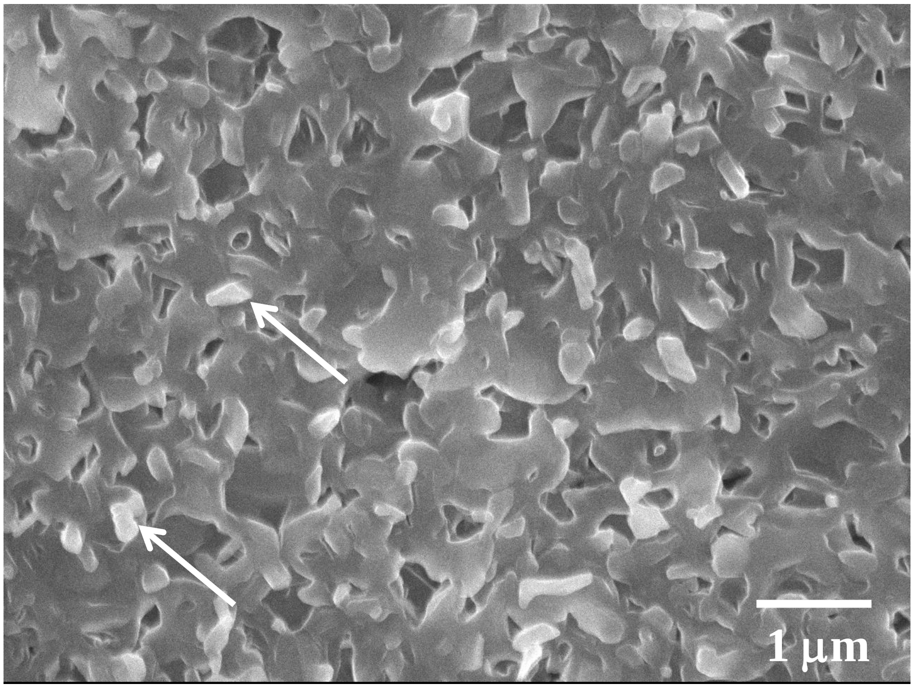

Figure 4.20. Surface SEM-SE image of water-quenched Pt_{84}:Al_{11}:Cr_3:Ru_2 (at.%) after 10 h oxidation in air at 1250°C, arrows indicate Pt-rich crystals.

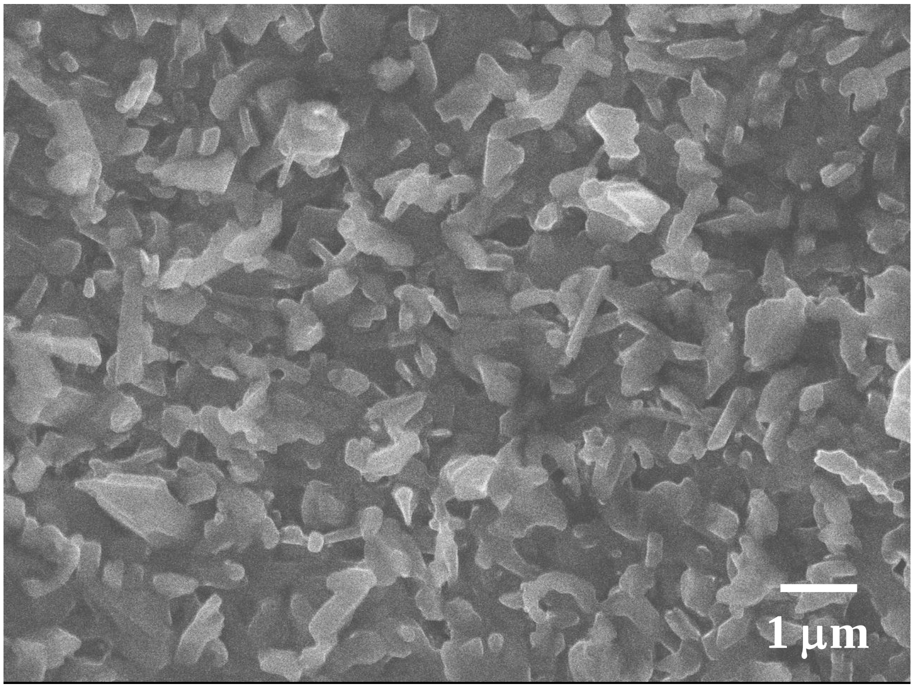

Figure 4.21. Surface SEM-SE image of water-quenched Pt_{84}:Al_{11}:Cr_3:Ru_2 (at.%) after 100 h oxidation in air at 1250°C.

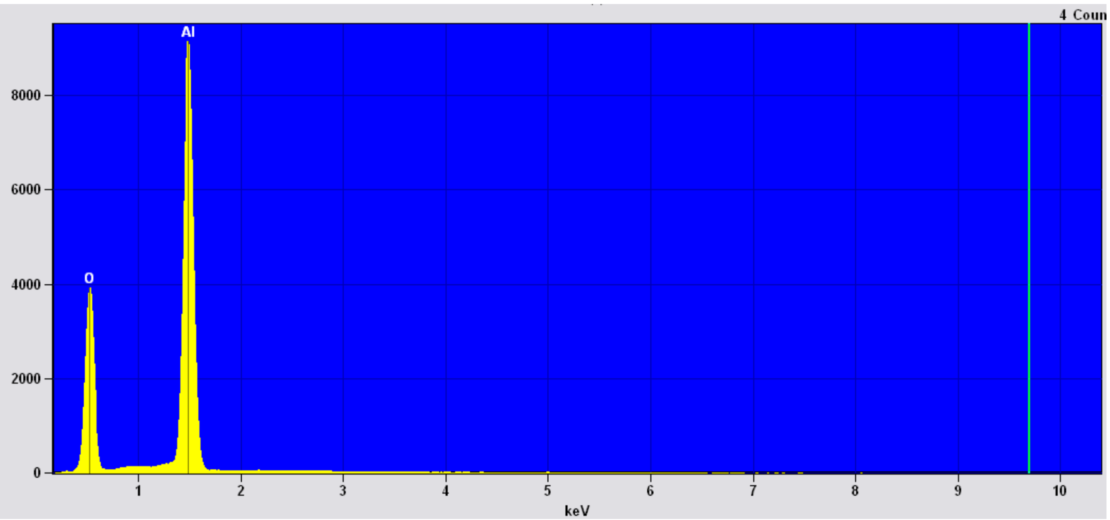

Figure 4.22. Overall surface EDS spectrum of water-quenched Pt_{84}:Al_{11}:Cr_3:Ru_2 (at.%) after 100 h oxidation in air at 1250°C, showing the presence of strong Al and O peaks only.

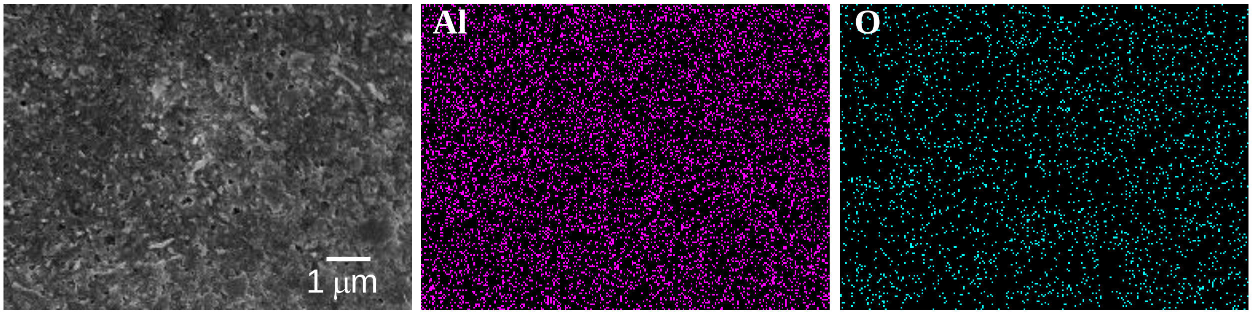

Figure 4.23. Surface elemental mapping images of Al and O (without any Pt, Cr or Ru) of water-quenched Pt_{84}:Al_{11}:Cr_3:Ru_2 (at.%) after 50 h oxidation in air at 1250°C.

Low magnification SEM-BSE images of the specimen surfaces after isothermal oxidation in air for up to 100 hours at 1350°C are presented in Figure 4.24. The scale developed after 1 h was non-uniform, but became increasingly uniform and covered the whole specimen surfaces at longer exposure times. The appearance of grain boundaries on the scale layers indicated grain boundary oxidation of the substrate. At exposures above 10 hours, the grain boundaries became less discernable, due to increased thickness of the oxide layer. Pores were also observed on the some of the specimens after oxidation. EDS of the oxidised specimen overall surfaces revealed that the scale layers were composed mainly of Al and O, corresponding to AlO_2 (Table 4.4). Since AlO_2 is not reported to exist, this shows that there is a problem with these particular results, which could be related to standards. These results are also contrary to the EDS results obtained from JEOL JSM-7500 FESEM (at CSIR Nanocentre), using a dry silicon drift EDS detector, as well as XRD and Raman spectrostropy results. Small amounts of Pt and Cr were also detected during the early stages of oxidation up to 10 hours, possibly from the interaction volume.

Table 4.4. EDS analyses (at.%) of the oxide scales on water-quenched Pt_{84}:Al_{11}:Cr_3:Ru_2 (at.%) after isothermal oxidation in air at 1350°C for up to 100 h.

Oxidation time (h)	Al	O	Pt	Cr	Ru
1	34.0 ± 1.8	63.8 ± 0.8	1.5 ± 0.9	0.7 ± 0.1	-
10	36.4 ± 1.4	63.4 ± 1.1	0.2 ± 0.9	-	-
50	36.9 ± 1.7	63.1 ± 0.9	-	-	-
100	37.1 ± 0.4	62.9 ± 0.4	-	-	-

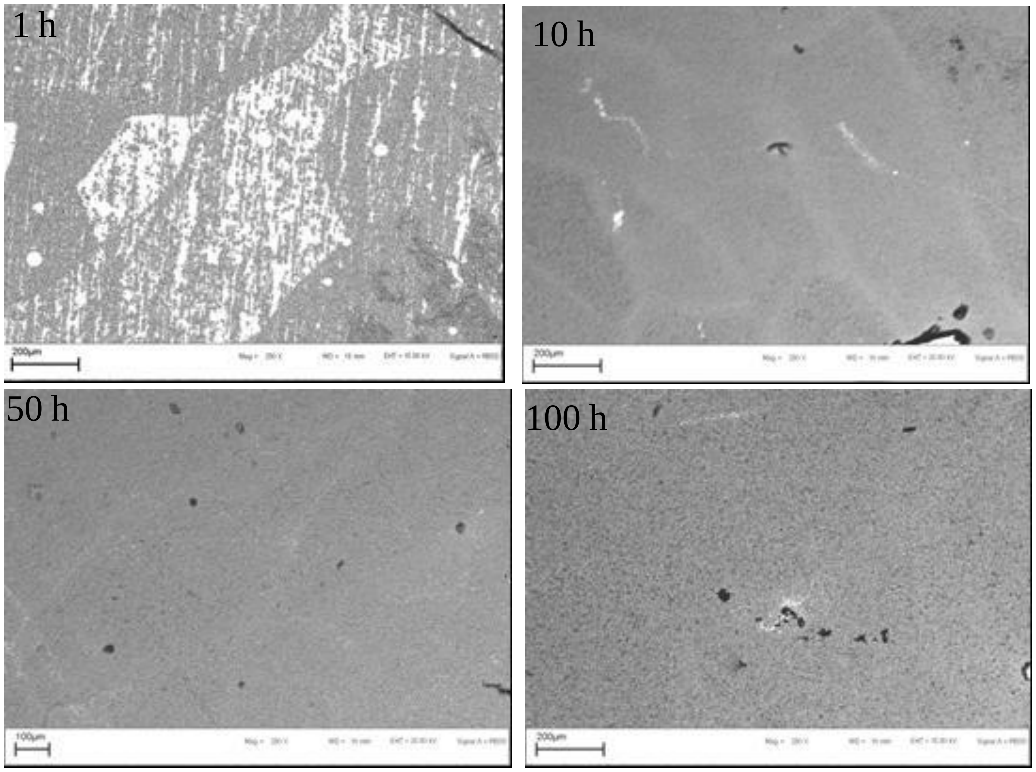

Figure 4.24. Low magnification SEM-BSE images of the scale formed on Pt_{84}:Al_{11}:Cr_3:Ru_2 (at.%) after isothermal oxidation in air at 1350°C for up to 100 h.

High magnification SEM images, which revealed increased oxide grain sizes with increased exposure times at 1350°C are presented in Figure 4.25. In the early stages of oxidation, the scale appeared porous, but as more and larger flakes were formed on the external surface with increased exposure time, this became less discernable. Instead of flakes, there were crystalline oxide grains of different sizes after 50 hours exposure. Large oxide grains of about 1.6 ± 0.6 µm grain size had grown after 100 hours exposure (Table 4.5).

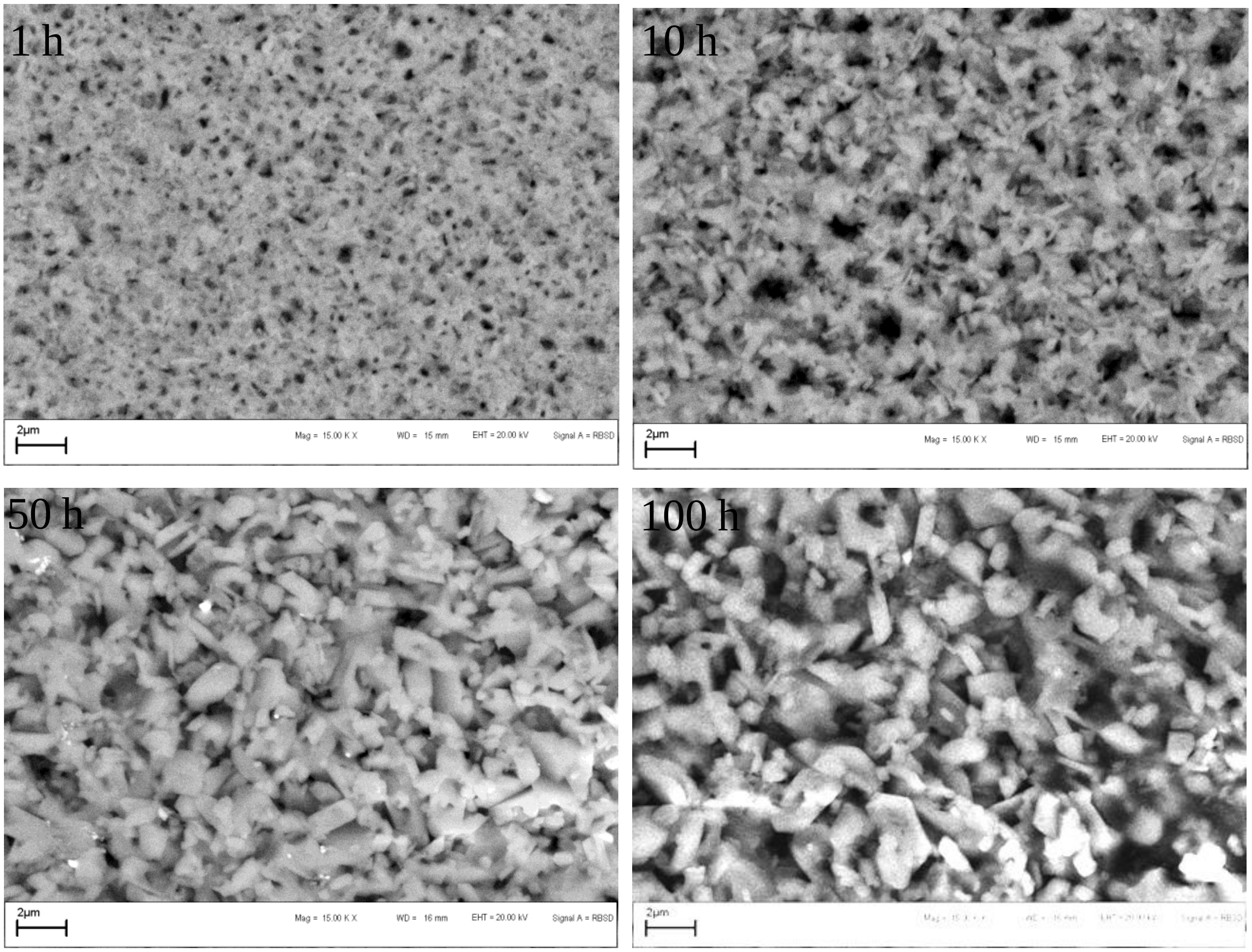

Figure 4.25. High magnification SEM-BSE micrographs of the scale formed on water-quenched Pt_{84}:Al_{11}:Cr_3:Ru_2 (at.%) after isothermal oxidation in air at 1350°C for up to 100 h.

Table 4.5. Grain size of Al_2O_3 scale on water-quenched Pt_{84}:Al_{11}:Cr_3:Ru_2 (at.%) after 100 h oxidation in air at 1250°C and 1350°C.

Temperature (°C)	**Grain size (μm)**
1250	0.5 ± 0.1
1350	1.6 ± 0.6

4.3.2.2 Air-cooled Specimens

The morphological features of the scale layers of the air-cooled Pt_{84}:Al_{11}:Cr_3:Ru_2 (at.%) after 1 hour oxidation have some similarity with those of water-quenched specimens. The scale formed was also well-adhering without spallation during cooling. At 1150°C, Pt-rich crystals (spot 1) were formed between the scale layers (spot 2) (Figure 4.26). The crystals were more common and coarser than those formed at higher exposure temperatures. The Pt-rich crystals also grew in between the scale at 1250°C, and were less facetted (Figure 4.27). However, fewer and smaller Pt-rich crystals were observed on the alumina scale with numerous pores at 1350°C (Figure 4.28). Also, the alumina scale appeared more crystalline and exhibited morphology different from those formed at lower temperatures.

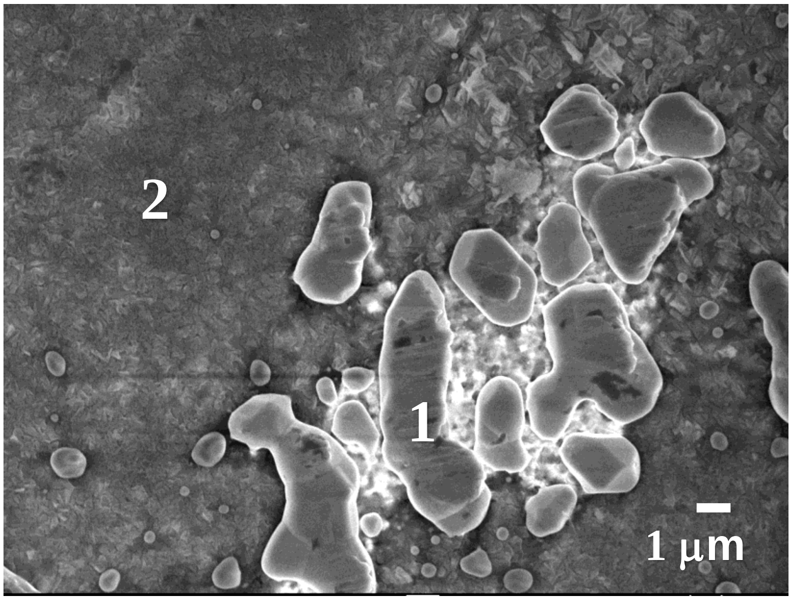

Figure 4.26. Surface SEM-SE image of air-cooled Pt_{84}:Al_{11}:Cr_3:Ru_2 (at.%) after 1 h oxidation in air at 1150°C, showing the presence of Pt-rich crystals between the alumina scale.

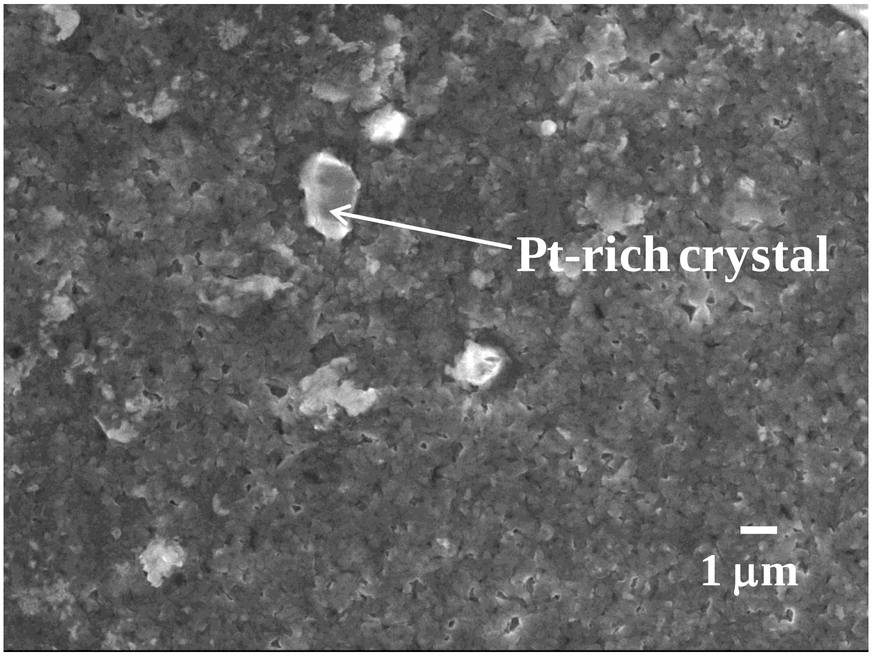

Figure 4.27. Surface SEM-SE image of air-cooled Pt_{84}:Al_{11}:Cr_3:Ru_2 (at.%) after 1 h oxidation in air at 1250°C, showing the presence of few Pt-rich crystals between the scale.

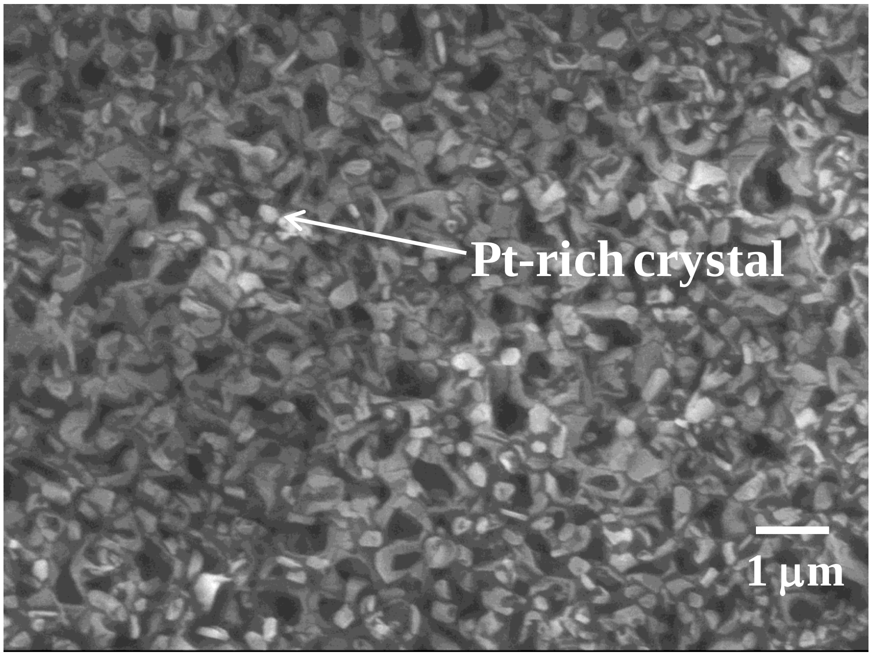

Figure 4.28. Surface SEM-SE image of air-cooled Pt_{84}:Al_{11}:Cr_3:Ru_2 (at.%) after 1 h oxidation in air at 1350°C, showing the presence of small grains of Pt-rich crystals on the scale.

The scale layer contents after 1 hour exposure were confirmed with the X-ray elemental maps in Figure 4.29, which revealed the presence of Al, O, Cr and Pt. The X-ray elemental maps also showed that the Pt-rich crystals contained very little or no Al or O, but Cr was present.

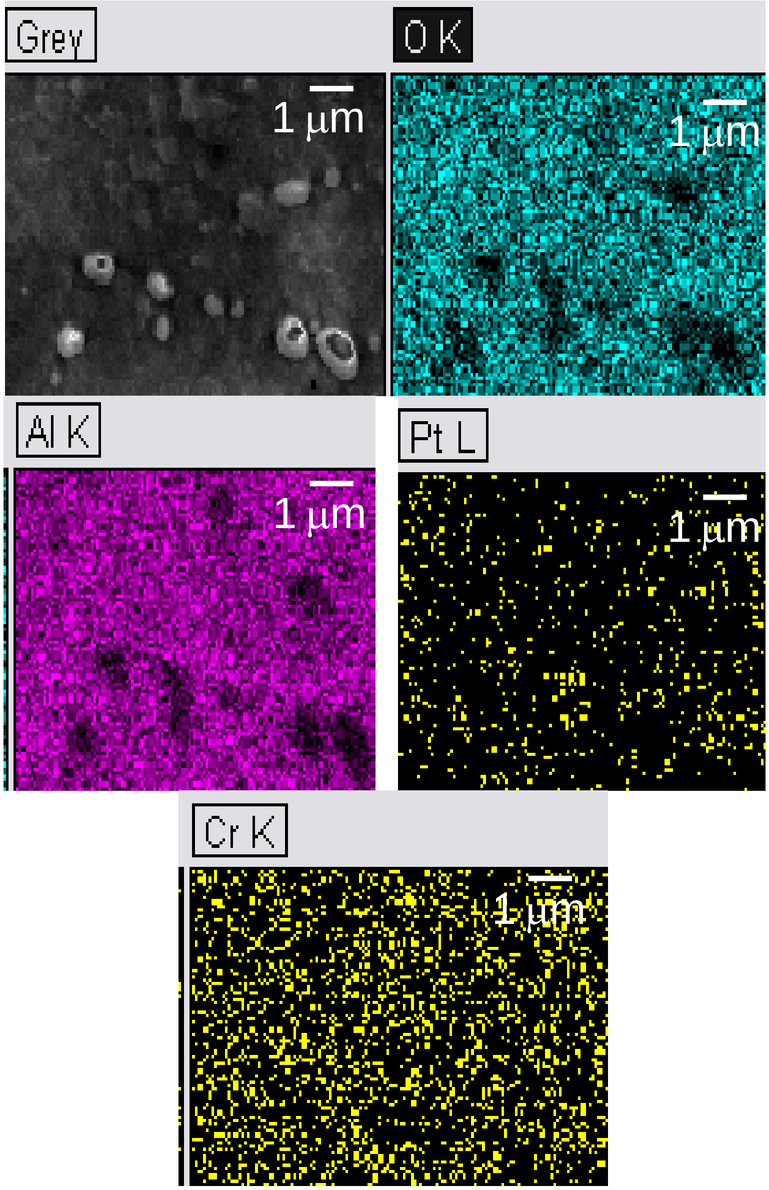

Figure 4.29. Surface EDS mapping images of Al, O, Pt and Cr of air-cooled Pt_{84}:Al_{11}:Cr_3:Ru_2 (at.%) after 1 h oxidation in air at 1150°C, showing absence of Al and O in the Pt-rich crystals.

EDS also showed the presence of Pt (~0.6 at.%) and Cr (~1.3 at.%) along with O (~59.1 at.%) and Al (~39.0 at.%) on the scale, after 10 hours oxidation at 1150°C (Figure 4.30a). Platinum and chromium were not identified on specimens oxidised for the same time at higher temperatures (Figure 4.30b). Above 50 hours, at all oxidation temperatures, mainly O (~60.0 at.%) and Al (~40.0 at.%) peaks were detected during the overall surface EDS analyses (Figure 4.31). However, a carbon peak was detected on some of the specimens because they were carbon coated in order to reduce the charging effect during the SEM analysis.

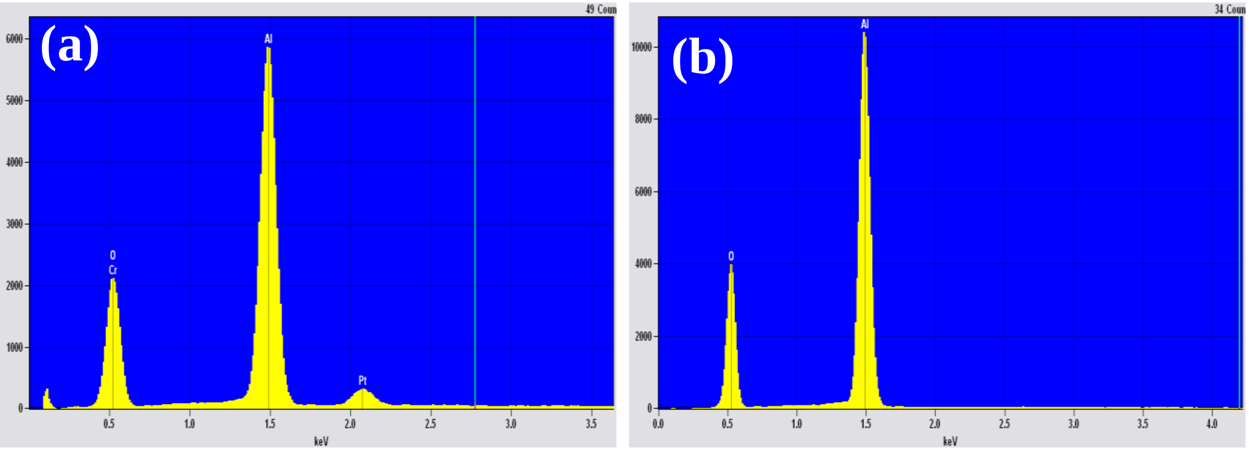

Figure 4.30. Surface EDS spectra of air-cooled Pt_{84}:Al_{11}:Cr_3:Ru_2 (at.%) oxidized in air for 10 h at: (a) 1150°C, showing the presence of Pt and Cr peaks along with Al and O (b) 1350°C, showing the presence of only Al and O peaks.

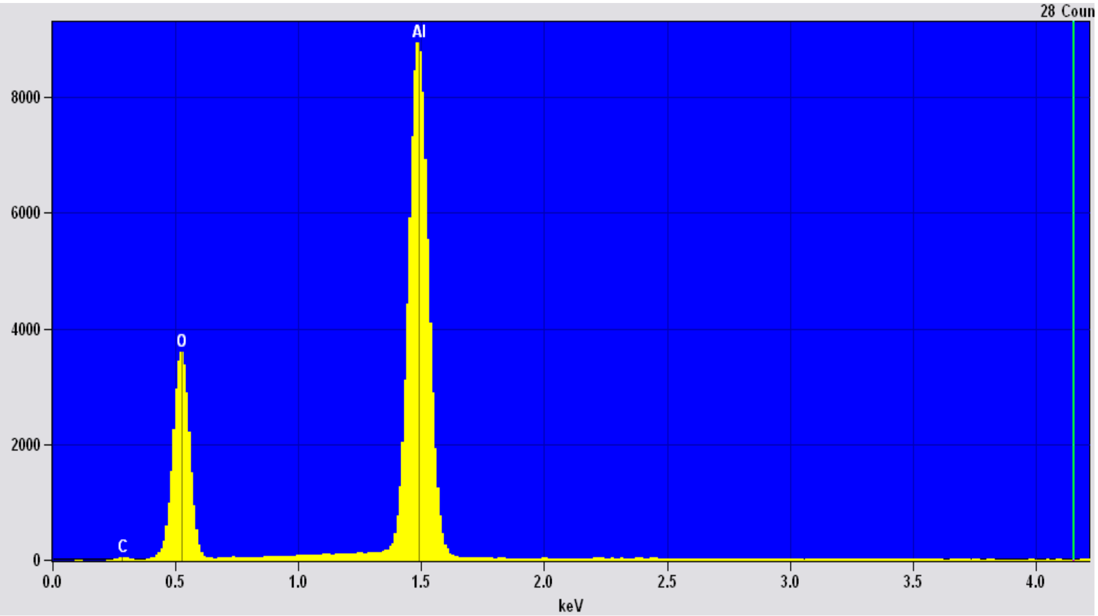

Figure 4.31. Surface EDS spectrum of air-cooled Pt_{84}:Al_{11}:Cr_3:Ru_2 (at.%) oxidized in air for 50 h at 1250°C, showing the presence of Al and O peaks as the major elements, with small carbon peak from carbon coating.

Figures 4.32-4.33 show the images of the oxide scales formed after oxidation for 100 hours and 200 hours at 1150°C. The oxide grown after 100 hours featured layered flakes morphology with small amount of needle-like oxides (Figure 4.32). Pores were observed at the points where the flakes joined. Some of the pores were rounded while some were not. After 200 hours, fewer pores were discerned as more regular grains of Al_2O_3 apparently formed on top of the flakes (Figure 4.33). Oxidation at 1250°C produced plate-like scale morphology with few needle-like oxides (Figures 4.34 and 4.35). As oxidation time increased from 100 hours to 200 hours, the pores got more rounded and became less discerned, while the oxide grains also increased. Similar morphology was also observed after 100 hours and 200 hours oxidation at 1350°C, except that the oxide grains appeared to be larger and more developed (Figures 4.36 and 4.37). After 200 hours oxidation at 1350°C, large and more rounded oxide grains of about 2.0 ± 0.4 µm grain size had grown (Table 4.6).

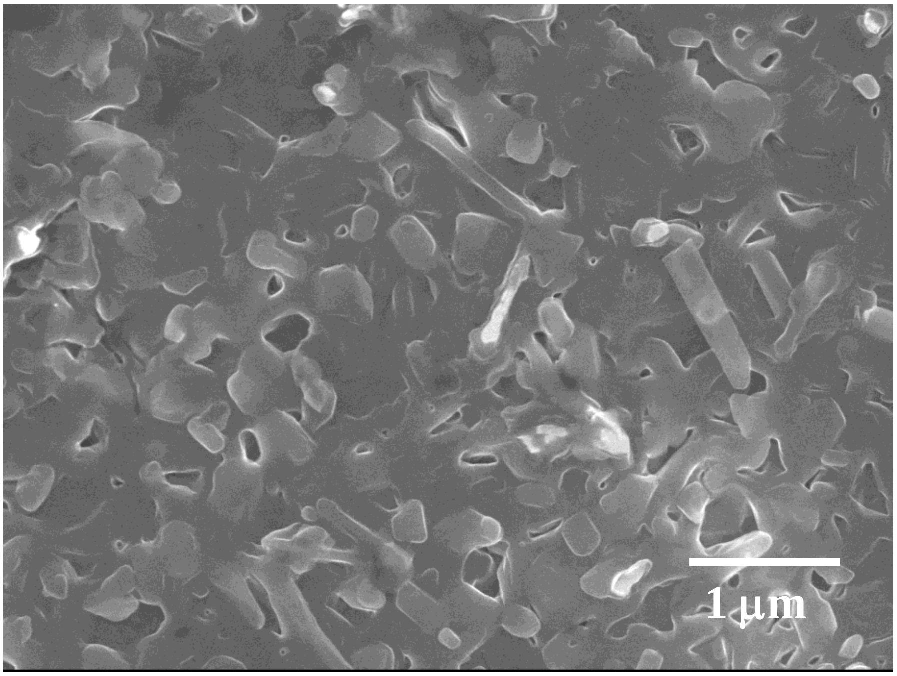

Figure 4.32. Surface SEM-SE images of air-cooled Pt_{84}:Al_{11}:Cr_3:Ru_2 (at.%) after 100 h oxidation in air at 1150°C.

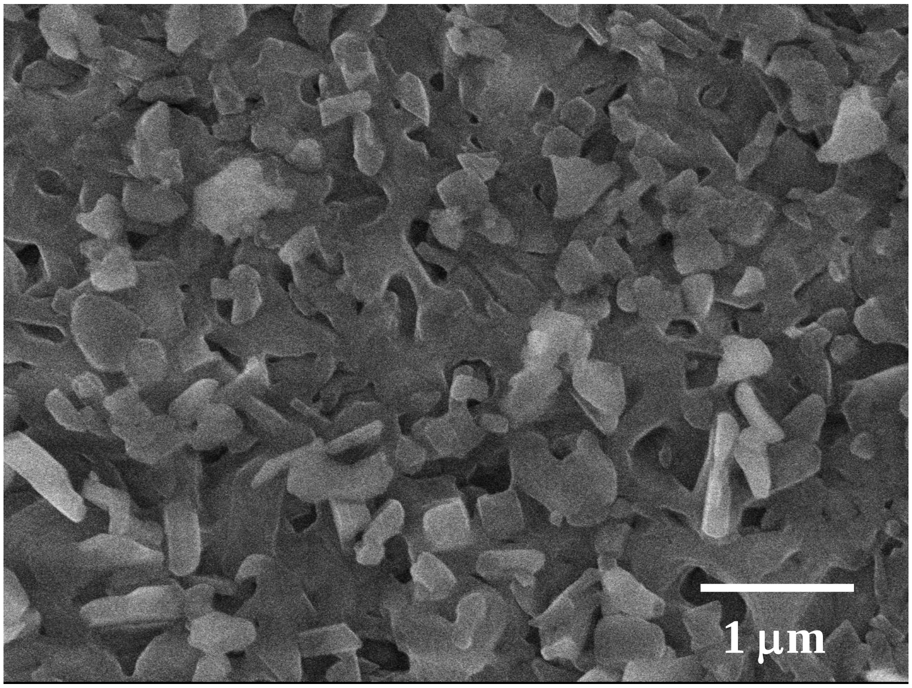

Figure 4.33. Surface SEM-SE images of air-cooled Pt_{84}:Al_{11}:Cr_3:Ru_2 (at.%) after 200 h oxidation in air at 1150°C.

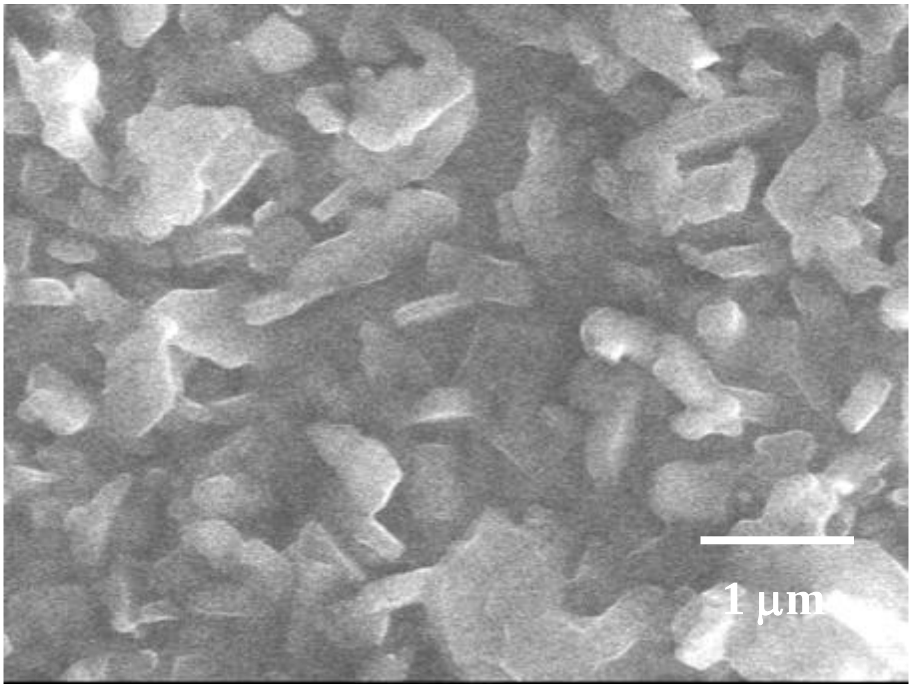

Figure 4.34. Surface SEM-SE images of air-cooled Pt_{84}:Al_{11}:Cr_3:Ru_2 (at.%) after 100 h oxidation in air at 1250°C.

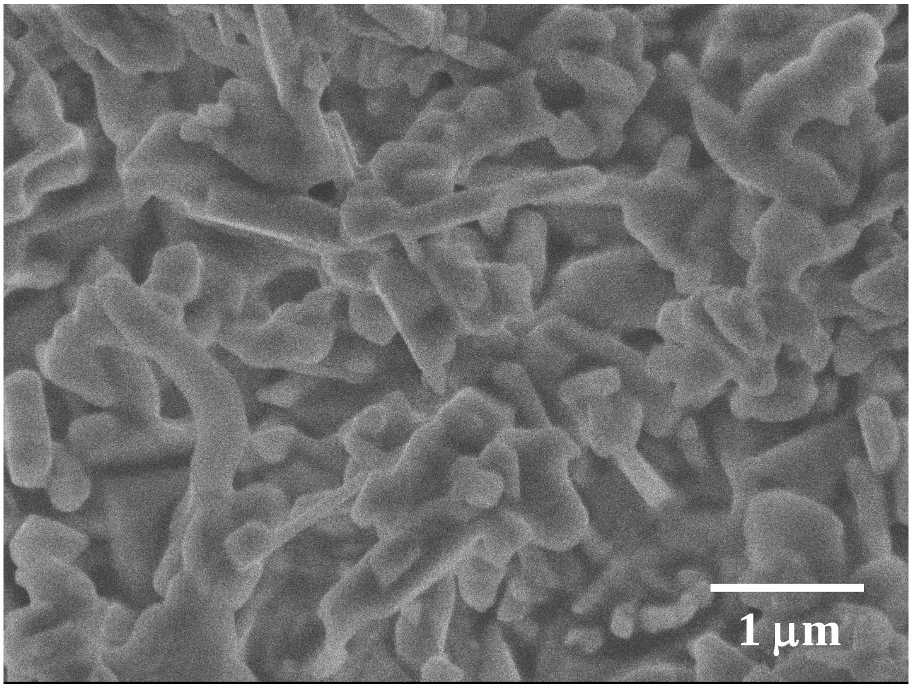

Figure 4.35. Surface SEM-SE images of air-cooled Pt_{84}:Al_{11}:Cr_3:Ru_2 (at.%) after 200 h oxidation in air at 1250°C.

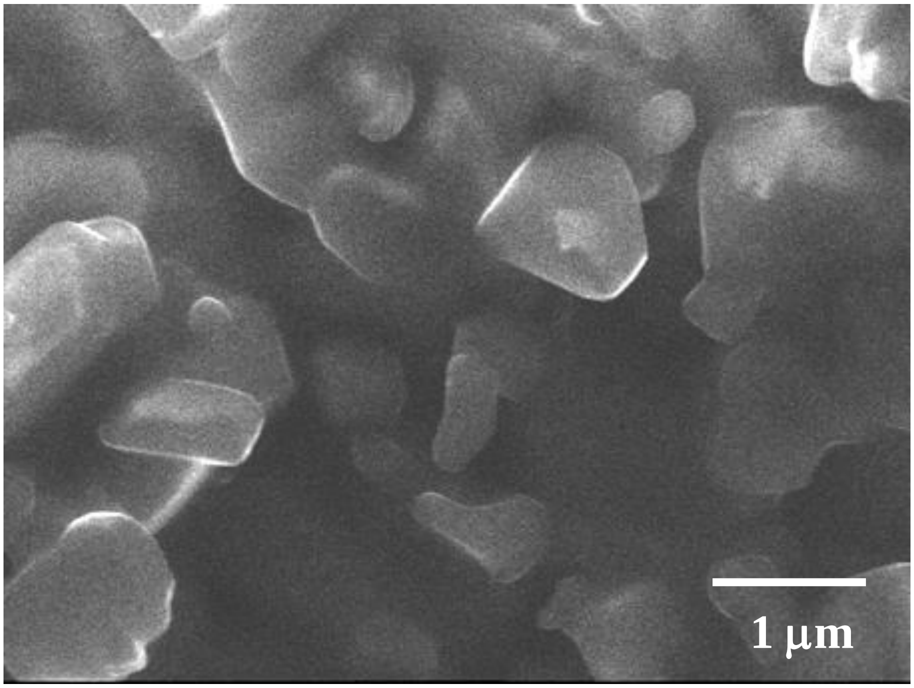

Figure 4.36. Surface SEM-SE images of air-cooled Pt_{84}:Al_{11}:Cr_3:Ru_2 (at.%) after 100 h oxidation in air at 1350°C.

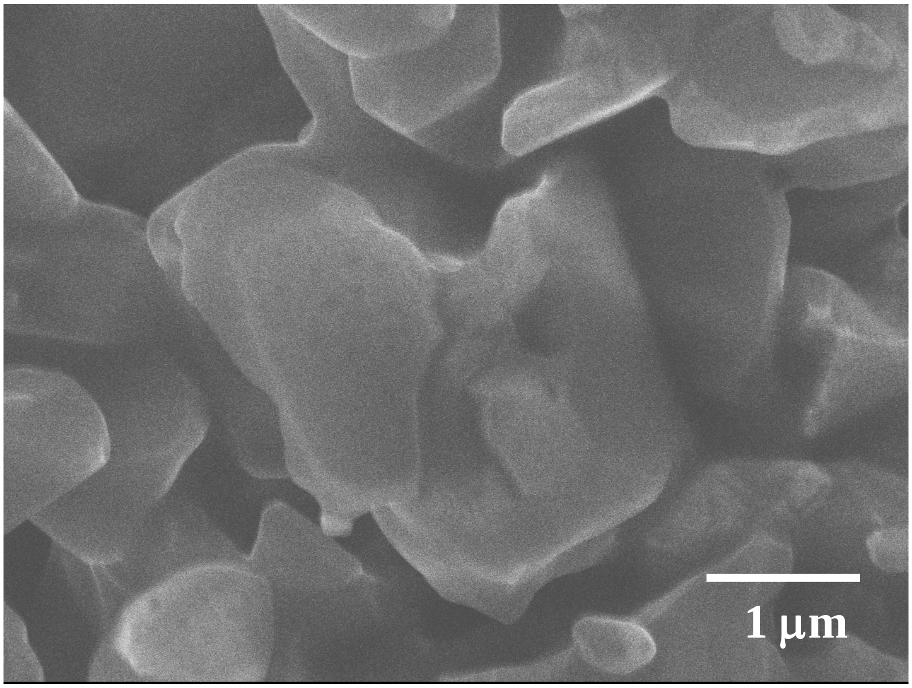

Figure 4.37. Surface SEM-SE images of air-cooled Pt_{84}:Al_{11}:Cr_3:Ru_2 (at.%) after 200 h oxidation in air at 1350°C.

Table 4.6. Grain size of Al_2O_3 scale on air-cooled Pt_{84}:Al_{11}:Cr_3:Ru_2 (at.%) oxidized in air at 1250°C and 1350°C.

Temperature (°C)	**Grain size (μm)**	
	100 h	200 h
1250	0.7 ± 0.2	0.8 ± 0.1
1350	1.5 ± 0.7	2.0 ± 0.4

4.4 Cross-Sectional Morphology of the Oxide Layers

4.4.1 Water-quenched Specimens

The cross-section SEM image (in secondary electron mode) of the oxide scale developed on a water-quenched specimen after 1 hour oxidation in air at 1150°C, revealed the growth of a protective and continuous external alumina scale with no evidence of spallation (Figure 4.38). The scale was well adherent to the substrate with no zone of discontinuous oxide or apparent internal oxidation. The presence of Pt-rich crystals on the scale showed that they formed along with aluminium oxide during the early stages of oxidation, and from the section appeared to be on top of the scale. X-ray elemental maps (Figure 4.39) confirmed that the scale was composed of Al and O, corresponding to aluminium oxide. The alloy substrate showed uniform distribution of Al and O. There was no obvious Al depletion zone, at least at the depth analysed.. However, the oxygen appeared to have a higher concentration than Al, which could be due to the aluminium at the specimen surface oxidizing during metallographic preparation. There was apparent different contrast between the scale and the substrate at the scale-alloy interface.

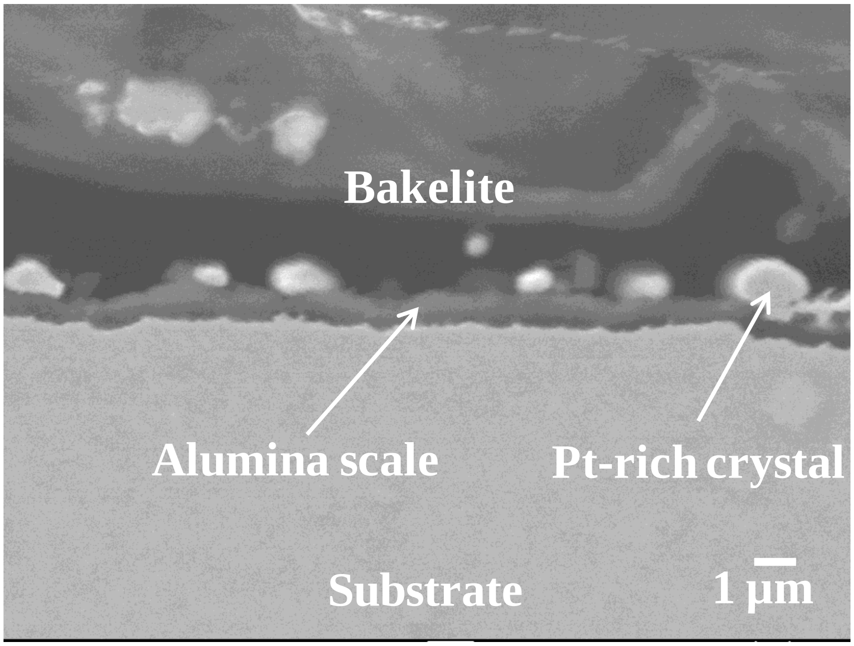

Figure 4.38. SEM-SE cross-sectional image of oxide scale formed on water-quenched Pt_{84}:Al_{11}:Cr_3:Ru_2 (at.%) after 1 h oxidation in air at 1150°C.

The scale thicknesses increased with increased exposure temperatures and times (Figure 4.40 and 4.41). The formation of oxide ridges, i.e. intrusions of the oxide at the scale-alloy interface and protrusions of the oxide at the scale-gas interface, increased the non-uniformity of the scale thicknesses. This effect increased with increased exposure temperatures and times (Figures 4.38, 4.41 and 4.42). This observation was responsible for large error bars mostly obtained after longer exposure times at higher temperatures (Table 4.7). There was apparently no void formation at the scale-alloy interface, and no zone of discontinuous oxides or any apparent internal oxidation.

The scales formed at all exposure temperatures and times were well-adhering with no evidence of oxide spallation. Although few scratches from metallographic preparation were observed on the alloy substrates (Figures 4.41 and 4.42). X-ray elemental maps (Figure 4.43) showed that the scale layer at longer oxidation time was only composed of Al and O, corresponding to aluminium oxide. However, due to high charging effect, which made specimen focusing difficult during SEM analyses, there was apparent different contrast at the scale-alloy interface. In addition, the scale-gas interface was also not apparent.

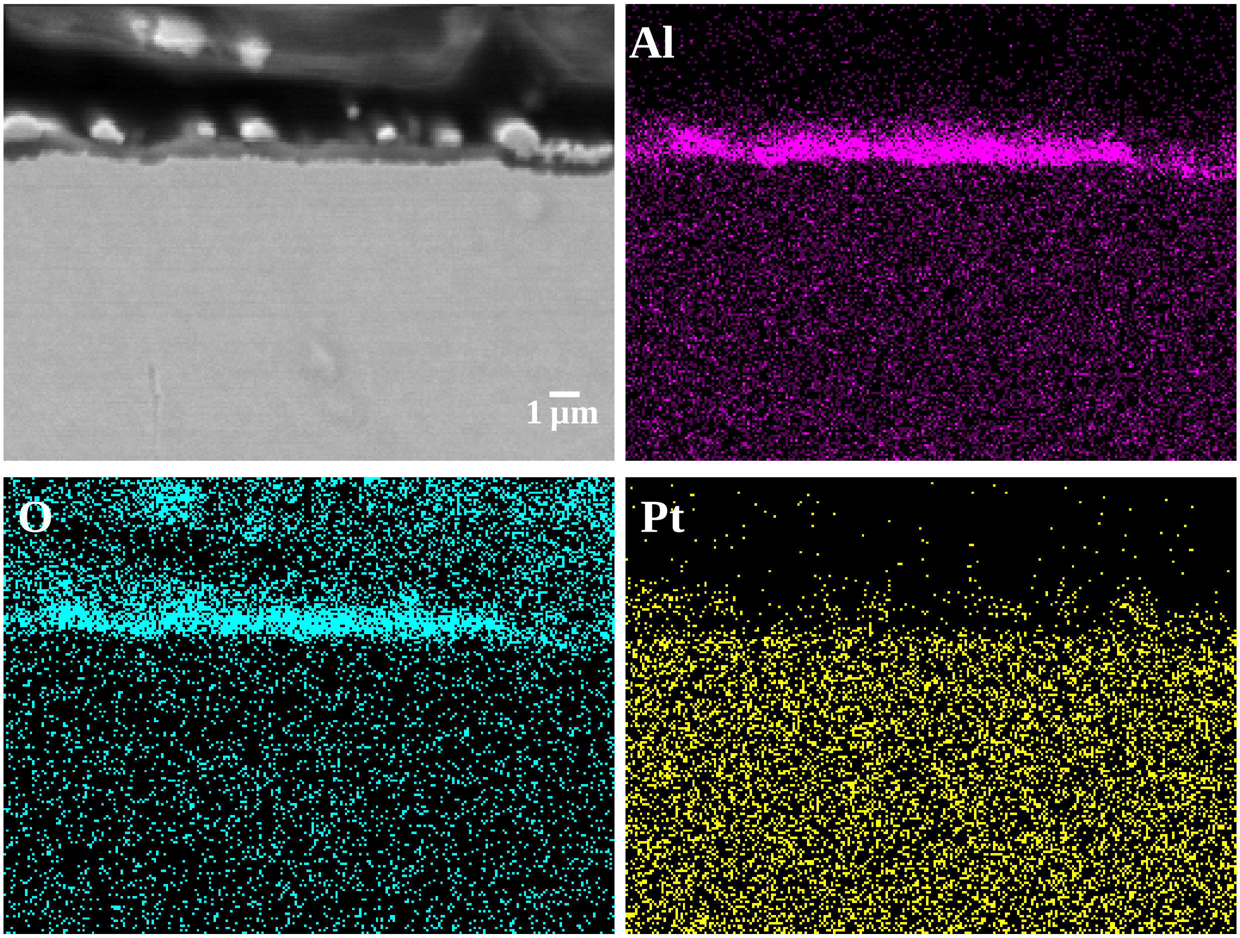

Figure 4.39. Cross-sectional EDS mapping images of Al, O and Pt of oxide scale (0.84 ± 0.06 µm thick) on water-quenched Pt_{84}:Al_{11}:Cr_3:Ru_2 (at.%) after 1 h oxidation in air at 1150°C.

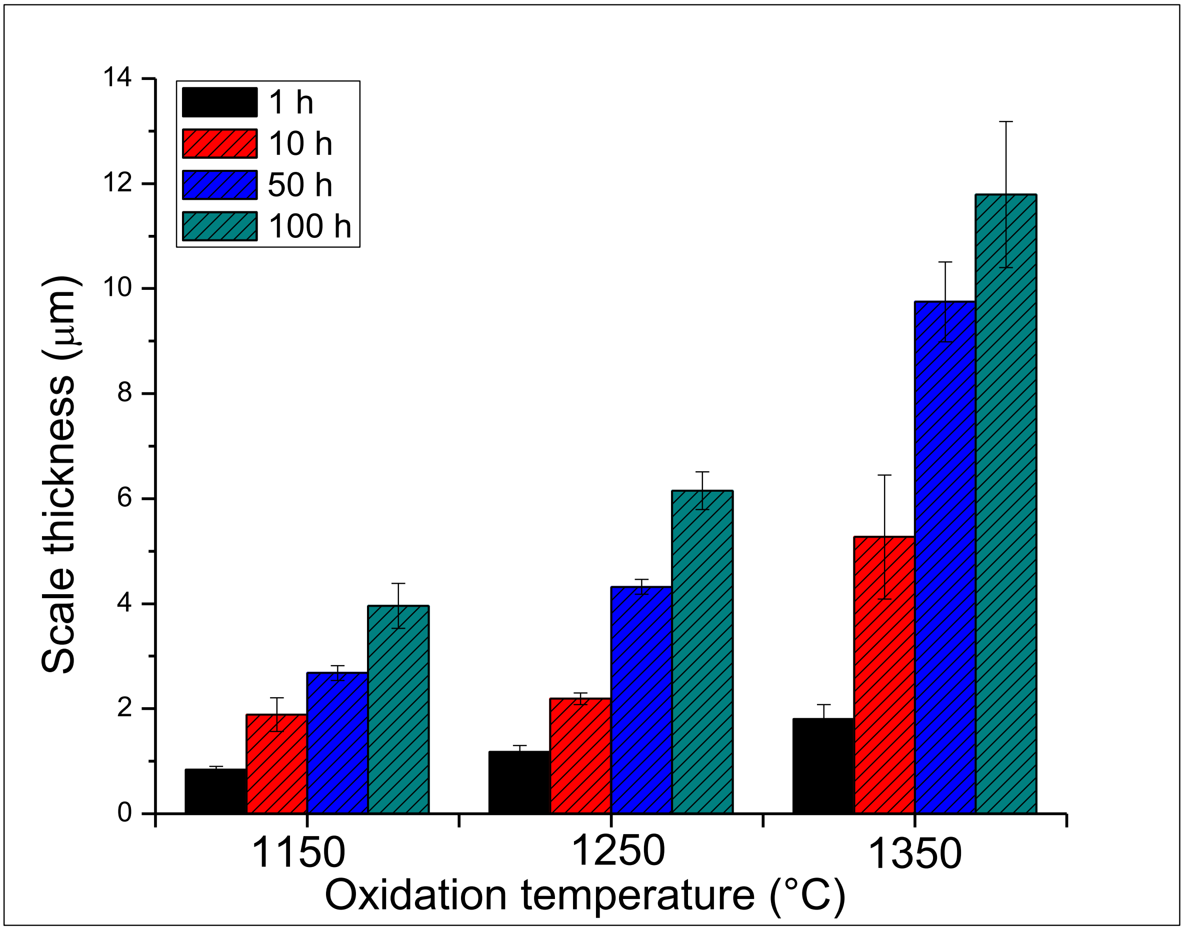

Figure 4.40. Effect of exposure temperature and time on scale thickness of water-quenched Pt_{84}:Al_{11}:Cr_3:Ru_2 (at.%) specimens after isothermal oxidation of in air at 1150°C, 1250°C and 1350°C.

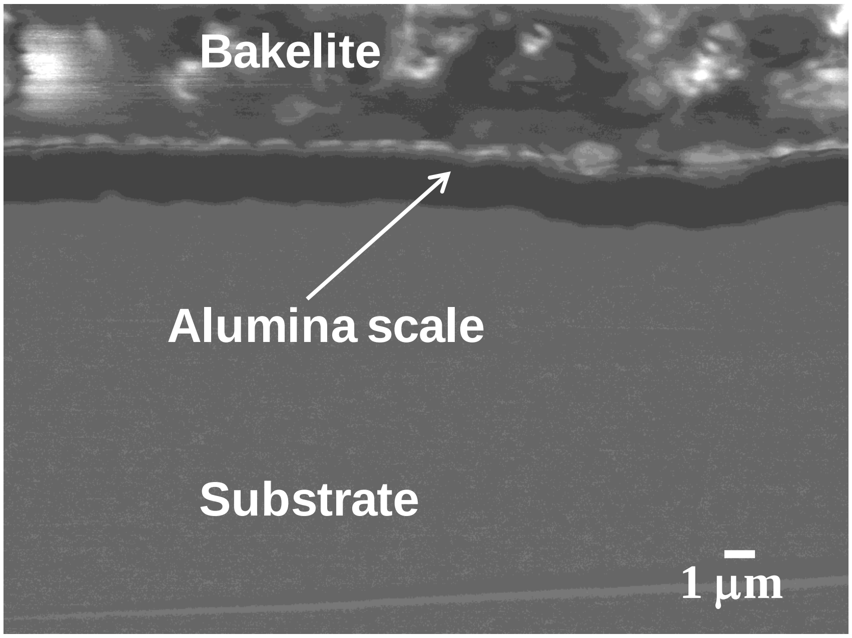

Figure 4.41. SEM-SE cross-sectional image of oxide scales on water-quenched Pt_{84}:Al_{11}:Cr_3:Ru_2 (at.%) after 1 h oxidation in air at 1350°C.

Table 4.7. Thickness values obtained from water-quenched Pt_{84}:Al_{11}:Cr_3:Ru_2 (at.%) specimens after oxidation in air at 1150°C, 1250°C and 1350°C for up to 100 h.

Oxidation time (hours)	**Mean scale thickness (μm)**		
	1150°C	**1250°C**	**1350°C**
1	0.84 ± 0.06	1.18 ± 0.12	1.85 ± 0.28
10	1.89 ± 0.32	2.19 ± 0.11	5.27 ± 1.18
50	2.68 ± 0.14	4.32 ± 0.14	9.75 ± 0.76
100	3.96 ± 0.43	6.15 ± 0.36	11.79 ± 1.39

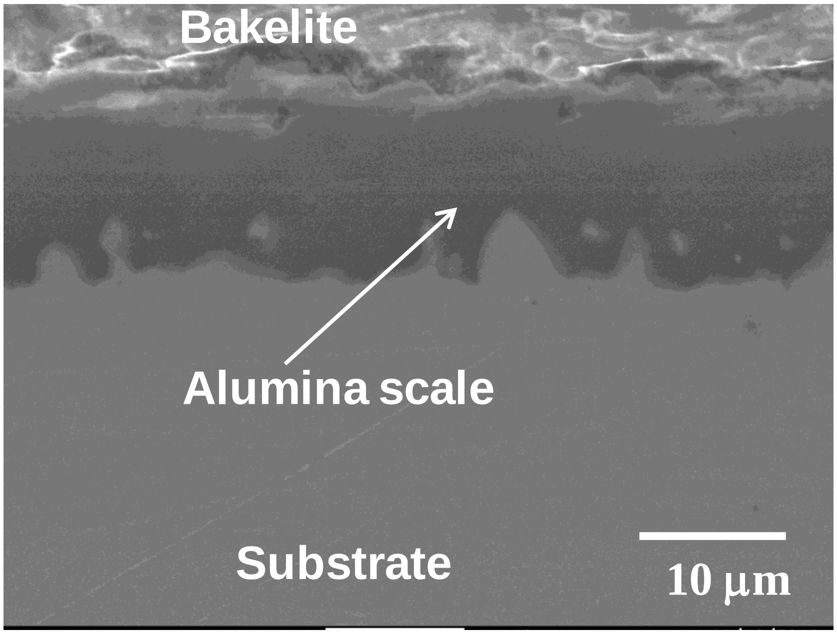

Figure 4.42. SEM-SE cross-sectional image of oxide scales on water-quenched Pt_{84}:Al_{11}:Cr_3:Ru_2 (at.%) after 100 h oxidation in air at 1350°C.

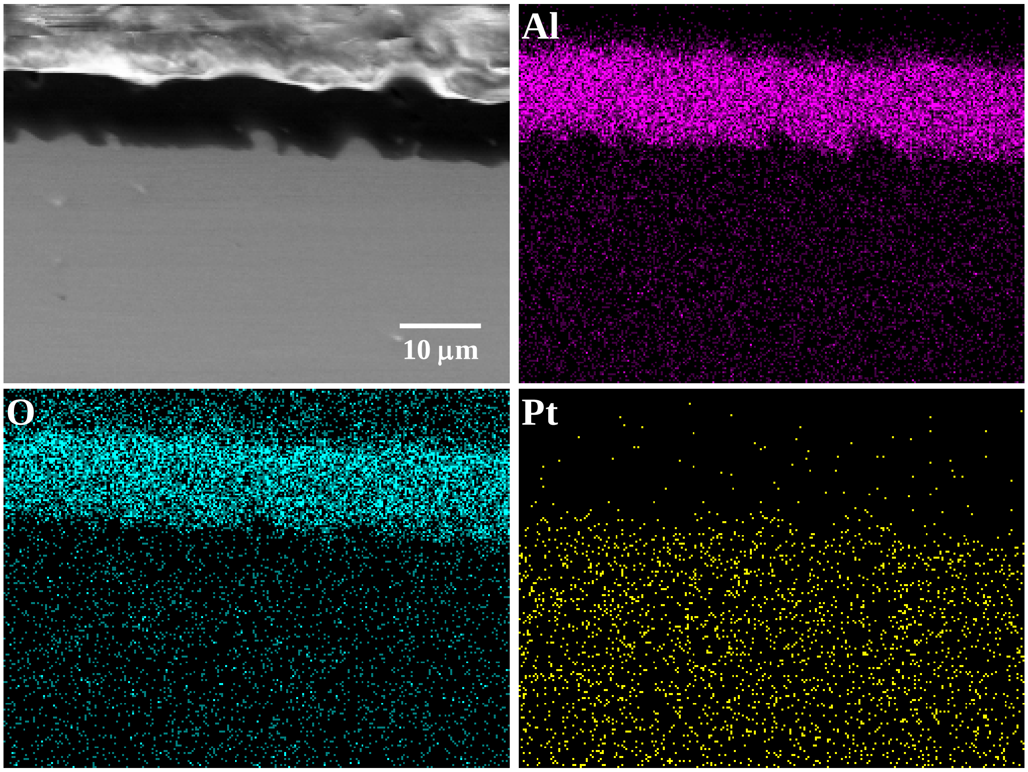

Figure 4.43. Cross-sectional EDS mapping images of Al, O and Pt of oxide scale (11.79 ± 1.39 μm thick) formed on water-quenched Pt_{84}:Al_{11}:Cr_3:Ru_2 (at.%) after 100 h oxidation in air at 1350°C.

Figure 4.44 shows the FIB-SEM images of the cross section oxide scales on the water-quenched specimens after oxidation in air at 1350°C, for up to 100 hours, which revealed that the scales were non-uniform in thickness with some porosity. Some of the pores were rounded while some look like microcracks. There was no apparent formation of void at the scale-alloy interface. No internal oxidation was also observed. The height of the protrusions and intrusions of the scales increased with increased oxidation times. Substrate enclosure within the scales was observed to be more pronounced as the protrusions of the substrate alloy into the scale became deeper.

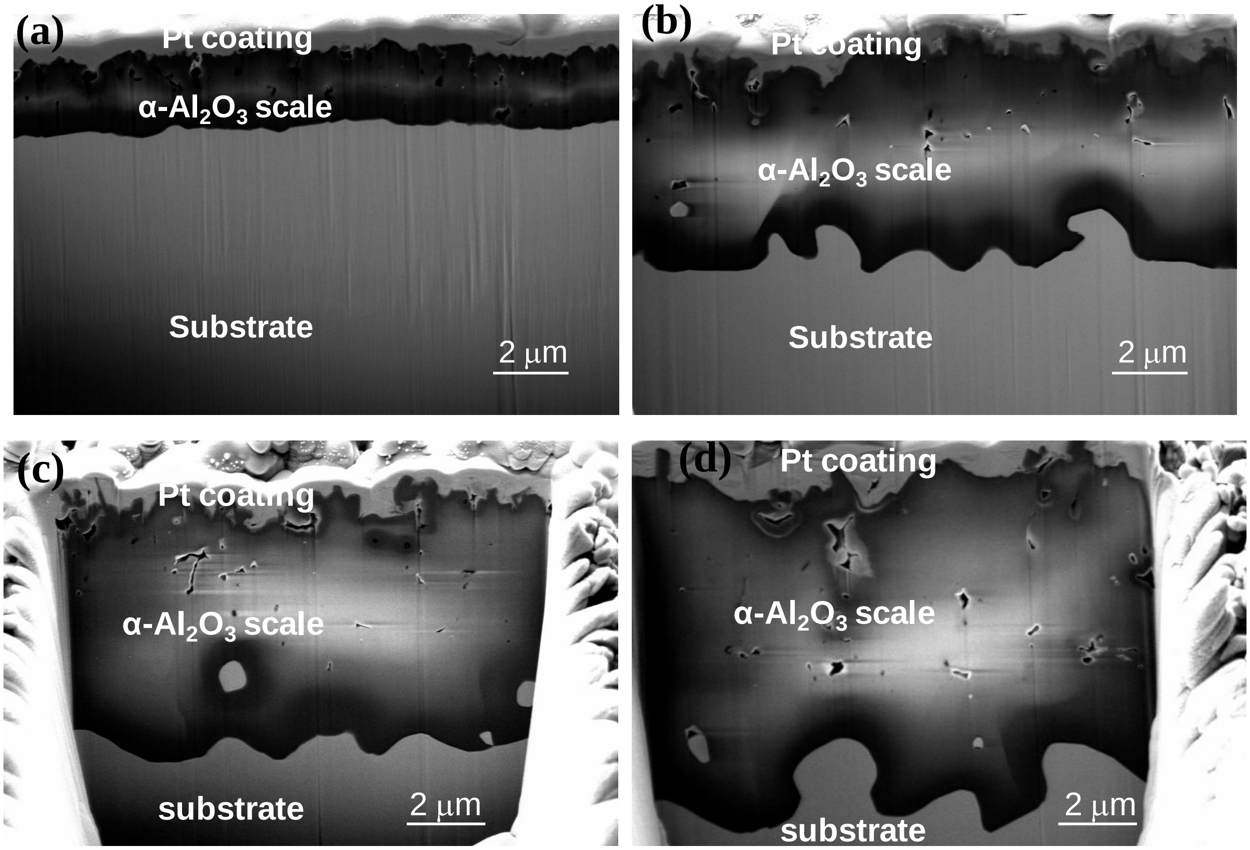

Figure 4.44. FIB-SEM cross-sectional images of oxide scales on water-quenched Pt_{84}:Al_{11}:Cr_3:Ru_2 (at.%) after oxidation in air at 1350°C for : (a) 1 h (b) 10 h (c) 50 h (d) 100 h.

4.4.2 Air-cooled Specimens

The morphological features of the cross sections of the scales on the air-cooled specimens were similar to those of water-quenched specimens. However, the scales on the air-cooled specimens were mostly thicker. The scales formed on the air-cooled specimens were also well-adhering to the substrate, with no evidence of spallation. The cross-section of the oxide scale after 1 hour oxidation at 1150°C revealed that the thickness of the scale was average ~0.88 µm, and increased with increased oxidation times (Figure 4.45 and Table 4.8). Above 10 hours at all oxidation temperatures, the error bars were larger as a result of increased oxide scale protrusions/intrusions. Figures 4.46-4.48 show the SEM images of the cross-sections of the oxide scales after different exposure temperatures and times. The protrusions of the alloy into the scale at the scale-alloy interface, as well as protrusions of the scales at the scale-gas interface increased with increased oxidation times across the investigated temperatures. The protrusions were more pronounced at longer exposure times at higher oxidation temperatures (Figures 4.46b, 4.47 and 4.48). The Pt-rich crystals could be causing the protuberances noted in the cross-sections. There was no discernable formation of voids at the scale-alloy interface or any internal oxidation. However, few pores were observed close to the scale-gas interface, especially after longer exposure times at 1350°C.

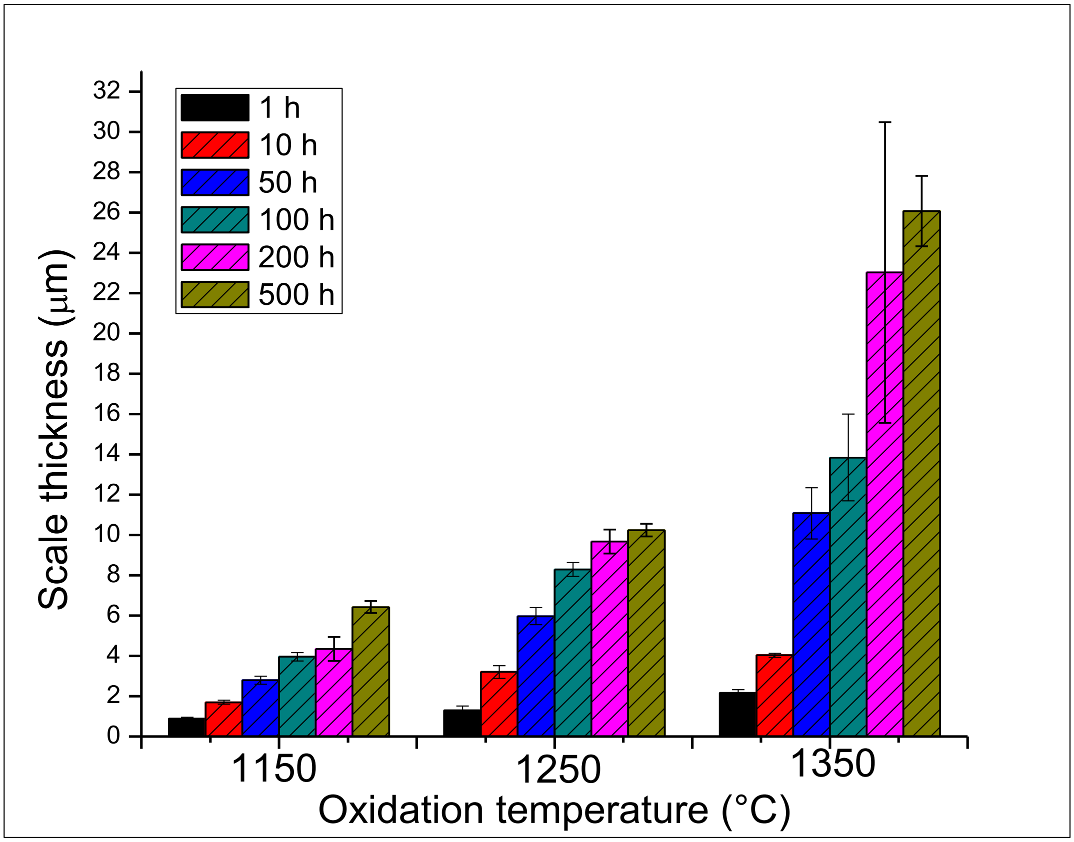

Figure 4.45. Effect of exposure temperature and time on scale thickness of air-cooled Pt_{84}:Al_{11}:Cr_3:Ru_2 (at.%) specimens after isothermal oxidation in air at between 1150°C-1350°C.

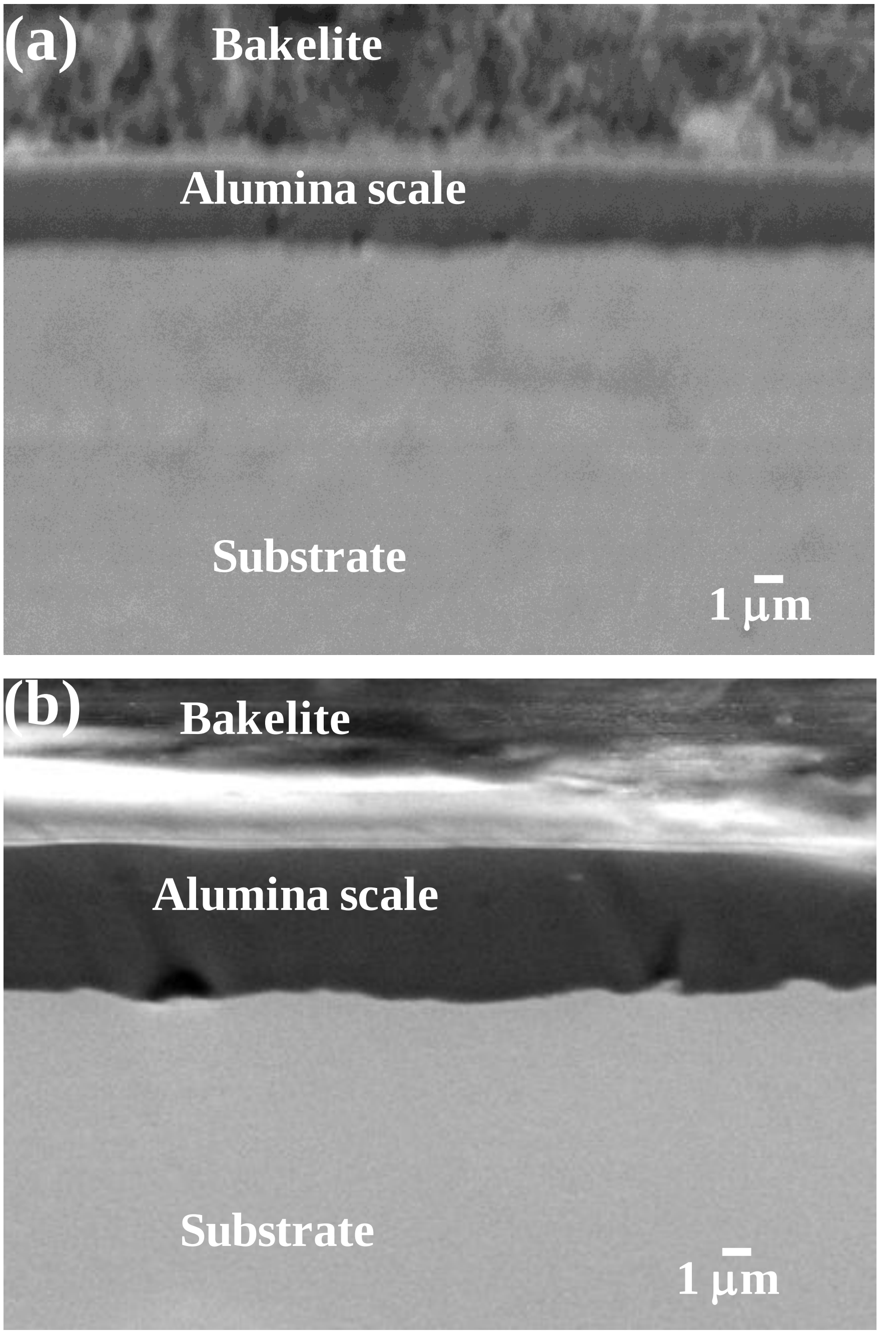

Figure 4.46. SEM-SE cross-sectional image of oxide scale on air-cooled Pt_{84}:Al_{11}:Cr_3:Ru_2 (at.%) after oxidation in air at 1150°C for : (a) 50 h (b) 500 h.

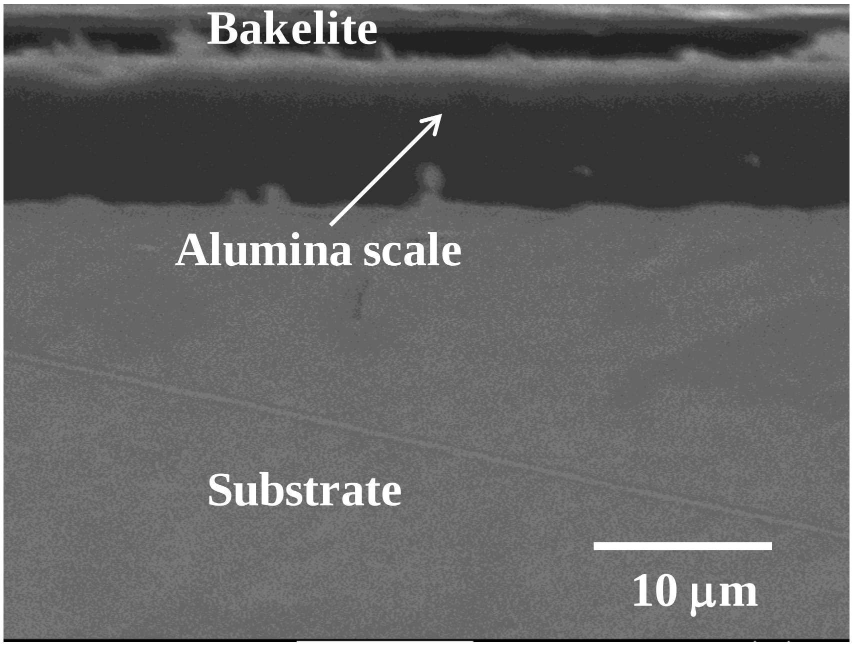

Figure 4.47. SEM-SE cross-sectional image of oxide scale on air-cooled Pt_{84}:Al_{11}:Cr_3:Ru_2 (at.%) after 100 h oxidation in air at 1250°C.

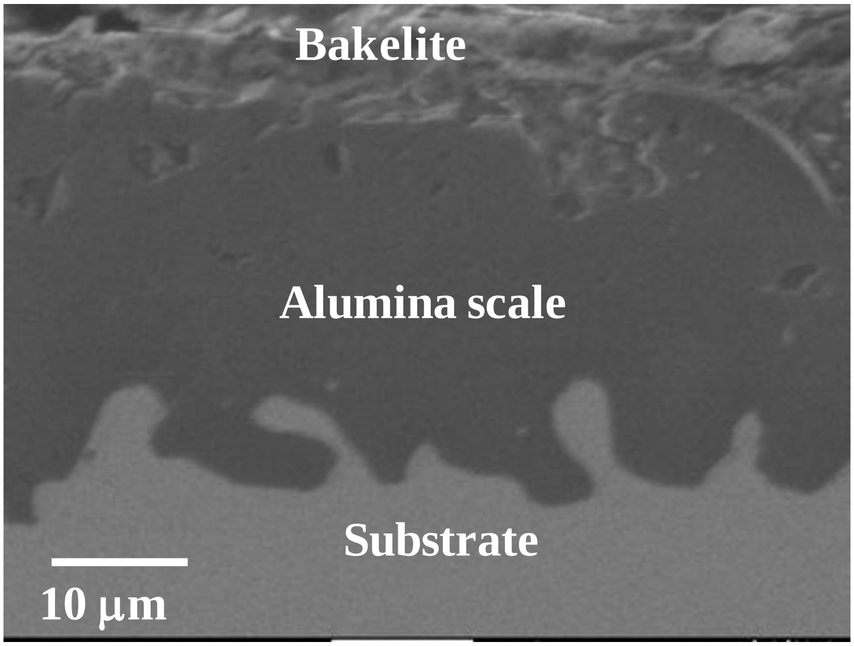

Figure 4.48. SEM-SE cross-sectional image of oxide scale on air-cooled Pt_{84}:Al_{11}:Cr_3:Ru_2 (at.%) after 200 h oxidation in air at 1350°C.

Table 4.8. Thickness values obtained from air-cooled Pt_{84}:Al_{11}:Cr_3:Ru_2 (at.%) specimens after oxidation in air at 1150, 1250 and 1350°C, for up to 500 h.

Oxidation time (hours)	**Scale thickness (μm)**		
	1150°C	**1250°C**	**1350°C**
1	0.88 ± 0.08	1.29 ± 0.22	2.16 ± 0.17
10	1.7 ± 0.10	3.2 ± 0.32	5.32 ± 0.10
50	2.79 ± 0.20	5.97 ± 0.43	11.07 ± 1.27
100	3.96 ± 0.21	8.29 ± 0.34	13.84 ± 2.15
200	4.34 ± 0.55	9.67 ± 0.60	23.02 ± 7.46
500	6.42 ± 0.30	10.24 ± 0.32	26.06 ± 1.75

X-ray elemental maps (Figure 4.49) were used to verify the scale layer content, and revealed the presence of Al and O, as well as regions of oxide extension (oxide ridges) into the substrate (shown by arrows in Figure 4.49). The alloy substrate was rich in Pt, which is the base metal, with homogenuous distribution of small amounts of Al and O. However, the maps showed apparent depletion of Al at the scale-substrate. The X-ray maps also showed that the scale layer contained small amount of Pt. However, the effect of charging affected the constrast at the interfaces, with some appeared darker (Figure 4.46b), and some blurred (Figures 4.46 and 4.49).

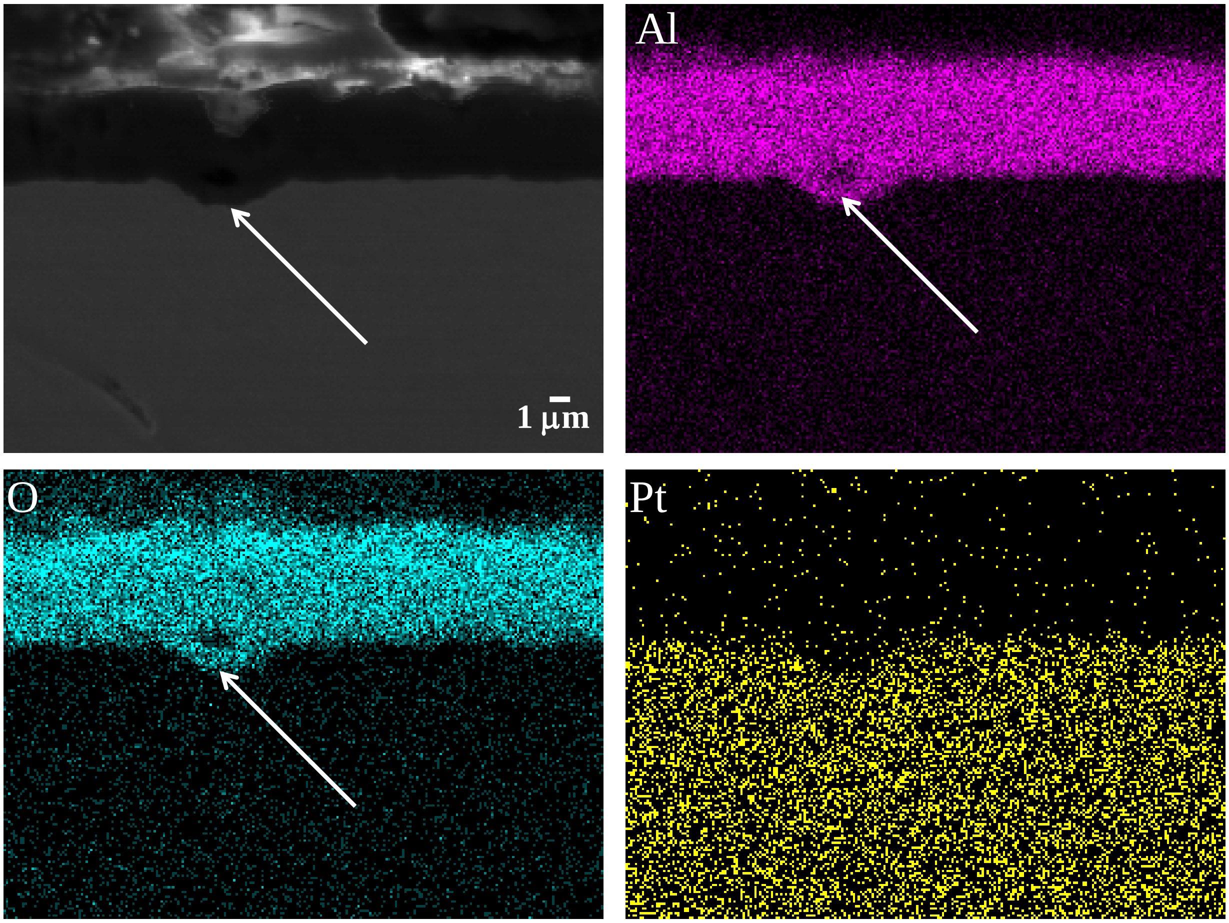

Figure 4.49. Cross-sectional EDS mapping images of Al, O and Pt of oxide scale (4.34 ± 0.55 µm thick) on air-cooled Pt_{84}:Al_{11}:Cr_3:Ru_2 (at.%) after 200 h oxidation in air at 1150°C, (arrow shows oxide ridges at scale-alloy interface).

4.5 X-ray Diffraction Analysis

4.5.1 Water-quenched Specimens

Figures 4.50-4.52 show the XRD patterns of the surfaces of the specimens after isothermal oxidation in air at 1150°C, 1250°C and 1350°C for various time intervals up to 100 h. The major phase of the oxide scales is α-Al_2O_3 (corundum) and the intensity of its peaks increased with increased exposure times, which showed that the alumina scale became thicker and covered the entire specimen surface area. Peaks corresponding to (Pt) matrix and $L1_2$-Pt_3Al phases were also detected. However, the intensities of these peaks decreased with increasing exposure times, due to increased scale thicknesses. Some of the weaker peaks observed after early oxidation times up to 10 h correspond to peaks of PtO_2 and CrO_3.

The diffraction patterns of all the specimens at all oxidation temperature and times were similar with only difference in the intensities of the peaks. At 1150°C, strong peaks corresponding to (Pt) matrix and $L1_2$-Pt_3Al phases was observed (at $2\theta = 46°$) after 1 h oxidation, whereas the intensities of the peaks of these phases after oxidation for the same time at 1250°C and 1350°C was very weak.

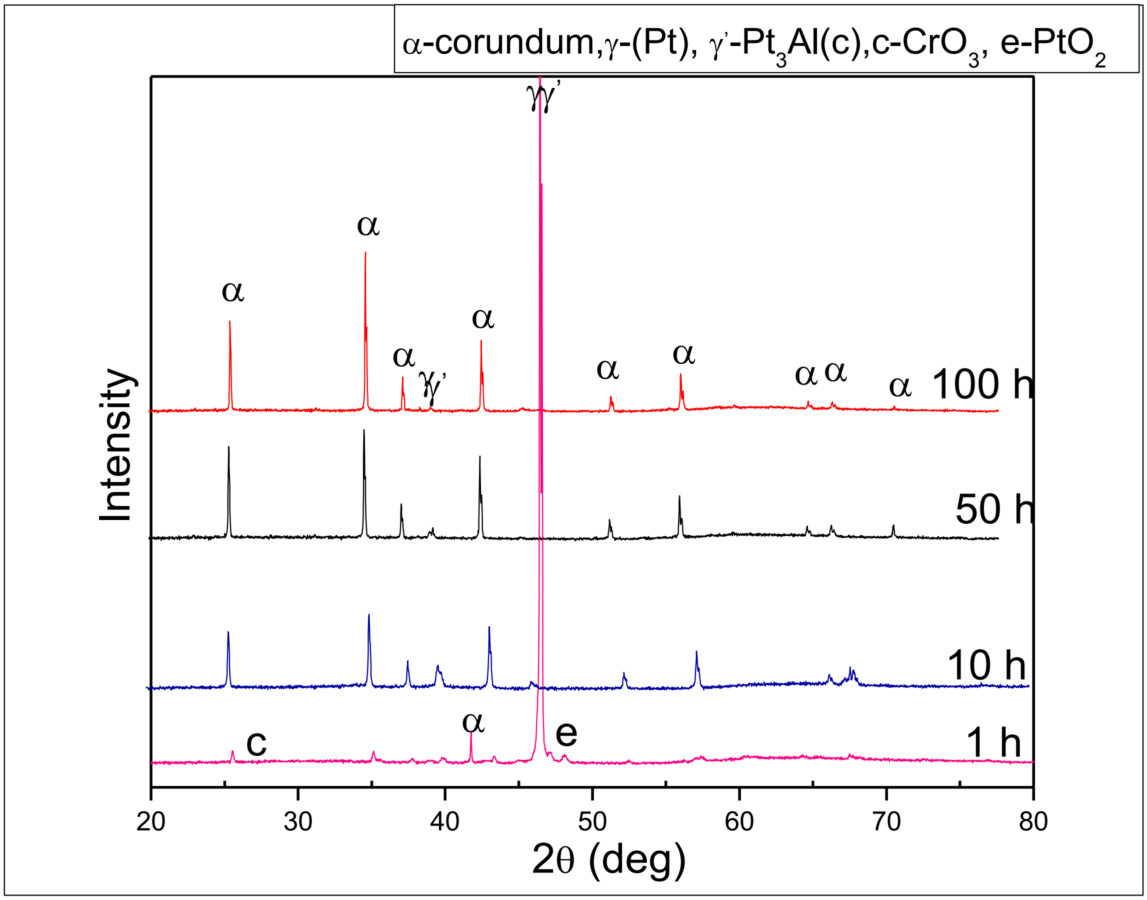

Figure 4.50. XRD patterns of water-quenched Pt_{84}:Al_{11}:Cr_3:Ru_2 (at.%) specimens after isothermal oxidation in air at 1150°C for up to 100 h.

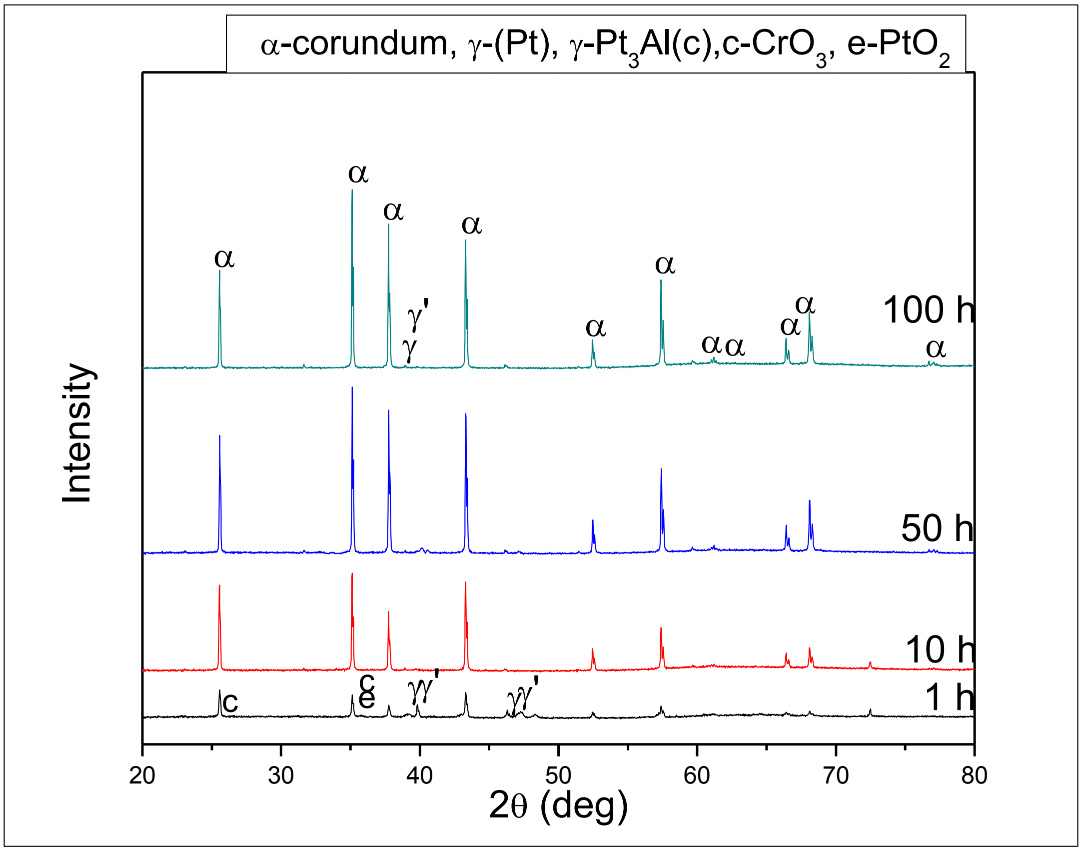

Figure 4.51. XRD patterns of water-quenched Pt_{84}:Al_{11}:Cr_3:Ru_2 (at.%) specimens after isothermal oxidation in air at 1250°C for up to 100 h.

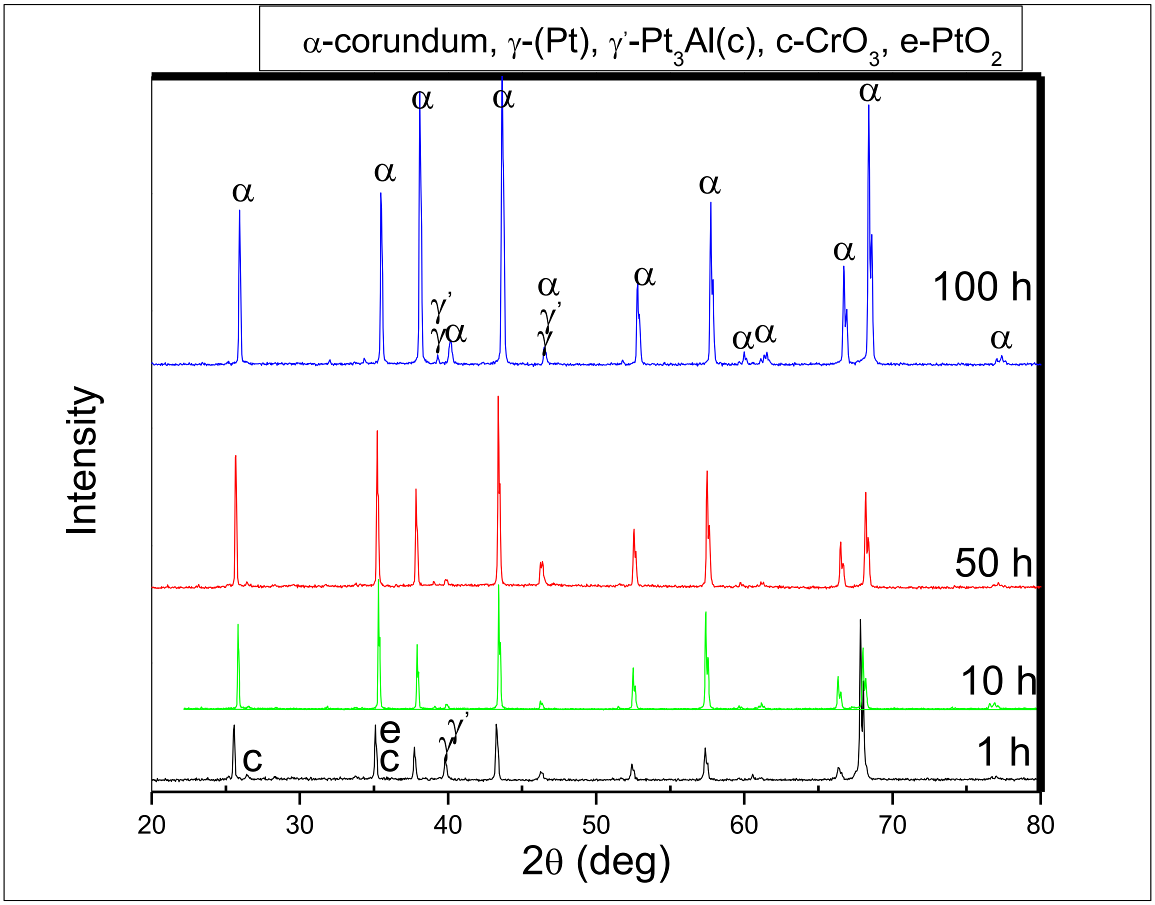

Figure 4.52. XRD patterns of water-quenched Pt_{84}:Al_{11}:Cr_3:Ru_2 (at.%) specimens after isothermal oxidation in air at 1350°C for up to 100 h.

4.5.2 Air-cooled Specimens

XRD patterns of all the specimens after oxidation in air at 1150°C -1350°C for up to 500 hours are presented in Figures 4.53-4.55. It is evident that the oxide scales have α-Al_2O_3 (corundum) as the principal phase, and the alumina peak intensities increased with increased exposure times across the oxidation temperatures. Diffraction peaks corresponding to (Pt) matrix and $L1_2$-Pt_3Al phases were also found, even at longer times. However, the intensities of these peaks decreased with increased exposure time, presumably due to the increase in oxide scale thicknesses. These observations are similar to results obtained from the water-quenched specimens. Very low intensities peaks of PtO_2 and CrO_3 were observed at exposure times up to 10 h.

High intensity peaks corresponding to (Pt) and ~Pt_3Al ($L1_2$) from the substrate were observed at 2θ ≈ 46° after 1 h. At 10 h oxidation at 1150°C the peak at 2θ ≈ 46° was still strong, although slightly reduced, whereas that at 2θ ≈ 40° was barely discernable. At 1250°C and 1 hour oxidation, the γ/γ' peak at 2θ ≈ 46° was very small, whereas that at 2θ ≈ 40° was very large. The smaller peak had gone after 10 hours, whereas the larger peak had mostly disappeared at 50 hours. At 1350°C, γ/γ' peak was observed at 2θ ≈ 68° along with alumina peak, and all the γ/γ' peaks soon disappeared. The diffraction patterns after 10 hours exposure at 1250°C and 1350°C were broad, while slight peak shift was noticed after the same time at 1150°C.

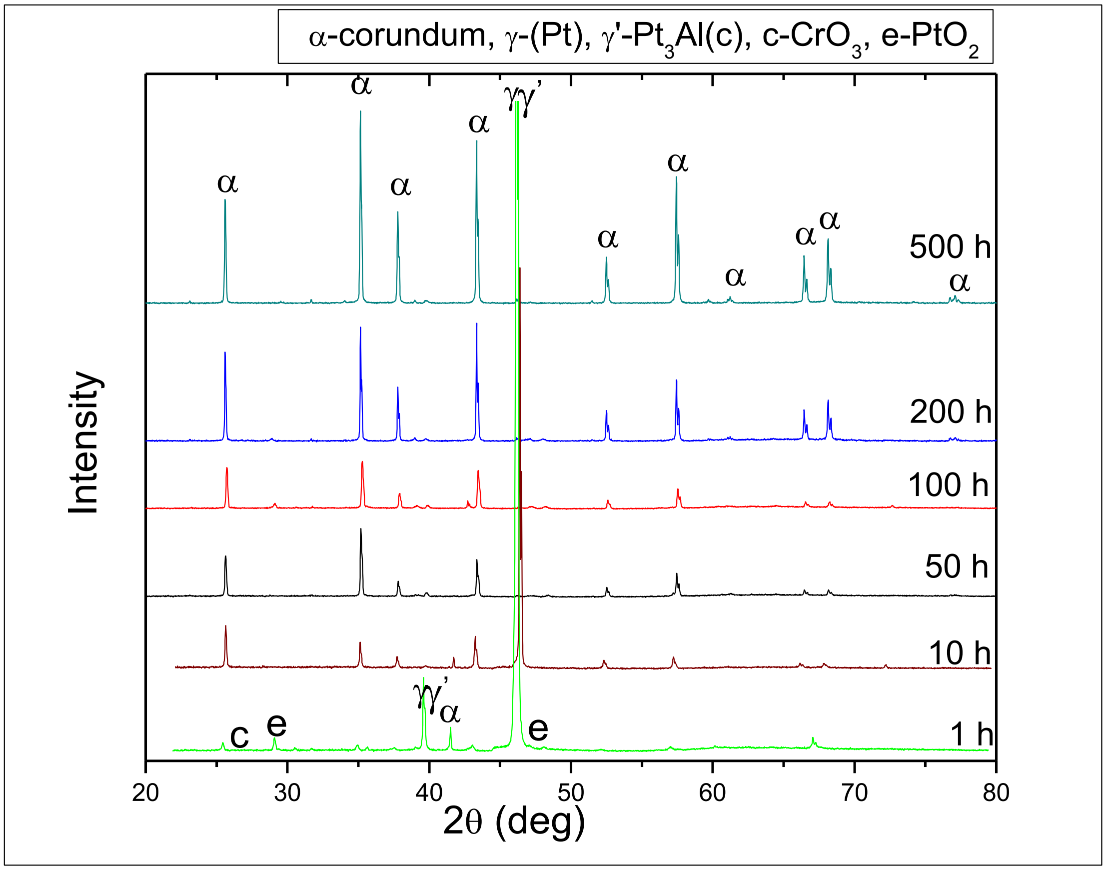

Figure 4.53. XRD patterns of air-cooled Pt_{84}:Al_{11}:Cr_3:Ru_2 (at.%) specimens after isothermal oxidation in air at 1150°C for up to 500 h.

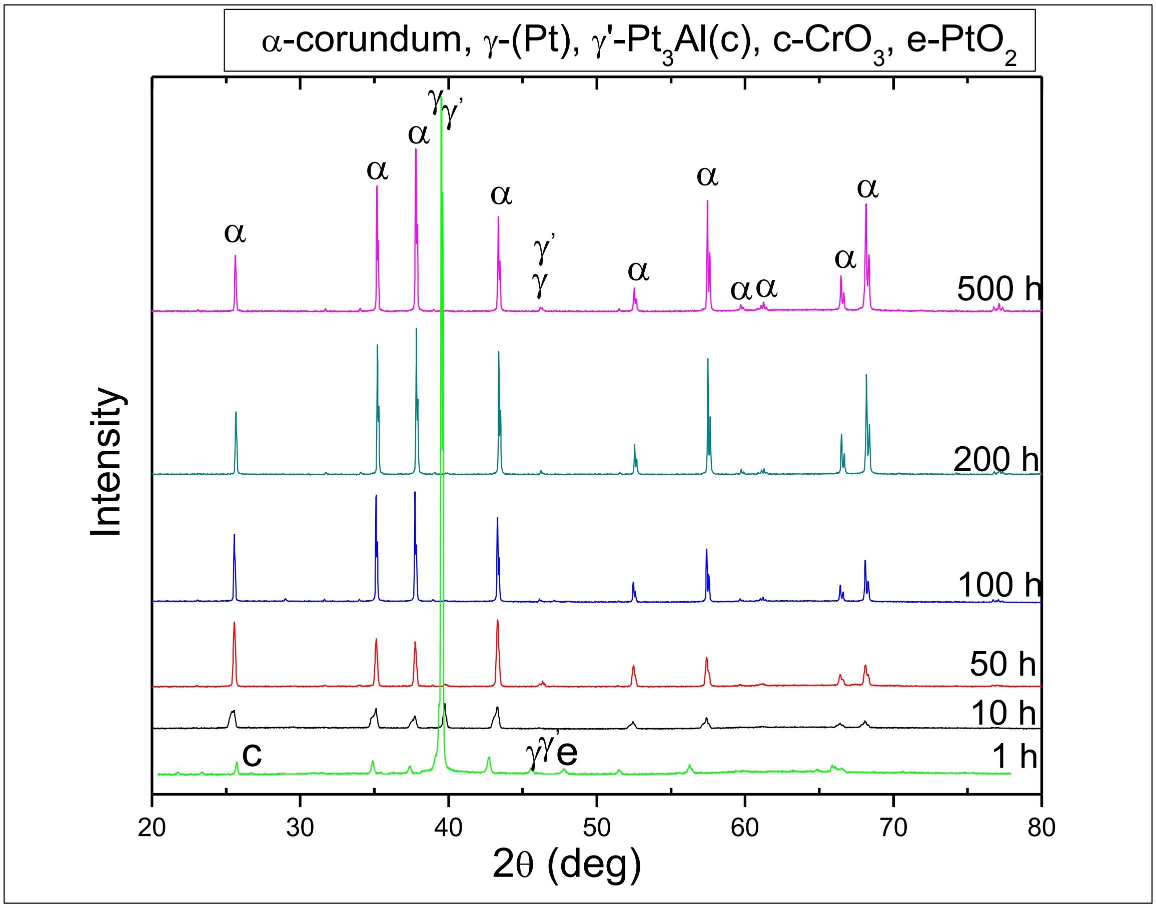

Figure 4.54. XRD patterns of air-cooled Pt_{84}:Al_{11}:Cr_3:Ru_2 (at.%) specimens after isothermal oxidation in air at 1250°C for up to 500 h.

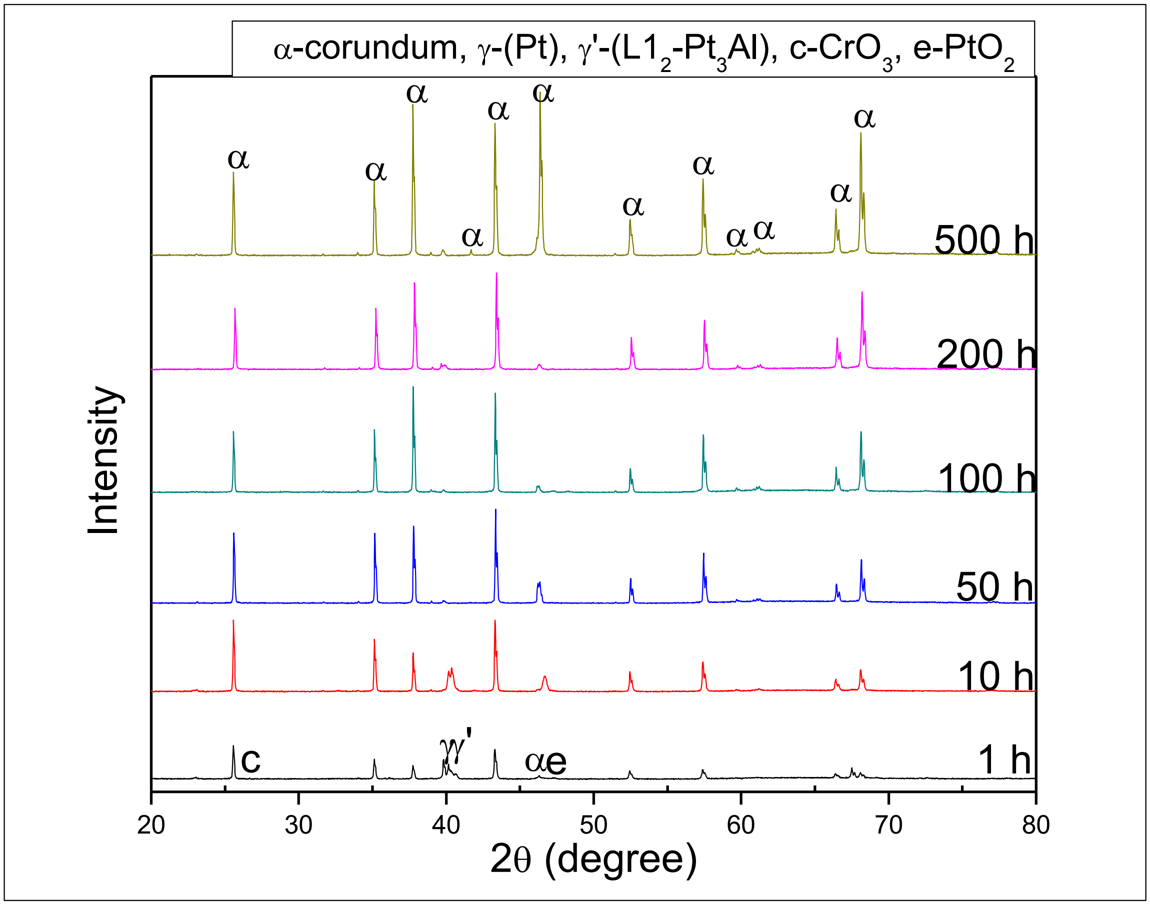

Figure 4.55. XRD patterns of air-cooled Pt_{84}:Al_{11}:Cr_3:Ru_2 (at.%) specimens after isothermal oxidation in air at 1350°C for 500 h.

4.6. Raman Spectroscopy Analysis

4.6.1 Water-quenched Specimens

The Raman spectra of water-quenched specimens are shown in Figures 4.56-4.58, which revealed the presence of corundum (α-Al_2O_3) on all the specimens. The peak intensities of the corundum increased with increased exposure time across the oxidation temperatures. At all exposure times and temperature, the peak at wavenumber 417.4 cm^{-1}, corresponding to the strongest corundum (α-Al_2O_3) peak, was also identified as the strongest peak. No peaks matching other phases, such as PtO_2 or CrO_3 were observed. This may be due to their very low concentrations in the scales. The low depth of penetration of the Ar+ laser probe, 500 nm – 1000 nm [2008Brã], may also be responsible.

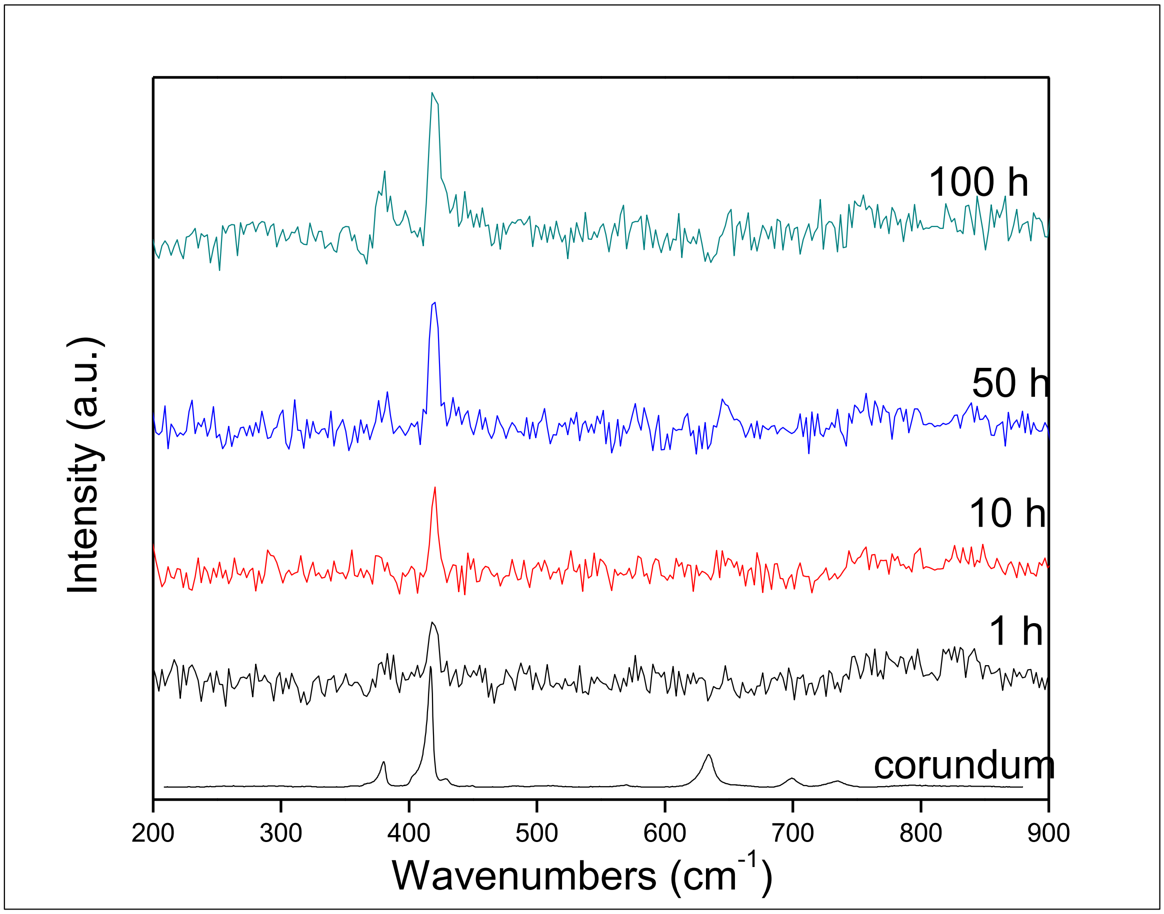

Figure 4.56. Raman spectra of the oxide scales formed on water-quenched Pt_{84}:Al_{11}:Cr_3:Ru_2 (at.%) specimens after isothermal oxidation in air at 1150°C for up to 100 h.

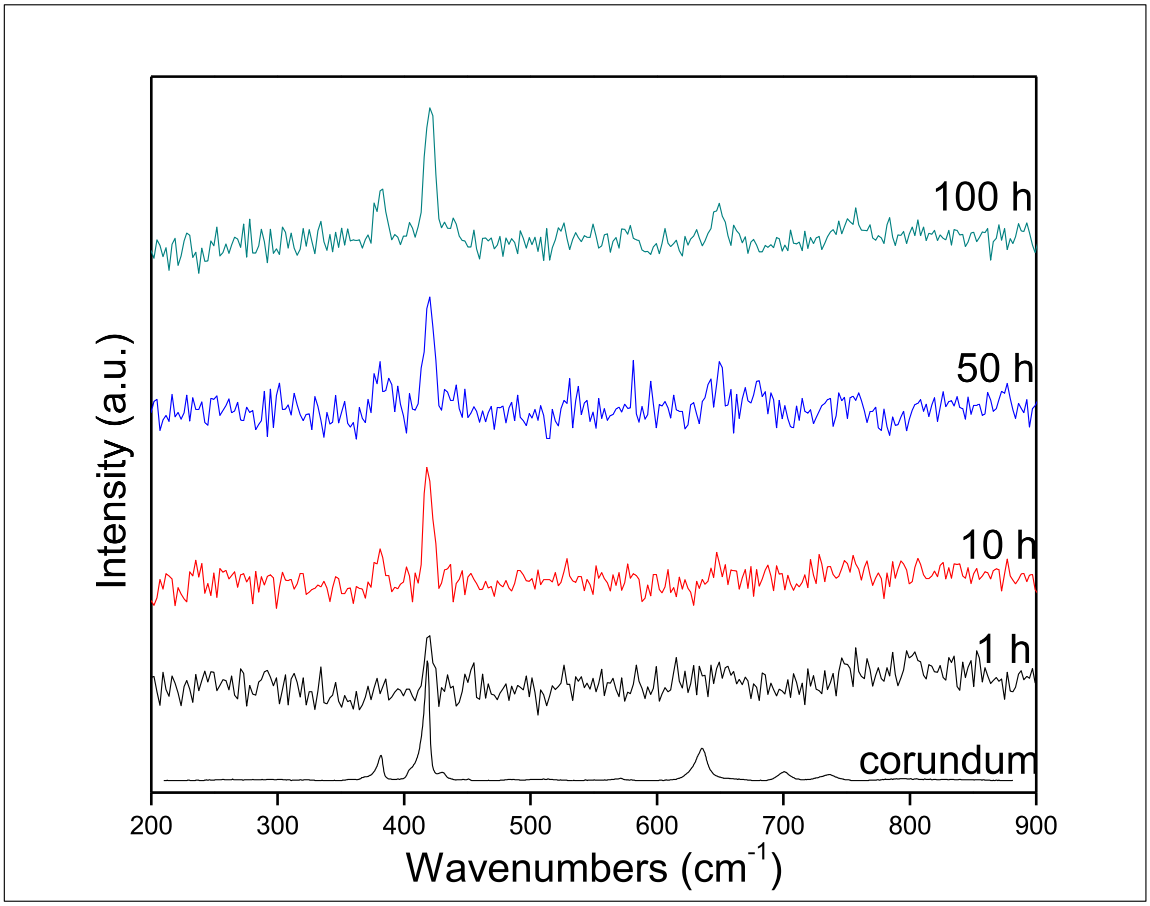

Figure 4.57. Raman spectra of the oxide scales formed on water-quenched Pt_{84}:Al_{11}:Cr_3:Ru_2 (at.%) specimens after isothermal oxidation in air at 1250°C for up to 100 h.

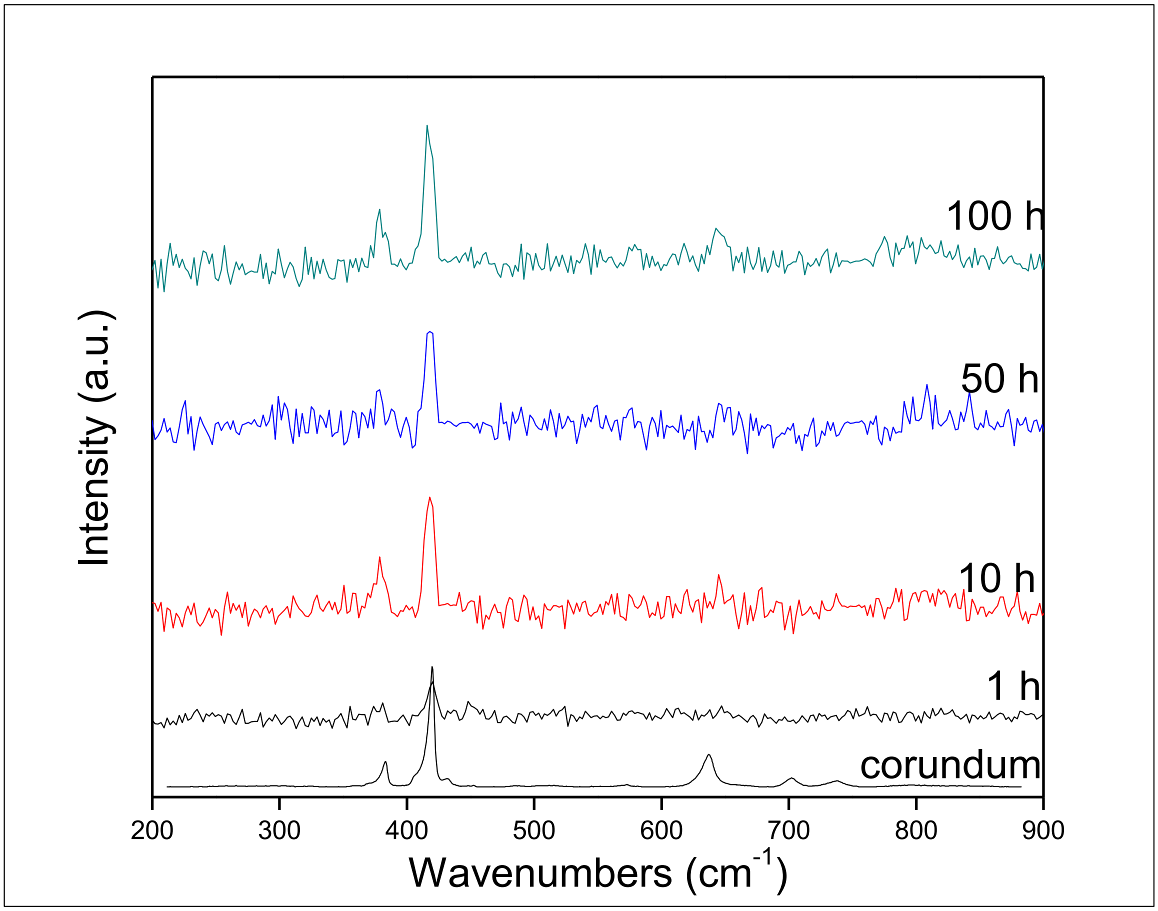

Figure 4.58. Raman spectra of the oxide scales formed on water-quenched Pt_{84}:Al_{11}:Cr_3:Ru_2 (at.%) specimens after isothermal oxidation in air at 1350°C for up to 100 h

4.6.2 Air-cooled Specimens

The Raman spectra of air-cooled alloy specimens were similar to those of the water-quenched specimens. Figures 4.59-4.61 show the Raman spectra of the oxide scales on the air-cooled specimens isothermally oxidised at 1150°C, 1250°C and 1350°C for various time intervals up to 500 h in air, which revealed the presence of corundum (α-Al_2O_3) at all exposure times. The intensities of the corundum peaks increased with increased exposure times across the oxidation temperatures, indicating increased scale thickness. The peak at wavenumber 417.4 cm^{-1}, corresponding to the strongest peak in the reference corundum, was also detected as the strongest peak. Again, no peaks matching PtO_2 or CrO_3 were detected. This may also be due to their low concentrations in the scales or the depth of penetration of the Ar^+ laser probe.

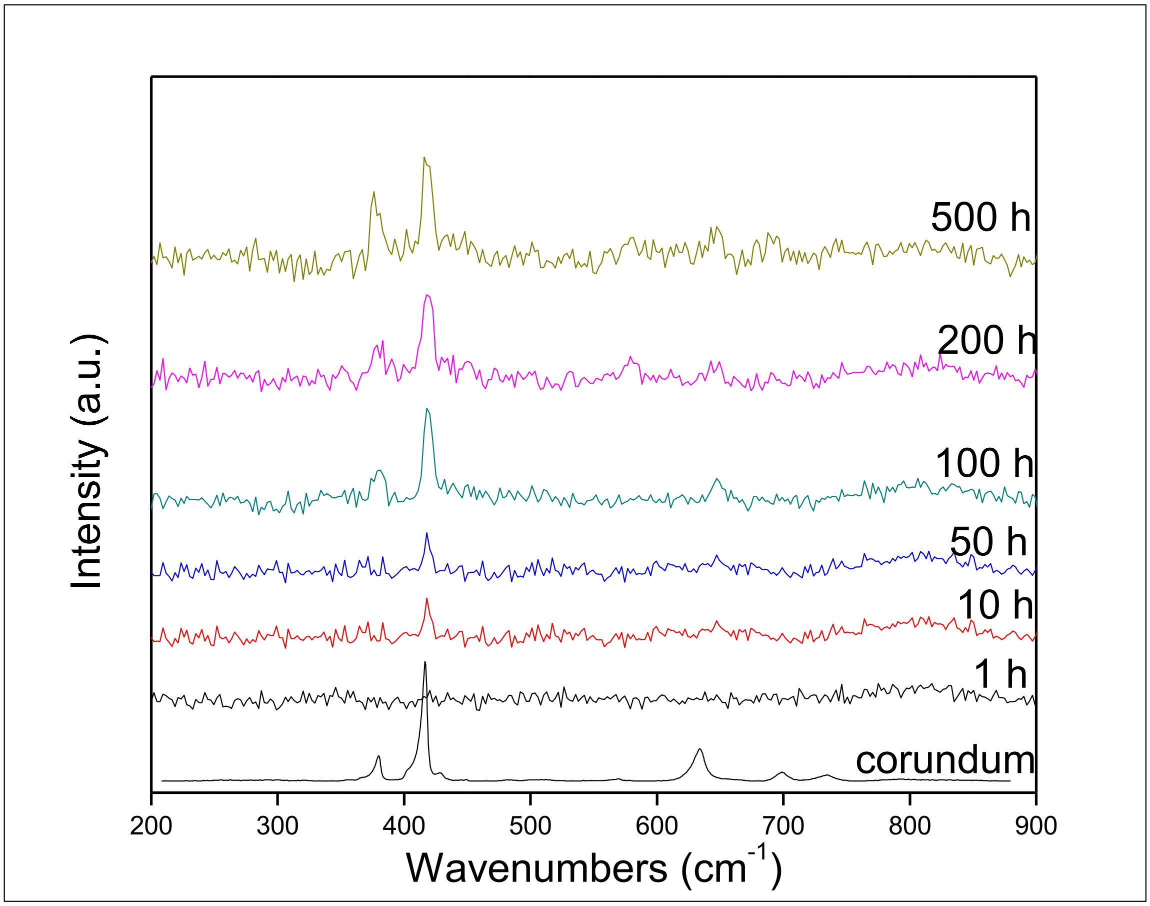

Figure 4.59. Raman spectra of the oxide scales formed on air-cooled Pt_{84}:Al_{11}:Cr_3:Ru_2 (at.%) specimens after isothermal oxidation in air at 1150°C for up to 500 h.

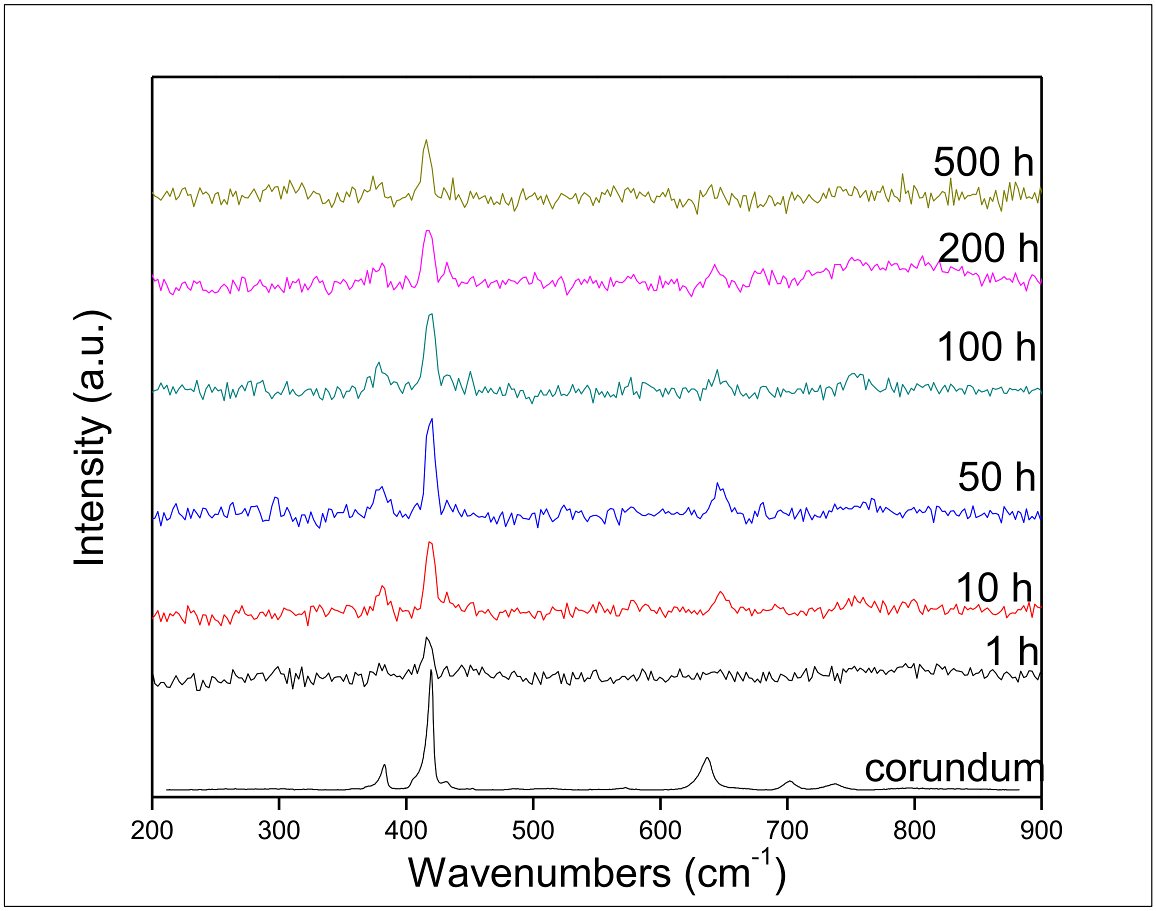

Figure 4.60. Raman spectra of the oxide scales formed on air-cooled Pt_{84}:Al_{11}:Cr_3:Ru_2 (at.%) specimens after isothermal oxidation in air at 1250°C for up to 500 h.

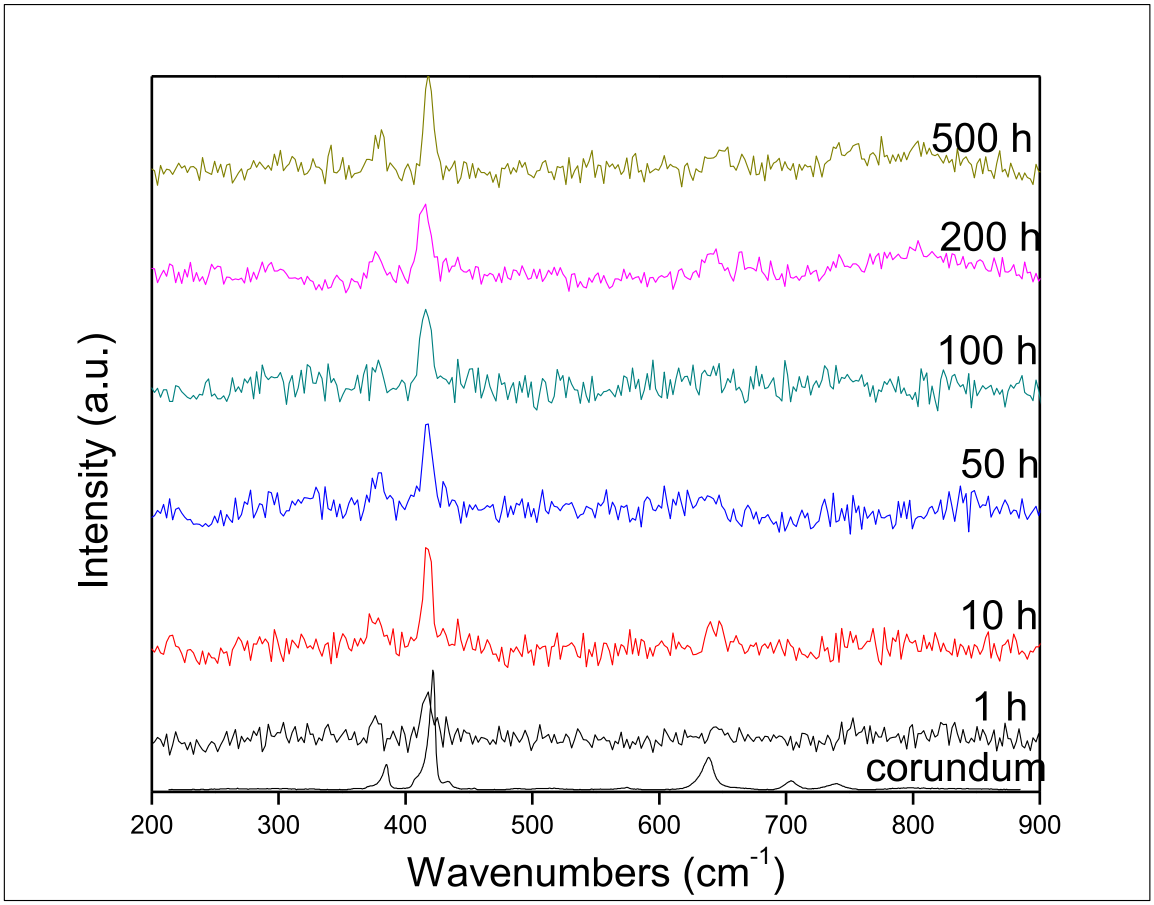

Figure 4.61. Raman spectra of the oxide scales formed on air-cooled Pt_{84}:Al_{11}:Cr_3:Ru_2 (at.%) specimens after isothermal oxidation in air at 1350°C for up to 500 h.

4.7 Stress Measurements

4.7.1 Water-quenched Specimens

Luminescence spectra were acquired from five randomly selected spots for each oxidized specimen surface. Figures 4.62-4.64 show the R-line luminescence spectra from the scales of the water-quenched Pt_{84}:Al_{11}:Cr_3:Ru_2 (at.%) specimens after oxidation at 1150°C-1350°C for up to 100 h in air. At all exposure times, strong R-line luminescence signals were obtained. The luminescence lines had shifted and broadened with respect to the spectrum of the reference stress-free ruby. The R-lines from the oxide scales always shifted to lower frequency, indicating that the scales were under residual compressive stress. The average in-plane stresses were calculated (Table 4.9) using Equation 2.27, and it was assumed that the scales were under biaxial compression. Figure 4.65 shows the room temperature residual stress in the scales of the specimens as a function of oxidation time throughout the exposure temperatures. Within the errors, the compressive residual stresses in the oxide scales became nearly constant above 10 hours exposure, at all oxidation temperatures. Furthermore, the low standard deviations showed that the room temperature compressive residual stresses at different spots on the scales were nearly constant. The stress after 1 hour oxidation at 1150°C was less than those at 1250°C and 1350°C. The stress increased after 1 hour exposure at 1150°C, then decreased before reaching a plateau, whereas at 1250°C and 1350°C, the stresses gradually decreased before nearing a constant.

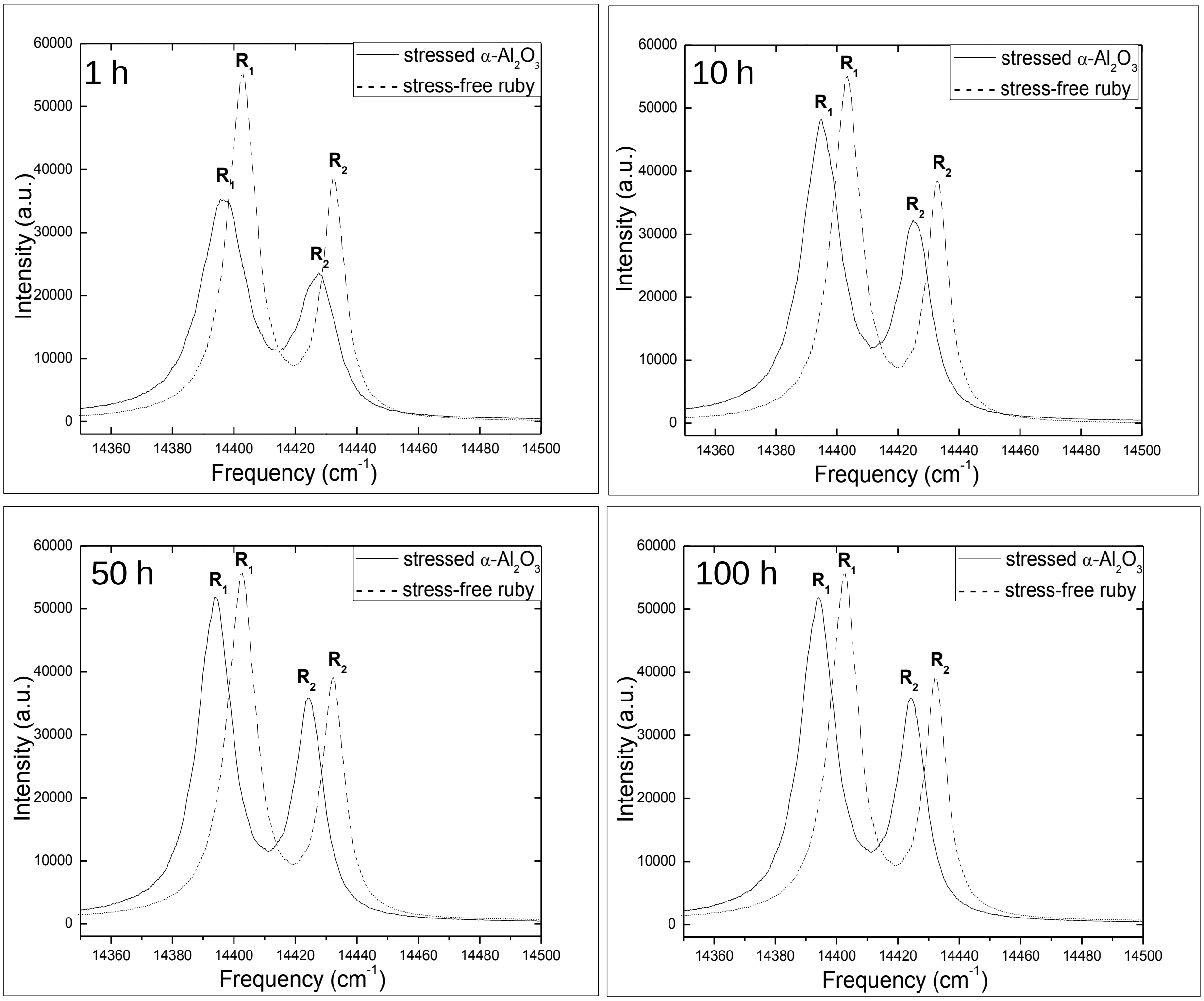

Figure 4.62. Luminescence spectra obtained from the stress-free ruby and oxide scales on water-quenched Pt_{84}:Al_{11}:Cr_3:Ru_2 (at.%) specimens after oxidation in air at 1150°C up to 100 h.

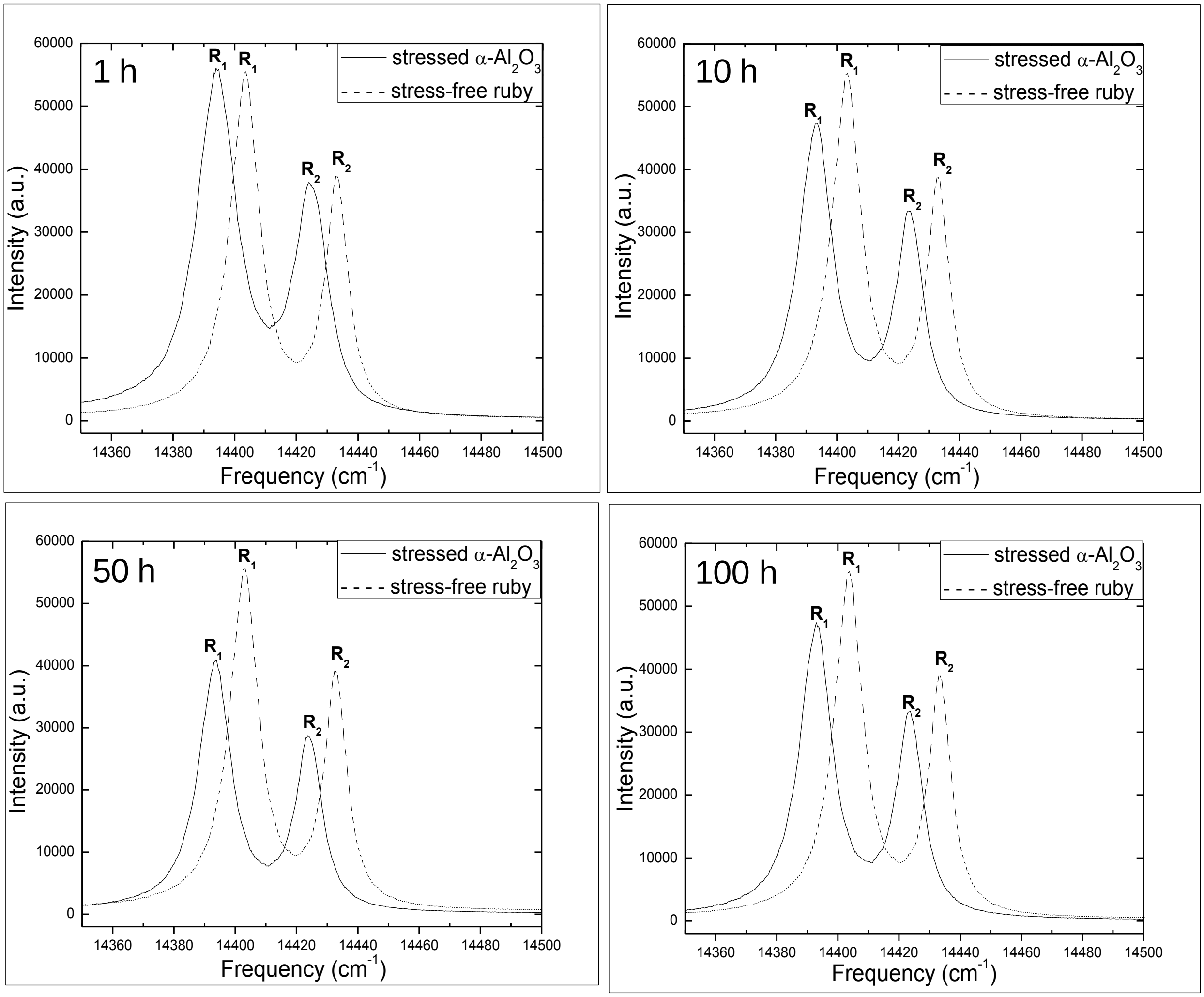

Figure 4.63. Luminescence spectra obtained from the stress-free ruby and oxide scales on water-quenched Pt_{84}:Al_{11}:Cr_3:Ru_2 (at.%) specimens after oxidation in air at 1250°C up to 100 h.

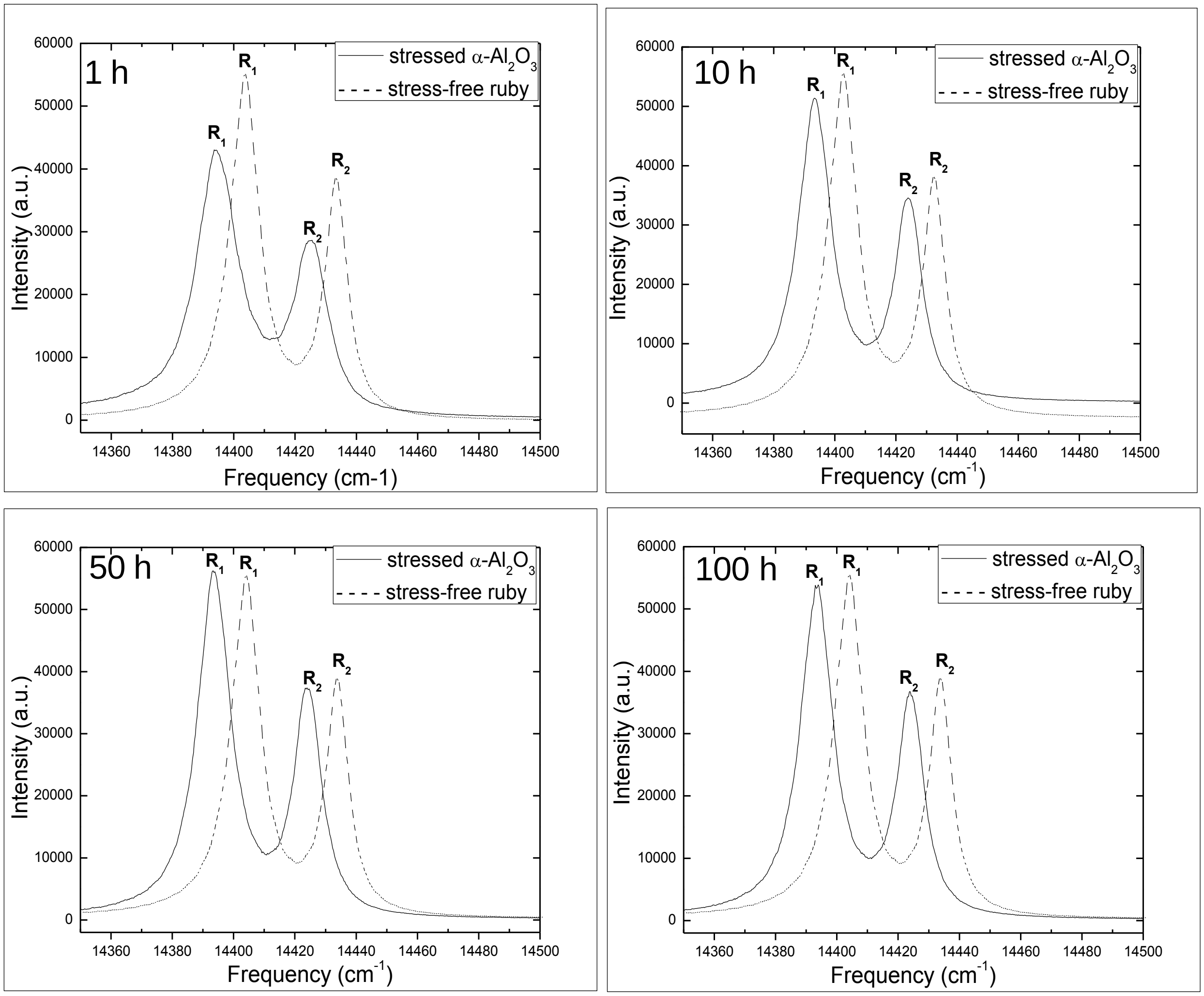

Figure 4.64. Luminescence spectra obtained from the stress-free ruby and oxide scales on water-quenched Pt_{84}:Al_{11}:Cr_3:Ru_2 (at.%) specimens after oxidation in air at 1350°C up to 100 h.

Table 4.9. Mean in-plane compressive stresses and peak widths of the oxide scales formed on water-quenched Pt_{84}:Al_{11}:Cr_3:Ru_2 (at.%) specimens after isothermal oxidation in air up to 100 h.

Oxidation time (hours)	**Mean in-plane compressive stress (GPa)**			**Mean peak width (cm^{-1})**		
	1150°C	**1250°C**	**1350°C**	**1150°C**	**1250°C**	**1350°C**
1	1.38 ± 0.29	1.81 ± 0.23	2.01 ± 0.14	14.80 ± 0.23	12.68 ± 0.33	13.46 ± 0.18
10	1.78 ± 0.11	1.79 ± 0.16	1.70 ± 0.14	13.06 ± 0.36	10.87 ± 0.34	10.54 ± 0.20
50	1.72 ± 0.16	1.76 ± 0.10	1.66 ± 0.14	11.05 ± 0.16	10.52 ± 0.06	10.66 ± 0.12
100	1.72 ± 0.11	1.76 ± 0.09	1.66 ± 0.24	10.92 ± 0.35	10.49 ± 0.18	10.72 ± 0.31

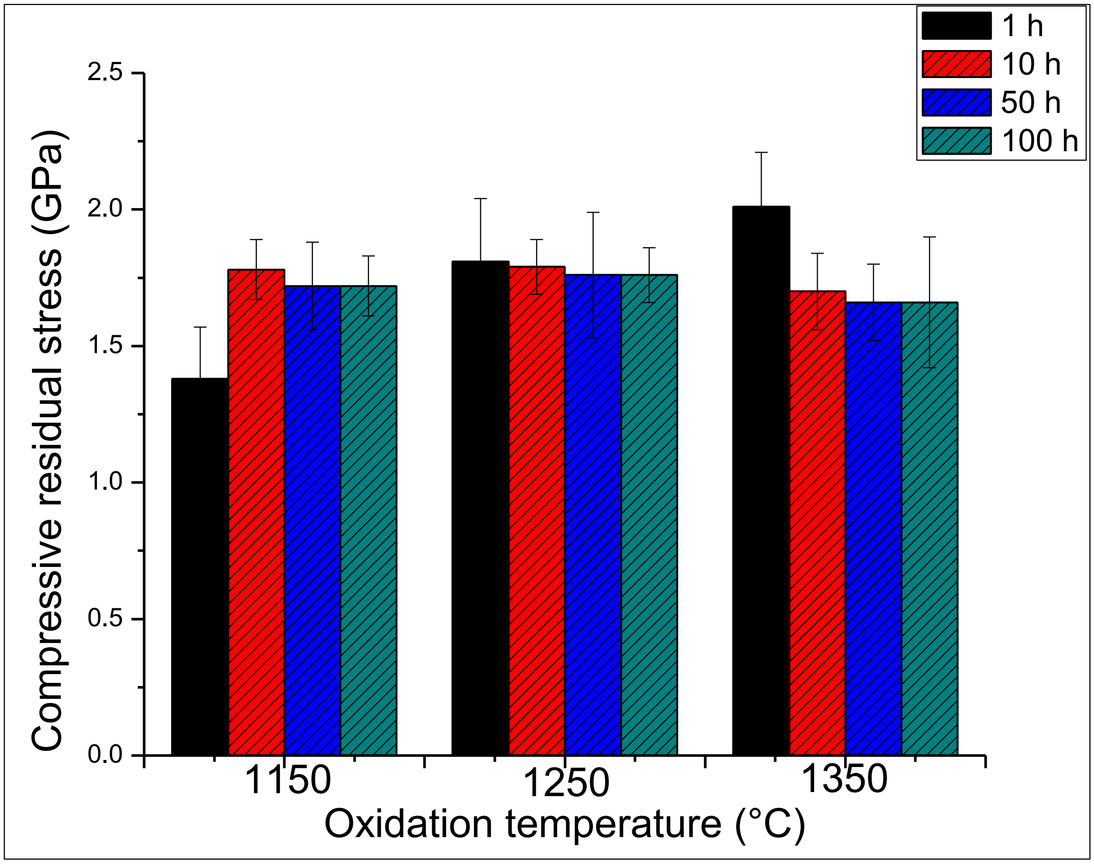

Figure 4.65. Mean stress in the oxide scales on water-quenched Pt_{84}:Al_{11}:Cr_3:Ru_2 (at.%) specimens calculated from the measured frequency shifts of the R2 luminescence line.

The broadening of the R2-line luminescence peak was used to determine the stress gradient through the scale thickness (Figure 4.66). The mean R2-line luminescence peak width for the reference ruby crystal was 9.17 ± 0.03 cm^{-1}, while those from the oxide scales were higher (Table 4.9). At all oxidation temperatures, the peak widths were larger at shorter exposure times when the oxide scales might not have covered the entire specimens' surfaces, and were thus non-uniform, indicating high stress gradients through the volume of the oxide scales. However, as the scale thickened and covered the whole specimens' surfaces with increased oxidation times, the peak width decreased and nearly became uniform above 50 hours oxidation. This indicates that the stress gradients through the volume of the oxide scales probed by the exciting laser also decreased, and then became nearly constant.

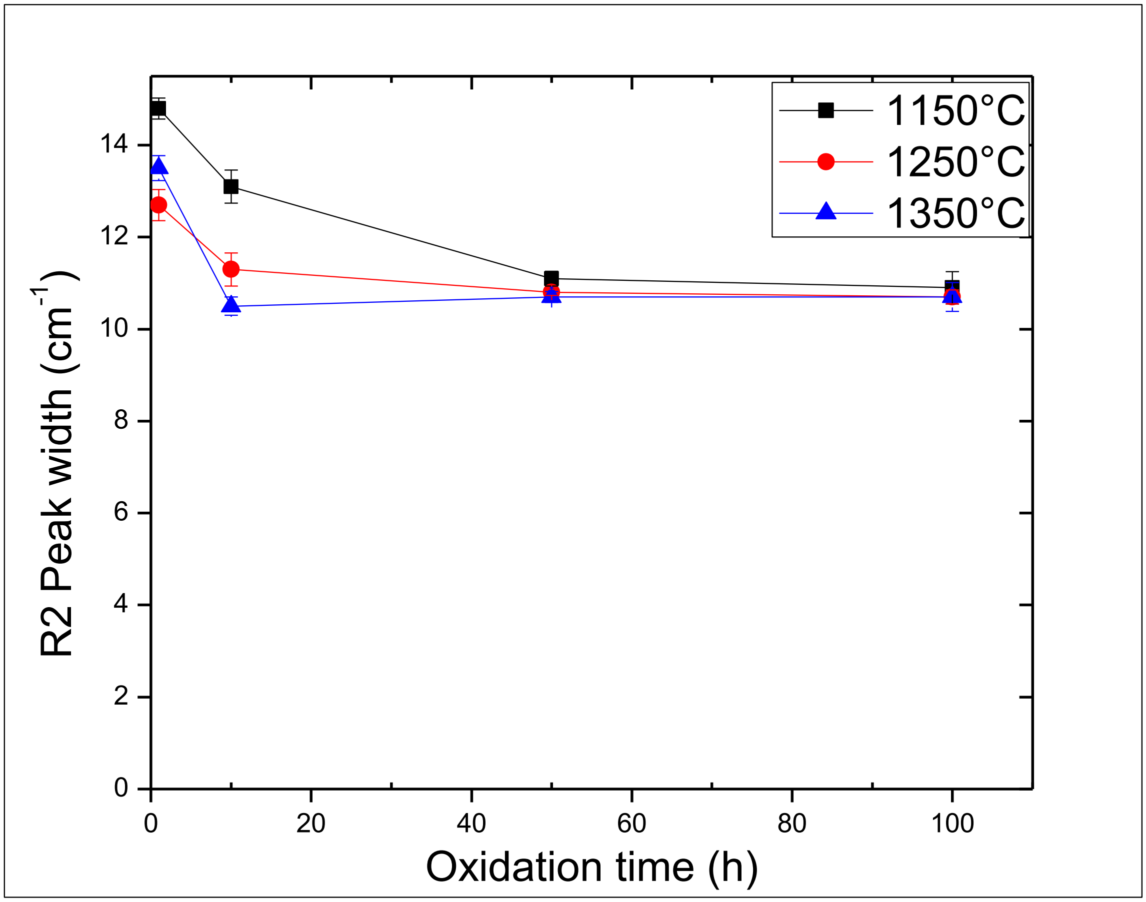

Figure 4.66. Peak widths of the R2 luminescence line showing the stress gradients through the scales thickness on water-quenched Pt_{84}:Al_{11}:Cr_3:Ru_2 (at.%) specimens as a function of oxidation time.

4.7.2 Air-cooled Specimens

Figures 4.67-4.69 show the R-line luminescence spectra from the oxide scales of the air-cooled Pt_{84}:Al_{11}:Cr_3:Ru_2 (at.%) specimens after oxidation at 1150°C-1350°C for up to 500 h in air. At all exposure times, strong R-line luminescence spectra from the oxide scales shifted to lower frequency and broadened with respect to the spectrum of the reference stress-free ruby. The mean residual compressive stresses in the oxide scales were calculated from the frequency shift using Equation 2.27, and are presented in Figure 4.70 and Table 4.10. At 50 hours exposure and above, the compressive stresses in the scales nearly became constant at all investigated temperatures. However, the high errors could be masking the variation before this time. The compressive stress in the scale after 1 hour exposure at 1150°C was the least, while the highest value was measured at 1350°C after the same time. However, the stress in the scale reached a peak after 10 hours exposure at 1150°C, and then decreased before reaching a plateau, whereas the stresses in the scales gradually decreased at 1250°C and 1350°C, and later became constant.

The broadening of the R2-line luminescence peaks was also used to determine the stress gradient through the scale thickness of the air-cooled specimens (Figure 4.71). The stress gradient through the scale decreased with increased exposure times at all oxidation temperatures, although there was a sudden increase in the stress gradient at 200 hours exposure at 1350°C. The high standard deviations during the early stages of oxidation showed that the stress gradients through the scale thickness at different spots were quite different.

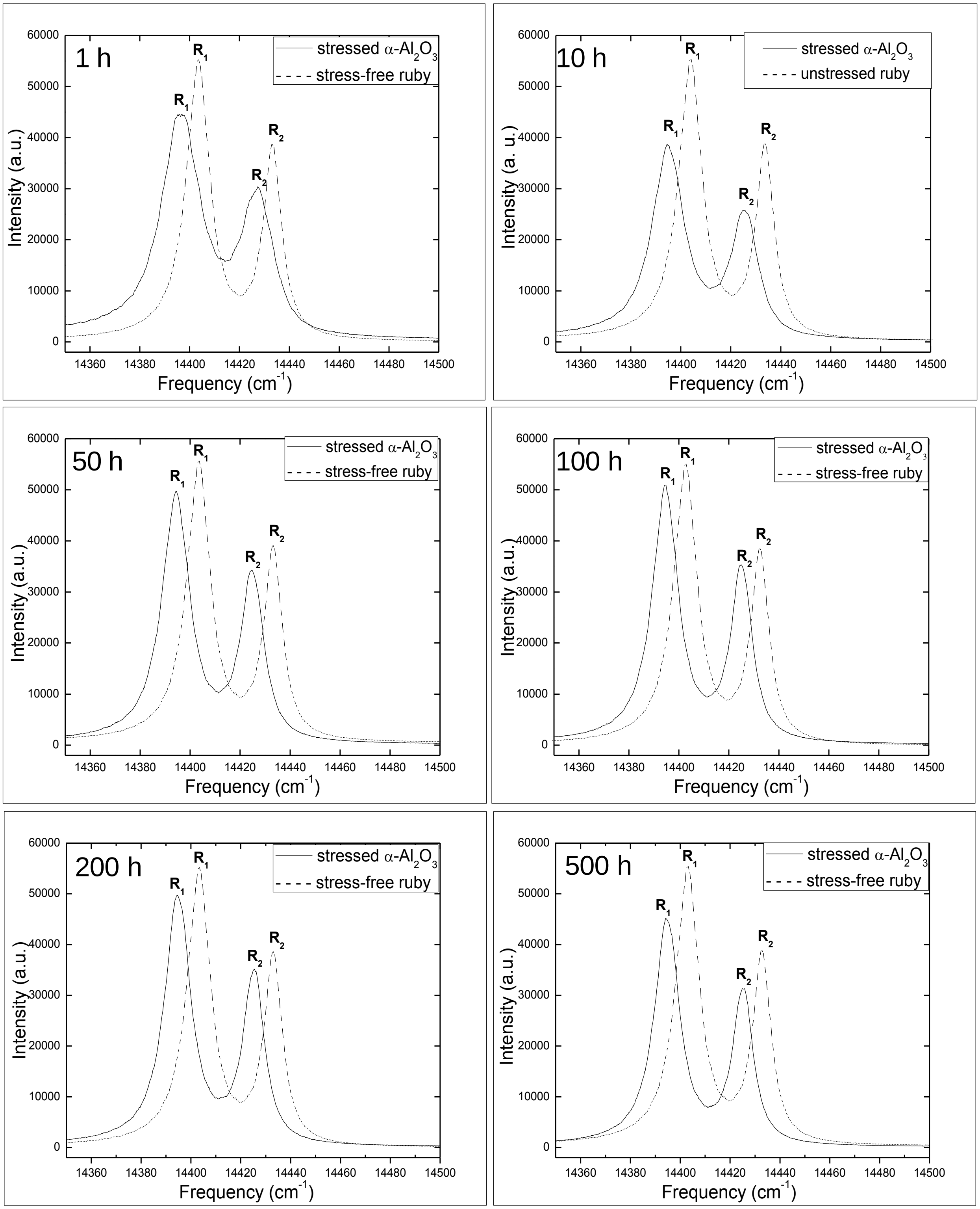

Figure 4.67. Luminescence spectra obtained from the stress-free ruby and oxide scales on air-cooled Pt_{84}:Al_{11}:Cr_3:Ru_2 (at.%) specimens after oxidation in air at 1150°C up to 500 h.

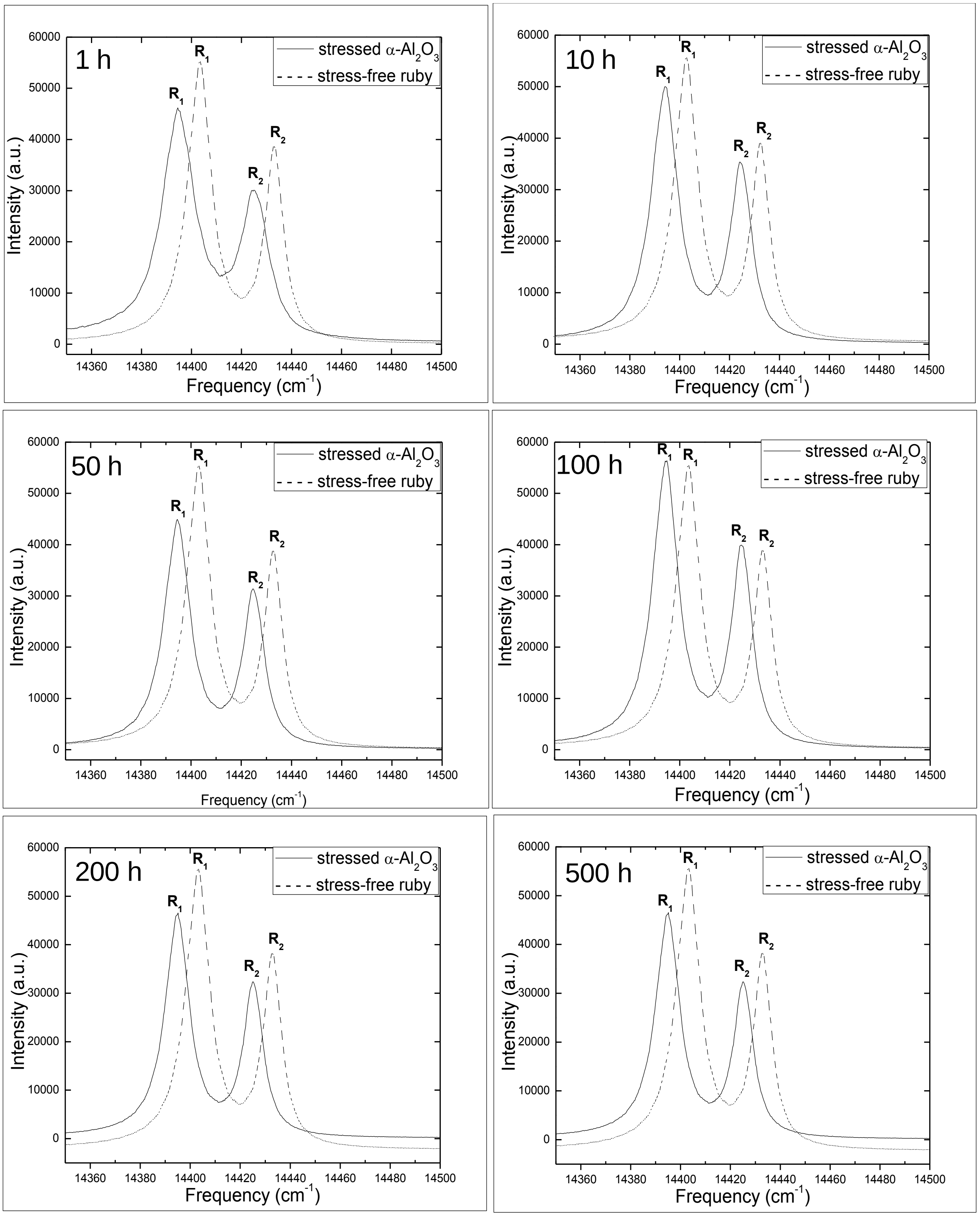

Figure 4.68. Luminescence spectra obtained from the stress-free ruby and oxide scales on air-cooled $Pt_{84}:Al_{11}:Cr_3:Ru_2$ (at.%) specimens after oxidation in air at 1250°C up to 500 h.

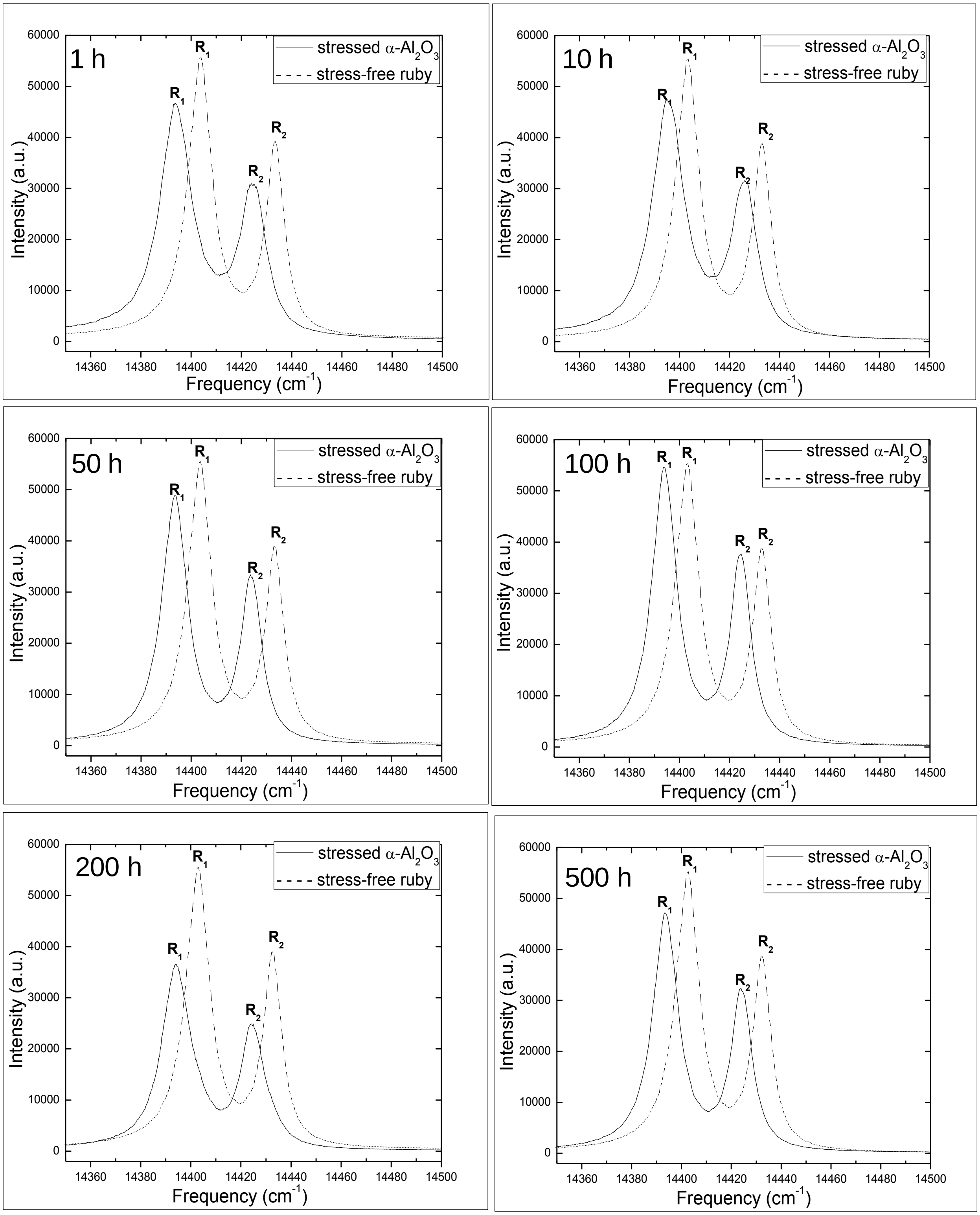

Figure 4.69. Luminescence spectra obtained from the stress-free ruby and oxide scales on air-cooled Pt_{84}:Al_{11}:Cr_3:Ru_2 (at.%) specimens after oxidation in air at 1350°C up to 500 h.

Table 4.10. Mean in-plane compressive stresses and peak widths of the oxide scales formed on air-cooled Pt_{84}:Al_{11}:Cr_3:Ru_2 (at.%) specimens after isothermal oxidation in air for up to 500 h.

Oxidation time (hours)	**Mean in-plane compressive stress (GPa)**			**Mean peak width (cm^{-1})**		
	1150°C	**1250°C**	**1350°C**	**1150°C**	**1250°C**	**1350°C**
1	1.46 ± 0.29	1.74 ± 0.37	1.95 ± 0.17	15.35 ± 0.32	13.01 ± 0.40	12.86 ± 0.67
10	1.58 ± 0.12	1.66 ± 0.06	1.76 ± 0.50	13.20 ± 0.08	10.64 ± 0.09	11.86 ± 0.55
50	1.66 ± 0.05	1.64 ± 0.05	1.70 ± 0.16	11.03 ± 0.14	10.39 ± 0.06	10.34 ± 0.57
100	1.66 ± 0.09	1.64 ± 0.06	1.66 ± 0.14	10.52 ± 0.12	10.26 ± 0.10	10.16 ± 0.28
200	1.66 ± 0.07	1.64 ± 0.07	1.66 ± 0.14	10.60 ± 0.08	10.04 ± 0.15	11.50 ± 0.25
500	1.66 ± 0.07	1.64 ± 0.06	1.66 ± 0.16	10.35 ± 0.10	9.87 ± 0.08	10.12 ± 0.19

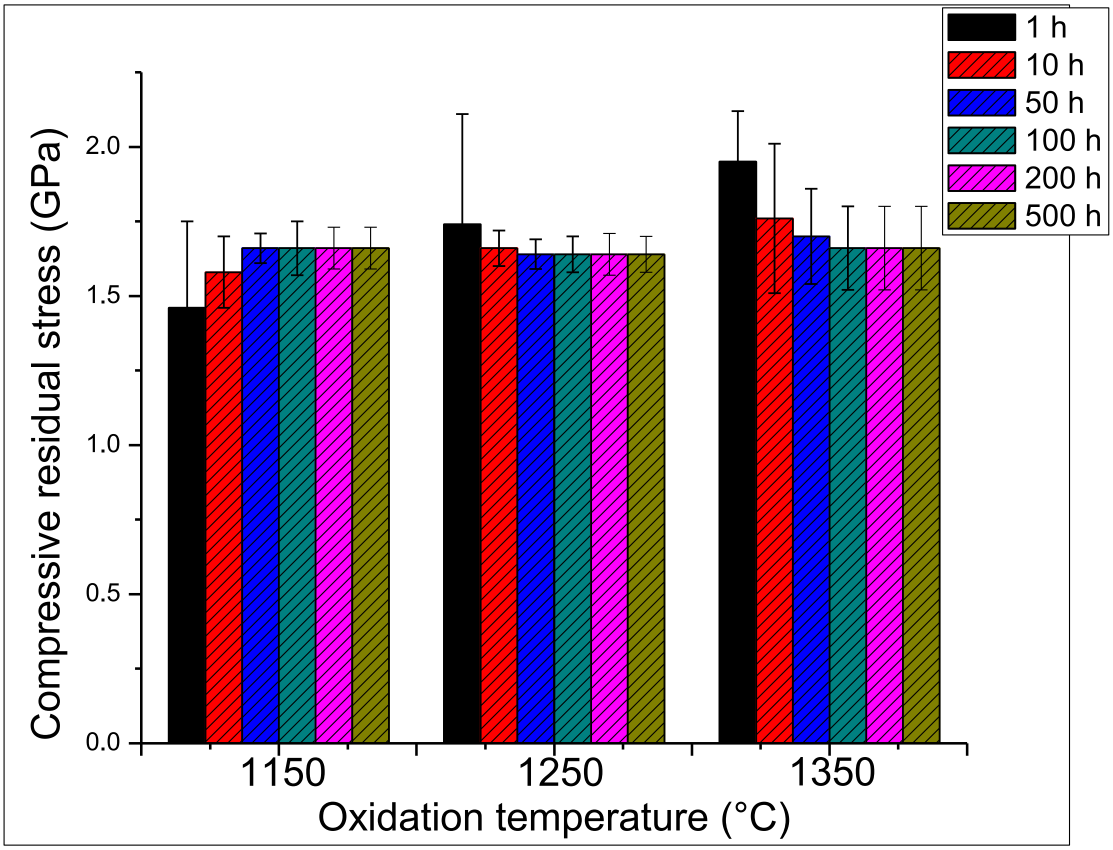

Figure 4.70. Mean stress in the oxide scales on air-cooled Pt_{84}:Al_{11}:Cr_3:Ru_2 (at.%) specimens calculated from the measured frequency shifts of the R2 luminescence line.

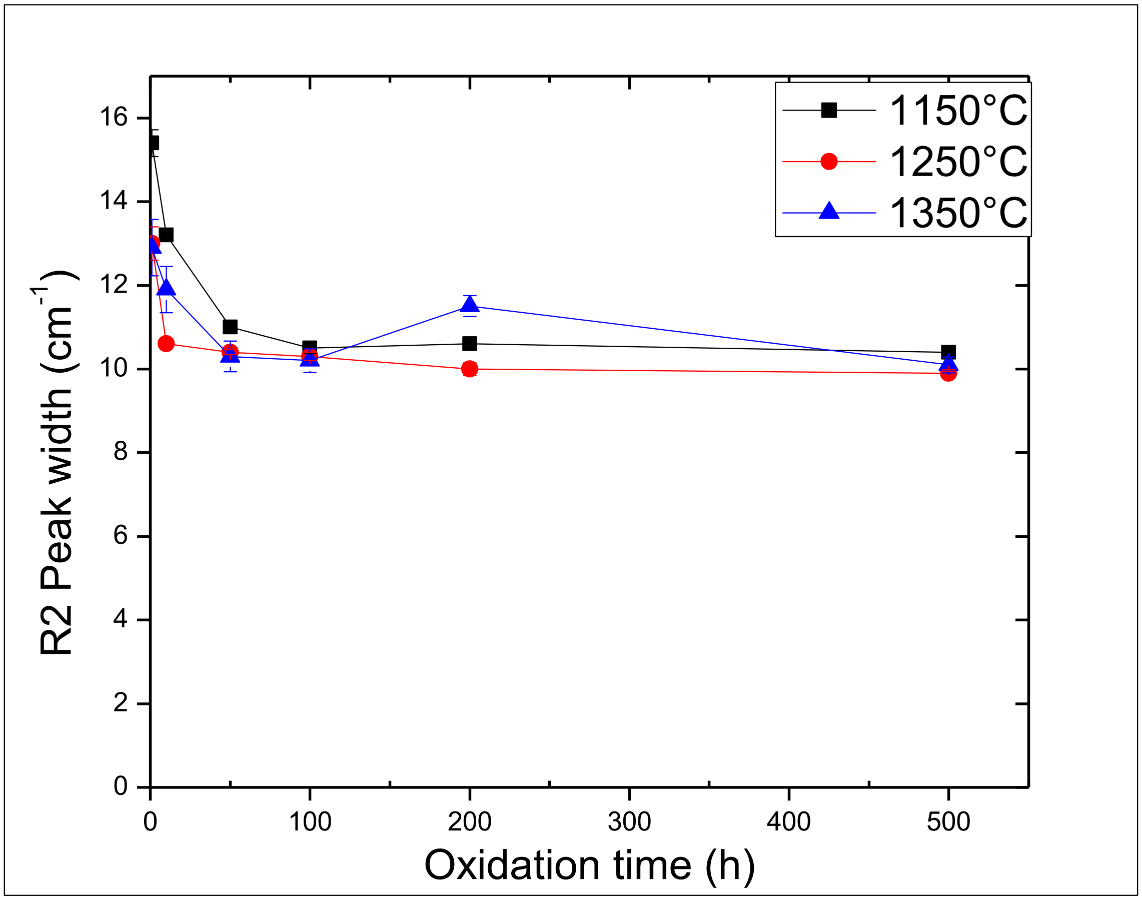

Figure 4.71. Peak widths of the R2 luminescence line showing the stress gradients through the scales thickness on air-cooled Pt_{84}:Al_{11}:Cr_3:Ru_2 (at.%) as a function of oxidation time.

CHAPTER FIVE

5.0 Discussion

5.1 Oxidation Kinetics and Activation Energies

Figure 5.1 compares the plots of specific mass gain as a function of oxidation time for both the water-quenched and air-cooled specimens after isothermal oxidation in air at 1150°C, 1250°C and 1350°C for up 100 hours. The curves showed that the parabolic mass increase law, $\Delta m = k_p.t^2 + C$ ([1962Kub, 1975Sme, 2006Bir], was obeyed throughout the exposure times, at all oxidation temperatures. This shows that the oxidation kinetics are controlled by the diffusion of reactive species (anions and/or cations) through the external scale and/or in the subjacent alloy [1962Kub, 1983Bir, 1988Kof], because diffusion-controlled high-temperature oxidation processes are governed by the parabolic rate law.

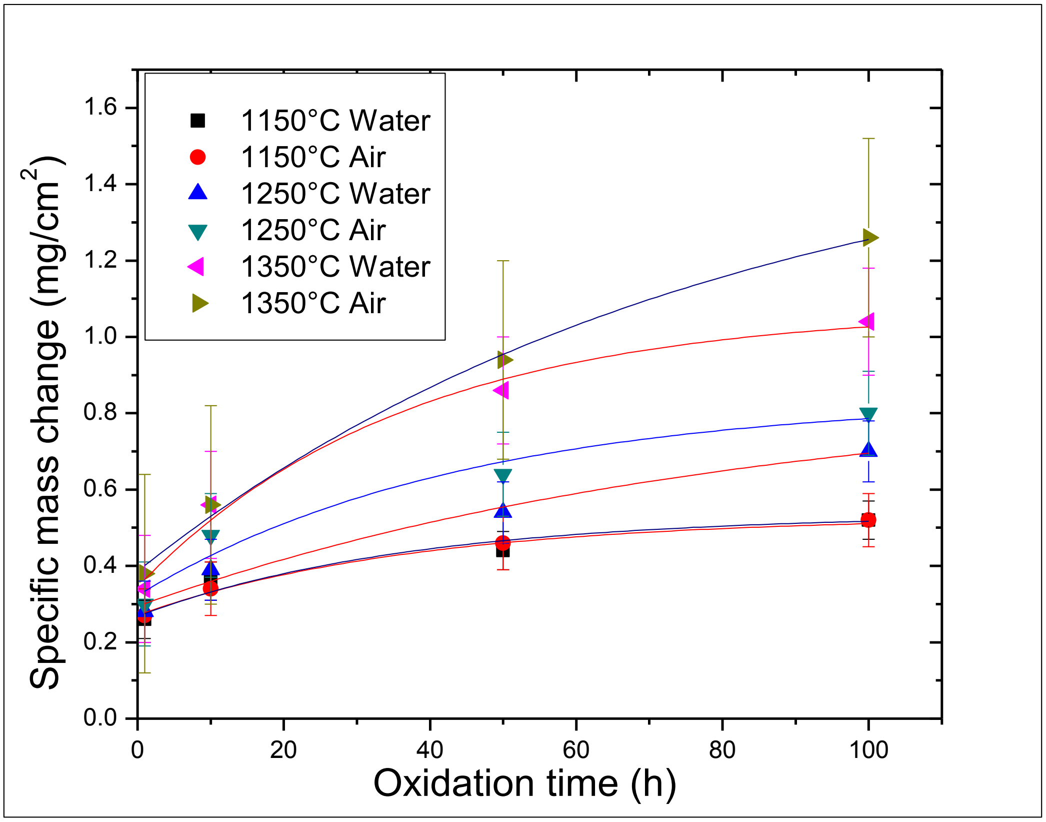

Figure 5.1. Specific mass change with time of water-quenched and air-cooled nominal Pt_{84}:Al_{11}:Cr_3:Ru_2 (at.%) specimens after isothermal oxidation in air at different temperatures (water-quenched curves in red; air-cooled curves in blue).

Similar parabolic behaviour was shown by Pt_{76}:Al_{22}:Ru_2 (at.%) and Pt_{82}:Al_{14}:Cr_4 (at.%) alloys when oxidized in air, for up to 500 hours between 1200°C and 1350°C by Hill et al. [2000Hil]. The isothermal oxidation behaviour of ternary Pt-based alloys, Pt_{86}:Al_{10}:X_4 (at.%) alloys, where X = Cr, Ru, Ti, Ta and Ir, was examined at 1350°C, for up to 1000 hours by Süss et al. [2001Süs1], and also showed that the scale growth kinetics of Pt_{86}:Al_{10}:Cr_4 (at.%), Pt_{86}:Al_{10}:Ta_4 (at.%) and Pt_{86}:Al_{10}:Ti_4 (at.%) alloys were in accordance with parabolic rate law after 100 hours exposure. Above 100 hours, the growth kinetics of Pt_{86}:Al_{10}:Cr_4 (at.%) became very slow. Thus, the parabolic scale growth kinetics changed to logarithmic kinetics as a result of slow rate of formation of the scale [1962Kub, 1965Hau]. However, the scale growth kinetics of alumina scale on a Pt_{86}:Al_{10}:Ru_4 (at.%) alloy was parabolic after 1000 hours oxidation. Wenderoth et al. [2007Wen2] showed that the specific mass of oxide scale formed on a Pt_{77}:Al_{12}:Cr_6:Ni_5 (at.%) alloy, during isothermal oxidation in air between 1100°C and 1300°C for up to 500 hours, increased according to a parabolic function of time.

A single crystal Ni-based superalloy, which contained 6.3 wt% Al, 6 wt% Cr and some Co, Ti, Mo, W and Ta, also showed similar parabolic growth kinetics when oxidized in air at 1000ºC [2003Li2]. During the isothermal oxidation of directionally solidified Ni-based superalloy DS951 in air between 1000°C and 1100°C, Huang et al. [2005Hua1] showed that a two-stage parabolic rate law was obeyed, as shown in Figure 5.2. The kinetics curves consisted of transient and steady-state sections, with the slope of transient stage being higher than that of steady-state stage. This showed that the oxidation rate was faster during the transient oxidation period, and later decreased once steady-state oxidation was established [2005Hua1]. This observation is consistent with the results of the current study. However, the transient oxidation period decreased with increased exposure temperatures (Figure 5.2b).

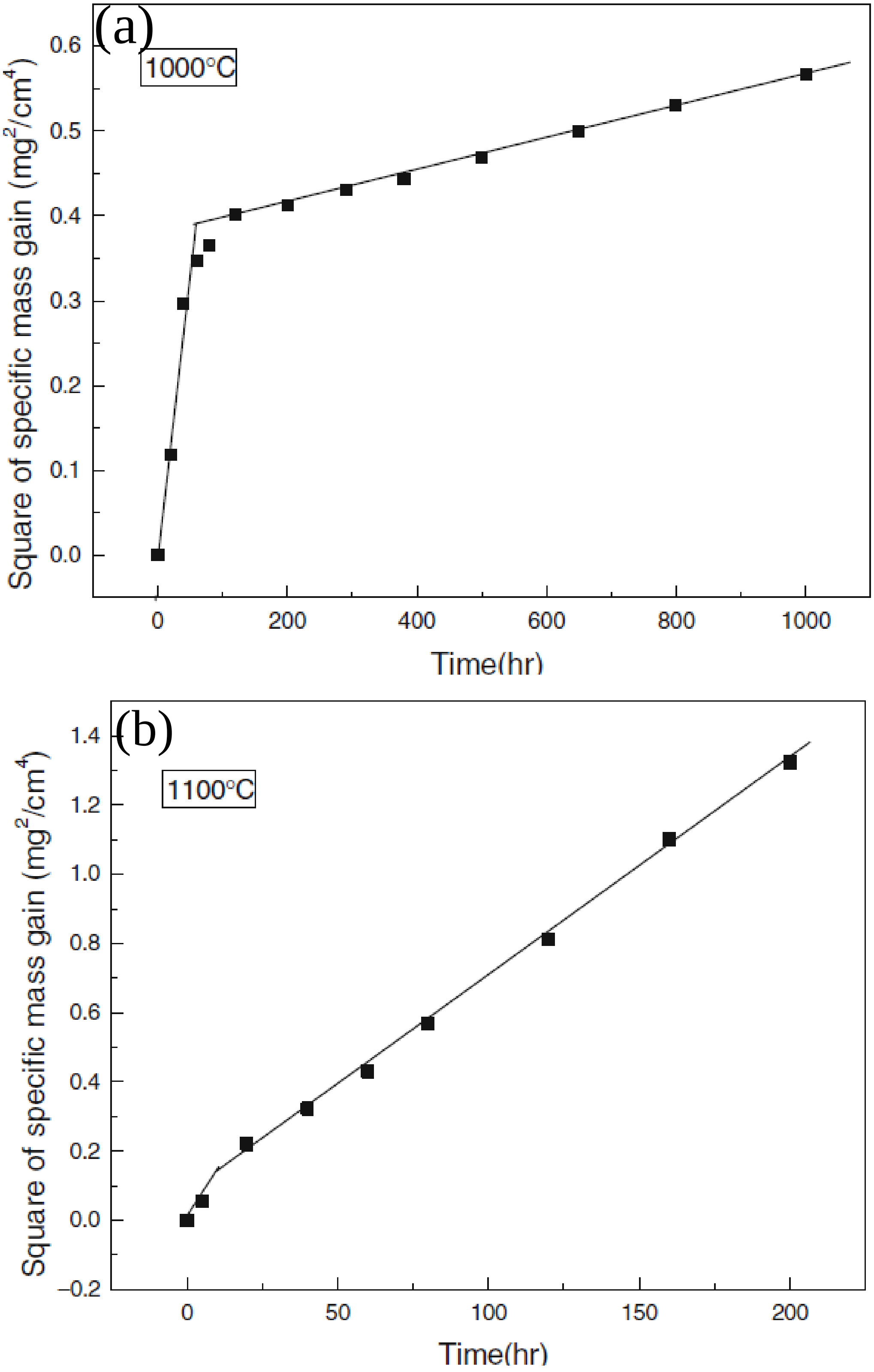

Figure 5.2. Square of the mass gain per unit area vs time for the Ni-based superalloy DS951 after oxidation in air at: (a) 1000°C (b) 1100°C [2005Hua1].

The curves also showed that the oxidation rate was rapid during the initial oxidation period, up to 10 hours, for almost all the specimens. This period coincided with the transient oxidation stage, as described by Hindam and Whittle [1982Hin]. Transient oxidation stage is characterized by the simultaneous formation of the oxides of every active element of an alloy [1982Hin]. This explains the formation of the oxides of Pt and Cr during the early oxidation stage, up to 10 hours in the current study. Scanning electron microscopy (SEM)/energy dispersive X-ray spectroscopy (EDX) results (Figures 4.12-4.14, 4.19-4.20, 4.26-428, 4.30 and Table 4.5) revealed the presence of Pt and Cr in the oxide scales during the transient oxidation stage. X-ray diffraction (Figures 4.50-4.52 and 4.53-4.55) also confirmed the formation of oxides of Pt and Cr during the early stage of oxidation, up to 10 hours. Above this oxidation time, the reaction kinetics became better fitted into the parabolic curves, after leaving the transient stage. This period was described as the steady-state stage by Hindam and Whittle [1982Hin], and is associated with the formation of protective and continuous scale layers through diffusion of reacting species across the oxide scale. Accelerated attack of the oxide, after the steady-state stage, may eventually lead to oxide breakaway [1982Hin]. The breakaway stage depends on the scale growth rate and component thickness, as well as spalling kinetics [1994Qua1, 1994Qua2, 2000Sto]. However, the component lifetime limit is more dependent on the duration of the steady state [1982Hin], which is governed by the amount and consumption rate of Al in the alloy matrix [2004Qua, 2000Sto].

Within the errors, the curves showed that the oxidation rates of both the water-quenched and air-cooled specimens were very close at 1150°C, and thus superposed throughout the exposure times. With higher temperatures, the mass-gain rate of the air-cooled specimens appeared faster than those of water-quenched specimens, although this might be masked by the overlapping errors. In addition, the curves were further away from leveling off, especially above 50 hours exposure at 1250°C and 1350°C, indicating that the steady state takes longer to reach at higher temperatures. The apparent lower mass gain values of water-quenched Pt_{84}:Al_{11}:Cr_3:Ru_2 (at.%) specimens at higher temperatures may be associated with the faster rate of formation of PtO_2, and thus loss of Pt. This is shown in Figures 4.12, 4.18 and 4.19, where large grains of Pt-rich crystals were observed on the alumina scale. However, above 200 hours exposure, the oxidation rates of the air-cooled specimens became very slow, nearing a plateau (Figure 4.4).

The mass-related parabolic rate constants, k_p, were obtained from the slopes of the plots of the kinetics data, Δm *vs* $t^{1/2}$ (Figure 5.3), where Δm is the specific mass gain, t is the time and C is the intercept, corresponding to specific mass-gain associated with transient period. Pieraggi [1987Pie] reported that the plot of Δm vs $t^{1/2}$ rather than $(\Delta m)^2$ vs t is better for accurate determination of the steady state parabolic constants, as well as for more precise analysis of the transient oxidation kinetics. This will allow for determination of initial mass gain of the scale during the transient oxidation stage, and this is obtained from the intercept, C. The plots of this study were not well fitted linearly during the transient oxidation stage. This may be due to the faster rate of formation of oxides of all the different reacting species (Al, Pt and Cr), rather than just alumina formation alone. At higher exposure times, the plots became better fitted linearly, indicating a diffusion-controlled oxidation process. The growth rate of diffusion-controlled oxidation process is usually govern by the parabolic rate law [1962Kub, 2009You], and can be represented linearly on either the plot of Δm vs $t^{1/2}$ or $(\Delta m)^2$ vs t [1987Pie]. The choice of the plot type is likely to depend on whether the scale formed during the transient oxidation stage was protective or not [1987Pie, 2005Pie]. If protective scale was formed during the initial transient period, the initial mass gain will contribute to the steady state kinetics after the transient period. Thus, Δm vs $t^{1/2}$ plot becomes suitable. However, if the transient scale is not protective, $(\Delta m)^2$ vs t plot may be appropriate. If the data points are well fitted linearly, it indicates that the parabolic kinetics are obeyed, and thus the oxidation process is diffusion-controlled. The growth rates of water-quenched specimens appeared to be lower, especially at higher exposure temperatures, indicating slower scale growth kinetics at higher temperatures (Figures 5.1 and 5.3), although the overlapping errors might indicate that this is inconclusive.

The k_p values obtained were compared with those obtained for other Pt-based alloys (Figure 5.4), as well as Ni- and Fe-based superalloys (Figure 5.5) using the plots of log k_p vs the reciprocal of the absolute temperature. Figure 5.4a shows that Pt_{84}:Al_{11}:Cr_3:Ru_2 (at.%) in the present study has smaller rate constants at all investigated temperatures, that is, the most shallow slopes (Figure 5.4b), compared to the rate constants of Pt_{76}:Al_{22}:Ru_2 (at.%) and Pt_{82}:Al_{14}:Cr_4 (at.%) [2000Hil]; Pt_{86}:Al_{10}:Ti_4 (at.%) [2001Süs1]; Pt-32Al (at.%) [1976Fel2] and Pt_{77}:Al_{12}:Cr_6:Ni_5 (at.%) [2007Wen2]. This indicated that the scale growth rate of the current alloy is slower, and may be due to its lower Al content compared with most of the other alloys, as well as beneficial effects of other alloying elements (Figure 5.4). Hutchings and Loretto [1978Hut] found that the k_p values increased with increasing aluminium content during the oxidation of NiAl and CoAl at 900°C. However, the rate constant of Pt_{86}:Al_{10}:Cr_4 (at.%) [2001Süs1] at 1350°C was slightly lower than the Pt_{84}:Al_{11}:Cr_3:Ru_2 (at.%) in both quenching media, possibly due to its slightly lower Al content or beneficial alloying elements. Figure 5.4a also shows that the rate constants of Pt_{76}:Al_{22}:Ru_2 (at.%) [2000Hil] displayed a two-stage parabolic rate kinetics, with smaller rate constants found at 1200°C and 1280°C, possibly due to slower scale growth kinetics, whereas faster growth kinetics that resulted in higher rate constant was observed at 1350°C. This may be due to oxide breakaway [1982Hin], which may have resulted from higher oxide scale thicknesses (large error bars from protrusions of the scale) after longer exposure times at 1350°C.

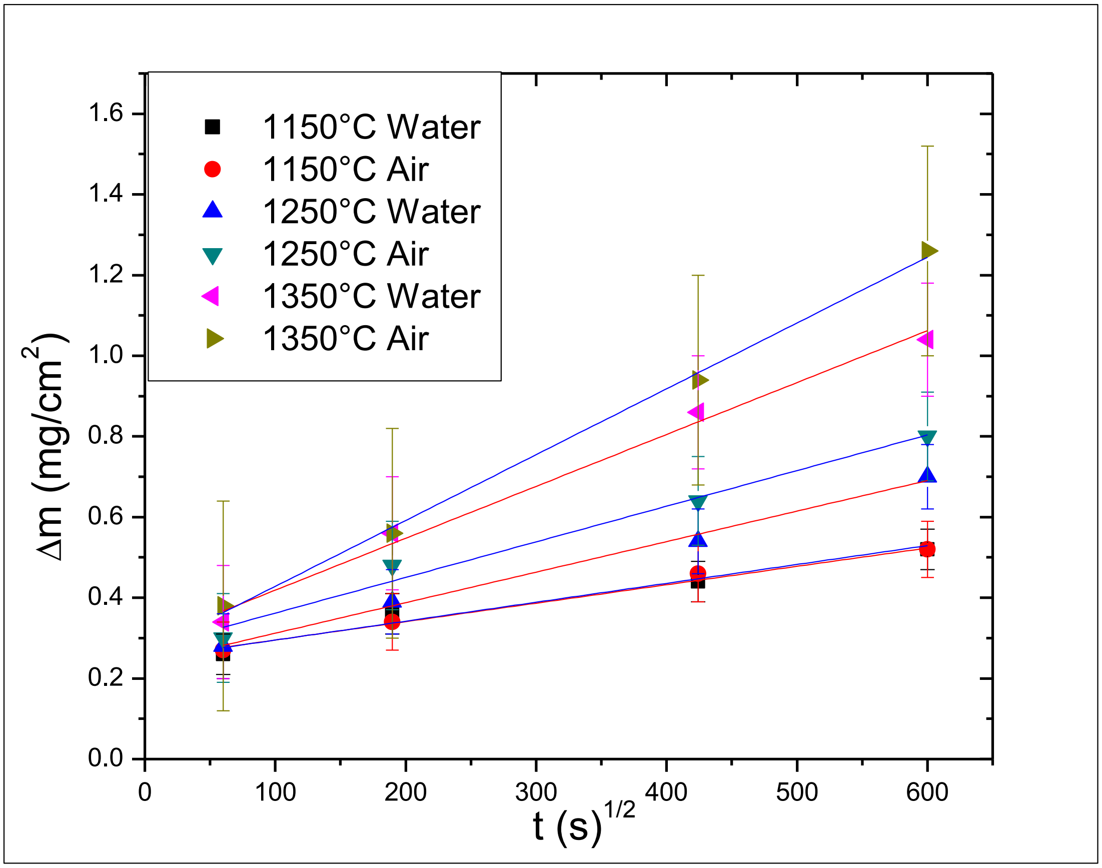

Figure 5.3. Plots of Δm vs $t^{1/2}$ for water-quenched and air-cooled nominal Pt_{84}:Al_{11}:Cr_3:Ru_2 (at.%) specimens after isothermal oxidation in air at different temperatures (water-quenched lines in red; air-cooled lines in blue).

Activation energies, Q_A for the growth of the scales were obtained from the slopes of the linearly fitted Arrhenius plots (Figure 5.4b), using the Arrhenius's equation [1962Kub] (Equation 5.1).

$$k_p = k_o.\exp\left(\frac{Q_A}{RT}\right) \tag{5.1}$$

where k_p is the mass-related parabolic rate constant ($g^2.cm^{-4}.s^{-1}$), k_o is the pre exponential factor, R is the gas constant (8.31J/Kmol) and T is the absolute temperature (Kelvin). Results from these calculations are presented in Table 5.1. The activation energy of the water-quenched Pt_{84}:Al_{11}:Cr_3:Ru_2 (at.%) specimens is the smallest, especially at higher oxidation temperature, due to their slower scale growth rates as shown in Figure 5.4a. Activation energies for the oxidation of Pt_{76}:Al_{22}:Ru_2 (at.%) [2000Hil] between 1200ºC and 1350ºC agree quite well with that of Pt_{82}:Al_{14}:Cr_4 (at.%) [2000Hil] oxidized within the same temperature ranges, but are almost double the values obtained from the alloy of both quenching media in the present study. However, due very slow scale growth kinetics of Pt_{76}:Al_{22}:Ru_2 (at.%) [2000Hil] between 1200ºC and 1280ºC (Figure 5.4a), the activation energy was found to be smaller compared to very high activation energy values obtained for the oxidation of the same alloy between 1280ºC and 1350ºC. Thus, two-stage slopes were developed, with shallow slope between 1200ºC and 1280ºC. This showed that the scaling kinetics was very fast at higher oxidation temperatures, and may be due to oxide breakaway resulting from the formation of very thick scales [1982Hin]. In addition, the activation energy for oxidation of Pt-32Al (at.%) [1976Fel2] is considerably higher than those of Pt_{84}:Al_{11}:Cr_3:Ru_2 (at.%) specimens in the present study. This indicated that the current alloy potentially possessed better oxidation properties than the binary [1976Fel2] and ternary Pt-based alloys [2000Hil]. Thus, the composition of the current alloy may play a decisive role, although from the SEM/EDS, XRD and Raman results, the contribution of Ru has not been identified. This may be due to its inhomogeneity in the alloy, as observed during EDS analysis of the alloy prior to oxidation. In addition, its low concentration in the alloy may be another reason. However, Ru additions to other alloys such as steels [1995Pot], titanium alloys [2001Lin] and WC-Co hardmetals [1999Wol2] was found to successfully increase their corrosion resistance.

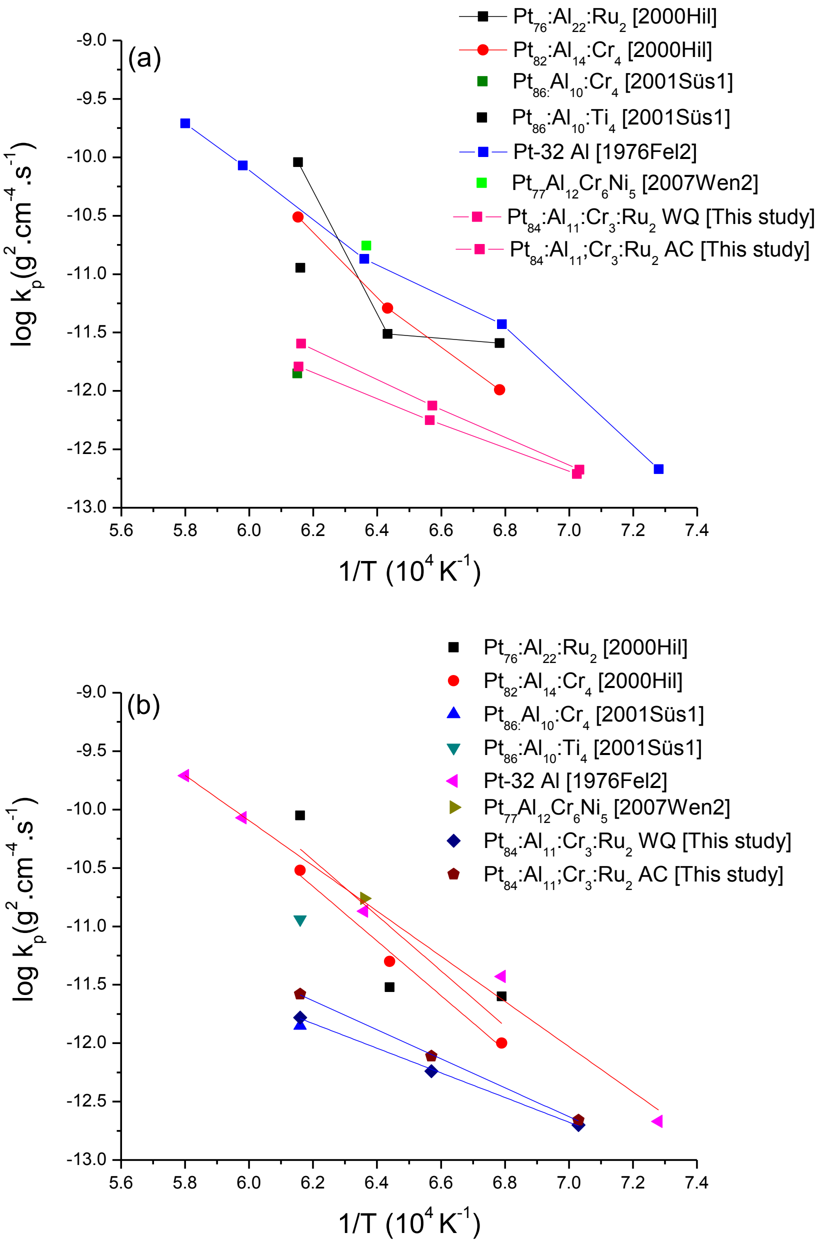

Figure 5.4. Arrhenius plots showing the variation of mass-related parabolic rate constants for water-quenched and air-cooled nominal Pt_{84}:Al_{11}:Cr_3:Ru_2 (at.%) specimens as compared to other Pt-based alloys (a) individual k_p values joined with straight lines (Pt_{84}:Al_{11}:Cr_3:Ru_2 (at.%) in both quenching media plots in pink) (b) linearly fitted plots (Pt_{84}:Al_{11}:Cr_3:Ru_2 (at.%) in both quenching media plots in blue).

Figure 5.5a shows that the parabolic rate constant for the Zr-doped sample was the least among the Ni-Al based alloys. The scale growth kinetics of Ni-52 Al between1150ºC and 1200ºC was slower (shallow slope) compared to the rate between 1200ºC and 1300ºC (Figure 5.5a). Thus, two-stage slopes were displayed for the scale growth kinetics, with lowest rate constants obtained at 1200ºC. This may be due to slower rate of formation of α-Al_2O_3 after the transient oxidation stage [1982Hin]. Both the water-quenched and air-cooled Pt_{84}:Al_{11}:Cr_3:Ru_2 (at.%) specimens displayed lower parabolic kinetics than the Ni- and Fe-based superalloys. These results showed that the parabolic rate constants of Pt_{84}:Al_{11}:Cr_3:Ru_2 (at.%) specimens (in both quenching media) are smaller than most of the other alloys, indicating potential better oxidation behaviour, through the formation of slow growing α-Al_2O_3 scale. However, the parabolic constants of the water-quenched specimens are lower, especially at higher exposure temperatures. This indicated slower scale growth kinetics, and thus better oxidation properties than the air-cooled specimens.

Activation energies, Q_A for the growth of the scales were obtained from the slopes of the linearly fitted Arrhenius plots (Figures 5.5b), and the results are shown in Table 5.1. Activation energy for oxidation of water-quenched Pt_{84}:Al_{11}:Cr_3:Ru_2 (at.%) specimens is the least, while those of the air-cooled Pt_{84}:Al_{11}:Cr_3:Ru_2 (at.%) specimens and Zr-doped NiAl alloy [1989Ryb] agree fairly well with each other. This may be due to beneficial effect of Zr in the alloy. However, the activation energy for oxidation of undoped Ni-52 Al alloy was very high between 1150ºC and 1200ºC, but was reduced during high temperature oxidation between 1200ºC-1300ºC. The whole error for curves were used for the points between 1150ºC-1200ºC and 1200ºC-1300ºC. The overall activation energy of the alloy from 1150ºC to 1300ºC was also quite high compared to those of the Pt_{84}:Al_{11}:Cr_3:Ru_2 (at.%) specimens in the current study. This indicated that the current alloy potentially possessed better oxidation properties that the undoped Ni-based alloys [1987Jed].

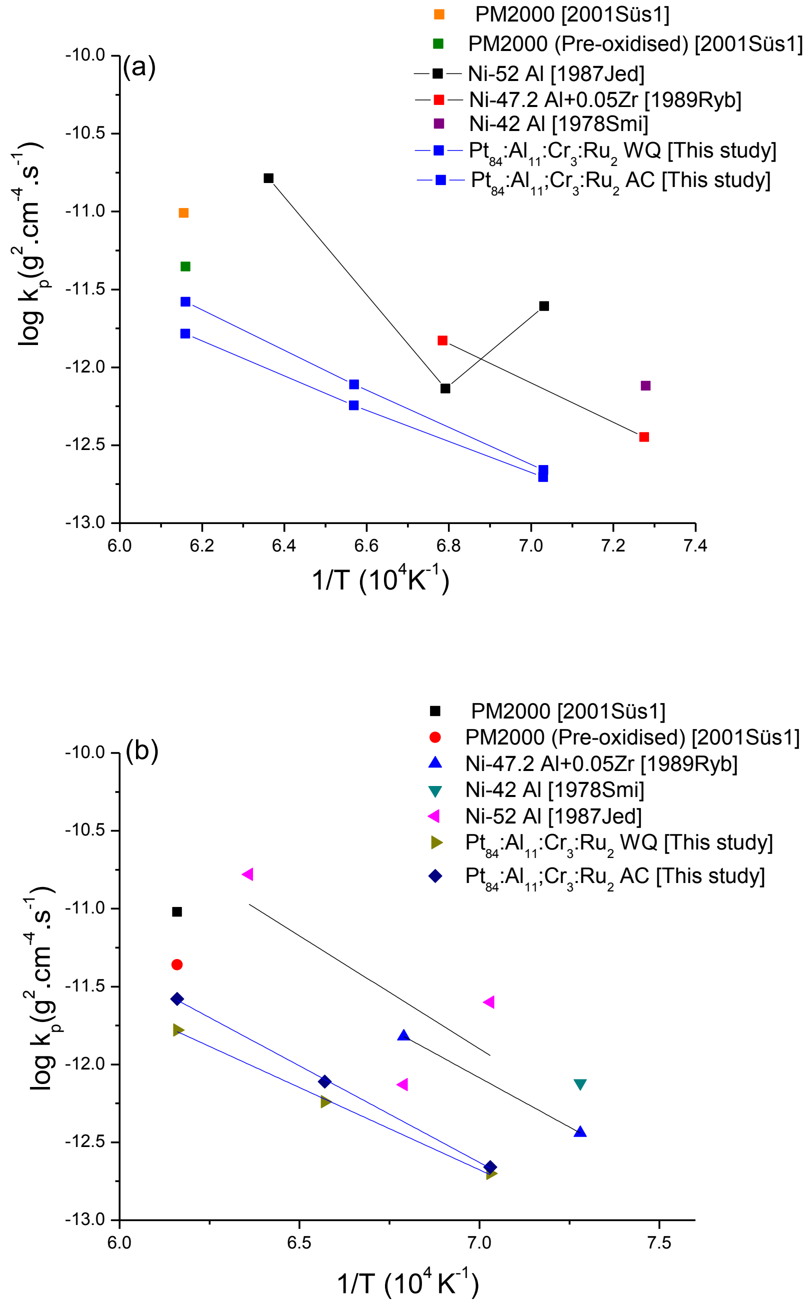

Figure 5.5. Arrhenius plots showing the variation of mass-related parabolic rate constants for water-quenched and air-cooled nominal Pt_{84}:Al_{11}:Cr_3:Ru_2 (at.%) specimens compared to other Ni- and Fe- based superalloys (a) individual k_p values joined with straight lines (b) linearly fitted plots (Pt_{84}:Al_{11}:Cr_3:Ru_2 (at.%) in both quenching media lines are in blue in both Figs.).

Table 5.1. Activation energies for the growth of Al_2O_3 scale on water-quenched and air-cooled Pt_{84}:Al_{11}:Cr_3:Ru_2 (at.%) alloys compared to other alumina-forming alloys.*

Alloy (at.%)	Time (h)	Atmosphere	Temperature range (°C)	Activation energy (KJ/mol)	Reference (for k_p value used)
Ni-47.2 Al + 0.05Zr	100	1 atm air	1100-1200	242.2 ± 0.5	[1989Ryb]
Ni-52 Al	200	1 atm O_2	1150-1300	274.5 ± 26.3	[1987Jed]
Ni-52 Al	200	1 atm O_2	1150-1200	-422.7 ± 26.3	[1987Jed]
Ni-52 Al	200	1 atm O_2	1200-1300	600.9 ± 26.3	[1987Jed]
Pt-32 Al	> 100	1 atm air	1100-1450	370.4 ±21.2	[1976Fel2]
Pt_{76}:Al_{22}:Ru_2	500	1 atm air	1200-1350	453.4 ± 27.2	[2000Hil]
Pt_{76}:Al_{22}:Ru_2	500	1 atm air	1200-1280	43.75 ± 27.2	[2000Hil]
Pt_{76}:Al_{22}:Ru_2	500	1 atm air	1280-1350	1004.9 ± 27.2	[2000Hil]
Pt_{82}:Al_{14}:Cr_4	500	1 atm air	1200-1350	446.9 ± 4.3	[2000Hil]
Pt_{84}:Al_{11}:Cr_3:Ru_2 (water-quenched)	100	1 atm air	1150-1350	202.2 ± 6.7	This study
Pt_{84}:Al_{11}:Cr_3:Ru_2 (air-cooled)	100	1 atm air	1150-1350	237.4 ± 5.3	This study

*mass-related parabolic rate constants of most of the alloys were used for the plots.

The oxidation kinetics of the specimens were further examined by the scale thickness measurements, because of the mass losses incurred by the formation of oxides, such as PtO_2 and CrO_3. Platinum oxide, PtO_2 was reported to form due to volatilization of Pt [1958Pow, 1965Cha, 1976Fel2], and similarly CrO_3 forms as a result of volatilization of Cr [1987Sto1, 1987Sto2], during the isothermal oxidation above 1000°C. Platinum-rich crystals were reported to grow on the scale either by decomposition of volatile PtO_2 at the scale surfaces or deposited from Pt vapour at 1000°C and above [1957Cha]. This could have been the origin of the Pt-rich crystals in the current work.

The combined plots of the scale thickness against the oxidation time of both types of quenching are presented in Figure 5.6. They showed that the oxide scale thicknesses increased according to a parabolic function of time. This is similar to observations made on Pt-Al alloys [1976Fel2]; Pt_{86}:Al_{10}:Cr_4 (at.%) and Pt_{86}:Al_{10}:Ru_4 (at.%) alloys [2001Süs1], and Pt_{77}:Al_{12}:Cr_6:Ni_5 (at.%) alloy [2007Wen2]. The plots also revealed that the oxidation kinetics were faster during the transient period that lasted for up to 10 hours. This may be due to formation of Al_2O_3 simultaneously with PtO_2 and CrO_3 as shown in Figures 4.12-4.15, 4.18-4.19 and 4.26-4.30. As a result of formation of thicker oxide scale above this exposure time, the oxidation process changed from a direct reaction between the alloy surfaces and air, to a reaction which was dependent on the rate of outward diffusion of metal cations and inward diffusion of oxygen anions through the oxide scale [2006Bir]. Thus, the scale growth rate became diffusion-controlled through the selective oxidation of Al to form only continuous and protective external α-Al_2O_3 scale as shown in Figures 4.17, 4.21, 4.22, 4.30a 4.21 and 4.33-4.37. XRD (Figures 4.50-4.52 and 4.53-4.55) and Raman spectroscopy (Figures 4.56-4.58 and 4.59-4.61) confirmed that the scale layers correspond to α-Al_2O_3 at longer exposure times.

During the formation of only α-Al_2O_3 scale, the oxidation rate became reduced, thereby leading to slower scale growth rate. This period corresponds to the steady state oxidation stage as reported by Hindam et al. [1982Hin], Huang et al. [2005Hua1] and Birk et al. [2006Bir]. Here for 1150°C and 1250°C (Figure 4.5), the scale growth rate became very slow after 200 hours exposure, nearing a plateau, whereas the plateau would have formed later for the 1350°C specimens. This observation showed that the scales are potentially protective, and consistent with the observation that the oxidation kinetics were diffusion-controlled [2007Wen2]. As the oxide grain sizes, as well as scale thicknesses increased with increased oxidation time (Tables 4.5 and 4.6), (Figures 4.40 and 4.45), potential diffusion paths for inward diffusing oxygen anions and outward diffusing metal cations decreased, thus resulting in slower scaling kinetics. It has been reported that α-Al_2O_3 scales grew either primarily by inward diffusion of oxygen along grain boundaries [1976Fel2, 1972Tie2, 1989Qua, 1994Doy] or by nearly exclusive outward diffusion of Al [1987Abd, 1987Jed] or by combination of inward oxygen diffusion and outward Al diffusion [1985You, 1987Abd, 1987Jed, 1989Qua].

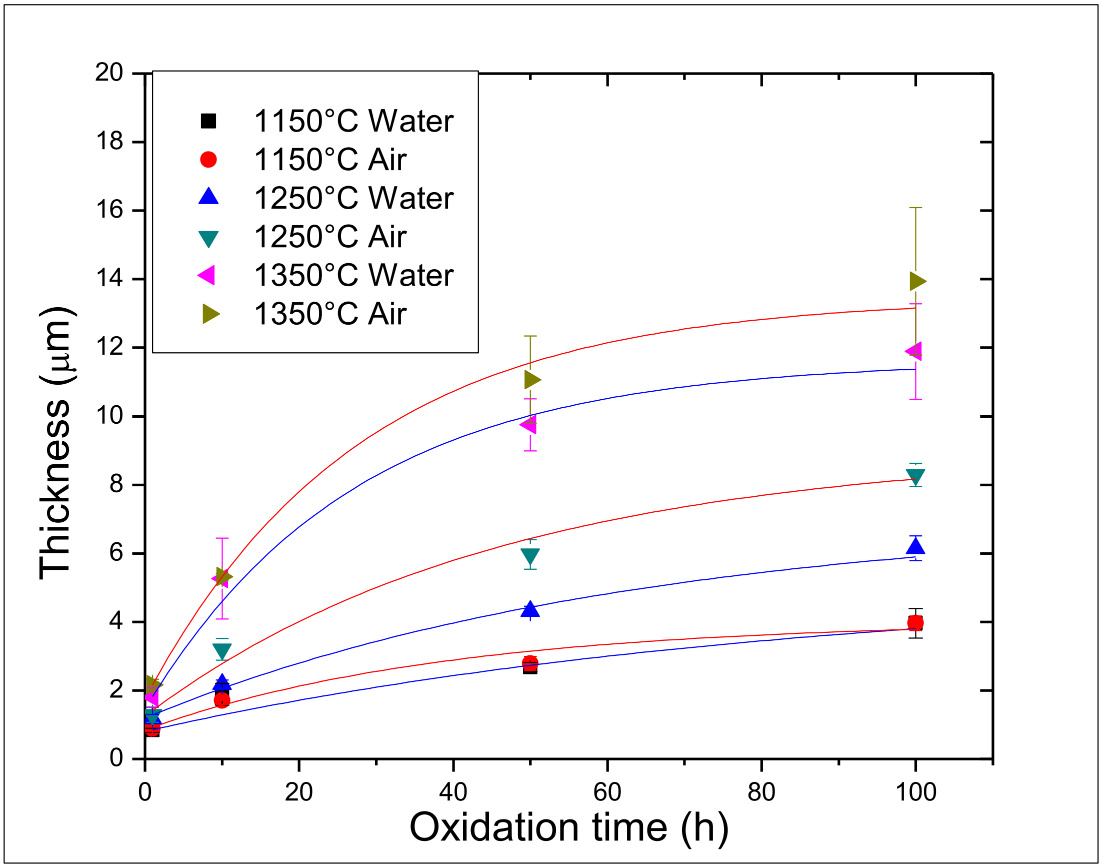

Figure 5.6. Oxide scale thickness as a function of time of water-quenched and air-cooled nominal Pt_{84}:Al_{11}:Cr_3:Ru_2 (at.%) specimens after isothermal oxidation in air at different temperatures (water-quenched curves in blue; air-cooled curves in red).

The scaling kinetics of both the water-quenched and air-cooled specimens were very close at 1150°C, and had started to level off at 100 hours exposure (Figure 5.6). At 1250°C, air-cooled specimens displayed faster growth kinetics than the water-quenched, and their curves were further away from leveling off after 100 hours exposure. This indicated that the steady-state kinetics were maintained for longer time at this temperature. The scale growth rates of both the water-quenched and air-cooled specimens were very close up to 10 hours at 1350°C. However, the curves later diverged, with the air-cooled specimens displaying faster kinetics. This observation might not be true though, since there are large errors. The scaling kinetics began to become faster after 50 hours exposures at higher exposure temperatures, thus giving rise to another stage of parabolic kinetics other than the initial and steady-stage oxidation (Figure 5.6).

The thickness-related parabolic constant, k_{ps} were calculated from the slope of the plots of scale thickness, y against the square-root of time, $t^{1/2}$ (Figure 5.7). The parabolic relations $y = k_{ps}.t^2 + C$ [1962Kub, 2006Bir] were used, where C is the intercept, corresponding to scale thickness during the initial transient period. The plots were well fitted linearly at 1150°C and 1250°C, but deviated for 1350°C. This may due to slower scaling kinetics at longer exposure times at higher temperatures. The comparison of the parabolic rate constants of the water-quenched and air-cooled Pt_{84}:Al_{11}:Cr_3:Ru_2 (at.%) specimens with those of other alumina forming superalloys are represented on an Arrhenius plot (Figure 5.8). The activation energies for the growth of oxide scale on the alloys were obtained from the slope of the regression lines in Figure 5.8a, and are presented in Table 5.2. The thickness versus time measurements were converted to ($g^2/cm^4.s$) by using the relationship k_{ps} (cm^2s) = 0.28 k_p (($g^2.cm^{-4}s^{-1}$) [1976Fel2]. The plots were not well fitted possibly due to waviness of the scale (Figure 5.8b), which gave large error bars (Figure 5.6). The Arrhenius plots (Figure 5.8) showed that the parabolic rate constants of both the water-quenched and air-cooled specimens were similar at 1150°C. This indicated that the scale growth rate of Pt_{84}:Al_{11}:Cr_3:Ru_2 (at.%) in both quenching media was very close, as shown in Figure 5.6. Without applying any fitting (Figure 5.8b), the shape given by the data for the air-cooled specimens was similar to the Pt_{77}:Al_{12}:Cr_6:Ni_5 (at.%) alloy [2007Wen2], whereas the water-quenched specimens were different. Thus, the results for 1250°C were less similar than for 1150°C and 1350°C.

Table 5.2. Activation energies for the growth of Al_2O_3 scale on water-quenched and air-cooled Pt_{84}:Al_{11}:Cr_3:Ru_2 (at.%) specimens and Pt_{77}:Al_{12}:Cr_6:Ni_5 (at.%).*

Alloy (at.%)	Time (h)	Atmosphere	Temperature range (°C)	Activation energy (kJ/mol)	References for k_{ps} value used
Pt_{77}:Al_{12}:Cr_6:Ni_5	0.4-400	1 atm air	1100-1300	284.3 ± 3.5	[2007Wen2]
Pt_{84}:Al_{11}:Cr_3:Ru_2 (water-quench)	1-100	1 atm air	1150-1350	262.5 ± 4.4	This study
Pt_{84}:Al_{11}:Cr_3:Ru_2 (air-cooled)	1-100	1 atm air	1150-1350	280.0 ± 1.7	This study

*thickness-related parabolic constants were converted to mass-related constants for the plot.

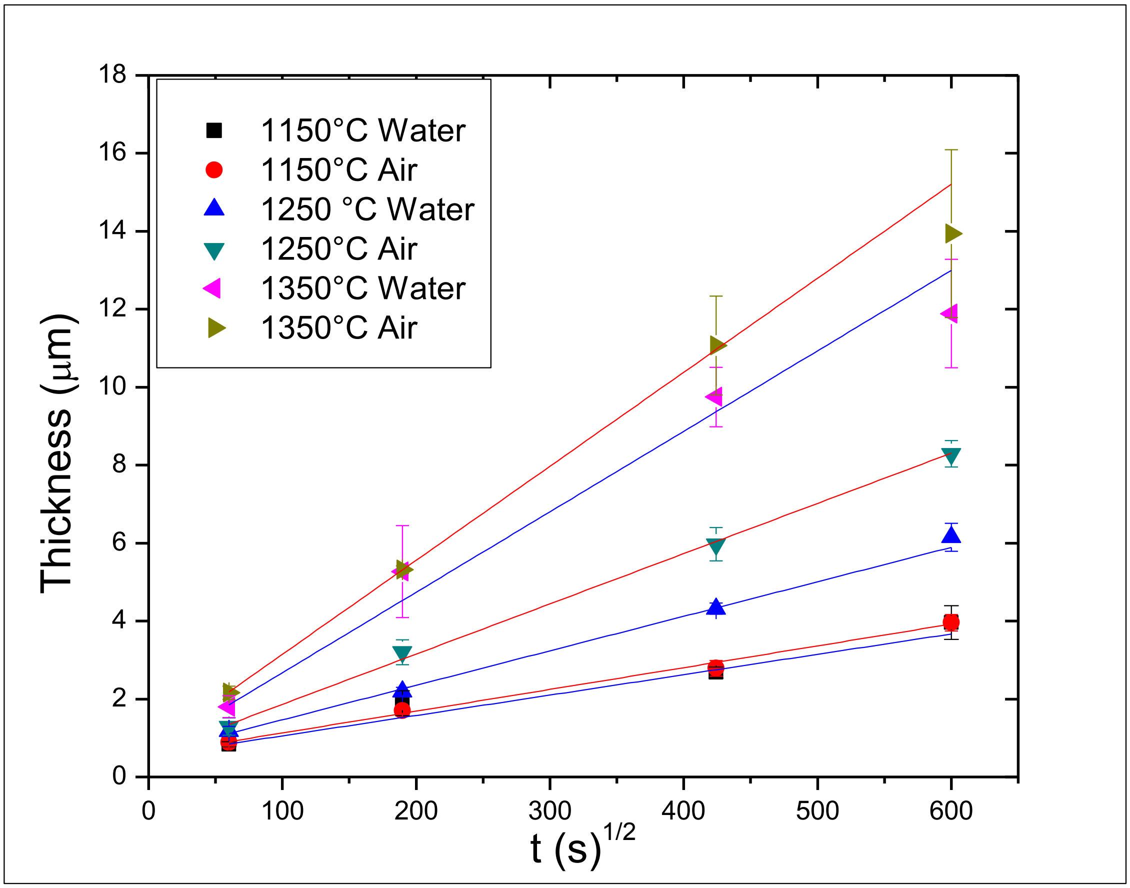

Figure 5.7. Plots of y vs $t^{1/2}$ for water-quenched and air-cooled nominal Pt_{84}:Al_{11}:Cr_3:Ru_2 (at.%) specimens after isothermal oxidation in air at different temperatures (water-quenched lines in blue; air-cooled lines in red).

The activation energies (Table 5.2) calculated for the air-cooled Pt_{84}:Al_{11}:Cr_3:Ru_2 (at.%) specimens and Pt_{77}:Al_{12}:Cr_6:Ni_5 (at.%) alloy agree quite well with each other. Wenderoth et al. [2007Wen2] determined the activation energy for the growth of Al_2O_3 on Pt_{77}:Al_{12}:Cr_6:Ni_5 (at.%) alloy between 1100°C and 1350°C and obtained 281 kJ/mol. This value slightly varied from the result obtained on the same alloy in the current study, although the variation is still within the errors. This variation may have resulted from approximation of the plotted data and possibly the constant values in Arrhenius equation [Appendix B]. Pt_{86}:Al_{10}:Cr_4 (at.%) displayed the slowest growth rate during oxidation at 1350°C [2001Süs1], but the activation energy cannot be computed from only one value.

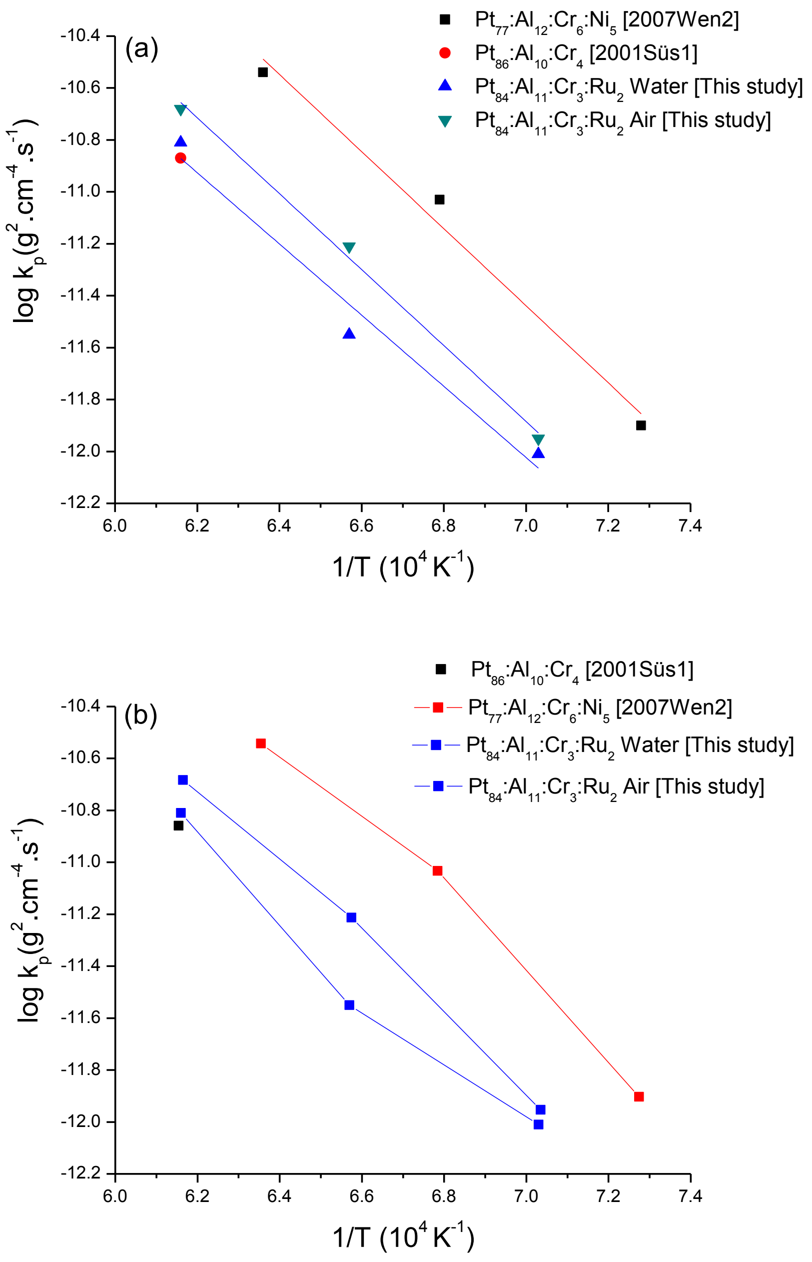

Figure 5.8. Arrhenius plots showing the variation of thickness-related parabolic rate constants for water-quenched and air-cooled nominal $Pt_{84}:Al_{11}:Cr_3:Ru_2$ (at.%) alloys as compared to other Pt-based superalloy (a) linearly fitted plots (b) individual k_p points joined with straight lines ($Pt_{84}:Al_{11}:Cr_3:Ru_2$ (at.%) specimens plots in blue and $Pt_{77}:Al_{12}:Cr_6:Ni_5$ (at.%) alloy in red in Figures a and b).

The activation energy of the water-quenched specimens is the least, indicating a slower growth rate than the air-cooled specimens and the Pt_{77}:Al_{12}:Cr_6:Ni_5 (at.%) alloy [2007Wen1]. In addition, the activation energies of both the water-quenched and air-cooled Pt_{84}:Al_{11}:Cr_3:Ru_2 (at.%) specimens are considerably lower than 356 kJ/mol (85kcal/mol), the value obtained by Felten et al. [1976Fel2] on Pt-6Al (wt%) ($Pt_{87.2}Al_{12.8}$ at.%) alloy. The activation energies obtained from the scale thickness data for the growth of alumina scale on Pt_{84}:Al_{11}:Cr_3:Ru_2 (at.%) specimens (in both quenching media) are higher than those obtained from mass-change data, this may be associated with the mass loss due to volatilization of Pt [1958Pow, 1965Cha, 1976Fel2] and Cr [1987Sto1, 1987Sto2] during the isothermal oxidation.

5.2 Modelling of the growth of α-Al_2O_3 scale on Pt_{84}:Al_{11}:Cr_3:Ru_2 (at.%) alloy

5.2.1 Introduction

A method was used for predicting the alumina scale-thickness of alloys after isothermal oxidation on Pt_{84}:Al_{11}:Cr_3:Ru_2 (at.%) specimens of both quenching media during isothermal oxidation between 1150°C-1350°C. The air-cooled specimens were oxidized up to 500 hours, while the water-quenched specimens were oxidized only up 100 hours, due to sample shortage. The calculated scale thicknesses were then compared to the measured thicknesses to determine the effectiveness of this method. The parabolic relations $y = k_{ps}.t^2 + C$ [1962Kub, 2006Bir] were used, where y is the instantaneous scale thickness after oxidation for time, t, C is the intercept, corresponding to scale thickness during the initial transient period, k_{ps} is the parabolic rate constant. It is assumed for the purpose of this prediction that the scale growth kinetics obeyed the parabolic rate law at all oxidation temperatures and times, even though the data did not lie fully on the parabolic plot. This also assumes that the parabolic rate constant does not change. Thus, this is a simplification only. The thickness of the scale at each oxidation time was calculated using the parabolic rate constant obtained from linearly fitted plots of y against $t^{1/2}$.

5.2.2 Derivation of the Scale Thickness Equation

The parabolic equation [1962Kub, 2006Bir] is:

$$y^2 = k_{ps} t + C \tag{5.2}$$

where y is the instantaneous scale thickness after oxidation for time, t, k_{ps} is the parabolic rate constant, and C is the intercept.

Differentiation of Equation 5.2 gives:

$$2ydy = \left(dk_{ps}\right)t + k_p\left(dt\right) + dC \tag{5.3}$$

where dk_{ps} is the error from the parabolic constant, dt is the time error, dC is the error from the measured intercept as given in Tables 4.2 and 4.3. Then, dy is the error contributions from different parameters, defined as

$$dy = \frac{\left(dk_{ps}\right)t + k_p\left(dt\right) + dC}{2\bar{y}} \tag{5.4}$$

$\bar{y}$ is the mean thickness value, and is given by:

$$\bar{y} = \sqrt{(\bar{k}_{ps})t + \bar{C}} \tag{5.5}$$

where $\bar{k}_{ps}$ is the mean parabolic rate constant, $\bar{C}$ is the mean intercept. Thus, the instantaneous scale thickness, y, a specific exposure time, t, after isothermal oxidation in air can be calculated from Equation 5.6:

$$y = \bar{y} \pm \Delta y \tag{5.6}$$

and (Δy ≈ dy) at all the oxidation temperatures and times.

The plots of measured and calculated scale thickness for the water-quenched specimens are presented in Figure 5.9. The calculated values agree fairly well with the measured values, although the calculated errors were smaller. The errors on the measured values represented the standard deviation, whereas the calculated errors were mostly instrumental errors. However, these errors are unrelated. There are a few places where the values slightly varied, and so the fitted curves for 1350°C crossed twice. Up until 100 h, the calculated values for thickness were below the experimental values, but at 100 h, the reverse was true. This could be due to the larger protrusions at 1350°C, which gave the larger error bars. Similar observations were observed on the air-cooled specimens as shown in Figure 5.10. Thus, the agreement between the measured and the calculated values were less good at 1350°C.

From the plots, it is observed that most of the calculated values fall within the range of measured scale thickness, with little variation for 1150°C and 1250°C. However, the results for 1350°C were different because the protrusions increased at higher temperatures (Figure 5.6). Even with this, the model can still be useful in predicting approximately the scale growth rate for longer exposure times using the parabolic rate constants obtained at reasonably shorter exposure times, say up to 100 hours. Longer exposure time predictions could be problematic since the curves for calculated and measured values diverged more with both time and temperature.

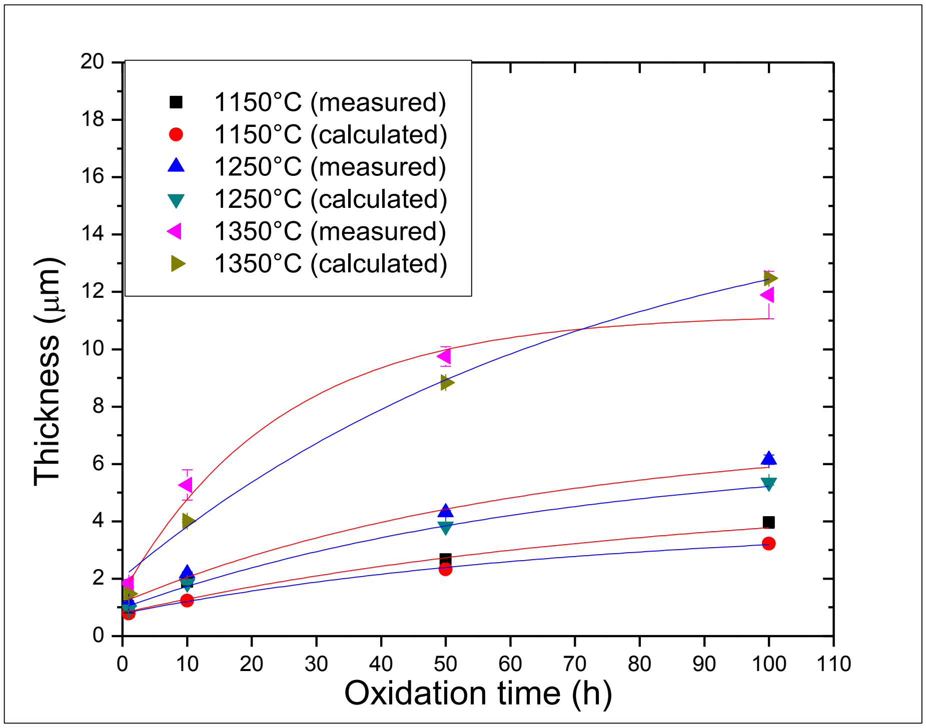

Figure 5.9. Comparison of variation of measured and calculated oxide scale thickness with time for water-quenched nominal Pt_{84}:Al_{11}:Cr_3:Ru_2 (at.%) specimens after isothermal oxidation in air (calculated values in blue and measured values in red).

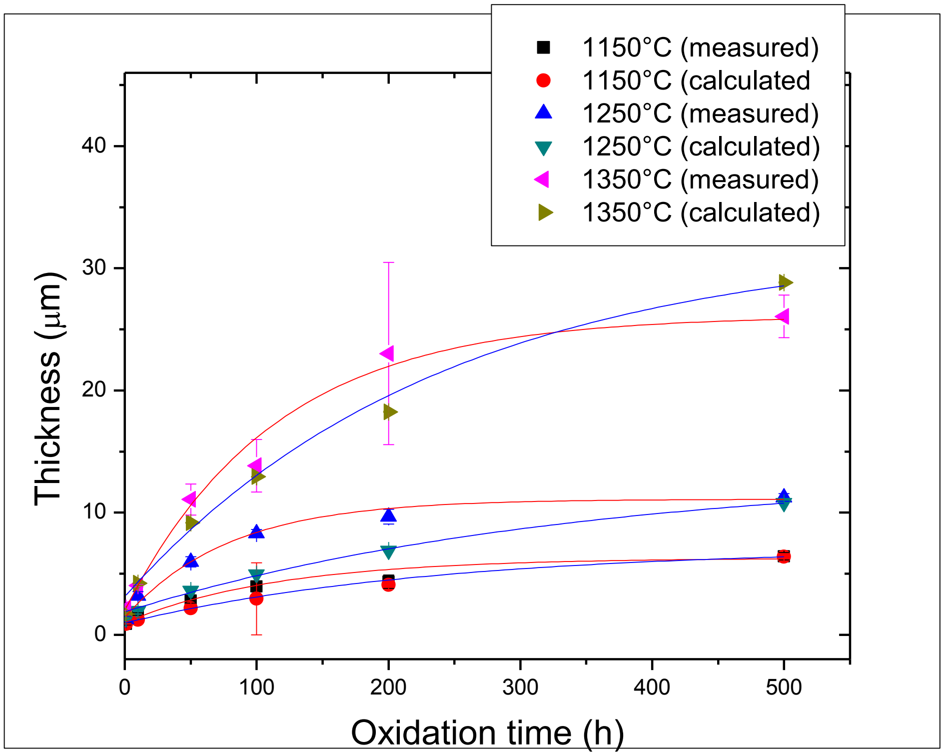

Figure 5.10. Comparison of variation of measured and calculated oxide scale thickness with time for air-cooled nominal Pt_{84}:Al_{11}:Cr_3:Ru_2 (at.%) specimens after isothermal oxidation in air (calculated values in blue and measured values in red).

5.3 Morphologies of the Scales

Examination of the surface morphologies of the oxides formed on Pt_{84}:Al_{11}:Cr_3:Ru_2 (at.%) specimens revealed that the the scales were composed of thin films of α-Al_2O_3 (submicron grain size) with Pt-rich crystals after 1 hour exposure at all oxidation temperatures (Figures 4.12, 4.18-4.19 and 4.26-4.28). The scale morphologies gradually changed from submicron thin films to coarse, large, irregular-shaped grains, a few microns across, with fewer discernable pores after longer exposure times (Figures 4.21, 4.25 and 4.32-4.37). A schematic diagram illustrating the gradual change of the scale morphology is shown in Figure 5.11. The relative intensity of the $(110)_\theta$ diffraction peaks after 100 hours exposure of water-quenched specimen was slightly stronger than expected as shown in Figure 4.52. This may be due to preferred growth direction of the needle-like grains in the scale, as identified by Rybicki et al. [1989Ryb]. However, all other major diffraction peaks of α-Al_2O_3 were found on the scales with their relative intensities nearly as expected at longer exposure times. Thus, the observed variations were not quite significant. Similar obervations were made on the XRD results of the air-cooled specimens after oxidation at higher temperatures (Figures 4.54 and 4.55).

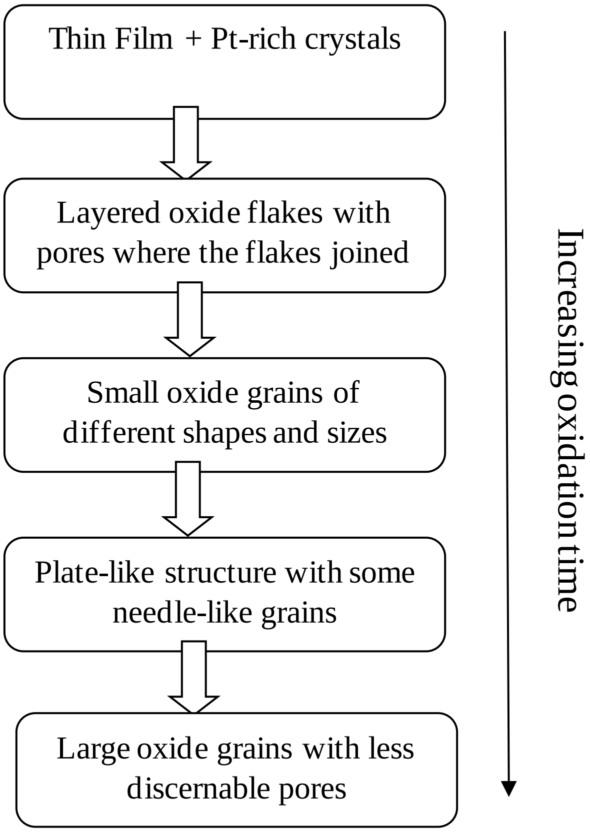

Figure 5.11. Schematic representation of the progressive development of oxide grains (as revealed by the surface morphologies) in the α-Al_2O_3 scales on water-quenched and air-cooled Pt_{84}:Al_{11}:Cr_3:Ru_2 (at.%) specimens during isothermal oxidation in air between 1150°C-1350°C.

The change in the oxide grain sizes with increased oxidation temperatures and times has been explained in terms of inward diffusion of oxygen along oxide boundaries as the major diffusing species [1978Smi, 1979All, 1979Gol], with a minor contribution from outward aluminium transport through the short circuit paths, such as pores, within the grains [1979Sto]. With increased scale thicknesses, further reactions between the substrate alloy and oxygen became diffusion-controlled. That is, inward diffusion of oxygen along oxide boundaries and/or outward

Al ions diffusion through the oxide scale will be the oxidation rate determining steps. Pores were observed on the scale surfaces in this work, but became less discernable with increased oxidation time. The uneveness of the scale surface may also be due to inward oxygen diffusion through the scale grain boundaries (Figures 4.6-4.11). As the scale thicknesses increased and covered the whole specimens' surfaces, the grain boundaries became less discernable and the uneven flakes of oxide grew to form oxide grains.

The cross-sectional images revealed that the α-Al_2O_3 scales formed on the Pt_{84}:Al_{11}:Cr_3:Ru_2 (at.%) specimens were non-uniform in thickness. The scales also exhibited localized oxide protrusions or ridges extending outward at the scale-gas interface, as well as, intrusions of oxide or ridges at the scale-alloy interface (Figures 4.38, 4.41, 4.42, 4.44 and 4.46-4.48), leading to irregular scale-gas and scale-alloy interfaces. Microcracks (Figure 4.44) and pores were observed close to the scale-gas interface, but there was no visible formation of pores at the scale-alloy interface. The pores were expected to become less discernable with the growth of denser scale at higher exposure times, whereas they became more apparent. This could have been due to damage from FIB or inadequate filling of the scale layer by the Pt coating prior to milling (Figure 4.44), or during the sample preparation for cross-sectional examination (Figure 4.48). However, it might also be a real effect, possibly due to depletion of Al in the substrate after longer exposure times, with not enough Al being present for the O, because it was mostly observed then (Figures 4.42, 4.44c, 4.44d and 4.48).

Several authors have reported similar observation that α-Al_2O_3 scales are non-uniform in thickness [1976Fel2, 1980Hin1, 1992Pre, 2000Smi, 2007Wen2]. Ridges or protrusions of oxide at the scale-gas interface, which usually resulted in localized thickening of the scale, were given as an evidence for outward diffusion of aluminium along the short circuit paths, such as pores or microcracks [1979Smi, 1983Smi]. Localized scale thickening also showed that grain boundaries act as diffusion paths for oxygen [1978Smi, 1976Fel1], or for both oxygen and aluminium [1978She, 1980Hin1] in Al_2O_3 scale. Formation of ridges or intrusions of oxide was considered to result from the growth of new oxide at the scale-alloy interface [1979Gol, 1980Sto]. Grain boundaries were also observed under the oxide scales in this work (Figures 4.6-4.8, 4.9-4.11 and 4.42), and could also be acting as diffusion paths for the reacting species. At higher exposure times, the substrate grain boundaries became less discernable due to increased scale thicknesses.

The enclosure of the substrate within the scale and vice versa, which was observed after longer exposure times at higher oxidation temperatures (Figures 4.44, 4.47 and 4.48), may have resulted from continuous lateral growth of the scale as a result of reaction between outward diffusing aluminium ion and inward diffusing oxygen ion at the grain boundaries [1980Gol]. The enclosure of the substrate might also depend on the region sectioned during metallographic sample preparation for cross-sectional examination, as shown in Figure 5.12. If the sample had been sectioned along the line shown in Figure 5.12, then the resulting section would possibly shown an island of substrate within the scale (A), or even (depending on the shape of the interface) an island of scale within the substrate (B).

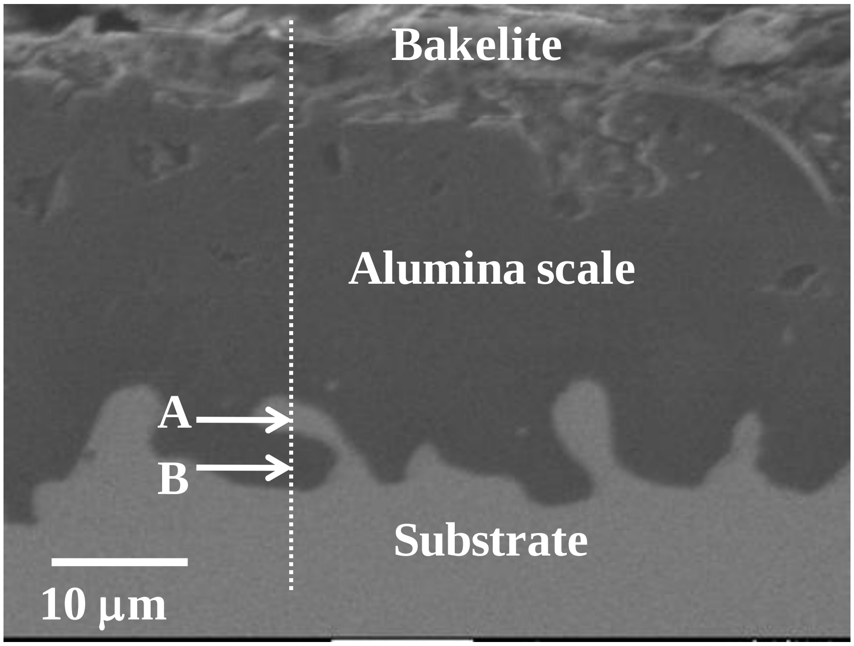

Figure 5.12. The cross-sectional image of Pt_{84}:Al_{11}:Cr_3:Ru_2 (at.%) specimen after 200 h oxidation in air at 1350ºC, showing that the presence of substrate within the scale or vice versa (as shown by the pointed arrows), may be due to region sectioned, during preparation of specimen for cross-section observation.

5.4 Mechanisms of the Scale Formation

Mechanisms of α-Al_2O_3 scale growth are related to the observed morphologies of the scale [1992Pre]. Surface and cross-sectional morphologies of scale layers mainly depend on the nature of oxide phase itself that formed on the scale, since it has been estabilshed that the morphologies of the transistion oxides, such as NiO or spinel [2005Hua1], as well as those of transistion alumina phases are different from that of the α-alumina phase [1982Hin, 1989Ryb, 1992Pre, 2003Sol]. In addition, alloy compositions, as well as oxidation temperatures also have significant contribution [1992Pre]. The presence of whiskers in the scale morphology as been associated with formation of θ-Al_2O_3 [1989Ryb, 1984Mos, 2003Sol]. However, transformation of θ-Al_2O_3 to α-Al_2O_3 at higher oxidation temperatures changed the scale morphology from whiskers to a network of ridges [1989Ryb] or to more crystalline oxide [1984Mos]. The growth kinetics of the scale layers may also influence the morphologies, and thus the growth mechanisms. Scanning electron images of the surface morphology of the oxide scales formed on the water-quenched and the air-cooled Pt_{84}:Al_{11}:Cr_3:Ru_2 (at.%) specimens during the early stages of oxidation, up to 10 hours, revealed the presence of Pt-rich crystals on the alumina scales (Figures 4.12, 4.18-4.19 and 4.26- 4.28). EDS analyses (Figures 4.13 and 4.14), as well as X-ray elemental maps (Figures 4.15, 4.29, and 4.30), also detected the presence of Pt with some Cr at exposure times up to 10 hours, although this could have been due to the interaction volume including some substrate. Similar observations were made on Pt-Al alloys [1976Fel1]; Pt_{87}:Al_{10}:Re_3 (at.%), Pt_{83}:Al_{14}:Re_3 (at.%) and Pt_{82}:Al_{14}:Ta_4 (at.%) alloys [2000Hil]; Pt_{86}:Al_{10}:Cr_4 (at.%) and Pt_{86}:Al_{10}:Ru_4 (at.%) alloys [2001Süs1]; and Pt_{77}:Al_{12}:Cr_6:Ni_5 (at.%) [2007Wen2]. A few diffraction peaks matching PtO_2 and CrO_3 were detected by X-ray diffraction (Figures 4.50-455), possibly due to their lower concentrations in the scale. The volatile platinum oxide, PtO_2 formed when platinum is heated above 1000°C [1976Fel2, 1958Pow, 1965Cha], because Pt is not completely inert to oxygen at high temperatures, as shown in Equation 5.7 [2009You].

$$Pt + O_2 = PtO_2, \Delta G = 164{,}300 - 3.89T \text{ (J/mol)} \tag{5.7}$$

With increasing oxidation times, the Pt-rich crystals from the volatile PtO_2 became embedded in the α-Al_2O_3 scales [1976Fou]. These crystals could be causing the protuberances noted in the cross-sections. In addition, formation of thicker, continuous and protective external alumina scale at higher exposure times protects the Pt from further oxidation [2009You], and thus the scale composed of only α-Al_2O_3 (Figures 4.16, 4.21, 4.32 and 4.32-4.37). EDS and X-ray elemental maps showed that the scale layers consisted of only Al and O at higher exposure times

(Figures 4.17, 4.22 and 4.31). This was confirmed to correspond to α-Al_2O_3 by X-ray diffraction (Figures 4.50-4.55) and Raman spectroscopy (Figures 4.56-4.61).

Protective α-Al_2O_3 scales were formed on the Pt_{84}:Al_{11}:Cr_3:Ru_2 (at.%) specimens because they were oxidized above 1000°C. In addition, the Al contents of the alloy also favoured the formation of protective α-Al_2O_3, rather than the less protective transition aluminas [1970Woo, 1992Pre], as shown below. Development of α-Al_2O_3 scale is accelerated on alloys oxidized above 1000°C [1970Woo, 1971Sto, and 1992Pre], and at sufficiently high Al contents (above 4 wt%) [1992Pre]. Boualam et al. [1993Bou] found that only α-Al_2O_3 was formed during oxidation of an Fe-Cr-Al alloy above 1000°C, while below 900°C, transition θ-Al_2O_3 developed. A study on the isothermal oxidation behavior of a Zr-doped NiAl alloy showed that below 900°C, only θ-Al_2O_3 formed, whereas between 900-1000°C, both θ-and α-Al_2O_3 grew, and at 1000°C and above, only α-Al_2O_3 developed [1989Ryb]. During the examination of oxidation behaviour of Ce- or La-modified Fe-20Cr-5Al alloys in air, it was found that stable α-Al_2O_3 was formed above 950°C [1991Sig].

Felten and Pettit (1976Fel2) reported similar experimental results to the current work, that continuous and well-adhering α-Al_2O_3 scales were developed on platinum-aluminium alloys containing aluminium between 0.5 and 6 wt% (4.1 and 12.8 at.%) during oxidation between 1000°C and 1450°C. In addition, it was also observed the oxide grain sizes of the Pt-Al alloys increased with increased oxidation times, similar to observation in the current study (Tables 4.4 and 4.6). Isothermal oxidation studies of Pt-Al-Cr and Pt-Al-Ru alloys between 1150°C-1350°C showed that a protective external α-Al_2O_3 scale was developed [2000Hil, 2001Süs1]. This was preceded by the formation of discontinuous oxide layers during an initial transient stage of up to 10 hours, on Pt_{84}:Al_{10}:Cr_4 and Pt_{84}:Al_{10}:Ru_4 alloys [2001Süs1]. A protective and continuous α-Al_2O_3 scale with no zone of discontinuous oxide or any internal oxidation was formed on Pt_{80}:Al_{14}:Cr_3:Ru_3 (at.%) isothermally oxidized in air at 1350°C for up to 500 h [2001Süs2]. Wenderoth et al. [2007Wen2] also observed the formation of alumina scale on a Pt_{77}:Al_{12}:Cr_6:Ni_5 (at.%) alloy, when isothermally oxidized in air between 1100°C and 1300°C for up to 400 h, according to parabolic rate law.

The α-Al_2O_3 scales on the Pt_{84}:Al_{11}:Cr_3:Ru_2 (at.%) specimens appeared slightly porous and uneven, forming well-defined grains of different sizes and shapes after 100 hours exposure at almost all the oxidation temperatures (Figures 4.21, 4.25 and 4.32-4.37). The oxide grain sizes gradually increased with increased oxidation time from thin films and small flakes to large coarse grains (Figure 5.11). This resulted in reduction of scale growth rates, indicating that inward diffusion of oxygen is more likely to be the rate-controlling process. The parabolic oxidation rate of Pt_{77}:Al_{12}:Cr_6:Ni_5 (at.%) alloy was also observed to decrease as the scale thickness and oxide grain sizes increased with time, during isothermal oxidation in air between 1100°C and 1300°C for up to 400 hours, as observed by Wenderoth et al. [2007Wen2]. The oxidation kinetics of Pt_{84}:Al_{11}:Cr_3:Ru_2 (at.%) specimens (Figures 5.1 and 5.6), as well as the morphologies of their scales are consistent with this observation. Furthermore, the presence of pores and microcracks near the scale-gas interface (Figures 4.44 and 4.48) also allowed outward aluminium diffusion to contribute to the scale growth, as identified by Felten and Pettit [1976Fel2] and Hindam and Whittle [1980Hin2]. The higher thickness values of the air-cooled specimens at higher oxidation temperatures (Figure 5.6) may have resulted from their faster growth rates, leading to fast cation outward diffusion mechanisms [1989Ryb]. Rybicki et al. [1989Ryb] reported that the high θ-Al_2O_3 growth rates on β-NiAl at 1080°C-1150°C was primarily by outward aluminium diffusion, based on the results of the ^{18}O radioactive tracer experiments.

Figure 5.13 is a schematic representation of development of irregular scale-alloy and scale-gas interfaces, resulting from protrusions of the alloy into the scale (P) and formation of oxide ridges (R), which is typical for diffusion-controlled scale growth [2006Bir]. Protrusions of the scale resulted from outward diffusion of aluminium along the short circuit paths, such as grain boundaries or pores, while oxide ridges showed that inward oxygen ions diffusion along the oxide grain boundaries and/or outward diffusion of aluminium ions through the pores or other short circuit paths have taken place. This explains the cross-sectional images of the scale formed on both the water-quenched and air-cooled specimens (Figures 4.42, 4.44, 4.47 and 4.48). Any inward protrusions of the scale-alloy interface will reduce the diffusion distance across the zone depleted in Al i.e., the substrate alloy, through outward diffusion of Al^{3+}. This is also true for the scale-gas interface. This may have resulted in an irregular interface due to further inward growth of the protrusions [2006Bir].

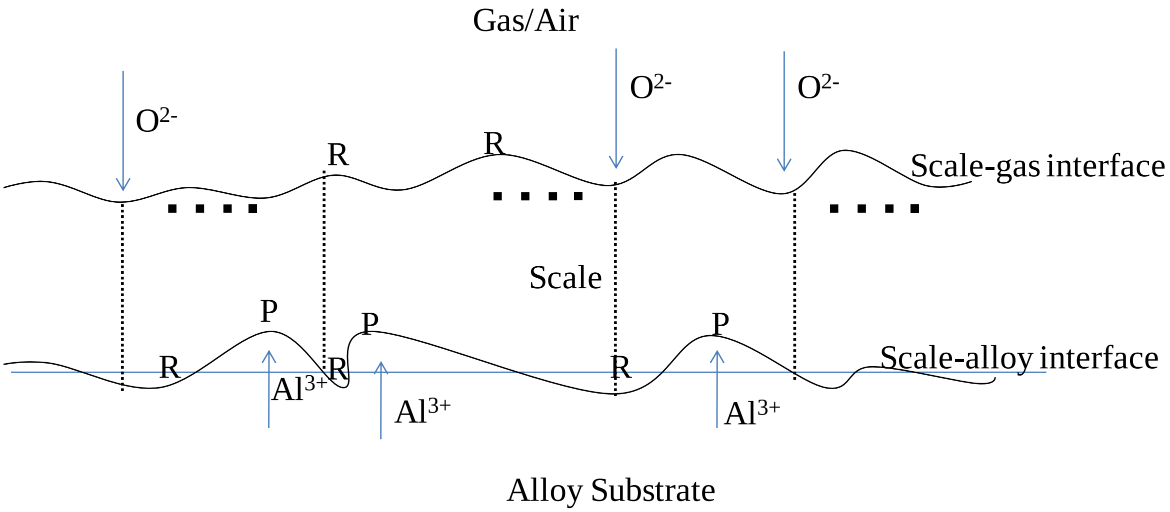

P- Protrusions of the alloy   R-Oxide ridges

Figure 5.13. Schematic representation of diffusion-controlled scale growth, showing the formation of oxide ridges and protrusions through counter-current diffusion of oxygen (anions) and aluminium (cations), leading to irregular scale-alloy and scale-gas interfaces (the dash lines represent grain boundaries, while the squares represent pores).

Tien et al. [1972Tie2] studied the oxidation behavior of an alumina-forming Fe-Cr-Al alloy using Pt markers. It was found that the markers remained at the oxide-gas interface during oxidation, which suggests that the scale grows by inward diffusion of oxygen along grain boundaries. Other studies on the growth mechanism of α-Al_2O_3 on Fe-Cr-Al alloys using an ^{18}O tracer, showed that alumina scales can grow by either a combination of outward diffusion of Al and inward oxygen diffusion [1989Qua, 1987Abd], or nearly exclusive outward diffusion of Al [1987Abd], to react with oxygen at the scale-gas interface. Alumina scales have also been reported to grow by almost exclusive inward diffusion of oxygen in yttria-modified Fe-Cr-Al alloys [1989Qua]. During oxidation of Fe-Cr-Al alloy, Hou et al. [2004Hou] revealed that grain boundaries were the preferred diffusion paths for oxygen. Doychak [1994Doy] showed that α-Al_2O_3 grows primarily by inward diffusion of oxygen along the grain boundaries of NiAl. This mechanism has also been proposed to be the rate controlling transport process during the oxidation of alumina-forming Ni_3Al [1974Kue] and a Ni-15 wt% Cr-6 wt% Al alloy [1979Red].

In Y- or Zr-modified Ni-Al-Cr alloys, it was found that alumina growth occurs by almost exclusive inward oxygen diffusion [1982Ree]. In β-NiAl, the α-Al_2O_3 scale growth was observed to occur by a combination of inward oxygen diffusion and outward Al diffusion [1985You, 1987Jed], while it occurred by only outward diffusion of Al in yttria-modified β-NiAl [1987Jed]. In the oxidation of Pt-Al alloys between 1000°C and 1450°C, it was proposed that the oxidation rates of the alloys appeared to be controlled by inward diffusion of oxygen along grain boundaries in the α-Al_2O_3 scales [1976Fel2].

The X-ray elemental maps of the cross-sections (Figures 4.39, 4.43 and 4.49) showed uniform distribution of Al and O in the substrate for each temperature, but the oxygen in the substrate is due to direct oxidation reaction between the Al and O, during the metallographic sample preparation and not likely from the experiment. No apparent depletion of Al was observed in the substrate after 1 hour exposure at 1150°C (Figure 4.39). Figure 4.43 (100 h oxidation at 1350°C) shows apparently less Al in the substrate and Figure 4.49 shows even less Al after 200 hours exposure at 1150°C. However, these X-ray maps cannot be compared directly, because the beam conditions were obviously different, since the noise above the scale (Bremsstrahlung) is slightly different across the different elements mapped. Although these are for different temperatures, it can be seen that aluminium content of the substrate is decreasing with increased oxidation time, as observed by Wenderoth et al. [2007Wen2] on Pt_{77}:Al_{12}:Cr_6:Ni_5 (at.%) alloy. Wenderoth et al. [2007Wen2] also found that the Al depletion depth increased with increased oxidation time and temperature. Considering the depletion depth of about ~529 µm that was observed after 400 hours oxidation at 1300°C in thicker Pt_{77}:Al_{12}:Cr_6:Ni_5 (at.%) samples (3-4 mm) [2007Wen2], there is a possibility that the depletion depths from the two sides of the current samples (approximately 1 mm thick) could have met, or would soon have met, in the current study. If this was this case, then the oxidation would cease. But this is unlikely, since the specimen oxidized at 1350°C for 200 hours had not reached a plateau (Figure 4.5). Thus, part of the Al depletion zone was observed in the current study (Figures 4.43 and 4.49), but not the depth of the Al depletion zone.

It is proposed that the depth of depletion zone of Pt_{84}:Al_{11}:Cr_3:Ru_2 (at.%) specimens (in both quenching media) will be smaller compared to Pt_{77}:Al_{12}:Cr_6:Ni_5 (at.%) [2007Wen2], because of the smaller oxide grain sizes and scale thickness of the Pt_{84}:Al_{11}:Cr_3:Ru_2 (at.%) alloy after 500 hours exposure at 1350°C. Alumina scale of about 26 µm had formed on Pt_{77}:Al_{12}:Cr_6:Ni_5 (at.%) isothermally oxidized by Wenderoth et al. [2007Wen2] after 400 hours exposure at 1300°C, whereas scale formed on air-cooled Pt_{84}:Al_{11}:Cr_3:Ru_2 (at.%) alloy was 26.06 ± 1.75 µm after 500 hours exposure at 1350°C. Thus, the alloy in this investigation had comparable scale thickness with Pt_{77}:Al_{12}:Cr_6:Ni_5 (at.%) alloy [2007Wen2] oxidized for less time and lower temperature. In addition, oxide grains of about 2-3 µm grew on Pt_{84}:Al_{11}:Cr_3:Ru_2 (at.%) after 500 hours exposure at 1350°C, while they were about 5-10 µm on Pt_{77}:Al_{12}:Cr_6:Ni_5 (at.%) after 400 hours exposure at 1300°C [2007Wen2]. This shows that the growth rate in the current alloy was lower at longer exposure times and higher temperatures than for the Pt_{77}:Al_{12}:Cr_6:Ni_5 (at.%) alloy [2007Wen2]. Furthermore, the parabolic rate constants (Figures 5.4, 5.5 and 5.8), as well as the activation energies (Tables 5.1 and 5.2) of Pt_{84}:Al_{11}:Cr_3:Ru_2 (at.%) alloy (in both quenching media) were smaller, indicating a slower scale growth rate. However, since the extent of depletion of Al in the scale will depend on its concentration and the scale growth rate [2006Bir], thus the Pt_{84}:Al_{11}:Cr_3:Ru_2 (at.%) alloy oxidized more slowly, and so the depth of Al depletion should be lower. A few weak peaks of γ' were also observed at higher temperatures and longer exposure times during the XRD analysis (Figures 4.50-4.55). This may be due to the penetration depth of the X-ray beams or indicating lower depth of Al depletion zone.

The scale growth kinetics data obtained in the current study support the assumption that the growth of the α-Al_2O_3 scale is controlled by thermal diffusion of oxygen along grain boundaries in the oxide scale [1962Kub, 1983Bir, 1988Kof], because the scale growth rate decreased with increased exposure times (Figures 5.1 and 5.6). With increased scale thicknesses and layer oxide grains, potential diffusion paths for oxygen and/or aluminium ions through the oxide scales decreased, thus leading to slower scale growth rates at higher exposure times. The irregular scale interfaces as well as the oxide protrusions and intrusions suggest that counter-current diffusion of ions within the scale and substrate may be responsible for the growth of the α-Al_2O_3 scale [1980Hin]. Furthermore, the activation energies obtained from the rate constants of the water and air-cooled Pt_{84}:Al_{11}:Cr_3:Ru_2 (at.%) specimens agree quite well with activation energies found in the literature for diffusion controlled processes [1979Ama, 1991Sig], as shown in Table 5.3. The activation energy for oxidation of Fe-20Cr-4Al + 0.04% Ce in air [1979Ama] agrees well with the activation energy obtained herein for water-quenched Pt_{84}:Al_{11}:Cr_3:Ru_2 (at.%) specimens.

The activation energy for either outward Al diffusion or inward oxygen diffusion along grain boundaries on alumina scale formed on Fe-20Cr-5Al + 0.005% Ce alloy in synthetic exhaust gas [1991Sig], also agrees fairly well with the activation energies calculated for both the air-cooled Pt_{84}:Al_{11}:Cr_3:Ru_2 (at.%) specimens and Pt_{77}:Al_{11}:Cr_3:Ru_2 (at.%) [2007Wen2]. Thus, the growth mechanism of the α-Al_2O_3 scales on the current Pt_{84}:Al_{11}:Cr_3:Ru_2 (at.%) is proposed to be mainly by inward diffusion of oxygen along the alumina scale grain boundaries, with a small but significant contribution from outward diffusion of Al along the short circuit paths of the scale, such as pores and grain boundaries.

Table 5.3. Activation energies of diffusion-controlled Ce-doped Fe-based superalloys [1979Ama, 1991Sig].

Alloy (wt%)	Temperature range (°C)	Activation energy kJ/gmol	References
Fe-20Cr-4Al + 0.04 Ce	1150-1250	262	[1979Ama]
Fe-20Cr-5Al + 0.005 Ce	950-1150	283 ± 7	[1991Sig]

5.5 Stresses in the Oxide Scales

The characteristic ruby R-line luminescence from Cr^{3+} ions in aluminium oxide obtained from the α-Al_2O_3 scales on both the water-quenched and air-cooled Pt_{84}:Al_{11}:Cr_3:Ru_2 (at.%) alloy specimens was very strong (Figures 4.63-4.65 and 4.68-4.70). This indicates that the technique is suitable for measuring the residual stress on scales formed on the Pt-based alloys. The spectra recorded from all the oxide scales shifted to lower frequency, indicating that the scales were under uniform residual compressive stress, which agrees with results obtained on other alumina-forming alloys and thermal barrier coatings [1996Lip, 1995He, 1997Lip, 1996Chr]. Within the errors, the room-temperature compressive stresses in the oxide scales on both the water-quenched and air-cooled Pt_{84}:Al_{11}:Cr_3:Ru_2 (at.%) specimens followed the same trend. At 1150°C, the room-temperature residual stresses in the scales after shorter oxidation times were low, and later increased to a maximum before reaching a plateau, all within the errors (Figures 4.69 and 4.70). However, at higher oxidation temperatures, the residual stresses decreased gradually with increased oxidation time until a plateau was reached, although high errors could be masking this (Figures 4.65 and 4.70). These observations are depicted in Figure 5.14, and they are consistent with the modelling results of Bull [1998Bul], which was used to predict the stress generation and relaxation in the oxide scales as a function of time and temperature. The predicted growth stress values were compared with measurements of alumina scales on Fe-20Cr-5Al + 0.045% Y + 0.08% Zr alloy oxidized between 1000°C and 1350°C. Bull [1998Bul] established that between 1273K (1000°C) and 1473K (1200°C), the scale growth stresses increased with increased oxidation time, reaching a peak, and then reduced reaching a plateau (Figure 5.15). However, the growth stresses in the scale are continuously relaxed with increased scale thickness or oxidation time between 1523K (1250ºC) and 1623K (1350ºC), as shown in Figure 5.15. Although the predicted growth stress values by Bull [1998Bul] are lower (Figure 5.15) than the compressive residual in the oxide scale of the current alloys, the stress in the oxide scale of the current alloy in this study followed the same trend with the predicted stress values. This low stress value predicted for the FeCrAlY scale may be due to the beneficial effect of Y or may be based on the simplified assumption for the scale growth rate.

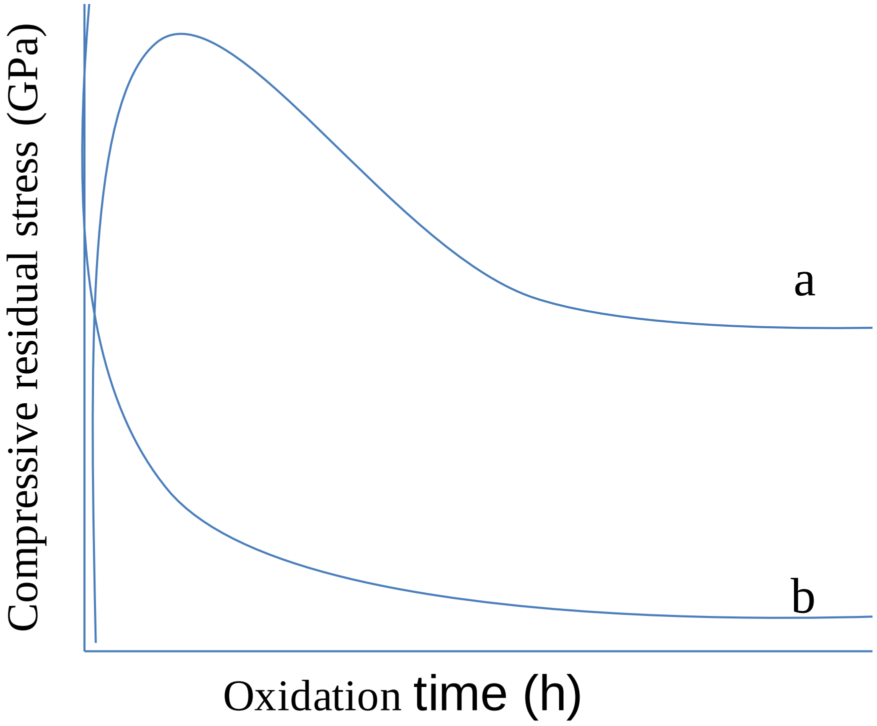

Figure 5.14. A sketch showing the variation of scale stress with time at (a) 1150°C (b) 1250°C and 1350°C.

Simultaneous formation of Pt-rich crystals along with the alumina scale during the transient oxidation stage as shown in Figures 4.12, 4.18, 4.19 and 4.26-4.28), may be responsible for high compressive stresses in the scales for up to 10 hours (Tables 4.9 and 4.10). Above 10 hours, the stresses in the oxide scale became reduced, possibly due to the incorporation of the Pt-rich crystals from volatile PtO_2 into the growing α-Al_2O_3 scale [1976Fou], which also resulted in the protuberances of the scales. Protrusions of the alloy into the scale have been reported to improve the stability of Pt-Al alloys [1976Fel2]. However, since protrusions of the scale increased with increased oxidation time (Figures 4.42, 4.44 and 4.48), lower compressive stresses are found in the scales at longer exposure times (Tables 4.9 and 4.10). Incorporation of Pt-rich crystals into the growing α-Al_2O_3 scale either enhances the stress relief mechanisms or reduces the growth stress generation, as observed by Fountain et al. [1976Fou] during oxidation of various single-phase or duplex iron-base and nickel-base alloy α-Al_2O_3 formers at 1100°C and 1200°C. This observation is consistent with the lower compressive stress in the oxide scales on Pt_{84}:Al_{11}:Cr_3:Ru_2 (at.%) alloy in the current study.

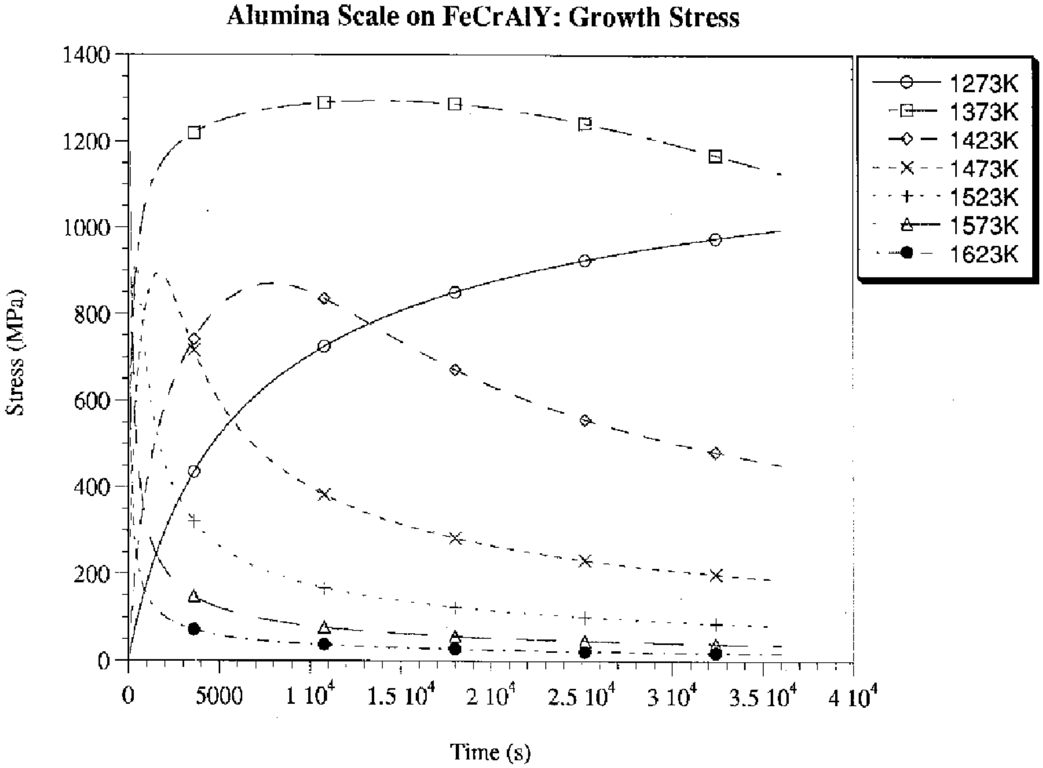

Figure 5.15. Predicted variation of scale stress with time for short-term isothermal oxidation at a range of temperatures (1.8 mm thick FeCrAlY sample, new scale-growth stress 1.4GPa) [1998Bul].

As the scale thickness increased with increased oxidation time (Figures 4.37 and 4.43), the stress induced in the substrate also increased. In addition, the tendency for the substrate to relieve the stresses by creep also increased at higher temperatures [1998Bul]. This explains the decrease in compressive biaxial stress with time in the current study. In addition, the amount of stress relaxation in the scale also increased with increased scale thickness, and became noticeable after longer oxidation times. At very short exposure times, the stresses in the scale are easily relaxed by a small amount of substrate creep because the growth stress in the scale is very low [1998Bul]. This can be a reason for the low compressive stress in the scales after 1 hour exposure at 1150°C, it must be remembered that there will be less creep at lower temperatures and shorter times. At higher temperatures and longer exposure times, the creep relieved the growth stresses in the oxide scale faster, resulting in lower compressive stresses in the scales on Pt_{84}:Al_{11}:Cr_3:Ru_2 (at.%) alloy in the current study (Tables 4.9 and 4.10). The relative independence of the compressive residual stresses with oxidation times after 50 hours exposure (Figures 4.65 and 4.70) signifies that the stresses are mainly due to thermal mismatch between the scales and the alloy substrate on cooling [1996Lip], since the growth stresses are being relieved by the high creep values at longer exposure times [1998Bul].

The coefficient of thermal expansion of Pt, which is the base metal of the alloy, is higher than that of α-alumina, as presented in Table 5.4. Thus, compressive stresses were developed in the scales during cooling, since the magnitude of the stress is proportional to the difference between the coefficient of thermal expansion of the metal and the oxide [2006Bir]. This explains the formation of compressive stresses in the scales on both the water-quenched and air-cooled specimens, in the current study. The coefficient of thermal expansion of Ni is higher than that of Pt, thus higher compressive stresses were found in the scales on the Ni-based alloys (Table 5.5). However, it has been proposed that the scale growth mechanism became diffusion-controlled after the transient oxidation stage (i.e. scale growth by both inward diffusion of oxygen and outward Al ions diffusion through the oxide scale), as represented in Figure 5.13. Thus, the stresses generated by inward oxygen diffusion were relaxed by the outward diffusion of the aluminium ions [2006Kem], thereby making the room-temperature residual stress on the scales nearing a plateau after longer exposure time (Figure 5.14).

Table 5.4. Coefficient of thermal expansion of Pt, Ni and α-Al_2O_3.

Material	Coefficient of thermal expansion, α (10^{-6} /K)	Temperature (K)	References
Pt	8.9	293	[1998Tay]
Ni	12.89	300	[1977Kol]
α-Al_2O_3 (// to c axis)	5.74	300	[1972Yat]
α-Al_2O_3 ($\perp$ to c axis)	5.01	300	[1972Yat]

The growth stress in the scale is low at shorter exposure times, when the scale thickness is very small, and thus the stress can easily be relaxed by small amount of substrate creep [1998Bul]. Rhines and Wolf [1970Rhi] suggested that inward diffusion of oxygen along oxide grain boundaries or microcracks may lead to stress generation in scale, if new oxide can form within the bulk oxide. Some of the growth stress may also be due to an epitaxial relationship between the first-formed oxide and the alloy substrate [1987Sto1], thereby causing the compressive stresses to peak after short exposures. However, some of the growth stresses could have relaxed upon cooling, thereby causing the frequency shift and hence biaxial stress to be independent of oxidation time. This suggests that a steady-state condition is reached under which the rate of stress accumulation is balanced by the rate of stress relaxation within the scale.

The stress gradients through the scale thicknesses obtained from the peak width of the R-lines luminescence of the scales compared with that of the stress-free ruby showed that a noticeable stress gradient exists in the oxide layers. The stress gradients decreased with increased oxidation time at all oxidation temperatures in both quenching media (Figures 4.67 and 4.72), indicating that they decreased as the scale thickens. However, there was an increase in the stress gradient of the air-cooled specimen after 200 hours exposure. This may be due to deeper protrusions of the scale into the substrate at the scale-alloy substrate interface (Figure 4.49b), giving rise to large variation in the scale thickness, and thus high stress gradients through the scale. The decrease in the stress gradients with increased scale thicknesses suggests that the scale stability increased with increased oxidation time, at least for the times tested. The growth kinetics data, as well as compressive stress values, also support this.

Table 5.5. Mean in-plane stress values of scales formed on Pt_{84}:Al_{11}:Cr_3:Ru_2 (at.%) alloy at 1150°C obtained from R-line luminescence as compared with those of other alumina-forming alloys at 1100°C [1996Lip].

Oxidation time (hours)	**Alumina-forming alloy**	**Mean in-plane compressive stress (GPa)**	**Level of scale spallation**
1	Fe-45Ni-25Cr-5Al	6.7 ± 0.6	"Substantial"
1	Fe-45Ni-25Cr-Al+0.01Y	6.4 ± 0.4	"Substantial"
1	Ni-26.5Al-5Cr	3.9 ± 0.2	"Moderate"
1	Ni-31Al-1Y	2.9 ± 0.3	"Moderate
10	Ni-based superalloy[b]	4.1 ± 0.1	"Minimal"
10	Ni-based superalloy[c]	4.1 ± 0.2	"Minimal"
1	Pt_{84}:Al_{11}:Cr_3:Ru_2[w]	1.4 ± 0.2	None
1	Pt_{84}:Al_{11}:Cr_3:Ru_2 [a]	1.5 ± 0.3	None
10	Pt_{84}:Al_{11}:Cr_3:Ru_2[w]	1.8 ± 0.1	None
10	Pt_{84}:Al_{11}:Cr_3:Ru_2 [a]	1.6 ± 0.1	None

[w] Water-quenched, [a]Air-cooled, [b]Ni-7.0Cr-6.2Al-7.5Co-6.5Ta-5.0W-1.5Mo-3.0Re-0.15Hf-0.05C-0.018Y, [c]Ni-7.2Cr-5.6Al-10.0Co-6.5Ta-6.4W-0.6Mo-3.0Re-1.0Ti-0.1Hf.

5.6 Oxide Scale Adherence

A well-adhering α-Al_2O_3 scale, which showed no evidence of spallation, was developed on the Pt_{84}:Al_{11}:Cr_3:Ru_2 (at.%) alloy specimens at all exposure times and temperatures. The absence of spallation showed that thermally induced stresses in the scale did not exceed the cohesive strength of the scale-substrate interface, as was recognized by [1974Gig]. The scale was continuous and protective, and showed a gradual increase in specific mass gain and thickness. Cross-sectional examination of the scale layers showed the protrusion of the alloy substrate into α-Al_2O_3 scale (Figures 4.42, 4.44, 4.47 and 4.48), giving rise to an irregular interface between the alloy substrate and the scale. The development of the irregular scale-substrate interface, by the growth of protrusions, improves the adhesion of the α-Al_2O_3 scale, probably due to mechanical keying as proposed by Felten and Pettit in Pt-Al alloys [1976Fel2].

The cross-sectional images also revealed that there was no discernable formation of pores at the scale-substrate interface, indicating that the scales were potentially protective. However, pores were observed further away from the scale-substrate interface closer to the scale-gas interface (Figures 4.44 and 4.48). Tien and Pettit [1972Tie2] reported that elimination of interfacial cavities improved the scale-substrate adhesion in a yttrium-doped Fe-Cr-Al alloys, such that oxide spallation was not observed. Contrary to this, a Ni-15.1 Ta-6.7 Al (wt.%) alloy doped with 0.04Y showed spallation of oxide scale during cooling. This showed that the thermally induced stresses must have exceeded the cohesive strength of the scale-substrate interface [1974Gig]. However, for an Hf-doped Ni-Ta-Al alloy of the same composition, there were oxide protrusions of HfO_2 that were enveloped with a thin layer of Al_2O_3, which provided improved scale adhesion to the alloy. Thus, virtually no oxide spallation was observed.

A number of studies have shown that the presence of Pt in alloys such as Ni-8Cr-6Al [1976Fel1], Ni-12Cr-9Co (RMJ 2012) and (IN792 +Hf) [1984Tat], FeCrAlY, NiCrAlY and NiCoCrAlY [1986Lut] and various single phase and duplex iron-based and Ni-based superalloys [1976Fou], improved their oxide scale adherence. It was proposed that the adherence was achieved by mechanical keying of the scale to the substrate due to irregularity of the oxide scale [1976Fel1, 1976Fel2], or as a result of decrease in the tendency of formation of convoluted scale, i.e. localized scale detachment from the alloy [1987Sto2], by Al_2O_3. Development of convoluted scale is caused by the scale growth mechanism, leading to development of compressive stress, and detachment of the scale from the alloy [1976Gol, 1979Gol, 1980Gol]. Incorpotation of Pt-rich crystals from volatile PtO_2 have been reported to significantly enhance the isothermal stability of α-Al_2O_3 scale, either by influencing the stress relief mechanisms or reducing oxidation growth stress generation [1976Fou]. The stress relief mechanism may be achieved through enhanced diffusional creep or grain boundary sliding of the alumina scale, while the reduction in growth stress generation may be by a mechanism similar to those proposed to explain the influence of reactive elements, such as yttriumin or zirconium on the growth and adhesion of Al_2O_3 scales on Fe-Cr-Al and Ni-Cr-Al superalloys, as explained by Fountain et al. [1976Fou]. Reactive elements improve the scale adherence through the development of inward growing pegs of the oxides of the reactive-elements, which are incorporated in the alumina scale, leading to irregular scale-alloy interface. Furthermore, Gleeson et al. [2009Gle] showed that the addition of Pt to β-NiAl and γ'-Ni_3Al + γ-Ni alloys promoted the formation and adhesion of Al_2O_3 scale, although the adhesion mechanisms were not reported.

From the present results, some factors are proposed to account for the good adhesion of the α-Al_2O_3 scale to the substrate of the water-quenched and air-cooled Pt_{84}:Al_{11}:Cr_3:Ru_2 (at.%) specimens. These factors include:

(1) Mechanical keying of the scale to the substrate due to the protrusions of the substrate into the scale, which gave rise to irregular scale-substrate interface;

(2) Absence of discernable pores at scale-substrate interface;

(3) Low compressive stresses in the α-Al_2O_3 scales formed on the specimens during cooling as a result of difference between the coefficient of thermal expansion of Pt and alumina, as well as growth stress relief through the scale growth mechanism and incorporation of Pt-rich crystals into the growing α-Al_2O_3 scale.

It can be concluded that the scale on the air-cooled specimens potentially possessed better adhesion than on the water-quenched specimens, based on higher protrusions of their scales into the substrate. This was a result of faster scale growth rates, leading to higher scale thicknesses (Tables 4.7 and 4.8). Vorberg et al. [2004Vor] showed that $Pt_{78.5}$:$Al_{12.5}$:Cr_3:Ni_6 (at.%) quenched in water after heat-treatment at 1500ºC contained small γ' precipitates with a volume fraction of about 3 %, whereas air-cooled samples were found to contain evenly distributed cuboidal-shaped γ' precipitates, with ~30 % volume fraction. The faster scale growth kinetics of the air-cooled specimens may be due to a higher volume fraction of γ' in the as-cast alloy. Here, the microstructure of the air-cooled specimens could not be resolved, but the Al content was less, which would be expected to give a lower volume fraction of γ'. In both studies, the air-cooled specimens had thicker scales. One reason for thicker scale could be more Al, but this was not true for the current alloys. Another reason could be more γ' (~Pt_3Al) precipitates, which would give more available Al for the scale. Vorberg et al. [2004Vor] noticed the depletion of Al near the surface was by the depletion of γ' precipitates. This shows the Al in the scale originates from the γ' precipitates, and so it is likely that the air-cooled specimens could have had more γ' precipitates, especially given that Pt_{85}:Al_7:Cr_5:Ru_3 (at.%) [2004Cor] had a ~ 30 % precipitate volume. These alloys have four components, and so the proportion of γ' (~Pt_3Al) precipitates might not be directly proportional to the Al content, since Al is in both phases, ~Pt_3Al and (Pt). It is thought that the faster scale kinetics of the air-cooled specimens, giving thicker scales, might have resulted from more ~Pt_3Al in those samples. In addition, lower room-temperature compressive stresses in the α-Al_2O_3 scales on the air-cooled specimens (Tables 4.9 and 4.10), may also be due to higher scale protrusions, and so played a beneficial role, although the errors were large.

CHAPTER SIX

6.0 Conclusions and Recommendations

6.1 Conclusions

Based on the results from the isothermal oxidation study of both the water-quenched and air-cooled nominal $Pt_{84}:Al_{11}:Cr_3:Ru_2$ (at.%) specimens in air at 1150°C, 1250°C and 1350°C, the following conclusions can be drawn.

1. Scanning electron microscopy (SEM) surface and cross-section examinations, as well as FIB-SEM cross-sectional examinations, showed that the oxide scales formed on the alloy specimens were continuous and adherent to the substrate. The scale layers were composed mainly of α-Al_2O_3, as confirmed by XRD and Raman spectroscopy.
2. The scale thicknesses, as well as specific mass of both the water-quenched and air-cooled specimens, increased with increased oxidation time according to the parabolic law, which is typical for protective oxide scale. However, the parabolic scaling rate of the air-cooled specimens is faster than the water-quenched specimens at least up to 100 hours, although errors could be masking this.
3. The activation energies and the kinetics data support the proposal that the growth of the α-Al_2O_3 scale is controlled by the diffusion of oxygen along grain boundaries in the oxide scale. The unevenness of the scale interfaces, as well as the oxide protrusions and intrusions suggest that counter-current diffusion of ions within the scale and substrate may be responsible for the growth of the α-Al_2O_3 scale.
4. During the stress measurement using photostimulated luminescence, the α-Al_2O_3 scales fluoresce due to excitation of trace concentrations of Cr^{3+} in the scales, giving rise to characteristic strong R-lines luminescence spectra. This indicates that this non-destructive and non-contact technique is suitable for measuring the stress development in the scales of Pt-based alloys.

5. The room temperature stresses in the scales of the current alloy were compressive and lower than those of the Ni- and Fe- based superalloys oxidized at lower temperatures. This indicates that current alloy potentially possesses better oxidation resistance.

6. The peak widths of the R-line over the range of oxidation times studied indicated a stress gradient in the scales. The reduction of the average peak width with increased oxidation time indicated that the scales had lower stress gradients, and hence became more stable as the adherence improved at higher exposure times.

7. Improved adhesion of the α-Al_2O_3 scale to the substrate of the Pt_{84}:Al_{11}:Cr_3:Ru_2 (at.%) specimens is proposed to be mainly dependent on the mechanical keying of the scale to the substrate due to protrusions of the alloy into the scale, which gave rise to an irregular scale-substrate interface. Other factors such as: absence of voids at the scale-substrate interface; and low compressive stresses in the α-Al_2O_3 scales formed on the specimens during cooling as a result of stress relief through the scale growth mechanism and incorporation of Pt-rich crystals into the growing α-Al_2O_3 scale as well as slightly smaller difference between the coefficient of thermal expansion of Pt-rich substrate and alumina.

8. Formation of protective, non-spalled α-Al_2O_3 scales and low room temperature compressive stress in the scale are essential criteria for long term stability of oxide scales developed during high temperatures exposure. Thus, it can be concluded that the current alloy possesses better oxidation resistance than the Fe-and Ni-based high-temperature alloys, and it has promising potential for high temperature applications, such as in turbine engines.

It has been established from the findings in this study that a well-adhering, continuous and protective external α-Al_2O_3 scale was developed on the nominal Pt_{84}:Al_{11}:Cr_3:Ru_2 (at.%) alloy. The room temperature compressive stresses in the scale have also been found to be low, which improved the scale adherence to the substrate. Oxidation kinetics of the alloy were presented along with the activation energies, while the growth mechanisms were discussed in relation to the scale morphologies. Factors were proposed to be responsible for the improved adhesion of the scale to the substrate alloy. Although the errors masked some of the differences between the water-quenched and air-cooled specimens, the results indicated that the water-quenched specimens potentially possess better oxidation properties.

6.1 Recommendations

Despite these encouraging findings, further modifications to the alloy or processing method is necessary to optimize the oxidation properties, as well as the mechanical properties of the alloy before commercialization. On this basis, the following suggestions are considered necessary for future study:

1. TEM studies of the scale-alloy interface may be necessary in order to understand the crystal structure orientation relationship between the scale and the substrate.
2. The contiguity of the scale with the underlying substrate needs to be further investigated, in order to understand the detailed mechanisms of diffusion in oxide scale as it affects the Al depletion zone. This can be achieved through etching of the cross-sectional samples to reveal the depletion zone.

REFERENCES

[1957Cha] J.C. Chaston, "Oxidation and Volatilisation of Platinum at High Temperature”, *Platinum Metals Review,* 1957, 1, (2), 55-57.

[1958Pow] A.R. Powell, “Behaviour of the Platinum Metals at High Temperatures”, *Platinum Metals Review,* 1958, 2, (3), 95-98.

[1961Sme] W.W. Smeltzer, R.R. Haering and J.S. Kirkaldy, "Oxidation of Metals by Short-Circuit and Lattice Diffusion of Oxygen ", *Acta Metallurgica,* 1961, 9, 880-885.

[1962Kni] J.B. Knight and B. Taylor, “Production and Properties of Grain Stabilised Platinum and Platinum alloys, *Powder Metallurgy*, 1962, 10, 108-118.

[1962Kub] O. Kubaschewski and B.E. Hopkins, "Oxidation of Metals and Alloys”, 2nd edition, 1962, Butterworths, London.

[1962Pal] A.E. Paladino and W.D. Kingery, “Aluminium Ion Diffusion in Aluminium Oxide”, *Journal of Chemical Physics,* 1962, 37, 957-963.

[1963Fle] R.L. Fleischer, "Substitutional Solution Hardening", *Acta Metallurgica*, 1963, 11, 203-210.

[1964Bar] D.J. Barber, “Electron Microscopy and Diffraction by Aluminium Oxide Whiskers”, *Philosopical Magazine,* 1964, 10, (103), 75-94.

[1965Tie] T.E. Tietz and J.W. Wilson, “Behavior and Properties of Refractory Metals”, Edward Arnold Ltd, London, 1965, 419.

[1965Cha] J.C. Chaston, “Reactions of Oxygen with Platinum Metals”, *Platinum Metals Review,* 1965, 9, (2), 51-56.

[1965Hau] K. Hauffe, "Oxidation of Metals", Plenum Press, New York, U.S.A. 1965.

[1966Kof] P. Kofstad, “High Temperature Oxidation of Metals, Wiley Interscience, New York, U.S.A., 1966.

[1968Dar]	A.S. Darling, G.L. Selman and A.A. Bourne, "Dispersion Strengthened Platinum Improved High Temperature Creep Properties", *Platinum Metals Review,* 1968, 12, (1), 7-13.
[1970Git]	W.H. Gitzen, "Alumina as a Ceramic Material" *Journal of American Ceramic Society*, 1970, 17.
[1970Rhi]	F.N. Rhines and J.S. Wolf, "The Role of Oxide Microstructure and Growth Stresses in the High-Temperature Scaling of Nickel", *Metallurgical and Materials Transactions B*, 1970, 1, 1701-1712.
[1970Woo]	G.C. Wood, "High Temperature Oxidation of Alloys", *Oxidation of Metals*, 1970, 2 (1), 11-57.
[1971Gig]	C. S. Giggins and F. S. Pettit, "The Oxidation of Ni-Cr-Al Alloys between 1100 and 1200°C", *Journal of Electrochemical Society,* 1971, 118, 1782-1790.
[1971Gow]	G.W. Goward and D.H. Boone, "Mechanisms of Formation of Diffusion Aluminide Coatings on Nickel-Base Superalloys", *Oxidation of Metals*, 1971, 3, 475-495.
[1971Kea]	B.H. Kear, F.S. Pettit, D.E. Fornwalt and L.P. Leamire, "On the Transient Oxidation of a Ni-15Cr-6Al Alloy", *Oxidation of Metals*, 1971, 3, 557-569.
[1971Sto]	F.H. Stott, G.C. Wood and M.G. Hobby, "Comparison of the Oxidation Behaviour of Iron-Chromium-Aluminium, Nickel-Chromium-Aluminum, and Cobalt-Chromium-Aluminium Alloys", *Oxidation of Metals,* 1971, 3(2), 103-113.
[1971Wal]	G.R.Wallwork and A.Z. Hed, "Some Limiting Factors in the Use of Alloys at High Temperatures", *Oxidation of Metals*, 1971, 3, 171.
[1972Cha]	G.A. Chadwick, "Metallography of Phase Transformations", Butterworths, London, 1972.
[1972Tie1]	J.K. Tien and R.P. Gamble, "Effects of Stress Coarsening on Coherent Particle Strengthening", *Metallurgical Transactions*, 1972, 3, 2157-2162.

[1972Tie2] J.K. Tien and F.S. Pettit, "Mechanism of Oxide Adherence on Fe-25Cr-4Al Yt or Sc Alloy", *Metallurgical Transactions*, 1972, 3, 1587-1596.

[1972Yat] B. Yates, R.F. Cooper and A.F. Pojur, "Thermal Expansion at Elevated Temperatures. II. Aluminium Oxide: Experimental Data between 100 and 800 K and their Analysis", *Journal of Physics C: Solid State Physics*, 1972, 5, 1046-1058.

[1973Han] P. Hancock, "What is the Role of Stress in Oxidation", Proceeding of High-Temperature Corrosion of Aerospace Alloys, Eds. J. Stringer, R.I. Jaffee and T.F. Kearns, 1973, 117-124.

[1973Jan] M.M.P. Janssen, "Diffusion in Nickel-rich Part of the Nickel-Aluminium System at 1000-1300°C", *Metallurgical Transactions*, 1973, 4, 1623-1631.

[1974Bur] J.J. Burke, A.E. Gorum and R.N. Katz (Eds.), "Ceramics for High-Performance Applications, Proceedings of the Second Army Materials Technology Conference, Hyannis, MA, USA, November 13-16, 1973, Brook Hill Publication Company, Chestnut Hill, MA, 772.

[1974Gig] C.S. Giggins, B.H. Kear, F.S. Pettit and J.K.Tien, "Factors Afffecting Adhesion of Oxide Scales on Alloys", *Metallurgical Transactions*, 1974, 1685-1688.

[1974Han] P. Hancock and R.C. Hurst, "Advances in Corrosion Science and Technology", Eds. R.W. Staehle and M.G. Fontana, 1974, Plenum Publisher, New York.

[1974Kue] J.D. Kuenzly and D.L. Douglass, "The Oxidation Mechanism of Ni_3Al Containing Yttrium", *Oxidation of Metals*, 1974, 8, 139-154.

[1974Kum] A. Kumar, M. Hasrallah and D.L. Douglass, "Effects of Yttrium and Thorium on the Oxidation Behaviour of Ni-Cr-Al Alloys", *Oxidation of Metals*, 1974, 8, 227-249.

[1974Law] K.R. Lawless, "The Oxidation of Metals", *Report on Progress in Physics*, 1974, 37, 231-316.

[1975Gig] C.S. Giggins, E.J. Felten and F.S. Pettit, “Growth Stress Induced Morphological Features of Al_2O_3 Scales Developed on Alloys during Oxidation”, in Stress Effects and the Oxidation of Metals, Ed. J.V. Cathcart, 1975, (Metallurgical Society of AIME).

[1975Raj] R. Raj and M.F. Ashby, “Intergranular Fracture at Elevated Temperature”, *Acta Metallurgica*, 1975, 2, 653-666.

[1975Sme] W.W. Smeltzer and D.J. Young, “Oxidation Properties of Transition Metals”, *Progress in Solid-State Chemistry*, 1975, 10, 17-54.

[1976Fel1] E.J. Felten and F.S. Pettit, “Use of Platinum and Rhodium to Improve Oxide Adherence on Ni-8Cr-6Al Alloys”, *Oxidation of Metals*, 1976, 10(3), 23-28.

[1976Fel2] E.J. Felten and F.S. Pettit, “Development, Growth and Adhesion of Al_2O_3 on Platinum-Aluminium Alloys”, *Oxidation of Metals*, 1976, 10(3), 189-223.

[1976Fou] J.G. Fountain, F.A. Golightly, F.H. Stott and G.C. Wood, “The influence of Platinum on the Maintenance of α-Al_2O_3 as a Protective Scale”, *Oxidation of Metals*, 1976, 10 (5), 341-345.

[1976Gol] F.A. Golightly, F.H. Stott and G.C. Wood, “The Influence of Yttrium Additions on the Oxide-Scale Adhesion to an Iron-Chromium-Aluminium Alloy”, *Oxidation of Metals*, 1976, 10, 163-187.

[1976Lie] C.H. Liebert, R.E. Jacobs, S. Stecura and C.R. Morse, “Durability of Zirconia Thermal Barrier Ceramic Coating on Air-cooled Turbine Blades in Cyclic Jet Engine Operation”, Report TMX-3410 (National Aeronautics and Space Administration, Washington, DC, 1976).

[1976Wal] G.R. Wallwork, “The Oxidation of Alloys”, *Report on Progress in Physics*, 1976, 39, 401-483.

[1977Gib] G.B. Gibbs and R. Hales, “The Influence of Metal Lattice Vacancies on the Oxidation of High Temperature Materials”, *Corrosion Science*, 1977, 17, 487-494.

[1977Kol] T.G. Kollie, “Measurement of the Thermal Expansion of Nickel from 300 to 1000 K and Determination of the Power-Law Constants near the Curie Temperature”, *Physical Review B*, 1977, 16, (11), 4872-4881.

[1978All] I.M. Allam, D.P. Whittle and J. Stringer, “The Oxidation Behaviour of Co-Cr-Al Systems Containing Active Element Additions”, *Oxidation of Metals*, 1978, 12, (1), 35-66.

[1978Hut] R. Hutchings and M.H. Loretto, “Compositional dependence of Oxidation Rates of NiAl and CoAl”, *Metal Science*, 1978, 12 (11), 503-510.

[1978She] J.S. Sheasby and D.B. Jury, “Electrical Properties of Growing Alumina Scales”, *Oxidation of Metals*, 1978, 12 (6), 527-539.

[1978Smi] J.L. Smialek, “Oxide Morphology and Spalling Model for NiAl”, *Metallurgical Transactions A*, 1978, 9, (3), 308.

[1978Spe] M.V. Speight and J.E. Harris, “The Generation of Stresses in Oxide Films Growing by Cation Diffusion” *Acta Metallurgical*, 1987, 26, 1043-1045.

[1979All] I.M. Allam, D.P. Whittle and J. Stringer, “Improvement in Oxidation Resistance by Dispersed Oxide Addition: Al_2O_3 Forming Alloys”, *Oxidation of Metals*, 1979, 13, 381-401.

[1979Ama] T. Amano, S. Yajima and Y. Saito, “High Temperature Oxidation Behaviour of Fe-20Cr-Al Alloys with Small Additions of Cerium”, *Transaction of Japan Institute of Metals*, 1979, 20, 431-441.

[1979Bra] E.F. Bradley (Editor), "Source Book on Materials for Elevated-Temperature Applications", 1979, American Society for Metals, USA.

[1979Doy] P.J. Doyle, “Glass-Making Today”, Portcullis Press Limited, Redhill, Surrey, United Kingdom, 1979, 242-245.

[1979Gol] F.A. Golightly, F.H. Stott and G.C. Wood, “The Relationship Between Oxide Grain Morphology and Growth Mechanisms for FeCrAl and FeCrAlY Alloys”, *Journal of Electrochemical Society,* 1979, 126, 1035-1042.

[1979Hou] L.D. Hou, S.K. Tiku, H.A. Wang and F.A. Kroger, “Conductivity and Creep in Acceptor-Dominated Polycrystalline Al_2O_3”, *Journal of Material Science,* 1979, 14, 1877-1889.

[1979Red] K.P.R. Reddy, “Oxygen Diffusion in Close Packed Oxides”, *Dissertation Abstracts International B,* 1979, 40 (5), 2314.

[1979Smi] J.L. Smialek, “The Relationship between Grain Morphology and Growth Mechanisms for Fe-Cr-Al and Fe-Cr-Al-Y alloys”, *Journal of Electrochemical Society,* 1979, 126, (12), 2275-2276.

[1979Sto] F.H. Stott, G.C. Wood and F.A. Golightly, “The Isothermal Oxidation Behaviour of Fe-Cr-Al and Fe-Cr-Al-Y alloys at 1200°C”, *Corrosion Science,* 1979, 18 (11), 869-887.

[1980All] I.M. Allam, H.C. Akuezue and D.P. Whittle, “Influence of Small Pt Additions on Al_2O Scale Adherence”, *Oxidation of Metals,* 1980, 14, 517-530.

[1980Del] D. Delaunay, A.M. Huntz and P. Lacombe, “Mechanical Stress Developed in High Temperature Resistant Alloys during Isothermal and Cyclic Oxidation Treatments: The Influence of Yttrium Additions on Oxide Scale Adherence”, *Corrosion Science,* 1980, 20, 1109-1117.

[1980Gol] F.A. Golightly, F.H. Stott and G.C. Wood, “The Early Stages of Development of Al_2O_3 Scales on the Fe-Cr-Al and Fe-Cr-Al-Y alloys at High Temperature”, *Oxidation of Metals*, 14, 1980, 217-234.

[1980Hin1] H. Hindam and W.W. Smeltzer, “Growth and Microstructure of α- Al_2O_3 on β-NiAl”, *Journal of Electrochemical Society*, 1980, 127, 1630-1635.

[1980Hin2] H. Hindam and W.W. Smeltzer, “Application of Auger Electron Spectroscopy and Inert Metal Marker Techniques to Determine Metal and Oxygen Transport in Oxide Films on Metals”, *Oxidation of Metals*, 1980, 18, 337-349.

[1980Ree] D.J. Reed and B.J. Wuensch, “Ion-Probe Measurement of Oxygen Self Diffusion in Single Crystal Al_2O_3”, *Journal of American Ceramic Society*, 1980, 63, 83-93.

[1980Row] P.C. Rowlands, M.I. Manning and J. Soo, “The Effects of Substrate Creep on the Structure of Oxide Scales Formed on Fe-9% Cr Steel”, *Proceedings of European Symposium on Interaction between Corrosion and Metal Stresses at High Temperature*, 1980, Petten, 289-294.

[1980Sto] F.H. Stott, G.C. Wood, M. Hirbod and F.A. Golightly, “The Growth and Microstructure of α-Alumina on the High-Temperature Iron-Chromium Base Alloys”, *Proceeding of Institution of Metallurgists Conference on Environmental Degradation of High Temperature Mater*ials, London, 1980, 2 (13), 1-7.

[1980Wan] H.A. Wang and F.A. Kroger, “Chemical Diffusion in Polycrystalline Al_2O_3”, *Journal of American Ceramic Society*, 1980, 63, 613-619.

[1981Gas] D. R. Gaskel, “Introduction to Metallurgical Thermodynamics”, 2nd edition, McGraw-Hill, New York, 1981.

[1981Gib] G.B. Gibbs, “On the Influence of Metal Lattice Diffusion on Oxidation of Metals and Alloys”, *Oxidation of Metals*, 1981, 16, 147.

[1981Smi] J.L. Smialek, “Microstructure of Al_20_3 Scales Formed on NiCrAl Alloys”, National Aeronautics and Space Administration Technical Memo, 81676, 1981.

[1982Eva] A.G. Evans, “Recent Advances in Creep of Engineering Alloy Structures”, Pineridge, Swansea, Eds. B. Wilshire and D.R.I. Owen, 1982, 53-59.

[1982Hin] H. Hindam and D.P. Whittle, “Microstructure, Adhesion and Growth Kinetics of Protective Scales on Metals and Alloys”, *Oxidation of Metals*, 1982, 18, 245-284.

[1982Mes] R.P. Messmer and C.L. Briant, “The Role of Chemical Bonding in Grain Boundary Embrittlement”, *Acta Metallugica*, 1982, 30, 457-462.

[1982Ree] K.P.R. Reedy, J.L. Smialek and A.R. Cooper, “Oxygen Tracer Studies of Al_2O_3 Scale Formation on NiCrAl Alloys”, *Oxidation of Metals,* 1982, 17, 429-443.

[1983Eva] A.G. Evans, G.B. Crumley and R.E. Demaray, “On the Mechanical Behaviour of Brittle Coatings and Layers”, *Oxidation of Metals,* 1983, 20, 193-216.

[1983Bir] N. Birks and G.H. Meier, “Introduction to High-Temperature Oxidation of Metals”, Edward Arnold (Publishers) Ltd., 1983, London, 198.

[1983Kro] F.A. Kroger, “Defects and Transport in SiO_2, Al_2O_3 and Cr_2O_3” in: High Temperature Corrosion, Ed. R.A. Rapp, NACE-6, 1983, Houston, 89-94.

[1983Rap] R.A. Rapp, “The High Temperature Oxidation of Metals Forming Cation-Diffusing Scales”, *Metallurgical Transaction A*, 1983, 15, 765-782.

[1983Ric] R.A. Ricks, A.J. Porter and R.C. Ecob, “The Growth of Gamma Prime Precipitates in Nickel-Base Superalloys”, *Acta Metallurgica,* 1983, 31, 43-53.

[1983Smi] J.L. Smialek and R. Gibala, “Diffusion Processes in Al_2O_3 Scales: Void Growth, Grain Growth and Scale Growth”, *High Temperature Corrosion*, 1983, NACE, 6, 274-283.

[1984Mos] P.T. Moseley, K.R. Hyde, B.A. Bellamy and G. Tappin, “The Microstructure of the Scale Formed during High Temperature Oxidation of a Fe-Cr Alloy Steel”, *Corrosion Science*, 1984, 24, (6), 547-565.

[1984Och] S. Ochiai, Y. Oya and T.Suzuki, “Alloying Behaviour of Ni_3Al, Ni_3Ga, Ni_3Si and Ni_3Ge”, *Acta Metallurgica*, 1984, 32, 289-298.

[1984Sme] J.G. Smeggil, A.W. Funkenbusch and N.S. Bornstein, “Mechanistic Effect of Laser Surface Processing and Reactive Element Addition on the Oxidation Performance of Protective Coating Compositions” Presented at the Spring Meeting of Electrochemical Society, Cincinnati, 1984, Ohio.

[1984Tat] G.J. Tatlock and T.J. Hurd, "Platinum and the Oxidation Behaviour of a Nickel Based Superalloys", *Oxidation of Metals*, 1984, 22, 201-226.

[1984Zha] J.G. Zhao and A.M. Huntz, "Theoretical Analysis of the Deflection Test used in Single-Surface Oxidation of Metallic Samples", *Journal of Materials Science*, 1984, 19, 3166-3172.

[1985Ati] H.V. Atkinson, "A review of the Role of Short-circuit diffusion in the Oxidation of Nickel, Chromium, and Nickel-Chromium alloys", *Oxidation of Metals*, 1985, 24, 177-197.

[1985Fun] A.W. Funkenbusch, J.G. Smeggil and N.S. Bornstein, "Reactive Element-Sulfur Interaction and Oxide Scale Adherence", *Metallurgical Transactions A*, 1985, 16, 1164-1694.

[1985Hon] Y. Honnorat, "Les Superalliages de Nickel. Clé des Technologies à Haute Température", Annales des Mines, 1985, 1-10.

[1985Liu] C.T. Liu, C.L. White and J.A. Horton, "Effect of Boron on Grain-Boundaries in Ni_3Al", *Acta Metallurgica*, 1985, 33, 213-229.

[1985Mis] Y. Mishima, S. Ochiai and T. Suzuki, "Lattice Parameters of Ni (γ), Ni_3Al (γ') and Ni_3Ga (γ') Solid Solutions with additions of Transition and B-Subgroup elements", *Acta Metallurgica*, 1985, 13, 1161-1169.

[1985Mro] S. Mrowec, "Transport of Gaseous Species in Growing Oxides", *Oxidation of Metals*, 1985, 23 (5/6), 266-270.

[1985Tag] T. Takasugi, E.P. George, D.P. Pope and O. Izumi, "Intergranular Fracture and Grain Boundary Chemistry of Ni_3Al and Ni_3Si", *Scripta Metallugica*, 1985, 19, 551-556.

[1985You] E.W.A. Young and J.H.W. deWit, "The Use of a ^{18}O tracer and Rutherford Back Scattering Spectrometry to Study the Oxidation Mechanism in NiAl", *Solid State Ionics*, 1985, 16, 39-46.

[1986Lut] K.L. Luthra and C.L.Briant, “Mechanism of Adhesion of MCrAlY Alloys*”,* *Oxidation of Metals,* 1986, 26 (5/6), 397-416.

[1986McA] A.J. McAlister and D.J. Kahan, “The Al-Pt (Aluminium-Platinum) System”, *Bulletin of Alloy Phase Diagrams*, 1986, 7, 45.

[1986Mis] Y. Mishima, Y. Oya and T. Suzuki, “$L1_2 \rightleftarrows D0_c$ Martensitic Transformation in Pt_3Al and Pt_3Ga”, Proceeding of International Conference on Martensitic Transformation, The Japan Institute of Metals, Sendai, Japan, 1986, 1009-1014.

[1986Smi] J.L. Smialek and R. Browning, “Current View Points on Oxide Adherence Mechanisms” *Proceeding of 168th Meeting of Electrochemical Society*, Las Vegas, Nevada, U.S.A., Eds. Z.A. Munir, D. Cubicciotti, 1986, 259-271.

[1987Abd] G.B. Abderazik, A. Moulin, A.M. Huntz, E.W.A. Young and J.H.W. deWit, “Growth Mechanism of Al_2O_3 Scales Developed on the Fe-Cr-Al alloys”, *Solid State Ionics*, 1987, 22, 285-294.

[1987Hun] A.M. Huntz, “Influence of Active Elements on the Oxidation Mechanism of M-Cr-Al Alloys”, *Materials Science and Engineering* A, 1987, 87, 251-260.

[1987Jed] J. Jedlinski and S. Mrowec, “The Influence of Implanted Yttrium on the Oxidation Behaviour of β-NiAl”, *Material Science and Engineering*, 1987, 87, 281-287.

[1987Oya] Y. Oya, U. Mishima and T. Suzuki, “$L1_2 \leftrightarrow DOc$ Martensitic Transformation in Pt_3Al and Pt_3Ga”, *Zeitschrift für Metallkunde,* 1987, 78, (7), 485-490.

[1987Pie] B. Pieraggi, “Calculations of Parabolic Reaction Rate Constants”, *Oxidation of Metals*, 1987, 27, 177-185.

[1987Sim] C.T. Sims, N.S. Stollof and W.C. Hagel, Superalloys II, Wiley Interscience, USA, 1987.

[1987Sto1] F.H. Stott, “The Protective Action of Oxide Scales in Gaseous Environments at High Temperature”, *Report on Progress in Physics*, 1987, 50, 861-913.

[1987Sto2] F.H. Stott and G.C. Wood, "Growth and Adhesion of Oxide Scales on Al_2O_3-Forming Alloys and Coatings", *Materials Science and Engineering*, 1987, 87, 267-274.

[1987Str1] J. Stringer, "High Temperature Corrosion of Superalloys", *Materials Science and Technology*, 1987, 3, (7), 482-493.

[1987Str2] J. Stringer, "Role of Coatings in Energy Producing Systems: An Overview", *Materials Science and Engineering*, 87, 1-10.

[1987Tat] G.J. Tatlock, T.J. Hurd and J.S. Punni, "High Temperature Degradation of Nickel Based Alloys: A consideration of the Role of Pt", *Platinum Metals Review*, 1987, 37, 26-31.

[1987Zha] J.G. Zhao and A.M. Huntz, "Détermination de la Distribution des Contraintes daus un Matériau Oxydé par une Méthode da la Courbure", *Revue de Physique. Appliquée*, 1987, 1145-1157.

[1988Cha] K.S. Chan and R.A. Page, "Inelastic Deformation and Dislocation Structure of a Nickel Alloy: Effects of Deformation and Thermal History", *Metallurgical Transactions A*, 1988, 19, 2477-2486.

[1988Kof] P. Kofstad, "High Temperature Corrosion", Elsevier Applied Science, New York, 1988.

[1988Smi] J.L. Smialek, J. Doychak and D.J. Gaydosh, "Oxidation Behavior of Fe-Al-Zr, Hf, B", *Workshop on Oxidation of High Temperature Intermetallics*, 1988, TMS, AME.

[1988Wha] M.V. Whalen, "The Compatibility of Dispersion-Strengthened Platinum with Candidate Propellants", *Platinum Metals Review*, 1988, 32, 1, 2-10.

[1989Kau] M.J. Kaufman, P.W. Voorhees, W.C. Johnson and F.S. Biancaniello, "An Elastically Induced Morphological Instability of a Misfitting Precipitates", *Metallurgical Transactions A*, 1989, 20, 2171-2175.

[1989Nat] M.V. Nathal, R.A. Mackay and R.V. Miner, “Influence of Precipitate Morphology on Intermediate Temperature Creep Properties of a Nickel-Base Superalloy Single Crystal”, *Metallurgical Transactions A*, 1989, 20, 133-141.

[1989Qua] W.J. Quadakkers, H. Holzbrecher, K.G. Briefs and H. Beske, “Differences in Growth Mechanisms of Oxide Scales Formed on ODS and Conventional Wrought Alloys”, *Oxidation of Metals*, 1989, 32, (1-2), 67-88.

[1989Ryb] G.C. Rybicki, J.L. Smialek and L.S. James, “Effect of the θ-α-Al_2O_3 Transformation on the Oxidation Behaviour of β-NiAl+Zr”, *Oxidation of Metals*, 1989, 31, 275-304.

[1989Sto] J.H. Stout, D.A. Shores, J.G. Goedjen and M.E. Armancanqui, “Stresses and Cracking of oxide Scales”, *Materials Science and Engineering* A, 1989, 120, 193-197.

[1990Ell] P. Elliot, “Practical Guide to High Temperature Alloys”, Nickel Development Institute, 1990, 1-10.

[1990Fle] R.L. Fleischer and R.J. Zabala, “Mechanical Properties of Diverse Binary High-Temperature Intermetallic Compounds”, *Metallurgical Transactions A,* 1990, 2709-2715.

[1990Lee] H.T. Lee and S.W. Lee, “The Morphology and Formation of Gamma Prime in Nickel-Base Superalloy”, *Journal of Materials Science Letters*, 1990, 9, 516-517.

[1990Mas] T.B. Massalski, “Binary Alloy Phase Diagrams”, 2nd Edition, ASM International, Materials Park, OH, 1990, Volume 1, 195-197.

[1991Chi] A. Chiba, S. Hanada and S. Watanabe, “Effect of γ and γ' Doping on Ductility of Ni_3Al”, *Scripta Metallurgica*, 1991, 25, 303-307.

[1991Fle] R.L. Fleischer, R.D. Field and C.L. Briant, “Mechanical Properties of High-Temperature Alloys of AlRu”, *Metallurgical Transactions A*, 1991, 22, 403.

[1991Liu] P. Liu and J. Skogsmo, “Space-Group Determination and Structure Model for K-Al_2O_3 by Convergent Beam Electron Diffraction (CBED)”, *Acta Crystallography*, 1991, B47, 425-433.

[1991Pan] P. Panfilov, A. Yermakov, V. Dmitriev and N. Timofeev, “The Plastic Flow of Iridium”, *Platinum Metals Review*, 1991, 35, (4), 196-200.

[1991Sig] D.R. Sigler, “Oxidation Behaviour of Fe-20Cr-5Al Rare Earth Alloys in Air and Synthetic Exhaust Gas”, *Oxidation of Metals*, 1991, 36, (1-2), 57-80.

[1991Sto] N.S. Stoloff and D.E. Alman, “Powder Processing of Intermetallic Alloys and Intermetallic Matrix Composites”, *Materials Science and Engineering A*, 1991, 144, 51-62.

[1992Bha] R.T. Bhatt and D.R. Berrendt, “Reaction-Bonded Si_3N_4 and SiC Matrix Composites”, in Flight-Vehicle Materials, Structures, and Dynamics, Assessment and Future directions, Eds. S.R. Levine, A.K. Noor and S.L. Venneri, Volume 3, 1992, *The American Society of Mechanical Engineers*, New York, 19-41.

[1992Bir] J. Birnie, C. Craggs, D.J. Gardiner and P.R. Graves, “Ex situ and In situ Determination of Stress Distributions in Chromium Oxide Films by Raman Microscopy”, *Corrosion Science*, 1992, 33 (1), 1-12.

[1992Bru] M.W. Brumn and H.J. Grabke, “The Oxidation Behaviour of NiAl-I: Phase Transformation in the Alumina Scale during Oxidation of NiAl and NiAl-Cr Alloys”, *Corrosion Science*, 1992, 33, 1677.

[1992Cha] K.M. Chang, R. Darolia and H.A. Lipsitt, “Cleavage Fracture in B2 Aluminides”, *Acta Metallurgica et Materialia*, 1992, 40, 2727-2737.

[1992Her] T.P. Herbell and W.A. Sanders, “Monolithic Ceramics” in Flight-Vehicle Materials, Structures, and Dynamics-Assessment and Future directions, Eds. S.R. Levine, A.K. Noor and S.L. Venneri, Volume 3, 1992, *The American Society of Mechanical Engineers*, New York, 19-41.

[1992Leh] R.L. Lehman, "Glass-Ceramic-Matrix Fiber Composites", in Flight-Vehicle Materials, Structures, and Dynamics- Assessment and Future directions, Eds. S.R. Levine, A.K. Noor and S.L. Venneri, Volume 3, 1992, *The American Society of Mechanical Engineers*, New York, 19-41.

[1992Maa] H.G. Maahs, "Carbon-Carbon Composites", in Flight-Vehicle Materials, Structures, and Dynamics- Assessment and Future directions, Eds. S.R. Levine, A.K. Noor and S.L. Venneri, Volume 3, 1992, *The American Society of Mechanical Engineers*, New York, 19-41.

[1992Pre] R. Prescott and M.J. Graham, "The Formation of Aluminium Oxide Scales on High-temperature Alloys", *Oxidation of Metals,* 1992, 38, (3-4), 233-249.

[1993Bou] M. Boualam, G. Beranger and M. Lambertin, "Oxidation of Alumina Forming Alloy: Morphological and Structural Study" in Microscopy of Oxidation 2, Eds., S.B. Newcomb, M.J. Bennet, Institute of Materials, London, 1993, 2, 243-252.

[1993Fle] R.L. Fleischer and D.W. Mckee, "Mechanical and Oxidation Properties of RuAl-Based High Temperature Alloys", *Metallurgical Transactions A*, 1993, 24, 759-763.

[1993Liu1] C. Liu, A.M. Huntz and J.L. Lebrun, "Origin and Development of Residual Stress in the Ni-NiO System: In situ Studies at High Temperature by X-ray Diffraction", *Materials Science and Engineering* A, 1993, 160, 113-126.

[1993Liu2] C. Liu, J.L. Lebrun, A.M. Huntz and F. Zibieude, "Advanced Technique for High Temperature X-ray Elastic Constant Measurement and Stress Determination", *Zeitschriff für Metallkunde*, 84 (2), 1993, 140.

[1993Ma] Q. Ma and D.R. Clarke, "Stress Measurement in Single-Crystal and Polycrystalline Ceramics Using their Optical Fluorescence", *Journal of American Ceramic Society*, 1993, 76, 1433.

[1993Sto] N.S. Stoloff, "Toughening Mechanisms in Intermetallics", *Metallurgical Transactions A*, 1993, 24, 561--567.

[1994Doy] J. Doychak, "Oxidation Behaviour of High Temperature Intermetallics", in Intermetallic Compounds: Principles and Practice, Volume 2, 1994, Eds., J.H. Westbrook and R.L. Fleischer, J. Wiley and Sons, Chichester, United Kingdom, 977-1016.

[1995Fri] K. Fritscher, C. Leyens and M. Peters, "Development of Low-Expansion Bond Coating for Ni-Base Superalloys", *Materials Science and Engineering A*, 1995, 90, (1-2), 253-258.

[1994Goe] J.G. Goedjen, J.H. Stout, G. Qiti and D.A. Shores, "Evaluation of Stresses in Ni-NiO and Cr-Cr_2O_3 during High Temperature Oxidation by In situ X-ray Diffraction", *Materials Science and Engineering A*, 1994, 177, 115-124.

[1994Qua1] W.J. Quadakkers and M.J. Bennett, "Oxidation Induced Lifetime Limits of Thin Walled, Iron Based, Alumina Forming, Oxide Dispersion Strengthened Alloy Components", *Materials Science and Technology*, 1994, 10, 126-131.

[1994Qua2] W.J. Quadakkers, "The Prediction of Breakway Oxidation for Alumina Forming ODS Alloys Using Oxidation Diagrams", *Materials and Corrosion*, 1994, 232-241.

[1995Bar] A. Bartels, C. Koeppe and H. Mecking, "Microstructure and Properties of Ti-48Al-2Cr after Thermomechanical Treatment", *Materials Science and Engineering A*, 1995, 192/193, 226-232.

[1995Hac] J.E. Hack, J.M. Brzeski and R. Darolia, "Fracture and Deformation of NiAl Single Crystals", *Surface and Coating Technology*, 1995, 201, 3016-3029.

[1995Jen] Y.L. Jeng, E.J. Lavernia, R.M. Hayes and J. Wolfenstine, "Creep Behaviour of Al-rich-Fe-Al Intermetallics", *Materials Science and Engineering A*, 1995, 192/193, 240-248.

[1995He] J. He and D.R. Clarke, "Determination of the Piezospectroscopy Coefficients for Chromium-Doped Sapphire", *Journal of the American Ceramic Society*, 1995, 78, 1347-1353.

[1995Hun] A.M. Huntz, "Stresses in NiO, Cr_2O_3 and Al_2O_3 Oxide Scales", *Materials Science and Engineering* A, 1995, 201, 211-218.

[1995Pot] J.H. Potgieter, A. van Bennekom and P. Ellis, "Investigation of the Active Dissolution Behaviour of a 22% Chromium Duplex Stainless Steel with Small Ruthenium Additions in Sulphuric Acid", *ISIJ International*, 1995, 35, 197-202.

[1995Sad] K. Sadananda and A.K. Vasudevan, "Fracture Crack Growth Behaviour in Titanium Aluminides", *Materials Science and Engineering A*, 1995, 192/193, 490-501.

[1995Woo] M. Wood and M. Ward-Close, "Fibre-Reinforced Intermetallic Compound by Physical Vapour Deposition", *Materials Science and Engineering A, 1995,* 192/193, 590-596.

[1996Chr] R.J. Christensen, D.M. Lipkin, D.R. Clarke and K. Murphy, "Nondesructive Evaluation of the Oxidation Stresses through Thermal Barrier Coatings Using Cr^{3+} Piezospectroscopy", *Applied Physics Letters,* 1996, 69 (24), 3754-3756.

[1996Deb] D. Deb, S. Ramakrishna Lyer and V.M. Radhakrishnan, "Assessment of High Temperature Performance of a Cast Nickel Base Superalloy in Corrosive Environment", *Scripta Materialia*, 1996, 35, (8), 947.

[1996Lip] D.M. Lipkin and D.R. Clarke, "Measurement of the Stress in Oxide Scales Formed by the Oxidation of Alumina-Forming Alloys", *Oxidation of Metals,* 1996, 45 (3-4), 267-280.

[1996Wol1] I.M. Wolff, "Synthesis of RuAl by Reactive Powder Processing", *Metallurgical and Materials Transactions A,* 1996, 27, 3688-3699.

[1996Wol2] I.M. Wolff and G. Sauthoff, "High-Temperature Behaviour of Precious Metal Base", *Metallurgical and Materials Transactions A*, 1996, 27, 2642-2652.

[1996Yam] Y. Yamabe, Y. Koizumi, H. Murakami, Y. Ro, T. Maruko and H. Harada, "Development of Ir-Base Refractory Superalloys", *Scripta Materialia,* 1996, 35, (2), 211-215.

[1997Che] J.H. Chen and J.A. Little, "Degradation of the Platinum Aluminide Coating on CMSX-4 at 1100°C", *Surface and Coatings Technology*, 1997, 443, 46-52.

[1997Dur] M. Durand-Charre, "The Microstructure of Superalloys", CRC Press, London, 1997, 124.

[1997Fis] B. Fischer, D. Freund and D. Lupton, Proceedings of the 21st International Precious Metals Conference, IPMI, San Francisco, U.S.A., 1997, 15th-18th June, 307.

[1997Lev] I. Levin, L.A. Bendersky, D.G. Brandon and M. Rühle, "Cubic to Monoclinic Phase Transformation in Alumina", *Acta Materialia*, 1997, 45, (9), 3659-3669.

[1997Lip] D.M. Lipkin, D.R. Clarke, M. Hollatz, M. Bobeth and W. Pompe, "Stress Development in Alumina Scales Formed Upon Oxidation of (111) NiAl Single Crystals", *Corrosion Science*, 1997, 39 (2), 231-242.

[1997Ric] D.W. Richerson, "Ceramics for Turbines", The American Society of Mechanical Engineers, New York, 1997.

[1997Sub] P.R. Subramanian, M.G. Mendiratta, D.M. Dimiduk and M.A. Stucke, "Advanced Intermetallic Alloys—Beyond Gamma Titanium Aluminides", *Materials Science and Engineering A*, 1997, 239-249, 1-13.

[1997Wol] I.M. Wolff and G. Sauthoff, "Role of an Intergranular Phase in RuAl with Substitutional Additions", *Acta Materialia*, 1997, 45, 2949-2969.

[1997Yam] Y. Yamabe-Mitarai, Y. Koizumi, H. Murakami, Y. Ro, T. Maruko and H. Harada, "Rh-Base Refractory Superalloys for Ultra High Temperature Use", *Scripta Materialia,* 1997, 36, 393-398.

[1998Bul] S.J. Bull, "Modeling of Residual Stress in Oxide Scales", *Oxidation of Metals*, 1998, 49, 1-17.

[1998Cal] G. Calvarin, A.M. Huntz, A. Hugot Le Goff, S. Joiret and M.C. Bernard, "Oxide Scale Stress Determination by Raman Spectroscopy Application to the

NiCr/Cr_2O_3 System and Influence of Yttrium", *Scripta Materialia*, 1998, 38 (11), 1649-1658.

[1998Gu] Y.F. Gu, Y. Yamabe-Mitarai, Y. Ro, T. Yokokawa and H. Harada, "Microstructures and Compressive Properties of Ir-15Nb Refractory Superalloy Containing Nickel", *Scripta Materialia*, 1998, 39, 723-728.

[1998Kri] G.R. Krishna, D.K. Das, V. Singh and S.V. Joshi, "Role of Pt Content in the Microstructural Development and Oxidation Performance of Pt-Aluminide Coatings Produced Using a High-Activity Aluminizing Process", *Materials Science and Engineering A*, 1998, 251, 40-47.

[1998Nan] M. Nanko, M. Ozawa and T. Maruyama, "External and Internal oxidation of Pt-Al alloys at High Temperatures", Symposium on High-Temperature Corrosion and Materials Chemistry, San Diego, USA, *Electrochemical Society inc.*, 1998, 500-511.

[1998Tay] R.E. Taylor, "Thermal Expansion of Solids", Ed. C.Y. Ho, 1998, ASM International, Materials Park, U.S.A., 293.

[1998Yam] Y. Yamabe-Mitarai, Y. Ro, T. Maruko and H. Harada, "Ir-Base Refractory Superalloys for Ultra High Temperature", *Metallurgical and Materials Transactions A*, 1998, 29, 537-549.

[1999Fis] B. Fischer, A. Behrends, D. Freund, D.F. Lupton and J. Merker, "High Temperature Mechanical Properties of the Platinum Group Metals", *Platinum Metals Review*, 1999, 43, (1), 18-28.

[1999Gu1] Y.F. Gu, Y. Yamabe-Mitarai and H. Harada, "Compressive Properties of B-Doped Ir-15Nb Two-Phase Refractory Superalloys", *Scripta Materialia*, 1999, 41, 1079--1083.

[1999Gu2] Y.F. Gu, Y. Yamabe-Mitarai, Y. Ro and H. Harada, "Microstructures and Deformation Behavior of Ir-Nb Two-Phase Refractory Superalloys for Various Nb Content", *Scripta Materialia*, 1999, 40, 1313-1319.

[1999Gu3] Y.F. Gu, Y. Yamabe-Mitarai, Y. Xu and H. Harada "Microstructures and Creep Properties of Ni-alloyed Rh-15 at.% Nb Two-Phase Refractory Superalloys", *Materials Letters*, 1999, 41, 45-51.

[1999Gu4] Y.F. Gu, Y. Yamabe-Mitarai, Y. Ro, T. Yokokawa and H. Harada, "Properties of the $Ir_{85}Nb_{15}$Two-Phase Refractory Superalloys with Nickel Additions", *Scripta Materialia*, 1999, 30, 262-2639.

[1999Hil] P.J. Hill, L.A. Cornish, M.J. Witcomb and P. Ellis, "Characterization of Pt-Rich Pt-Al-Ru Alloys", Proceedings of Microscopy Society of South Africa, Volume 29, Bloemfontein, 1st-3rd December, 1999, 28.

[1999Li] M. Li, T. Li, W. Gao and Z. Liu, "Determination of Oxide Growth Stress by a Novel Deflection Method", *Oxidation of Metals*, 1999, 51, (5-6), 333-351.

[1999Lu] D.C. Lu and T.M. Pollock, "Low Temperature Deformation and Dislocation Substructure of RuAl Polycrystals", *Acta Materialia*, 1999, 47, 1035-1042.

[1999Sie] B. Siebert, C. Funke, R. Vaβen and D. Stöver, "Change in Porosity and Young's Modulus Due to Sintering of Plasma Sprayed Thermal Barrier Coatings", *Journal of Materials Processing and Technology*, 1999, 92-93, 217-223.

[1999Wol1] I.M. Wolff and P.J. Hill, "Evidence of a Substructure in Single-Phase Pt-Al", in Proceedings of Microscopy Society of South Africa, Volume 29, Bloemfontein, 1st-3rd December, 1999, 29.

[1999Wol2] I. Wolff, T.L. Shing, S. Luyckx and I.T. Northrop, "The Effect of Ruthenium Additions on the Hardness", *European Conference on Advances in Hard Materials Production*, Turin, Italy, 8th-10th November, 1999.

[1999Yam1] Y. Yamabe-Mitarai, Y. Ro, T. Maruko and H. Harada, "Precipitation Hardening of Ir-Nb and Ir-Zr Alloys", *Scripta Materialia*, 1999, 40, 109-115.

[1999Yam2] Y. Yamabe-Mitarai, Y.F. Gu, Y. Ro, S. Nakazawa, T. Maruko and H. Harada, "Effect of Precipitation Morphology on Strength of Ir-Nb Alloys with Two-Phase Coherent structures", *Scripta Materialia*, 1999, 41, 305-311.

[1999Yu1] X.H Yu, Y. Yamabe-Mitarai and H. Harada, “Phase Separation in Two Kinds of $L1_2$-Ni_3Al and Ir_3Nb of Refractory Superalloys”, *Scripta Materialia*, 1999, 41, 1153-1159.

[1999Yu2] X.H Yu, Y. Yamabe-Mitarai, Y. Ro, Y.F. Gu and H. Harada, “Development of Quaternary Ir-Ta-Ni-Al Refractory Superalloys”, *Scripta Materialia,* 1999, 41, 651--657.

[1999Zha] Y. Zhang, J.A. Haynes, W.Y. Lee, I.G. Wright, B.A. Pint and K.M. Cooley “Synthesis and Cyclic Oxidation Behaviour of a (Ni, Pt) Al Coating on a Desulfurized Ni-Based Superalloy”, *Metallurgical and Materials Transactions A*, 1999, 30, 2679-2687.

[2000Fai1] G.B. Fairbank, C.J. Humphreys, A. Kelly and C.N. Jones, “Ultra-High Temperature Intermetallics for the Third Millenium”, *Intermetallics*, 2000, 8, 1091-1100.

[2000Fai2] G.B. Fairbank, C.J. Humphreys, A. Kelly and C.N. Jones, “New Platinum Alloys for Ultra High Temperature Applications", Fifth International Charles Parsons Turbine Conference, Cambridge, UK, 3rd-7th, July 2000.

[2000Hil] P.J. Hill, L.A. Cornish, M.J. Witcomb and I.M. Wolff, “The Oxidation Behaviour of Pt-Al-X Alloys at Temperatures Between 1473 and 1623K", Proceedings of the International Symposium on High Temperature Corrosion and Protection 2000, Sappora, Japan, *Science Reviews,* 2000, 185-190.

[2000Lup] D.F. Lupton, J. Merker, B. Fischer and R. Völkl, “Platinum Materials for the Glass Industry”, 24th International Precious Metals Conference, Williamsburg, Virginia, USA, 11th-14th June, 2000.

[2000Smi] J.L. Smialek, "Maintaining Adhesion of Protective Al_2O_3 Scales”, *Journal of Metals*, 2000, 22-25.

[2000Sto] F.H. Stott and N. Hiramatsu, "Breakdown of Protective Scales during the Oxidation of Thin Films of Fe-20Cr-5Al Alloys at High Temperatures", *Materials at High Temperatures*, 2000, 17 (1), 93-99.

[2000Wol] I.M. Wolff and P.J. Hill, "Platinum Metals-based Intermetallics for High-Temperature Service", *Platinum Metals Review*, 2000, 44, (4), 158-166.

[2000Yam] Y. Yamabe-Mitarai, S. Nakazawa and H. Harada, "Creep Behaviour of Ir-Nb and Ir-Zr Alloys", *Scripta Materialia*, 2000, 43, 1059-1064.

[2000Yu] X.H Yu, Y. Yamabe-Mitarai, Y. Ro and H. Harada, "New Developed Quaternary Refractory Superalloys", *Intermetallics*, 2000, 619-622.

[2001Big1] T. Biggs, P.J. Hill, L.A. Cornish and M.J Witcomb, "An Investigation of The Pt-Al-Ru Diagram to Facilitate Alloy Development", *Journal of Phase Equilibra*, 2001, 22, (3), 214-218.

[2001Big2] T. Biggs, "An Investigation into Displacive Phase Transformation in Platinum Alloys", Ph.D. Thesis, University of the Witwatersrand, Johannesburg, South Africa, 2001.

[2001Fis] B. Fischer, "New Platinum Materials for High Temperature Applications", *Advanced Engineering Materials*, 2001, 3, 10, 811-820.

[2001Hil1] P.J. Hill, L.A. Cornish, P. Ellis and M.J. Witcomb, "The Effects of Ti and Cr Additions on the Phase Equilibra and Properties of Pt/Pt_3Al Alloys", *Journal of Alloys and Compounds*, 2001, 322, 166-175.

[2001Hil2] P.J. Hill, T. Biggs, P. Ellis, J. Hohls, S.S. Taylor and I.M. Wolff, "An Assessment of Ternary Precipitation-Strengthened Pt Alloys for Ultra-High Temperature Applications", *Materials Science and Engineering A*, 2001, 301, 167-179.

[2001Hil3] P.J. Hill, G.B. Fairbank and L.A. Cornish, "New Developments in High-Temperature Platinum Alloys", *Journal of Metals*, 2001, *53*, 19-20.

[2001Hil4] P.J. Hill, Y. Yamabe-Mitarai and I.M. Wolff, "High Temperature Compression Strengths of Precipitation-Strengthened Ternary Pt-Al-X Alloys", *Scripta Materialia*, 2001, 44, 43-48.

[2001Hil5] P.J. Hill, Y. Yamabe-Mitarai, H. Murakami, L.A. Cornish, M.J. Witcomb, I.M. Wolff and H. Harada, "The Precipitate Morphology and Lattice Mismatch of Ternary (Pt)/Pt_3Al Alloys", 3rd International Symposium on Structural Intermetallics, TMS, Snow King Resort, Jackson Hole, Wyoming, U.S.A., September 2001, resheduled for 28th April-1st May, 2002, 527-533.

[2001Hil6] P.J. Hill, "Superalloy Analogues Based on Platinum for Ultra-High Temperature Applications", Ph.D. Thesis, University of the Witwatersrand, Johannesburg, South Africa, 2001.

[2001Lin] E. van der Lingen and R.F. Sandenbergh, "The Cathodic Modification Behaviour of Ruthenium Additions to Titanium in Hydrochloric Acid", *Journal of Corrosion Science*, 2001, 43, 577-590.

[2001Pur] A.L. Purvis and B.M. Warnes, "The Effects of Platinum Concentration on the Oxidation Resistance of Superalloys Coated with Single-Phase Platinum Aluminide", *Surface Coating Technology*, 2001, 146, 1-6.

[2001Süs1] Süss, P.J. Hill, P. Ellis and I.M Wolff, "The Oxidation Resistance of Pt-base gamma/gamma prime Analogues to Ni-base Superalloys", 7th European Conference on Advanced Materials and Processes, Rimini, Italy, 10th-14th June, 2001, Paper No. 287, CD-ROM, ISBN 8885298397.

[2001Süs2] R. Süss, P.J. Hill, P. Ellis and L.A. Cornish, "The Oxidation Resistance of Pt-based superalloy Pt_{80}: Al_{14}: Cr_3: Ru_3 Compared to that of Pt_{86}:Al_{10}:Cr_4", Proceedings of Microscopy Society of Southern Africa, Johannesburg, South Africa, 2001, 31, 5-7.

[2001Zha] Y. Zhang, J.A. Haynes, W.Y. Lee, I.G. Wright, B.A. Pint and K.M. Cooley, "Effects of Pt Incorporation on the Isothermal Oxidation Behavior of Chemical

Vapor Deposition Aluminide Coatings", *Metallurgical and Materials Transactions A*, 2001, 32, 1727-1741.

[2002Dav] A.W. Davis and R.N. Mahapatra, "Oxidation Behavior of Rh-xTi Refractory Alloys", *Oxidation of Metals*, 2002, 57, (1-2), 181-191.

[2002Cor] L.A. Cornish, J. Hohls, P. J. Hill, S. Prins, R. Süss and D.N Compton, "The Development of Platinum-Based Alloys and their Thermodynamic Database", *Journal of Mining and Metallurgy*, 2002, 38, (3-4) B, 197-204.

[2002Gu] Y.F. Gu, Y. Yamabe-Mitarai, S. Nakazawa and H. Harada, "Creep Behavior of Ni-added $Ir_{85}Nb_{15}$ Two-Phase Refractory Superalloys at 1800°C", *Scripta Materialia*, 2002, 46, 137-142.

[2002Hil] P.J. Hill, N. Adams, T. Biggs, P. Ellis, J. Hohls, S.S. Taylor and I.M. Wolff, "Platinum Alloys Based on (Pt)/Pt_3Al for Ultra-High Temperature Use", *Materials Science and Engineering A*, 2002, 329-331, 295-304.

[2002Lev] S.R. Levine, E.J. Opila, M.C. Halbig, J.D. Kiser, M. Singh and J.A. Salem, "Evaluation of Ultra-High Temperature Ceramics for Aeropropulsion Use", *Journal of the European Ceramic Society*, 2002, 22, 2757-2767.

[2002Lin] H.T. Lin and M.K. Ferber, "Mechanical Reliability Evaluation of Silicon Nitride Ceramic Components after Exposure in Industrial Gas Turbines", *Journal of the European Ceramic Society*, 2002, 22, 2789-2797.

[2002Nic] J.R. Nicholls, N.J. Simms, W. Chan and H.E. Evans, "Smart Overlay Coatings-Concept and Practice", *Surface Coatings Technology*, 2002, 149, (2-3), 236-244.

[2002Pad] N.P. Padture, M. Gell and E.H. Jordan "Thermal Barrier Coatings for Gas-Turbine Engine Applications", *Science*, 2002, 296, 280-284.

[2002Süs2] R. Süss, D. Freund, R. Völkl, B. Fischer, P.J. Hill, P. Ellis J. Hohls and I.M. Wolff, "The Creep Behaviour of Platinum-Based γ/γ' Analogues of Nickel-Based Superalloys at 1300°C", *Metallurgical and Materials Transactions A*, 2002, 338, 133-141.

[2002Yam] Y. Yamabe-Mitarai, Y.F. Gu and H. Harada, “Two-Phase Iridium-Based Refractory Superalloys”, *Platinum Metal Review*, 2002, 46, 74-81.

[2003Bha] H.K.D.H. Bhadesia, “Nickel-Based Superalloys”, http://www.msm.cam.ac.uk/phase-*trans/2003/Superalloys/superalloys.html*, Accessed 23 October, 2008.

[2003Bew] B.P. Bewlay, M.R. Jackson, J.C. Zhao and P.R. Subramanian, “A Review of Very-High Temperature Nb-Silicide-Based Composites”, *Metallurgical and Materials Transactions A*, 2003, 34A, 2043-2052.

[2003Cho] L.H. Chown and L.A. Cornish, “The Influence of Cobalt Additions to Pt-Al and Pt-Al-Ru-Cr Alloy Systems”, in ‘African Materials Research Society Conference’, University of the Witwatersrand, Johannesburg, South Africa, 8th-11th December, 2003, 136-137.

[2003Cla] D.R. Clarke and C.G. Levi, “Materials Design for the Next Generation Thermal Barrier Coatings”, *Annual Review of Materials Research*, 2003, 33, 383-417.

[2003Cor] L.A. Cornish, B. Fischer and R. Völkl, “Development of Platinum-Group-Metal Superalloys for High-Temperature Use”, *MRS Bulletin*, 2003, Vol. 28, (9), 622-632.

[2003Fai] G.B. Fairbank, “Development of Platinum Alloys For High-Temperature Service”, Ph.D. Thesis, Department of Materials Science and Metallurgy, University of Cambridge, Cambridge, 2003.

[2003Gla] L. Glaner and L.A Cornish “The Effect of Ni Additions to the Pt-Al-Cr-Ru System”, in Proceedings of Microscopy Society of South Africa, Volume 33, Cape Town, 3rd-5th December, 2003, 11.

[2003Gur] I. Gurrappa, “Influence of Alloying Elements on Hot Corrosion of Superalloys and Coatings: Necessity of Smart Coatings for Gas Turbine Engines”, *Materials Science and Technology*, 2003, 19, (2), 178-183.

[2003Li1] M.H. Li, X.F. Sun, J.G. Li, T.Y. Zhang, T. Jin, H.R. Guan and Z.Q. Hu, “Oxidation Behaviour of a Single-Crystal Ni-Base Superalloy in Air-I: at 800 and 900°C”, *Oxidation of Metals,* 2003, 59, 591.

[2003Li2] M.H. Li, X.F. Sun, T. Jin, H.R. Guan and Z.Q. Hu, “Oxidation Behaviour of a Single-Crystal Ni-Base Superalloy in Air-II: at 1000, 1100 and 1150°C”, *Oxidation of Metals,* 2003, 60, 195-210.

[2003Sch] U. Schultz, C. Leyens, K. Fritscher, M. Peters, B. Saruhan-Brings, O. Lavinge, J. Dorvaux, M. Poulain, R. Mevrel and M. Caliez, “Some Recent Trends in Research and Technology of Advanced Thermal Barrier Coatings”, *Aerospace Science and Technology,* 2003, 7, 73-80.

[2003Sol] F. Soldera, N. Ilíc, S. Brannstrom, I. Barrientos, H. Gobran and F. Mucklich, “Formation of Al_2O_3 Scales on Single-Phase RuAl Produced by Reactive Sintering”, *Oxidation of Metals,* 2003, 59, 529--542.

[2003Süs] R. Süss, L.A. Cornish, P.J. Hill and J. Hohls, “Properties of New Series of Superalloys Based on Pt_{80}: Al_{14}: Cr_3: Ru_3”, Proceedings of Advanced Materials and Processes for Gas Turbines, 301-307, Eds. G. Fuchs, A. James, T. Gabb, M. McLean and H. Harada, September 22-26, 2002, Copper Mountain, Colorado, USA, TMS, 2003.

[2003Yam1] Y. Yamabe-Mitarai and H. Aoki, “An Assessment of Ir-Pt-Al Alloys for High-Temperature Materials”, *Journal of Alloys and Compounds,* 2003, 359, 143-152.

[2003Yam2] Y. Yamabe-Mitarai and H. Harada, “Face centered Cubic and $L1_2$ Two-Phase Structure of Ir-Nb-Zr Alloys”, *Journals of Alloys and Compounds*, 2003, 361, 169-179.

[2003Yam3] Y. Yamabe-Mitarai, Y.F. Gu and H. Harada, “Compressive Strength and Creep Properties of Ir-Nb-Zr alloys between 1473K and 2073K”, *Metallurgical and Materials Transactions A*, 2003, 34, 2207-2115.

[2003Yok] T. Yokokawa, Y. Koizumi, O. Makoto, K. Nishida, T. Kobayashi and H. Harada, “Partitioning Behaviour of Platinum Group Metals on the Gamma and Gamma Prime Phases of Ni-based Superalloys at High Temperatures”, *Scripta Materialia*, 2003, 49, 1041-1046.

[2003Zha] J.C. Zhao and J.H. Westbrook, “Ultra High Temperature Materials for Jet Engines”, *MRS Bulletin*, 2003, 28 (9), 622-627.

[2004Cho] L.H. Chown, L.A. Cornish and B. Joja, “Structure and Properties of Pt-Al-Co Alloys”, in Proceedings of Microscopy Society of South Africa, Volume 34, Pretoria, 30th November-3rd December, 2004, 11.

[2004Cor] L.A. Cornish, R. Süss, L.H. Chown, A. Douglas, L. Glaner and S.N. Prins, “Platinum-Based Alloys for High Temperature and Special Applications”, in “*International Platinum Conference 'Platinum Adding Value”*, Sun City, South Africa, 3rd-7th October, 2004, Symposium Series S38, 329-335, The Southern African Institute of Mining and Metallurgy, Johannesburg, South Africa.

[2004Dou] A. Douglas “Microstructure and Deformation of Ternary Platinum Alloys as Superalloy Analogues”, Ph.D. Thesis, University of Port Elizabeth, South Africa, 2004.

[2004Fen] Q. Feng, T.K. Nandy, B. Tryon and T.M. Pollock, “Deformation of Ru-Al-Ta Ternary Alloys”, *Intermetallics*, 2004,12, 755-762.

[2004Hou] P.Y. Hou, X.F. Zhang and R.M. Cannon, “Impurity Distribution in Al_2O_3 Formed in a FeCrAl Alloy”, *Scripta Materialia*, 2004, 50, 45-55.

[2004Ker] T. Keraan, “High Temperature Mechanical Properties and Behaviour of Platinum-Base Alloys”, M.Sc. Dissertation, University of Cape Town, South Africa, 2004.

[2004Mah] R.N. Mahapatra, S.K. Varma, C. Lei and V.V. Agarwala, “Oxidation Behavior of Rh-30Ni-18Nb Refractory Alloy”, *Oxidation of Metals*, 2004, 62, 92-102.

[2004Qua] W.J. Quadakkers, D. Naumenko, E. Wessel and V. Kochubey, “Growth Rates of Alumina scales on Fe-Cr-Al Alloys”, *Oxidation of Metals*, 2004, 61, 17-37.

[2004Vor] S. Vorberg, M. Wenderoth, B. Fischer U. Glatzel and R. Völkl, "Pt-Al-Cr-Ni Superalloys: Heat Treatment and Microstructure", *Journal of Metals*, 2004, 56, 40-43.

[2005For] B. Formanek, K. Szymański, B. Szczucka-Lasota and A. Włodarczyk, "New Generation of Protective Coatings Intended for the Power Industry", *Journal of Materials Processing Technology*, 2005, 164-165, 850-855.

[2005Hua1] L. Huang, X.F. Sun, H.R. Guan and Z.Q. Hu, "Oxidation Behaviour of the Directionally Solidified Ni-Based Superalloy DS951 in Air", *Oxidation of Metals*, 2005, 64, (5-6), 303-318.

[2005Hua2] C. Huang, Y. Yamabe-Mitarai, X.H. Yu, S. Nakazawa and H. Harada, "Partial Phase Relationships in Ir-Nb-Ni-Al and Ir-Nb-Pt-Al Quaternary Systems and Mechanical Properties of Their Alloys", *Metallurgical and Materials Transactions A*, 2005, 36, 539-545.

[2005Hua3] C. Huang, Y. Yamabe-Mitarai, S. Nakazawa, K. Nishida and H. Harada, "Investigation on Phase Relationships and Creep Properties of Ir-Nb-X (X= Hf, Ta, or Ti) Ternary Alloys", *Materials Science and Engineering A*, 2005, 412, 191-197.

[2005Hül] M. Hüller, S. Wenderoth, S. Vorberg, B. Fischer, U. Glatzel and R. Völkl, "Optimization of Composition and Heat Treatment of Age-Hardened Pt-Al-Cr-Ni alloys", *Metallurgical and Materials Transactions A*, 2005, 36, 681-689.

[2005Müc] F. Mücklich and N. Ilić, "RuAl and Its Alloys. Part I. Structure, Physical Properties, Microstructure and Processing", *Intermetallics*, 2005, 13, 5-21.

[2005Pie] B. Pieraggi, "Comments on Growth Rates of Alumina Scales on Fe-Cr-Al Alloys", *Oxidation of Metals*, 2005, 64, 397-403.

[2005Pom] M.J. Pomeroy, "Coatings for Gas Turbine Materials and Long Term Stability Issues", *Materials and Design*, 2005, 26, 223-231.

[2005Vor] S. Vorberg, M. Wenderoth, B. Fischer, U. Glatzel and R. Völkl, “A TEM Investigation of the *γ/γ'* Phase Boundary in Pt-Based Superalloys”, *Journal of Metals*, 2005, 57, 49-51.

[2005Wen1] M. Wenderoth, R. Völkl, S. Vorberg, Y. Yamabe-Mitarai, H. Harada and T. Yokokawa, “High-Temperature Strength of Pt-base Superalloys with Different *γ'* Volume Fractions”, *Scripta Materialia*, 2005, 54, 275-279.

[2005Wen2] M. Wenderoth, R. Völkl, S. Vorberg, L.A. Cornish, R. Süss, B. Fisher and U. Glatzel, “On the Development and Investigation of Quaternary Pt-Based Superalloys with Ni Additions”, *Metallurgical and Materials Transactions A*, 2005, 36, 567-575.

[2005Yam] Y. Yamabe-Mitarai, H. Harada, Y. Gu and C. Huang, “Compressive Creep Properties of Ir-Base Refractory Superalloys”, *Metallurgical and Materials Transactions A*, 2005, 36, 547-557.

[2006Pin] B.A. Pint, J.R. DiStefano and I.G. Wright, “Oxidation Resistance: One Barrier to Moving Beyond Ni-Base Superalloys”, *Materials Science and Engineering A*, 2006, 415, (1-2), 255.

[2006Bir] N. Birks, G.H. Meier and F.S. Pettit, “Introduction to the High-Temperature Oxidation of Metals”, Second Edition, 2006, Cambridge University Press, Cambridge, United Kingdom, 2006, 338.

[2006Cor] L.A. Cornish, R. Süss, L.H. Chown, A. Douglas, M. Matema, L. Glaner and G. Williams, “New Pt-based Alloys for High Temperature Application in Aggressive Environments: The Next Stage”, International Platinum Conference 'Platinum Surges Ahead', Sun City, South Africa, 8th-12th October, 2006, Symposium Series S45, 57-66, The Southern African Institute of Mining and Metallurgy, Johannesburg, South Africa.

[2006Gur] I. Gurrappa and A.S. Rao, “Thermal Barrier Coatings for Enhanced Efficiency of Gas Turbine Engines", *Surface and Coatings Technology*, 2006, 201, 3016-3029.

[2006Kem] M. Kemdehoundja, J.F. Dinhut, J.L. Grosseau-Poussard and M. Jeannnin, "High Temperature Oxidation of $Ni_{70}Cr_{30}$: Determination of Oxidation Kinetics and Stress Evolution in Chromia Layers by Raman Spectroscopy", *Materials Science and Engineering* A, 2006, 435-436, 666-671.

[2006Mal] N.B. Maledi, J.H. Potgieter, M. Stephton, L.A. Cornish, L. Chown and R. Süss, "Hot Corrosion Behaviour of Pt-Alloys for Application in the Next Generation of Gas Turbines", Second International Platinum Conference 'Platinum Surges Ahead', Sun City, South Africa, 8th-12th October, 2006, Symposium Series S45; 81-90, The Southern African Institute of Mining and Metallurgy, Johannesburg, South Africa.

[2006Pru] J. Pruessner, M. Wenderoth, S. Prins, R. Völkl and U. Glatzel, "Platinum Alloy Development-The Pt-Al-Cr-Ni System", Second International Platinum Conference 'Platinum Surges Ahead', Sun City, South Africa, 8th-12th October, 2006, Symposium Series S45, 103-106, The Southern African Institute of Mining and Metallurgy, Johannesburg, South Africa.

[2006Ree] R.C. Reed, "The Superalloys: Fundamental and Applications", Cambridge University Press, Cambridge, United Kingdom, 2006.

[2006Sat] A. Sato, H. Harada, T. Yokokawa, T. Murakumo, Y. Koizumi, T. Kobayashi and H. Imai, "The Effects of Ruthenium on the Phase Stability of Fourth Generation Ni-base Single Crystal Superalloys", *Scripta Materialia*, 2006, 54, 1679-1684.

[2006Völ] R. Völkl, M. Wenderoth, J. Preussner, S. Vorberg, B. Fischer and U. Glatzel, "A Review on the Progress towards Pt-base Superalloys for Ultra High Temperature Applications", Second International Platinum Conference 'Platinum Surges Ahead', Sun City, South Africa, 8th-12th October, 2006, Symposium Series S45; 67-71, The Southern African Institute of Mining and Metallurgy, Johannesburg, South Africa.

[2007Cao] F. Cao, T.K. Nandy, D. Stobbe and T.M. Pollock, "Oxidation of Ruthenium Aluminide-Based Alloys: The Role of Microstructure and Platinum Additions", *Intermetallics*, 2007, 15, 34-43.

[2007Cor] L.A. Cornish, R. Süss, L.H. Chown, A. Douglas, R. Völkl, N.B. Maledi, L. Glaner, S. Vorberg, B. Fischer, T., Murakumo, J. Pruessner, U. Glatzel, D. Lupton, M. Wenderoth, J.H. Potgieter, M. Sephton and G. Williams, "Overview of the Development of New Pt-based Alloys for High Temperature Application in Aggressive Environments", *Journal of the Southern African Institute of Mining and Metallurgy*, 2007, 107, 697-711.

[2007Dou] A. Douglas, J.H. Neethling, R. Santamarta, D. Schryvers and L.A. Cornish, "Unexpected Ordering Behaviour of Pt_3Al Intermetallic Precipitates", *Journal of Alloys and Compounds*, 2007, 432, (1-2), 96.

[2007Mal] N.B. Maledi, "Corrosion Behaviour of Pt-Based Superalloys Intended for High Temperature Applications, M.Sc. Thesis, University of the Witwatersrand, Johannesburg, South Africa, 2007.

[2007Wen1] M. Wenderoth, R. Völkl, S. Vorberg, Y. Yamabe-Mitarai, H. Harada and U. Glatzel, "Microstructure, Oxidation Resistance and High-Temperature Strength of Gamma Prime Hardened Pt-Base Alloy", *Intermetallics*, 2007, 15, 539-549.

[2007Wen2] M. Wenderoth, R. Völkl, S. Vorberg, B. Fisher and U. Glatzel, "Isothermal Oxidation Behaviour of a Precipitation-Hardened Pt-Base Alloy with Additions of Al, Cr, and Ni", *International Journal of Materials Resources*, 2007, 98, (6), 463-467.

[2007You] C.M. Younes, G.C. Allen and J.A. Nicholson, "High Temperature Oxidation Behaviour of Single-Crystal Superalloys RR3000 and CMSX-4", *Corrosion Engineering Science and Technology*, 2007, 42, (1), 80-89.

[2008Bră] M. Brănescu, C. Naudin, M. Gartner and G. Nemes, "Depth Profiling Raman Spectroscopy of a Thin $YBa_2Cu_3O_{7-\delta}$ Film", *Thin Solid Films*, 2008, 516, 8190-8194.

[2008Gur] I. Gurrappa, "Identification of a Smart Bond Coating for Gas Turbine Engine Applications", *Journal of Coating Technology and Resources*, 2008, 5, (3), 385-391.

[2008Ohr] E.K. Ohriner, "Processing of Iridium and Iridium Alloys: Methods from Purification to Fabrication", *Platinum Metals Review*, 2008, 52, (3), 186-197.

[2008Rud] Y. Rudnik, R. Völkl, S. Vorberg and U. Glatzel, "The Effect of Ta Additions on the Phase Compositions and High Temperature Properties of Pt Base Alloys", *Metallurgical and Materials Transactions A*, 2008, 479, 306-312.

[2008Sho] M.B. Shongwe, L.A. Cornish and R. Süss, "Improvement of ~Pt_3Al Volume Fraction and Hardness in a Pt-Al-Ru-Cr Superalloy", Advanced Metals Initiatives Conference, Gold Reef City, Johannesburg, South Africa, 18th-19th November, 2008.

[2008Süs] R. Süss, A. Douglas, L.H. Chown, L. Glaner, N. Maledi, W. Tshawe and L.A. Cornish, "Pt-based Alloys for Aggressive Environments", Advanced Metals Initiative Conference, Gold Reef City, Johannesburg, South Africa, 18th-19th November, 2008, on CD-ROM.

[2008Wen] M. Wenderoth, R. Völkl, S. Vorberg, Y. Yamabe-Mitarai, H. Harada and B. Fischer, "Influence of Nb, Ta and Ti on Microstructure and High-Temperature Strength of Precipitation-Hardened Pt-base Alloys", *Metallurgical and Materials Transactions A*, 2008, 483-484, 509-511.

[2009Cor1] L.A. Cornish, R. Süss, L.H. Chown, A. Douglas and L. Glaner, "The Platinum Development Initiative: Platinum-Based Alloys for High Temperature and Special Applications: Part I", *Platinum Metals Review*, 2009, 53, (1), 2-10.

[2009Cor2] L.A. Cornish, R. Süss, L.H. Chown, and L. Glaner, "The Platinum Development Initiative: Platinum-Based Alloys for High Temperature and Special Applications: Part III", *Platinum Metals Review*, 2009, 53, (3), 155-163.

[2009Dou] A. Douglas, P.J. Hill, L.A. Cornish and R. Süss, "The Platinum Development Initiative: Platinum-Based Alloys for High Temperature and Special Applications: Part II", *Platinum Metals Review*, 2009, 53, (2), 69-77.

[2009Gle] B. Gleeson, N. Mu and S. Hayashi, "Compositional Factors Affecting the Establishment and Maintenance of Al_2O_3 Scales on Ni-Al-Pt Systems", *Journal of Materials Science*, 2009, 44, 1704-1710.

[2009You] D.J. Young, "High Temperature Oxidation and Corrosion of Metals", Elsevier online series, Amsterdam, United Kingdom, 2009.

[2010Pot] J.H. Potgieter, N.B. Maledi, M. Sephton and L.A. Cornish, "Platinum-Based Alloys for High temperature and Special Applications: Part IV", *Platinum Metals Review*, 2010, 54, (2), 112-118.

APPENDICES

Appendix A. XRD Reference Data

Table A1. XRD peak list for corundum (α-Al_2O_3) with reference code-00-046-1212

No	**h**	**K**	**l**	**d-spacing (Å)**	**2 Theta (deg)**	**Intensity (%)**
1	0	1	2	3.47975	25.579	45
2	1	0	4	2.55085	35.777	100.0
3	1	1	0	2.37947	37.777	21.0
4	0	0	6	2.16542	41.676	2.0
5	1	1	3	2.08532	43.356	66.0
6	2	0	2	1.96432	46.176	1.0
7	0	2	4	1.74007	52.550	34.0
8	1	1	6	1.60156	57.497	89
9	2	1	1	1.54667	59.741	1.0
10	1	2	2	1.51506	61.118	2.0
11	0	1	8	1.51506	61.118	14.0
12	2	1	4	1.40452	66.521	23.0
13	3	0	0	1.37372	68.214	27.0
14	1	2	5	1.33599	70.420	1.0
15	2	0	8	1.27555	74.299	2.0
16	1	0	10	1.23915	76.871	29.0
17	1	1	9	1.23434	77.226	12.0
18	2	1	7	1.19315	80.422	1.0

Table A2. XRD peak list for Pt_3Al-L1_2 (cubic) with reference code-00-065-3255

No	**h**	**k**	**l**	**d-spacing (Ǻ)**	**2 Theta (deg)**	**Intensity (%)**
1	1	0	0	3.87600	22.926	27.4
2	1	1	0	2.74075	32.646	20.2
3	1	1	1	2.23781	40.268	100
4	2	0	0	1.93800	46.840	48.1
5	2	1	0	1.73340	52.768	9.2
6	2	1	1	1.58237	58.261	6.7
7	2	2	0	1.37037	68.404	26.1
8	2	2	1	1.29200	73.198	3.8
9	3	1	0	1.22570	77.873	2.4
10	3	1	1	1.16866	82.467	27.5

Table A3. XRD peak list for Pt with reference code-00-004-0802

No	**h**	**k**	**l**	**d-spacing (Ǻ)**	**2 Theta (deg)**	**Intensity (%)**
1	1	1	1	2.26500	39.765	100.0
2	2	0	0	1.96160	46.244	53.0
3	2	2	0	1.38730	67.456	31.0
4	3	1	1	1.18260	81.289	33.0

Table A4. XRD peak list for CrO_3 with reference code-00-032-0285

No	**h**	**k**	**l**	**d-spacing (Ǻ)**	**2 Theta (deg)**	**Intensity (%)**
1	0	2	0	4.28000	20.737	20.0
2	0	1	1	4.19000	21.187	90.0
3	1	2	0	3.43500	25.918	100.0
4	1	1	1	3.38300	26.323	65.0
5	2	0	0	2.87400	31.093	45.0
6	0	3	1	2.45400	36.588	4.0
7	0	0	2	2.39800	37.474	18.0
8	2	1	1	2.37000	37.934	18.0
9	1	3	1	2.25500	39.948	18.0
10	0	4	0	2.13900	42.215	2.0
11	0	2	2	2.09100	43.233	2.0
12	1	4	0	2.00600	45.163	8.0
13	1	2	2	1.96580	46.139	10.0
14	2	3	1	1.86570	48.771	2.0
15	2	0	2	1.84240	49.429	5.0
16	3	2	0	1.74910	52.259	10.0
17	3	1	1	1.74350	52.439	12.0
18	2	4	0	1.71670	53.322	5.0
19	2	2	2	1.69210	54.160	3.0
20	0	5	1	1.61120	57.122	3.0
21	0	4	2	1.59540	57.740	2.0

Table A4 continued

22	0	1	3	1.57060	58.740
23	1	5	1	1.55120	59.548
24	1	4	2	1.53800	60.112
25	1	1	3	1.51590	61.081
26	3	3	1	1.50970	61.359
27	4	0	0	1.43660	64.850
28	0	6	0	1.42620	65.382
29	3	2	2	1.41240	66.102
30	2	5	1	1.40620	66.431
31	2	4	2	1.39560	67.002
32	2	1	3	1.37950	67.889
33	1	3	3	1.35550	69.260
34	2	6	0	1.27730	74.180

Table A5. XRD peak list for PtO_2 with reference code-01-075-0978

No	**h**	**k**	**l**	**d-spacing (Ǻ)**	**2 Theta (deg)**	**Intensity (%)**
1	1	1	0	3.18929	27.953	100.0
2	0	1	1	2.58010	34.742	45.3
3	1	0	1	2.57172	34.858	65.0
4	0	2	0	2.26650	39.737	15.5
5	2	0	0	2.24400	40.153	12.1
6	1	1	1	2.23681	40.287	7.6

Table A5 continued

7	1	2	0	2.02315	44.759	0.5
8	2	1	0	2.01107	45.043	0.1
9	1	2	1	1.70038	53.875	26.5
10	2	1	1	1.69319	54.122	31.1
11	2	2	0	1.59464	57.770	10.9
12	0	0	2	1.56900	58.806	6.1
13	1	3	0	1.43202	65.083	6.3
14	2	2	1	1.42063	65.670	6.0
15	1	1	3	1.40785	66.343	12.6
16	0	3	1	1.36139	68.918	6.7
17	3	0	1	1.35039	69.560	6.0
18	1	3	1	1.30278	72.495	0.1
19	0	2	2	1.29005	73.326	4.1
20	2	0	2	1.28586	73.604	4.1
21	2	3	0	1.25335	75.845	0.1
22	3	2	0	1.24855	76.188	0.1
23	1	2	2	1.23985	76.820	0.1
24	2	1	2	1.23705	77.026	0.1
25	2	3	1	1.16394	82.875	4.8

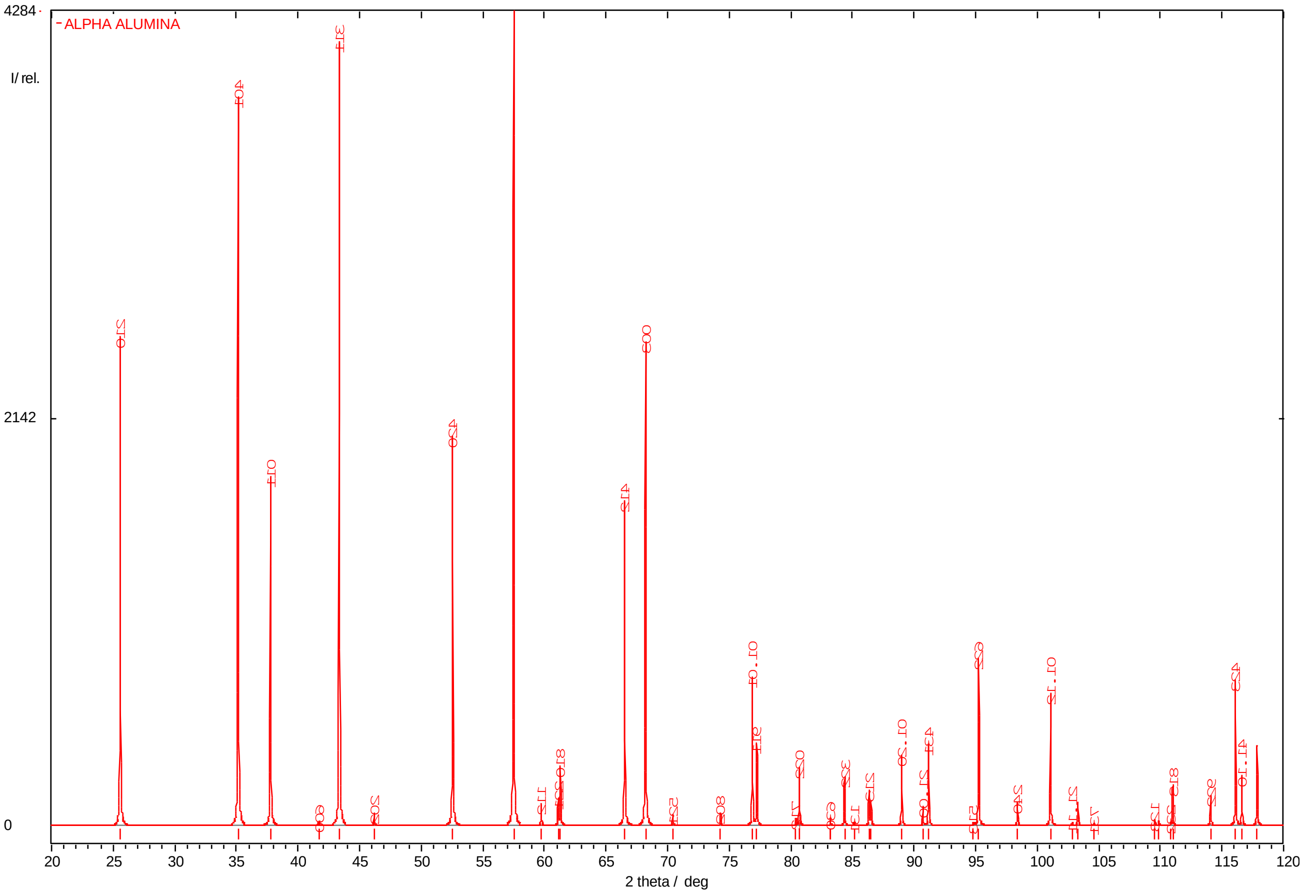

Figure A1. Simulated diffraction peaks for alpha alumina using Powdercell.

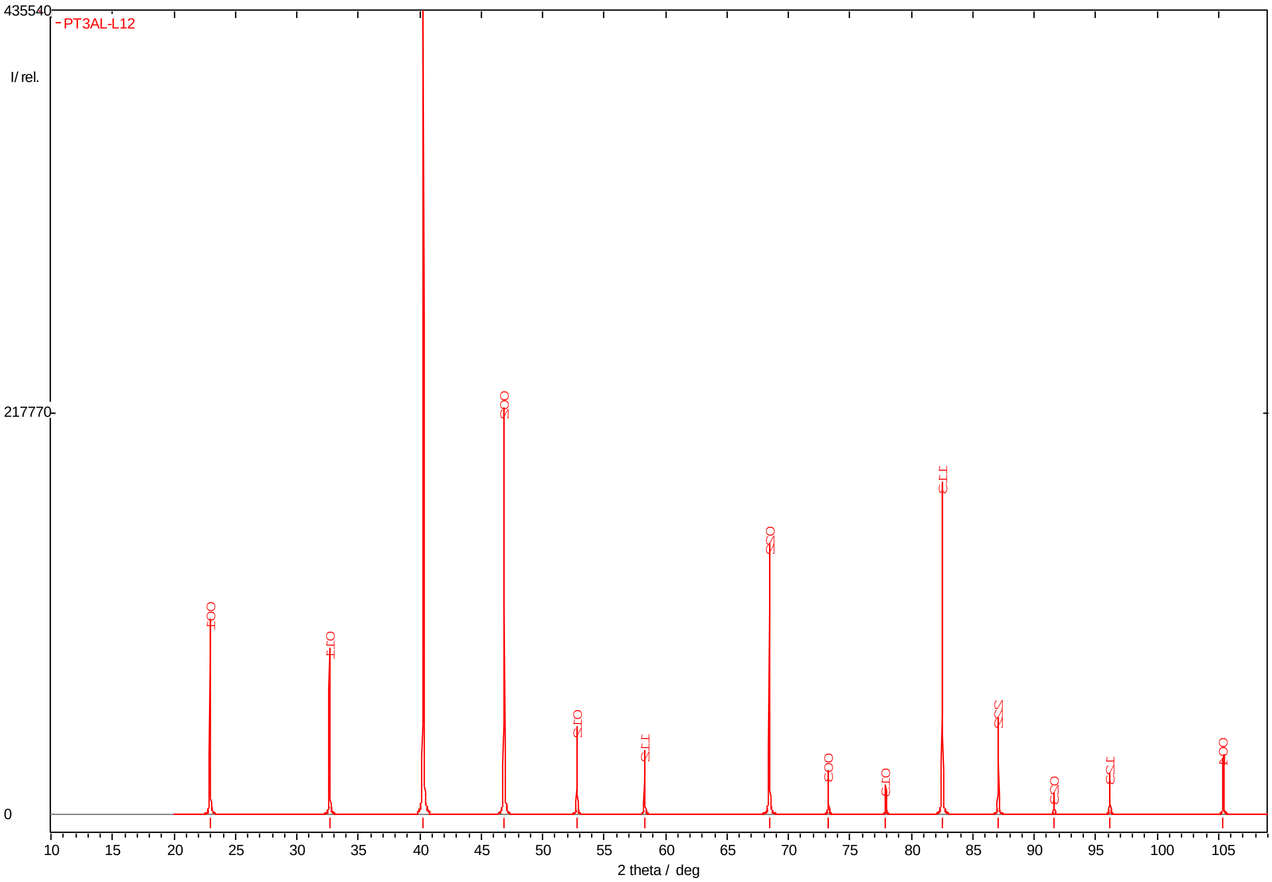

Figure A2. Simulated diffraction pattern for Pt_3Al-L12 using Powdercell.

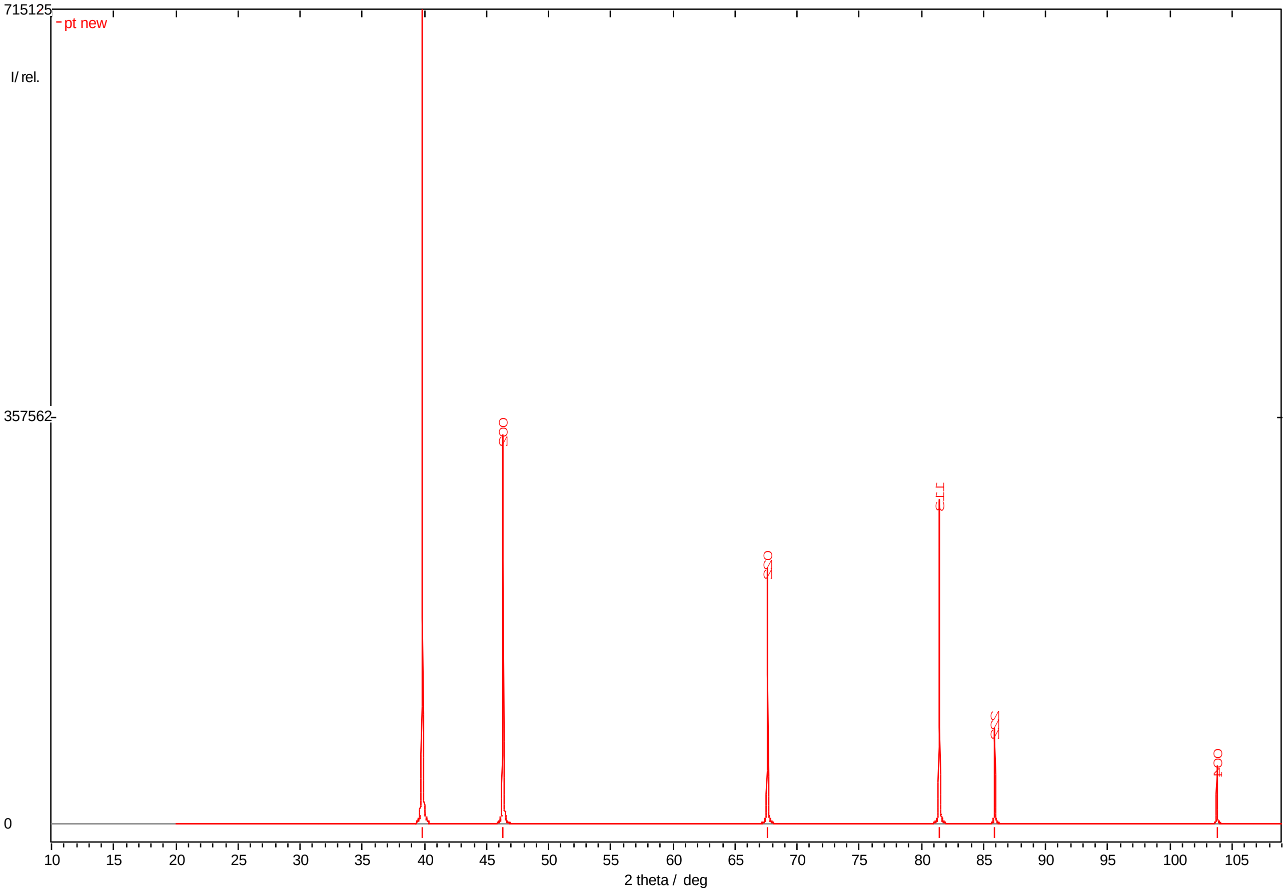

Figure A2. Simulated diffraction pattern for Pt using Powdercell.

Appendix B. Calculation of activation energy, Q_A, from Arrhenius equation.

Arrhenius equation [1962Kub] is:

$$k_p = k_o \ .\exp\left(\frac{-Q_A}{R\ .T}\right)$$

where k_p is the parabolic rate constants ($g^2/cm^4.s$), k_o is the pre exponential factor, R is the gas constant (8.31J/Kmol) and T is the absolute temperature (Kelvin).

Take the natural log of both side of the Equation yields,

$$lnk_p = \ln k_o - \frac{Q_A}{R.T}$$

Divide both sides of the equation by 2.303 to convert to $\log_{10}$

$$\frac{\ln k_p}{2.303} = \frac{\ln k_o}{2.303} - \frac{Q_A}{2.303.R.T}$$

and

$$logk_p = \log k_o - \frac{Q_A}{19.14}\ .\frac{1}{T}$$

Thus, the slope of the plot of $logk_p$ against $\frac{1}{T}$ will be $-\frac{Q_A}{19.14}$, where:

$$Q_A = -\ \text{slope} \times 19.14\ \text{(J/mol)}$$

Appendix C. Conference Presentations

The following presentations were made during the course of this study:

1. J.K.Odusote, L.A. Cornish, L.H. Chown and K. Pruessner, Oxidation Behaviour of a Precipitation Hardened Pt-based Superalloy $Pt_{84}:Al_{11}:Cr_{3}:Ru_{2}$ (at.%) in air at 1350ºC, Proceeding of the Microscopy Society of Southern Africa, Warmbath Conference, Volume 40, (2010), p.51.
2. O.M. Bill, J.K. Odusote and K. Pruessner, Effect of Preparation on the Surface Quality of Ni-based and Pt-based Superalloys, Procceding of the 54th Annual Conference of the South Africa Institute of Physics, University of KwaZulu-Natal, 6th-10th July, 2009, p.71.